UNIVERSITY OF SOUTHAMPTON

FACULTY OF PHYSICAL SCIENCES AND ENGENEERING

School of Physics and Astronomy
Southampton High Energy Physics

Understanding and predicting low-energy neutrino parameters with leptogenesis

by

Michele Re Fiorentin

Thesis for the degree of Doctor of Philosophy

May 2016

UNIVERSITY OF SOUTHAMPTON

ABSTRACT

FACULTY OF PHYSICAL SCIENCES AND ENGENEERING
School of Physics and Astronomy
Southampton High Energy Physics

Doctor of Philosophy

UNDERSTANDING AND PREDICTING LOW-ENERGY NEUTRINO PARAMETERS WITH LEPTOGENESIS

by Michele Re Fiorentin

In this work, we address two major problems of the Standard Model of particle physics: the baryon asymmetry of the Universe and neutrino masses and mixing. A strict link between these two aspects can be established by the seesaw mechanism and leptogenesis. This connection can be fruitfully exploited to gain information on neutrino parameters. To this aim, we first introduce the type-I seesaw mechanism and leptogenesis, moving then to the strong thermal leptogenesis scenario. Here a large pre-existing asymmetry is efficiently erased by leptogenesis, and an analytical lower bound on the absolute neutrino mass scale can be derived. We then consider $SO(10)$-inspired leptogenesis, in which a set of conditions kindred to those realised in $SO(10)$ Grand Unification Theories is imposed on the seesaw setup. A rigorous analytical study of this scenario is performed, allowing us to obtain analytical explanations of the numerous predictions on neutrino parameters. $SO(10)$-inspired and strong thermal $SO(10)$-inspired leptogenesis appear then to represent a very interesting scenario, rich of definite predictions on neutrino parameters that will be in the reach of forthcoming experiments. Finally, we examine the supersymmetric extension of $SO(10)$-inspired leptogenesis, analysing how the constraints on neutrino parameters change. The lower bound imposed by thermal leptogenesis on the reheating temperature is carefully studied, in light of the gravitino problem. We conclude that the thermal leptogenesis scenario represents an intriguing and viable mechanism also in the supersymmetric framework.

Contents

II Understanding and predicting neutrino parameters 85

List of Figures

List of Tables

Declaration of Authorship

I, Michele Re Fiorentin, declare that the thesis entitled *"Understanding and predicting low-energy neutrino parameters with leptogenesis"* and the work presented in the thesis are both my own, and have been generated by me as the result of my own original research. I confirm that:

- this work was done wholly or mainly while in candidature for a research degree at this University;
- where any part of this thesis has previously been submitted for a degree or any other qualification at this University or any other institution, this has been clearly stated;
- where I have consulted the published work of others, this is always clearly attributed;
- where I have quoted from the work of others, the source is always given. With the exception of such quotations, this thesis is entirely my own work;
- I have acknowledged all main sources of help;
- where the thesis is based on work done by myself jointly with others, I have made clear exactly what was done by others and what I have contributed myself;
- parts of this work have been published as: [1–6]

Signed:..

Date:.........12/05/2016...

Acknowledgements

Writing the acknowledgements of a work such as a doctoral thesis is indeed complicated for me. Many people have provided me with their precious assistance, and dropping someone out, in a moment of distraction, is unfortunately almost inevitable.

First and foremost I would like to thank my supervisor, Pasquale Di Bari, for his help and support during these years. The experience I gained during my PhD is mostly due to him, as well as my professional development and growth. I am deeply obliged to him for his scientific guidance and human understanding.

I wish to acknowledge the support of the School of Physics and Astronomy in several, sometimes complicated, circumstances. In this regard, I would like to thank Stefano Moretti, Steve King, Tim Morris as well as Tony Bird and Christian Knigge. I am very grateful for their help.

I must also thank the Southampton Theory Astrophysics and Gravity (STAG) Research Centre for the financial support during my PhD.

I am profoundly indebted to Fiorenza Donato, Nicolao Fornengo and all the Physics Department of the University of Torino for the kind hospitality. Many thanks also go to Mariaelena Boglione. Words cannot do justice to their invaluable help.

I cannot forget my family, which provided me with constant support along this adventure, in the happy as well as in the harder moments. This work is dedicated to them.

Finally, I want to acknowledge my friends. I am very grateful for the length of their list, however, it is impossible for me to write it down exhaustively here.
Firstly, I must mention my Southampton friends that cheered up my stay and helped me in uncountable ways. In strict alphabetical order: Sophie King, Luca Marzola, Elena Mavrona, Thomas Neder, Luca Panizzi, Francesco Sanfilippo, Tobi Tsang, ...
Then, I must express my warmest gratitude to all the other dear friends of mine that have walked with me for a long, or a short, part of my life, being always ready to advise, comfort and forgive. Always in alphabetical order: Lorenzo Bianchi, Andrea Celon, Martina Cornagliotto, Setareh Fatemi, Raquel Gomez, Mattia Ivaldi, Riccardo Longo, Enrico Perucca, Amedeo Primo, Sara Siragusa, Barbara Šoda, Eugenio Valdano, ...
To all of them, as well, this work is dedicated.

Abbreviations

$0\nu\beta\beta$	Neutrinoless Double-Beta (Decay)
BAO	Baryon Acoustic Oscillations
BBN	Big Bang Nucelosynthesis
CKM	Cabibbo-Kobayashi-Maskawa
C.L.	Confidence Level
CMB	Cosmic Microwave Background
DE	Dark Energy
DM	Dark Matter
EW	Electroweak
EWSSB	Electroweak Spontaneous Symmetry Breaking
GUT	Grand Unified Theory
IO	Inverted Ordering
LH	Left Handed
NO	Normal Ordering
PDF	Probability Density Function
PMNS	Pontecorvo-Maki-Nakagawa-Sakata
RH	Right Handed
SM	Standard Model
VEV	Vacuum Expectation Value

Such wilt thou be to me, who must,
Like th' other foot, obliquely run;
Thy firmness makes my circle just,
And makes me end where I begun.

— John Donne, *Songs and Sonnets*

Chapter 1

Introduction

With the discovery of the Higgs boson at the LHC [7–9], the Standard Model (SM) [10–12] confirmed once more its validity in the description of particle physics. Intensive searches have been carried out on the experimental side to put to test this model, in order to understand its validity regime. So far, collider experiments have only been able to highlight some faint deviations from the SM paradigm, without showing any substantial discrepancy form theoretical predictions. However, several issues have been raised, pointing out that the SM cannot be the complete theory of nature.

Firstly, it is clear that the SM, with its quantum field theory foundations, is not able to explain gravity in the same way as the other fundamental interactions. For this reason, already from the point of view of scientific speculation, the SM necessarily appears as a non-exhaustive theory.

In addition to this, several experimental evidences highlight the incompleteness of this model. Cosmological observations have pointed out that the Universe is mainly composed of constituents which are not accounted for in the SM: Dark Energy (DE) and Dark Matter (DM). At the same time, in the SM there is no satisfactory justification for the preponderance of matter over antimatter in the Universe. The experimental evidence of the matter/antimatter asymmetry of the Universe cannot be explained within the SM framework, thus requiring new physics contributions.

Inconsistencies inside the SM itself have been found as well. In the model, neutrinos are described as massless fields. However, it has been proven that these particles oscillate among flavours, a phenomenon that cannot take place if all neutrinos are massless. Neutrino oscillations therefore represent another clear support for physics not contemplated in the SM.

In this work we shall put aside the striking issues of DM and DE, and we shall deal with the dynamical production of the matter/antimatter asymmetry of the Universe, in connection with neutrino oscillations. Let us now introduce these two problems.

1.1 The baryon asymmetry of the Universe

It is an experimentally solid evidence that the amount of matter in the Universe is larger than that of antimatter. An equal amount of matter and antimatter would have basically resulted in a general annihilation into an "empty" Universe, filled only with radiation. Since this is not the case, the necessity to account for this fundamental asymmetry arises. Although this problem can be ascribed to the indisputable initial conditions of the Universe, it is more interesting and more scientific to look for a dynamical mechanism able to generate the asymmetry we observe, starting from an initially symmetric Universe. This is the approach we will undertake. We shall now discuss the fundamental features of such a mechanism.

1.1.1 Sakharov's conditions

A dynamical mechanism able to produce a final asymmetry between matter and antimatter starting from symmetric initial conditions, must satisfy three conditions, first pointed out by A. Sakharov [13].

1. **Baryon number violation**. The dominant amount of matter in the Universe is represented by baryons. Therefore, the matter/antimatter asymmetry is more precisely referred to as *baryon asymmetry.* In the SM, baryons are associated to an accidental global $U(1)$ symmetry that, at the classical level, implies the conservation of its related charge: the baryon number B. However, in the SM baryon number (together with the lepton number L) is violated at the quantum level by non-perturbative processes that we shall analyse in more detail in the following chapter (see subsection 2.2.1.1).
   Nevertheless, in order to have an asymmetry between baryons and antibaryons starting from an initially symmetric Universe, we necessarily need some asymmetry production processes that violate the baryon number, $\Delta B \neq 0$.

2. C **and** CP **violation**. It is clear that in order to generate an asymmetry between particles and antiparticles we must violate the charge conjugation symmetry, C. However, if our theory distinguishes between chiralities, we need to violate also the charge-parity symmetry, CP.
   Let us consider the decay of particle N into left-handed (LH) particles, $N \to l_L$ and into right-handed (RH) particles $N \to l_R$. If C is violated we have that the charged-conjugated reaction rates are different

$$\Gamma(N \to l_L) \neq \Gamma(\overline{N} \to \overline{l_L}), \quad \text{and} \quad \Gamma(N \to l_R) \neq \Gamma(\overline{N} \to \overline{l_R}). \tag{1.1}$$

However, if CP is *not* violated, we have that the rates of the CP-conjugated reactions are the same

$$\Gamma(N \to l_L) = \Gamma(\overline{N} \to \overline{l_R}), \quad \text{and} \quad \Gamma(N \to l_R) = \Gamma(\overline{N} \to \overline{l_L}). \tag{1.2}$$

If we now consider the total decay rates into particles and antiparticles, due to eq. (1.2) we have

$$\Gamma(N \to l_L) + \Gamma(N \to l_R) = \Gamma(\overline{N} \to \overline{l_R}) + \Gamma(\overline{N} \to \overline{l_L}). \tag{1.3}$$

Total decays into particles and antiparticles proceed at the same rate, and it is then impossible to generate an asymmetry. Therefore, in order to produce an asymmetry, both C and CP must be violated.

3. **Departure from thermal equilibrium**. Even if baryon number is violated, if thermal equilibrium is enforced, no net change ΔB can occur during the Universe evolution. Indeed, in thermal equilibrium we can compute the thermal average of B

$$\begin{aligned}\langle B\rangle_T &= \mathrm{tr}\Big[e^{-H/T}B\Big] = \mathrm{tr}\Big[(CPT)(CPT)^{-1}e^{-H/T}B\Big] \\ &= \mathrm{tr}\Big[e^{-H/T}(CPT)^{-1}B(CPT)\Big] = -\mathrm{tr}\Big[e^{-H/T}B\Big]\,,\end{aligned} \tag{1.4}$$

hence $\langle B\rangle_T = 0$. Here we have used that CPT is a conserved symmetry, that the hamiltonian H commutes with CPT and the fact that B is CPT odd.

A dynamical mechanism able to generate a final baryon asymmetry must satisfy all these three conditions simultaneously. In chapter 2 we shall study in detail how these are satisfied within a real class of models.

1.1.2 The baryon-to-photon ratio

The mechanism we are looking for must be able to produce the asymmetry in the correct amount, matching the experimental results obtained from cosmological observations. In order to quantify the baryon asymmetry, it is customary to define the quantity

$$\eta_B \equiv \frac{n_B - n_{\bar{B}}}{n_\gamma}, \tag{1.5}$$

where n_B, $n_{\bar{B}}$ and n_γ are the number densities of baryons, antibaryons and photons respectively. Given that we do not observe a significant antibaryon density, we can set $n_{\bar{B}} = 0$, so that η_B actually measures the *baryon-to-photon ratio* of the Universe. It is possible to obtain the value of η_B mainly from the study of Big Bang Nucleosynthesis (BBN) and from the Cosmic Microwave Background (CMB) radiation.

1.1.2.1 η_B from the Big Bang Nucleosynthesis

BBN is the process, within the cosmological standard model, by which light elements are produced in the Early Universe. It takes place at temperatures around $T_{\text{BBN}} \simeq 0.1\,\text{MeV}$, when the abundances of light nuclei, mainly ^{4}He, reach their final values. BBN can be regarded as a brilliant success of the cosmological standard model, due to the excellent agreement of its prediction with the actual measurements of primordial light nuclei abundances.
Primordial abundances basically depend on three parameters.

- **Neutron half-life τ_n.** This particle physics parameter rules the weak interaction reactions that keep neutrons and protons in equilibrium. Indeed the neutron-proton interaction rate is $\Gamma_{\text{np}} \propto T^5/\tau_n$. These reactions fall out of thermal equilibrium at a certain freeze-out temperature T_F at which the rate becomes slower than the Universe expansion rate, $\Gamma_{\text{np}}/H < 1$. This temperature is directly linked to the value of τ_n and for its experimental value we have $T_F \simeq 1\,\text{MeV}$. A larger value of τ_n would decrease the interaction rate, giving higher values of T_F and hence higher values of the neutron-to-proton ratio. This in turn would imply a larger production of light elements, especially ^{4}He.

- **Number of relativistic degrees of freedom g_*.** The expansion rate is proportional to the number of relativistic degrees of freedom $H \propto g_*^{1/2} T^2$. A change in the value of g_* implies a change in the freeze-out temperature T_F, and hence a change in the final light element abundances. This feature can also be employed in order to gain information on the number of relativistic degrees of freedom, constraining, for instance, the number of neutrino species.

- **Baryon-to-photon ratio η_B.** The value of the abundances is proportional to the baryon-to-photon ratio. In particular, higher values of η_B would allow an earlier growth of deuterium and ^{3}He abundances, which in turn would then be burnt into ^{4}He. A larger value of η_B would then imply a higher ^{4}He abundance. Moreover, the same D, ^{3}He, together with ^{7}Li abundances show a peculiar sensitivity to the value of η_B, thus representing a very important probe.

From cosmological observations of the primordial element abundances and employing the most precise determination of the other free parameters, it is then possible to determine the value of the baryon-to-photon ratio from BBN. Employing data on deuterium and ^{4}He it was recently obtained [14]

$$\eta_B^{\text{BBN}} = (6.172 \pm 0.195) \times 10^{-10}. \tag{1.6}$$

1.1.2.2 η_B from the Cosmic Microwave Background

The baryon-to-photon ratio can be very precisely measured by means of the analysis of the CMB anisotropies angular power spectrum. The CMB was "accidentally" discovered in 1964 [15] as very highly isotropic radiation field coming from the Universe. It is made of the photons released in the Early Universe at the recombination era, $T_0 \simeq 0.3\,\mathrm{eV}$, when neutral atoms were formed and photon interaction with matter suddenly became very suppressed, thus decoupling matter and radiation. It shows a perfect black-body spectrum with an average temperature $T_{\rm today} \simeq 2.72\,\mathrm{K}$, as predicted by the standard cosmological model. However, the most interesting feature of the CMB is provided by its subtle temperature anisotropies around the sky. It is therefore possible to map the sky and expand the temperature fluctuation field in terms of spherical harmonics functions, as

$$\frac{\Delta T}{\langle T \rangle}(\hat{n}) = \sum_{l,m} a_{lm} Y_{lm}(\hat{n}), \tag{1.7}$$

where $\hat{n}$ gives a specific direction in the sky. Hence, a power spectrum can be obtained as a function of the multipole moment l

$$C_l = \frac{1}{2l+1} \sum_{m=-l}^{l} \langle |a_{lm}|^2 \rangle. \tag{1.8}$$

This angular power spectrum is physically originated by the oscillations of baryons and radiation in the gravitational potential wells provided by Dark Matter. These oscillations created more dense and more rarefied regions in the Early Universe, which left a clear signature on the temperature of the photons released at recombination. Therefore, the CMB angular power spectrum is extremely powerful at determining the content of the Early Universe. In particular, for our purposes, it is possible to precisely measure the baryonic density $\omega_B = \Omega_B\, h^2$, where

$$\Omega_B \equiv \frac{\rho_B}{\rho_c}, \qquad H_0 = 100\, h\, \mathrm{km\, s^{-1}\, Mpc^{-1}}, \tag{1.9}$$

$\rho_c \equiv 3H^2 M_{\rm Pl}^2/8\pi$ is the critical density, ρ_B is the baryon energy density and H_0 the Hubble constant at the present day. Increasing the baryon density results in an enhancement of the odd peaks in the power spectrum with respect to the even ones, so that the amplitude ratio of the second and third peaks is particularly sensitive to ω_B [16].

From Ω_B it is then easy to obtain the value of the baryon-to-photon ratio

$$\eta_B = \frac{n_B}{n_\gamma} = \frac{\rho_B}{m_p\, n_\gamma} = \frac{\Omega_B \rho_c}{m_p\, n_\gamma} \simeq 273.6\, \Omega_B h^2, \tag{1.10}$$

where m_p is the proton mass. The CMB angular power spectrum is often combined with other cosmological measurements in order to reduce some degeneracies and help constraining the parameters. Particularly powerful complementary data are provided by Baryon Acoustic Oscillations (BAO) and, more recently, by the study of CMB polarisation. From the latest Planck results [17], we can conservatively obtain

$$\eta_B^{\mathrm{CMB}} = (6.1 \pm 0.1) \times 10^{-10}. \tag{1.11}$$

The evolution of the baryon number density n_B after recombination is ruled by Universe expansion only (i.e. we assume no other mechanism changes the number of baryons in the era between recombination and the present day), so that

$$n_B(T_{\mathrm{today}}) = \frac{s(T_{\mathrm{today}})}{s(T_0)} n_B(T_0), \tag{1.12}$$

where $s(T)$ is the entropy density. We therefore have

$$\eta_B(T_{\mathrm{today}}) = \frac{n_B(T_{\mathrm{today}})}{n_\gamma(T_{\mathrm{today}})} = \frac{s(T_{\mathrm{today}})}{s(T_0)} \frac{n_\gamma(T_0)}{n_\gamma(T_{\mathrm{today}})} \frac{n_B(T_0)}{n_\gamma(T_0)} = \frac{s(T_{\mathrm{today}})}{s(T_0)} \frac{n_\gamma(T_0)}{n_\gamma(T_{\mathrm{today}})} \eta_B^{\mathrm{CMB}}. \tag{1.13}$$

Since $s(T) \propto g_*^s(T) T^3$ and $n_\gamma(T) \propto T^3$, we have

$$\eta_B(T_{\mathrm{today}}) = \frac{g_*^s(T_{\mathrm{today}})}{g_*^s(T_0)} \eta_B^{\mathrm{CMB}}, \tag{1.14}$$

where $g_*^s(T)$ counts the relativistic degrees of freedom contributing to the entropy density. However, the relativistic degrees of freedom in the SM do not change from the recombination era to the present day, therefore $g_*^s(T_{\mathrm{today}}) = g_*^s(T_0)$, so that the baryon-to-photon ratio measured from the CMB is a measure of present day η_B as well.
In the rest of this work, we shall employ the CMB measurement of the baryon-to-photon ratio, eq. (1.11), as the fiducial experimental estimation of the baryon asymmetry of the Universe. Therefore, our sought production mechanism will be required to be able to reproduce this experimental value.

It must be mentioned that the SM itself can satisfy the Sakharov's conditions. Indeed, baryon number is violated by non-perturbative processes such as electroweak sphalerons, *C* and *CP* are violated by the Cabibbo-Kobayashi-Maskawa (CKM) quark mixing matrix while the out-of-equilibrium dynamics can be provided by the Electroweak Spontaneous Symmetry Breaking (EWSSB). Exploiting these features, it is in principle possible to generate a baryon asymmetry within the SM, through the so-called *electroweak baryogenesis* [18]. However, this scenario ultimately fails to produce the required size of *CP* asymmetry [19] and appears in conflict with the found value of the Higgs boson mass. For these reasons, the baryon asymmetry of the Universe indeed represents a problem that cannot be solved in the framework of the SM.

1.2 Neutrino oscillations

Neutrino oscillations were first theoretically predicted by B. Pontecorvo in 1957 [20], but solid experimental evidences were found only in the last few decades.
The first experimental hint at neutrino oscillations came from the so-called "solar neutrino problem". The Homestake experiment results showed a critical deficit of measured neutrino flux [21] with respect to the prediction of the Standard Solar Model, mainly developed by J. Bahcall [22]. This result was confirmed by other experiments such as SAGE [23], GALLEX [24] and Super-Kamiokande [25]. The puzzle was finally solved by the SNO experiment [26] in 2001. The first experiments detected neutrinos via charged-current interactions or elastic scattering, thus being only sensitive to electron neutrinos. By using a heavy-water Čerenkov detector, the SNO experiment was sensitive to all flavours, through neutral current interactions. The total flux measured by SNO was in agreement with the Standard Solar Model prediction, thus supporting the idea that the deficit in the electron neutrino flux could be due to the "disappearance" of ν_e's that had oscillated into ν_μ's and ν_τ's in their propagation.
In the meantime, the Super-Kamiokande experiment highlighted a different issue in the flux of neutrinos produced by cosmic rays in the atmosphere. The measured flux of muon neutrinos and antineutrinos showed an anomalous dependence on the zenith angle [27], which was not registered in the electron (anti)neutrino flux. This anomaly took the name of "atmospheric neutrino problem" and could naturally find an explanation in the oscillation $\nu_\mu \to \nu_\tau$ and $\bar{\nu}_\mu \to \bar{\nu}_\tau$.
The solar and atmospheric neutrino problems thus solidly established that neutrinos oscillate among different flavours, in contrast with the prediction of the SM. For the discovery of neutrino oscillations both the SNO and Super-Kamiokande experiments were awarded the Nobel Prize for Physics in 2015, in the persons of Arthur McDonald and Takaaki Kajita respectively.
In the following years, several other experiments have joined the challenge of determining with precision the parameters ruling neutrino oscillations. Together with solar and atmospheric neutrinos, also antineutrinos from nuclear reactors have been measured and studied. It is worth mentioning the contribution of KamLAND [28] in the determination of the so-called "solar mixing angle" and, later, of DayaBay [29], followed by RENO [30] and DoubleChooz [31], in the precise measurement of the "reactor mixing angle".
Moreover, also neutrino beams from accelerators have been detected and studied. Particularly interesting is the T2K experiment, that has firmly established the electron neutrino appearance in a beam of muon neutrinos, thus helping constraining several mixing parameters [32, 33]. The OPERA experiment has also provided strong direct evidence of $\nu_\mu \to \nu_\tau$ oscillation [34].
We shall now briefly overview the theoretical description of neutrino oscillations[1] and

---

[1] We shall deal here with the standard plane-wave approximation, while not considering the more correct and detailed wave-packet treatment (see e.g. [35]). This is enough for our purposes of pointing out the basic features and the involved low-energy neutrino parameters.

its consequences, highlighting the parameters that are required and experimentally measured.

1.2.1 Neutrino mixing

Neutrino interactions in the SM take place only through weak charged and neutral currents, coupled to the W and Z bosons respectively. We can define the neutrino states that are produced in the weak interactions as *flavour eigenstates* $|\nu_\alpha\rangle$, since, via charged currents, they always interact with the charged lepton of corresponding flavour. If we now assume, as in the SM, that neutrinos are massless, then the hamiltonian eigenstates $|\nu_i\rangle$, that are involved in the propagation, can be made coincide with the flavour eigenstates. Interaction and propagation eigenstates are then the same and no particular phenomenon occurs.

However, considering massive neutrinos can spoil this alignment. The hamiltonian eigenstates, that we can now also call *mass eigenstates*, do not necessarily coincide with flavour eigenstates. Assuming 3 mass eigenstates and a misalignment between flavour and mass eigenstates we can write

$$|\nu_\alpha\rangle = \sum_{i=1}^{3} U_{\alpha i}^{*}\, |\nu_i\rangle, \tag{1.15}$$

that is, flavour eigenstates can be seen as a linear combination of mass eigenstates through the unitary matrix U.

We can now consider a neutrino produced by weak interaction in a certain flavour α and study its propagation through spacetime to a detector in which it is measured by another weak interaction. The neutrino will therefore propagate until time t, $|\nu_\alpha(t)\rangle$, at which it is measured in the detector. We can compute the probability of measuring the propagated neutrino along the flavour β

$$P_{\nu_\alpha \to \nu_\beta}(t) \equiv |\langle \nu_\beta | \nu_\alpha(t)\rangle|^2 . \tag{1.16}$$

Since now flavour and hamiltonian eigenstates do not coincide, the time evolution of state $|\nu_\alpha\rangle$ gets less trivial, depending on the evolution of states $|\nu_i\rangle$. Employing the time evolution operator, we obtain

$$|\nu_\alpha(t)\rangle = \sum_{i=1}^{3} U_{\alpha i}^{*}\, e^{-iE_i t} |\nu_i\rangle, \tag{1.17}$$

being $|\nu_i\rangle$ the mass/hamiltonian eigenstate of eigenvalue E_i. We therefore have

$$P_{\nu_\alpha \to \nu_\beta}(t) = \sum_{i,j} U_{\alpha i}^{*} U_{\beta i} U_{\alpha j} U_{\beta j}^{*}\, e^{-i(E_i - E_j)t}, \tag{1.18}$$

where we used the normalisation $\langle \nu_i | \nu_j \rangle = \delta_{ij}$.
For the hamiltonian eigenstate with mass m_i we can approximate

$$E_i \simeq E + \frac{m_i^2}{2E}, \tag{1.19}$$

where $E = |\vec{p}|$, neglecting the mass contribution. Therefore we have

$$E_i - E_j \simeq \frac{\Delta m_{ij}^2}{2E}, \tag{1.20}$$

where we defined the squared-mass differences

$$\Delta m_{ij}^2 = m_i^2 - m_j^2. \tag{1.21}$$

Moreover, since neutrinos are ultrarelativistic, we can also take $t = L$ so that

$$P_{\nu_\alpha \to \nu_\beta}(t) = \sum_{i,j} U_{\alpha i}^* U_{\beta i} U_{\alpha j} U_{\beta j}^* \exp\left(-i \frac{\Delta m_{ij}^2 L}{2E} \right). \tag{1.22}$$

We can see, therefore, that even if $\beta \neq \alpha$, there is a certain probability of measuring, at time t in the detector, a neutrino of a different flavour than what was produced. The probability $P_{\nu_\alpha \to \nu_\beta}$ with $\alpha \neq \beta$ is called *transition probability*, while for $\alpha = \beta$ it takes the name of *survival probability*. From eq. (1.22), we can notice that the oscillation probability depends on the entries of the unitary matrix U and on the mass-squared differences Δm_{ij}^2. It is clear that in order to account for the observed neutrino oscillations it is necessary that at least two neutrinos are massive and non-degenerate, so that $\Delta m_{ij}^2 \neq 0$. The experimental discovery of neutrino oscillations thus implies that neutrinos cannot be massless as considered in the SM. For this reason, the SM must be expanded in order to provide a description and an explanation for neutrino masses and mixing.

From oscillation experiments, two mass-squared differences have been determined, Δm_{atm}^2 and Δm_{sol}^2, with $\Delta m_{\text{atm}}^2 \gg \Delta m_{\text{sol}}^2$. However, these experiments are not sensitive to neutrino absolute masses, therefore these two mass differences can be accommodated in the neutrino mass spectrum in two different ways. Always assuming the pattern $m_1 < m_2 < m_3$, we can have

$$m_3^2 - m_2^2 = \Delta m_{\text{atm}}^2, \qquad m_2^2 - m_1^2 = \Delta m_{\text{sol}}^2, \tag{1.23}$$

which is referred to as Normal Ordering (NO), or

$$m_3^2 - m_2^2 = \Delta m_{\text{sol}}^2, \qquad m_2^2 - m_1^2 = \Delta m_{\text{atm}}^2, \tag{1.24}$$

which takes the name of Inverted Ordering (IO). These two patterns are still both viable, even though, as we shall see in the rest of this work, they generally provide different

theoretical predictions.
It is useful to define two mass scales

$$m_{\text{atm}} \equiv \sqrt{m_3^2 - m_1^2}, \qquad m_{\text{sol}} \equiv \sqrt{\Delta m_{\text{sol}}^2}, \tag{1.25}$$

so that

$$\text{NO} \begin{cases} m_2 = \sqrt{m_1^2 + m_{\text{sol}}^2} \\ m_3 = \sqrt{m_1^2 + m_{\text{atm}}^2} \end{cases}, \qquad \text{IO} \begin{cases} m_2 = \sqrt{m_1^2 + m_{\text{atm}}^2 - m_{\text{sol}}^2} \\ m_3 = \sqrt{m_1^2 + m_{\text{atm}}^2} \end{cases}. \tag{1.26}$$

From global analysis of neutrino oscillation data we obtain [36]

$$m_{\text{atm}} \simeq 0.0495\,\text{eV}, \qquad m_{\text{sol}} \simeq 0.0087\,\text{eV}. \tag{1.27}$$

Neutrino mass spectra given by eq. (1.26) using the experimental values in eq. (1.27) are plotted in fig. 1.1. We can notice that for $m_1 \lesssim 3\,\text{meV}$ neutrino spectrum is fully hierarchical, in particular for NO. For higher neutrino masses $m_1 \gtrsim m_{\text{atm}}$ we can say that neutrino masses are *quasi-degenerate*.

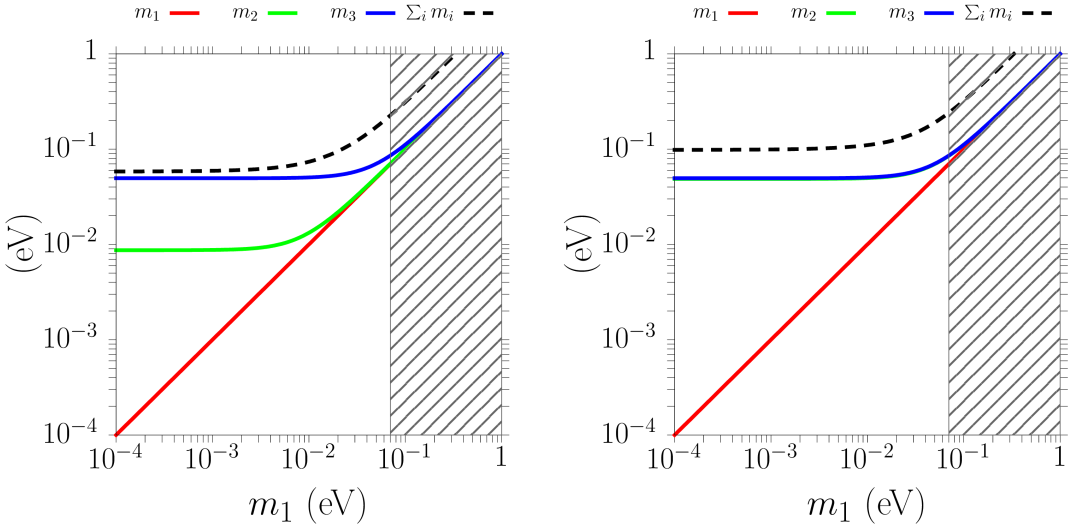

(a)

(b)

Figure 1.1: Neutrino masses vs. m_1 for NO (left panel) and IO (right panel). Red, green and blue lines are m_1, m_2 and m_3 respectively, obtained from eqs. (1.26) and (1.27). The dashed black line represents the sum of the neutrino masses $\sum_i m_i$. The hatched region marks the cosmological upper bound eq. (1.43).

The unitary matrix U is referred to as *neutrino mixing matrix* or PMNS matrix, after Pontecorvo-Maki-Nakagawa-Sakata [37, 38]. As shown in the following chapter, in its general form it can be expressed in terms of 3 mixing angles, θ_{13}, θ_{12}, θ_{23}, and 3 phases δ, ρ, σ. The three angles take also the name of "reactor", "solar" and "atmospheric" mixing angle respectively. The three phases all introduce a *CP* violation, δ is referred to as Dirac phase, while ρ and σ are the Majorana phases. For normally ordered neutrino masses, we have[2]

$$U = \begin{pmatrix} c_{12}c_{13} & s_{12}c_{13} & s_{13}e^{-i\delta} \\ -s_{12}c_{23} - c_{12}s_{23}s_{13}e^{i\delta} & c_{12}c_{23} - s_{12}s_{23}s_{13}e^{i\delta} & s_{23}c_{13} \\ s_{12}s_{23} - c_{12}c_{23}s_{13}e^{i\delta} & -c_{12}s_{23} - s_{12}c_{23}s_{13}e^{i\delta} & c_{23}c_{13} \end{pmatrix} \begin{pmatrix} e^{i\rho} & 0 & 0 \\ 0 & 1 & 0 \\ 0 & 0 & e^{i\sigma} \end{pmatrix}, \tag{1.28}$$

where $c_{ij} \equiv \cos\theta_{ij}$ and $s_{ij} \equiv \sin\theta_{ij}$. Respecting our convention of always labelling neutrino masses as $m_1 < m_2 < m_3$, in Inverted Ordering the mixing matrix is obtained from eq. (1.28) through a permutation, as

$$U^{(\mathrm{IO})} = \begin{pmatrix} s_{13}e^{-i\delta} & c_{12}c_{13} & s_{12}c_{13} \\ s_{23}c_{13} & -s_{12}c_{23} - c_{12}s_{23}s_{13}e^{i\delta} & c_{12}c_{23} - s_{12}s_{23}s_{13}e^{i\delta} \\ c_{23}c_{13} & s_{12}s_{23} - c_{12}c_{23}s_{13}e^{i\delta} & -c_{12}s_{23} - s_{12}c_{23}s_{13}e^{i\delta} \end{pmatrix} \begin{pmatrix} e^{i\sigma} & 0 & 0 \\ 0 & e^{i\rho} & 0 \\ 0 & 0 & 1 \end{pmatrix}. \tag{1.29}$$

If neutrinos are Dirac particles, the phases ρ and σ are non-physical and can be dropped. However, the probability expression in eq. (1.22) is invariant under rephasing $U_{\alpha i} \to e^{i\eta_\alpha} U_{\alpha i} e^{i\phi_i}$, so that oscillation experiments are not sensitive to the Majorana phases ρ and σ.

From [40] we can obtain the best fit values and 3σ ranges for NO and IO, which are reported in tab. 1.1 and will be employed in the rest of this work. It must be noticed that all mixing angles differ from zero with more than 5σ significance, thus definitively ruling out the $U = 1$, i.e. non-oscillation, possibility.

	Normal Ordering		Inverted Ordering	
	1σ	3σ	1σ	3σ
θ_{13}	$8.8° \pm 0.4°$	$7.6° - 9.9°$	$8.9° \pm 0.4°$	$7.7° - 9.9°$
θ_{12}	$33.7° \pm 1.1°$	$30.6° - 36.8°$	$33.7° \pm 1.1°$	$30.6° - 36.8°$
θ_{23}	$41.4°^{+1.9°}_{-1.4°}$	$37.7° - 52.3°$	$42.4°^{+8.9°}_{-1.8°}$	$38.1° - 52.3°$

Table 1.1: Best-fit, 1σ and 3σ ranges for the three mixing angles from global neutrino analysis [40], for NO and IO.

The Dirac phase δ is still loosely constrained, indeed we have [40]

$$\text{NO} \quad \delta/\pi = -0.61^{+0.38}_{-0.27}, \qquad \text{IO} \quad \delta/\pi = -0.69^{+0.29}_{-0.33}, \tag{1.30}$$

---

[2] Our parameterisation differs form the PDG one [39] in the definition of the Majorana phases. Thereby we find $\mathrm{diag}\Big(1,\, e^{i\alpha_{21}/2},\, e^{i\alpha_{31}/2}\Big)$, so that, with respect to our conventions, we have $\alpha_{21} = -2\rho$ and $\alpha_{31} = 2(\sigma - \rho)$.

while at 3σ the whole variability range $[-\pi,\, \pi]$ is still allowed.

Several current and forthcoming experiment have taken up the challenge of determining the neutrino mass ordering. In particular, we can mention the JUNO reactor experiment [41], together with the proposed PINGU [42] extension of the IceCube experiment and the currently data-taking long-baseline accelerator experiment NOνA [43]. The determination of the mass ordering basically depends on the exploitation of matter-induced resonant conversion of neutrinos (if NO) or antineutrinos (if IO). For this reason, ordering determination relies on a precise determination of the *CP* violating phase δ. Therefore, a combination of different experiments such as NOνA, T2K and the proposed LBNE [44], has the highest chances to obtain a significative result [45].

1.2.2 Neutrino masses

Given the sensitivity of neutrino oscillation experiments to mass-squared differences only, it is necessary to consider other complementary experiments in order to determine the absolute neutrino mass scale m_1.

1.2.2.1 Neutrino masses from beta decay

In a rather general way, it is possible to obtain information on the absolute neutrino masses by measuring the energy spectrum of the electron emitted by a β-decaying nucleus N_i of atomic mass and number A and Z

$$N_i(A, Z) \longrightarrow N_f(A, Z+1) + e + \bar{\nu}_e. \tag{1.31}$$

Given the Q-value of the decay

$$Q_\beta \equiv M_{N_i} - M_{N_f} - m_e, \tag{1.32}$$

the maximal kinetic energy of the electron is given by Q_β if the emitted neutrino is massless. However, if neutrinos are massive, we get that the maximal electron kinetic energy is

$$E_{\text{kin}}^{\text{max}} = Q_\beta - m_{\nu_e}. \tag{1.33}$$

Therefore, massive neutrinos imply a distortion around the endpoint of the electron energy spectrum. However, as noticed above, electron neutrino is not a mass eigenstate and mixing must be taken into account. Hence, this effect is more conveniently studied in terms of the *effective electron neutrino mass*

$$m_\beta \equiv \sum_i |U_{ei}|^2\, m_i^2, \tag{1.34}$$

on which the currently most stringent upper bound is provided by the Troitzk experiment [46]

$$m_\beta < 2.05\,\text{eV} \quad (95\%\,\text{C.L.}). \tag{1.35}$$

The most promising experiment on β-decay, employing tritium nuclei, is KATRIN [47, 48], that may probe m_β with a sensitivity of about 0.2 eV in the near future [49, 50].

1.2.2.2 Neutrino masses from neutrinoless double-beta decay

While β-decay can prove neutrino masses in a general way, if neutrinos are Majorana particles (as specified and explained in detail in the following chapter) it is possible to study a characteristic phenomenon: the *neutrinoless double-β decay* ($0\nu\beta\beta$).
Double β decay takes place naturally for certain nuclei that decay into lighter ones via two simultaneous β decays

$$N_i(A,Z) \longrightarrow N_f(A,Z+2) + 2e + 2\bar{\nu}_e, \tag{1.36}$$

as in fig. 1.2(a). However, if neutrinos are Majorana particles, it is possible to connect the two neutrino lines into the propagator of a virtual Majorana neutrino, as in fig. 1.2(b). This way, no neutrinos appear in the final state and the process results into

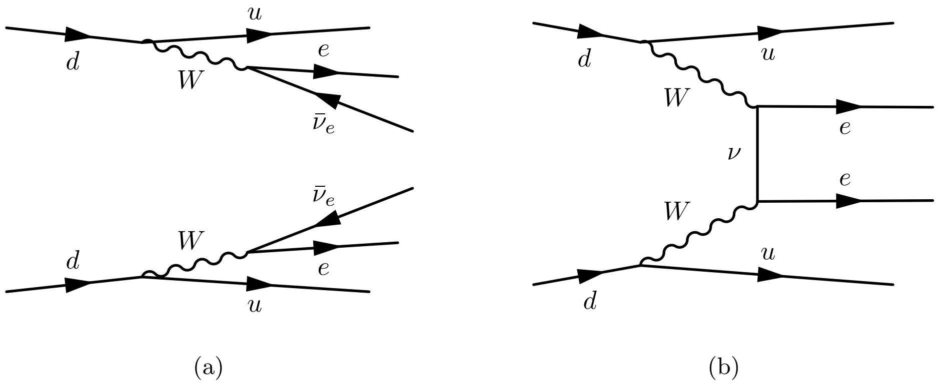

(a) (b)

Figure 1.2: Double β decay, panel (a) and neutrinoless double β decay, panel (b).

$$N_i(A,Z) \longrightarrow N_f(A,Z+2) + 2e, \tag{1.37}$$

that is a double β decay without outgoing neutrinos [51]. It must be noticed that $0\nu\beta\beta$ decay is possible if and only if neutrinos are Majorana particles [52], independently of other contributions from new physics. Therefore, experiments trying to detect $0\nu\beta\beta$ decays are of the utmost importance in determining whether neutrinos are Dirac or

Majorana particles.
The half-life of a $0\nu\beta\beta$ decaying nucleus can be expressed as

$$T_{1/2}^{0\nu\beta\beta} = (\Phi^{0\nu\beta\beta})^{-1} \left|\mathcal{M}^{0\nu\beta\beta}\right|^{-2} m_{ee}^{-2}, \tag{1.38}$$

where $\Phi^{0\nu\beta\beta}$ is the phase-space factor, $\mathcal{M}^{0\nu\beta\beta}$ is the nuclear matrix element while m_{ee} is the *effective* $0\nu\beta\beta$ *decay mass* defined as

$$m_{ee} \equiv \left|\sum_i U_{ei}^2\, m_i\right|. \tag{1.39}$$

Employing the mass scale values as in eq. (1.27), the mixing angles as in table 1.1, and taking δ, ρ, σ in their whole variability range, we can study the behaviour of m_{ee} vs. m_1, both for NO and IO. The result is shown in fig. 1.3 (adapted from [35, 53]). Thereby, the horizontal hatched region marks the current conservative upper bound obtained from experiments. The current experimental constraints on the effective $0\nu\beta\beta$ decay mass are reported in tab. 1.2. It must be noticed that experimental results on $0\nu\beta\beta$ decay must face high theoretical uncertainties in the determination of the nuclear matrix element

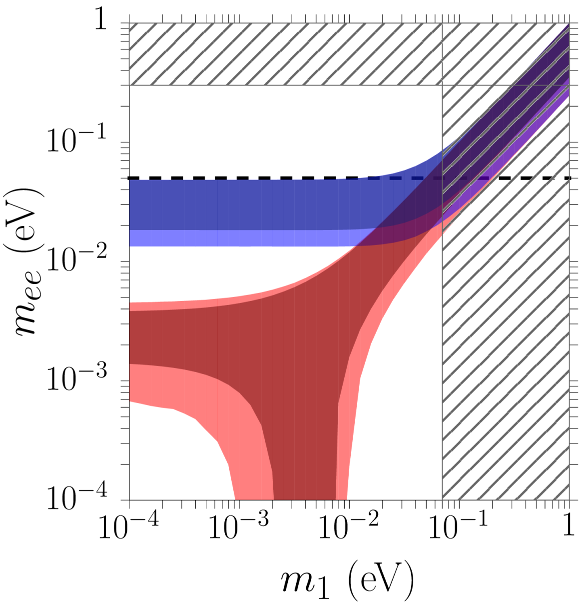

Figure 1.3: Effective $0\nu\beta\beta$ decay mass vs. m_1 for NO (red region) and IO (blue region). The lighter regions are obtained with mixing angles varying within their 3σ ranges as in tab. 1.1, while the darker regions are obtained by using their best-fit values. The vertical hatched region marks the current upper bound on m_1 imposed by cosmological observations, eq. (1.43), while the horizontal hatching marks the current conservative experimental upper bound on m_{ee}, eq. (1.40). The horizontal dashed line indicates the expected future experimental sensitivity. Plot adapted from [35, 53].

Experiment	Result at 90% C.L.
GERDA [54]	$m_{ee} < 0.22 - 0.64\,\mathrm{eV}$
EXO-200 [55]	$m_{ee} < 0.2 - 0.69\,\mathrm{eV}$
KamLAND-Zen [56]	$m_{ee} < 0.15 - 0.52\,\mathrm{eV}$

Table 1.2: Experimental upper bounds on the effective $0\nu\beta\beta$ decay mass.

$\mathcal{M}^{0\nu\beta\beta}$. We can therefore employ as a conservative upper bound on the effective $0\nu\beta\beta$ decay mass

$$m_{ee} \lesssim 0.2\,\mathrm{eV}, \tag{1.40}$$

which is marked in fig. 1.3 with the horizontal hatched region.
Experiments such as MAJORANA [57] and GERDA [58], are expected to reach, in the near future, a sensitivity around 0.05 eV (marked by the dashed line in fig. 1.3). This would be particularly interesting since it would severely constrain quasi-degenerate neutrino masses ($0.02\,\mathrm{eV} \lesssim m_1 \lesssim 0.07\,\mathrm{eV}$) while starting probing the fully hierarchical IO spectrum ($m_1 \to 0$).

1.2.2.3 Neutrino masses from cosmology

The currently most stringent information on neutrino masses comes from cosmology, which is most sensitive to their sum[3]. The massive nature of neutrinos causes modifications in the CMB angular power spectrum from what would be obtained in the massless neutrino scenario. Massive neutrinos can impact the spectrum by modifying the cosmic evolution through a shift of the matter-radiation equality, as well as by affecting secondary anisotropies via, for instance, the Integrated Sachs-Wolfe effect. However, the sensitivity to neutrino masses of the CMB spectrum alone is in practice quite little to provide solid results. For this reason, it is much more useful to combine CMB data with other observations, such as BAO data. Combining the Planck2015 CMB spectrum with polarisation data and BAO information, it is possible to place the upper bound [17]

$$\sum_i m_i < 0.17\,\mathrm{eV} \quad (95\%\,\mathrm{C.L.}). \tag{1.41}$$

In the rest of this work, we shall more conservatively employ the upper bound obtained from the Planck2013 release, [60]

$$\sum_i m_i < 0.23\,\mathrm{eV} \quad (95\%\,\mathrm{C.L.}), \tag{1.42}$$

---

[3] In principle, the mass splittings between the different neutrino mass states can be seen in the matter power spectrum probing large scale structures in the Universe. However, this effect is still too subtle to be measured with significance even by future surveys [59].

which, using the mass values in eq. (1.27), translates into an upper bound on m_1 valid for both NO and IO

$$m_1 \lesssim 0.07\,\mathrm{eV}. \tag{1.43}$$

This is the upper bound derived from cosmology shown in fig. 1.3 and in the figures that will appear in what follows.
We shall comment more in detail on how cosmological data can further constrain the bound on the sum of the neutrino masses in chapter 4.

1.3 Two problems, one solution?

We have introduced two serious problems of modern physics that unavoidably call for an extension of the SM. The baryon asymmetry of the Universe needs a dynamical mechanism able to explain the observed baryon-to-photon ratio, while neutrino masses and mixing require a theoretical justification. In the rest of this work we shall consider an interesting possible extension of the SM that, on the one hand, is able to naturally account for neutrino masses via the so-called *seesaw mechanism*, while on the other hand can provide a way to produce the baryon asymmetry of the Universe, via *leptogenesis*. This theoretical framework turns out to be particularly interesting not only because it can solve two problems at the same time, but also because it creates a strict link between two phenomenological domains: cosmology and neutrino oscillation physics. This way, cosmological evidences, like the baryon asymmetry of the Universe, can be employed to gain more information on the physics ruling neutrino masses and mixing, through a theoretical explanation and prediction of the seesaw free parameters. This is indeed the main aim of this work: exploiting the link between neutrino phenomenology and cosmology in order to constrain and predict the otherwise free parameters introduced by the seesaw extension of the SM.

This work is divided into two main parts: in the first part we shall introduce the theoretical framework and the needed formalism, while in the second we will derive constraints and predictions on neutrino parameters.
Part one includes chapters 2 and 3. In chapter 2 we shall address the problem of neutrino masses and mixing and introduce the seesaw mechanism and leptogenesis, pointing out its main features. In chapter 3 we shall expand the leptogenesis paradigm by introducing flavour effects and considering a particular scenario, called N_2-dominated. We shall highlight two important theoretical motivations that naturally lead to it: *strong thermal leptogenesis* and $SO(10)$*-inspired leptogenesis*. These two theoretical frameworks will turn out to be particularly rich of phenomenological consequences, giving interesting predictions and constraints on neutrino masses and mixing parameters.
In the second part we shall analyse in detail these results. In chapter 4 strong thermal leptogenesis will be considered, while in chapter 5 we will derive the predictions

obtained within $SO(10)$-inspired leptogenesis. In chapter 6 we will study the supersymmetric extension of $SO(10)$-inspired leptogenesis, commenting on the differences with the non-supersymmetric scenario and focusing on the implications on the reheating temperature of the Universe.

Finally, in chapter 7 we will summarise the results obtained in the preceding chapters and draw our conclusions.

Part I

The framework

Chapter 2

The seesaw mechanism and leptogenesis

In this chapter, we shall analyse how it is possible to extend the SM lagrangian to account for a mass term for neutrinos. We shall see the basic ways it can be accomplished and then devote ourselves to a very interesting realisation: the *seesaw mechanism*. In particular, we will focus on a direct consequence entailed by the seesaw mechanism: *leptogenesis*. In the second part of this chapter, the basic features of leptogenesis will be explored and the main formalism will be laid out.

2.1 How to give mass to neutrinos?

In the SM [10–12], neutrinos are massless and purely LH. However, as discussed in the Introduction, experimental results have nowadays firmly established that neutrinos of different flavours oscillate into each other. The main consequence of this experimental phenomenon is that neutrinos cannot be all massless. Therefore, we are compelled by evidence to expand the SM lagrangian in order to accomodate a mass term for neutrinos.

2.1.1 Dirac masses

Perhaps the most immediate way to give mass to neutrinos consists in extending the Higgs mechanism to neutrinos as well. This of course requires the addition of RH neutrino fields, which must be singlets under the SM gauge group, since they do not appear to take part into any interaction. In a basis in which charged lepton Yukawa matrix is diagonal, we can add to the SM lagrangian a term such as

$$\mathcal{L}_D = -Y_{\alpha i}\,\overline{l_\alpha}\,N'_{Ri}\tilde{\Phi} + \text{h.c}, \tag{2.1}$$

where $Y_{\alpha i}$ are Yukawa couplings, l_α are the LH lepton doublets, defined as

$$l_\alpha \equiv \begin{pmatrix} \nu_{L\alpha} \\ \ell_{L\alpha} \end{pmatrix}, \tag{2.2}$$

and $\tilde{\Phi} \equiv i\sigma_2 \Phi^*$ is the Higgs doublet Φ transformed by means of the second Pauli matrix σ_2 in order to act on the down part of the lepton doublet. Sum over repeated indices is understood, unless specified otherwise. After electroweak spontaneous symmetry breaking (EWSSB) we get a term

$$\mathcal{L}_D = -vY_{\alpha i}\,\overline{\nu_{L\alpha}} N'_{Ri} + \text{h.c.}, \tag{2.3}$$

where v is the Higgs Vacuum Expectation Value (VEV) $v \simeq 174\,\text{GeV}$.
In order to get a mass term for the neutrinos, the Yukawa matrix must be diagonalised via a bi-unitary transformation such as

$$U^\dagger Y V_R = D_Y, \tag{2.4}$$

where D_Y is diagonal with diagonal entries y_i real and non-negative. Inserting it into the lagrangian we can rotate the neutrino fields as

$$\nu_{Li} \equiv {U^\dagger}_{i\alpha}\nu_{L\alpha}, \qquad N_{Ri} \equiv V^\dagger_{Rij} N'_{Rj}, \tag{2.5}$$

so that we have

$$\mathcal{L}_D = -v\sum_i y_i\,\overline{\nu_{Li}} N_{Ri} + \text{h.c.} = -\sum_i m_i\,\overline{\nu_i}\nu_i, \tag{2.6}$$

where we defined the fields $\nu_i = \nu_{Li} + N_{Ri}$ and the masses $m_i \equiv v y_i$. In this way we have obtained massive neutrino fields ν_i, through a rotation of the fields appearing in the lagrangian.

The unitary matrix U in eq. (2.5) is then the PMNS neutrino mixing matrix.
This is in principle a generic $N \times N = 3 \times 3$ unitary matrix, which is determined by $N^2 = 9$ parameters. Any unitary matrix can be written in terms of $N(N-1)/2$ angles and $N(N+1)/2$ phases, so that in our $N = 3$ cases we have in general 3 angles and 6 phases. It is possible to show that a generic 3×3 unitary matrix U can be written as

$$U = D_L\, R^{23}\, \Delta\, R^{13}\, \Delta^\dagger\, R^{12} D_R, \tag{2.7}$$

where, setting $c_{ij} \equiv \cos\theta_{ij}$ and $s_{ij} \equiv \sin\theta_{ij}$,

$$D_L = \text{diag}\left(e^{i(\omega_1-\rho)},\, e^{i\omega_2},\, e^{i(\omega_3-\sigma)}\right), \tag{2.8}$$

$$D_R = \text{diag}\left(e^{i\rho},\, 1,\, e^{i\sigma}\right), \tag{2.9}$$

$$\Delta = \text{diag}\left(e^{i\delta},\, 1,\, 1\right), \tag{2.10}$$

and

$$R^{12} = \begin{pmatrix} c_{12} & s_{12} & 0 \\ -s_{12} & c_{12} & 0 \\ 0 & 0 & 1 \end{pmatrix}, \quad R^{13} = \begin{pmatrix} c_{13} & 0 & s_{13} \\ 0 & 1 & 0 \\ -s_{13} & 0 & c_{13} \end{pmatrix}, \quad R^{23} = \begin{pmatrix} 1 & c_{23} & s_{23} \\ 0 & -s_{23} & c_{23} \\ 0 & 0 & 1 \end{pmatrix}. \tag{2.11}$$

The angles can be limited to the interval $0 \leq \theta_{ij} \leq \pi/2$. Defining the vector of the LH components of the neutrino mass eigenstates ν_i

$$\boldsymbol{n}_L \equiv \begin{pmatrix} \nu_{L1} \\ \nu_{L2} \\ \nu_{L3} \end{pmatrix}, \tag{2.12}$$

we can insert eq. (2.7) in the expression of the charged current

$$J^\mu_W = \overline{\boldsymbol{n}_L} U^\dagger \gamma^\mu \boldsymbol{\ell}_L = \overline{\boldsymbol{n}_L} \left(D_L R^{23} \Delta \, R^{13} \Delta^\dagger R^{12} D_R \right)^\dagger \gamma^\mu \boldsymbol{\ell}_L \tag{2.13}$$

$$= \overline{\boldsymbol{n}_L} D_R^\dagger \, (R^{12})^t \Delta \, (R^{13})^t \, \Delta^\dagger (R^{23})^t \, D_L^\dagger \gamma^\mu \boldsymbol{\ell}_L. \tag{2.14}$$

Our lagrangian is invariant under global $U(1)$ transformations of the neutrino mass eigenstates

$$\boldsymbol{n}_L \longrightarrow D_R \, \boldsymbol{n}_L, \tag{2.15}$$

and under global $U(1)$ transformations of the charged lepton fields

$$\boldsymbol{\ell}_L \longrightarrow D_L^\dagger \, \boldsymbol{\ell}_L. \tag{2.16}$$

Therefore, by performing a rephasing of $\boldsymbol{n}_L$ and $\boldsymbol{\ell}_L$, matrices D_R and D_L drop out of the charged current expression. Since these phases do not appear anymore, anywhere, in the lagrangian, they are clearly non-physical, and they can be neglected in the parameterisation of the mixing matrix U. In the case of Dirac neutrino masses, we can therefore write the mixing matrix as

$$U = R^{23} \Delta R^{13} \Delta^\dagger R^{12} \tag{2.17}$$

$$= \begin{pmatrix} c_{12}c_{13} & s_{12}c_{13} & s_{13}e^{-i\delta} \\ -s_{12}c_{23} - c_{12}s_{23}s_{13}e^{i\delta} & c_{12}c_{23} - s_{12}s_{23}s_{13}e^{i\delta} & s_{23}c_{13} \\ s_{12}s_{23} - c_{12}c_{23}s_{13}e^{i\delta} & -c_{12}s_{23} - s_{12}c_{23}s_{13}e^{i\delta} & c_{23}c_{13} \end{pmatrix} \tag{2.18}$$

which coincides with eq. (1.28) if ρ and σ are dropped. In this case then, only the Dirac *CP* violating phase δ remains.

It must be noticed that, for simplicity, we have considered here the NO case. As already mentioned, with our conventions, the IO case can be obtained via a permutation of the columns in U.

We can also notice that, in order to get as small neutrino masses as those required by experimental evidence, it is necessary to fix the Yukawa couplings to small values. This tuning of the Yukawas lacks of elegance, therefore more natural ways to explain the smallness of neutrino masses are generally sought.

2.1.2 Majorana masses

We have seen that the Dirac mass term requires the two chirality components of the field $\nu = \nu_L + N_R$. However, in the case of neutrinos, which have zero electric charge, it is possible to build a mass term using only one independent chirality component. The generic fermion mass term connects a LH and a RH field, but in the case of neutrino it is possible to obtain one chiral field from the other. We can consider for instance the RH field N_R, and make use of the charge conjugation matrix $\mathcal{C}$ which satisfies

$$\mathcal{C}^\dagger = \mathcal{C}^{-1} \tag{2.19}$$

$$\mathcal{C}^t = -\mathcal{C} \tag{2.20}$$

$$\mathcal{C}\,(\gamma^\mu)^t\,\mathcal{C}^{-1} = -\gamma^\mu \tag{2.21}$$

$$\mathcal{C}\,(\gamma_5)^t\,\mathcal{C}^{-1} = \gamma_5 \tag{2.22}$$

$$\mathcal{C}\,(\sigma^{\mu\nu})^t\,\mathcal{C}^{-1} = -\sigma^{\mu\nu}. \tag{2.23}$$

From the RH field N_R, it is possible to build a field, up to an arbitrary phase, as

$$N_R^C \equiv \mathcal{C}\,\overline{N_R}^t, \tag{2.24}$$

which is LH. Indeed we have

$$P_R\,N_R^C = P_R\,\mathcal{C}\,\overline{N_R}^t = \mathcal{C}\left(\overline{N_R}\,P_R\right)^t = \mathcal{C}\left(N^\dagger\,P_R^\dagger\gamma^0 P_R\right)^t = \mathcal{C}\left(\overline{N}\,P_L\,P_R\right)^t = 0, \tag{2.25}$$

where we used eq. (2.22). Therefore, using the field in eq. (2.24) it is possible to build a fermion mass term connecting a LH and a RH field actually using only one independent chirality component. We have therefore

$$\mathcal{L}_M = -\frac{1}{2}m\,\overline{N_R^C}N_R + \text{h.c.}, \tag{2.26}$$

which is the so-called Majorana mass term. It is important to notice the factor 1/2, needed to avoid the double counting due to the fact that the LH and the RH fields are not independent. Expanding the hermitian conjugate we get the full lagrangian

$$\mathcal{L}_M = -\frac{1}{2}m\left(\overline{N_R^C}N_R + \overline{N_R}N_R^C\right) = -\frac{1}{2}m\,\overline{\nu}\nu. \tag{2.27}$$

In the last equality we have defined a four component spinor field

$$\nu = N_R^C + N_R, \tag{2.28}$$

whose RH component is the field N_R and the LH component is obtained from N_R by eq. (2.24). Such field is called Majorana field and, applying the charge conjugation eq. (2.24), it can be seen that ν is equal to its charge conjugate ν^C. It is clear then that Majorana fields must be neutral under the electric charge, since the charge conjugation relates particles and antiparticles.

The Majorana mass term can be easily extended to the multi-generation case. Introducing RH neutrino fields N'_{Ri}, we have

$$\mathcal{L}_M = -\frac{1}{2}\overline{N'^C_{R\,i}}\, M_{ij}\, N'_{Rj} + \text{h.c.} \tag{2.29}$$

where M_{ij} is a complex symmetric matrix. Indeed, rewriting the mass term as

$$-\frac{1}{2}\overline{N'^C_{R\,i}}\, M_{ij}\, N'_{Rj} + \text{h.c.} = \frac{1}{2} N'^t_{Ri}\, \mathcal{C}^\dagger\, M_{ij} N'_{Rj}, \tag{2.30}$$

we can then take the transpose in the spinor space and relabel the indices as

$$\frac{1}{2} N'^t_{Ri}\, \mathcal{C}^\dagger\, M_{ij} N'_{Rj} = -\frac{1}{2} N'^t_{Rj}\, (\mathcal{C}^\dagger)^t\, M_{ij} N'_{Ri} = \frac{1}{2} N'^t_{Ri}\, \mathcal{C}^\dagger\, M_{ji} N'_{Rj}. \tag{2.31}$$

Comparing the first and the last terms we conclude that $M_{ij} = M_{ji}$, so that the Majorana mass matrix M must be symmetric. Since it is a complex symmetric matrix, it can be diagonalised via Takagi diagonalisation as

$$V_R^t\, M\, V_R = D_M, \tag{2.32}$$

where D_M is a diagonal matrix with diagonal entries m_i real and non-negative. Inserting eq. (2.32) in the lagrangian, we can define new fields as

$$N_{Ri} \equiv V^\dagger_{Ril}\, N'_{Rl}, \tag{2.33}$$

so that we have

$$\mathcal{L}_M = -\frac{1}{2}\sum_i \overline{N^C_{R\,i}}\, m_i N_{Ri} + \text{h.c.} \tag{2.34}$$

Completing the hermitian conjugate, we can define the fields $\nu_i \equiv N^C_{R\,i} + N_{Ri}$ which are mass eigenstates with masses m_i. Similarly to the Dirac case, the rotation due to the matrix V_R implies the appearance of a mixing matrix U in the charged current, so that also in the Majorana case we have neutrino oscillations.

It must be noticed that the Majorana mass term eq. (2.26) is not invariant under global $U(1)$ transformations of neutrino fields. This is indeed the global symmetry that ensures

the conservation of the leptonic current and hence the lepton number. In this case, since the Majorana mass term explicitly breaks this symmetry, we must conclude that the lepton number is not conserved when a Majorana mass term is introduced.
This remark is important also with respect to the determination of the mixing matrix U. Indeed, it is not possible anymore to perform the transformation eq. (2.15) on the neutrino fields, therefore we cannot anymore drop the matrix D_R in the parameterisation of U, eq. (2.7). Therefore, in the case of Majorana mass term, we have

$$U = R^{23}\Delta R^{13}\Delta^\dagger R^{12}\, D_R \tag{2.35}$$

$$= \begin{pmatrix} c_{12}c_{13} & s_{12}c_{13} & s_{13}e^{-i\delta} \\ -s_{12}c_{23} - c_{12}s_{23}s_{13}e^{i\delta} & c_{12}c_{23} - s_{12}s_{23}s_{13}e^{i\delta} & s_{23}c_{13} \\ s_{12}s_{23} - c_{12}c_{23}s_{13}e^{i\delta} & -c_{12}s_{23} - s_{12}c_{23}s_{13}e^{i\delta} & c_{23}c_{13} \end{pmatrix} \begin{pmatrix} e^{i\rho} & 0 & 0 \\ 0 & 1 & 0 \\ 0 & 0 & e^{i\sigma} \end{pmatrix}, \tag{2.36}$$

which coincides with the parameterisation presented in the introduction, eq. (1.28).

Finally, it is evident that the Majorana mass term is not a simple extension of the SM as in the case of the Dirac mass, where the Higgs mechanism was simply extended to neutrinos. Using the SM field content, it is possible to obtain a Majorana mass term only via non-renormalisable operators. In particular, the lowest dimensional operator that generates a Majorana mass term is the so-called Weinberg dimension-5 operator

$$\mathcal{L}_5 = \frac{y_{\alpha\beta}}{\Lambda}\left(l'^{\,t}_{L\alpha}\,\sigma_2\,\Phi\right)\mathcal{C}^\dagger\left(\Phi^t\,\sigma_2\,l'_{L\beta}\right) + \text{h.c.}, \tag{2.37}$$

where $y_{\alpha\beta}$ is a symmetric matrix of couplings and Λ is a high scale with dimension one. After the electroweak symmetry breaking a Majorana mass term for neutrinos appears

$$\mathcal{L}_M = \frac{1}{2}\frac{v^2}{\Lambda} y_{\alpha\beta}\,\nu'^{\,t}_{L\alpha}\,\mathcal{C}^\dagger\,\nu'_{L\beta} + \text{h.c.} \tag{2.38}$$

The neutrino masses are then obtained from the matrix

$$m_{\alpha\beta} = \frac{v^2}{\Lambda} y_{\alpha\beta}. \tag{2.39}$$

Therefore, the mass scale is given by the interplay between the electroweak scale v and the high-scale Λ. Due to the largeness of Λ, this relation ensures that neutrino masses are smaller than the typical electroweak scale, as pointed out by the experiments. Such relations, in which the neutrino masses are proportional to the electroweak scale suppressed by a higher scale take the name of *seesaw* relations. It will be a feature of the seesaw mechanism which we will deal with in the next section and that will implement it without effective, non-renormalisable operators.

2.1.3 The seesaw mechanism

So far we have explored two distinct ways of adding a mass term for neutrinos to the SM lagrangian. It is possible, however, to combine them so to have a Dirac-Majorana mass term. We can thus take into account LH fields $\nu'_{L\alpha}$ and RH fields N'_{Ri}, with $\alpha = e, \mu, \tau$ and $i = 1, 2, 3$. Considering these LH and the RH fields independent (i.e. not related by conjugation relations), we can in principle build three different mass terms. A Dirac mass term involving both LH and RH fields, a Majorana mass term with LH fields only and a Majorana mass term with RH fields only. However, choosing to respect the SM gauge group, the LH fields $\nu'_{L\alpha}$ would not provide a Majorana mass term invariant under $SU(2)_L \times U(1)_Y$. For this reason, we are left with only one Majorana mass term, made of the RH fields, which, not being constrained by the SM, can be chosen to be singlets under $SU(3)_C \times SU(2)_L \times U(1)_Y$. Considering for completeness also the charged leptons, we have

$$\mathcal{L} \supset -Y'_{\ell\,\alpha\beta}\,\overline{l'}_\alpha\,\ell'_{R\beta}\Phi - Y'_{\alpha i}\,\overline{l'_\alpha}\,N'_{Ri}\tilde{\Phi} - \frac{1}{2}\overline{N'^{\,C}_{Ri}}\,M'_{ij}\,N'_{Rj} + \text{h.c.} \tag{2.40}$$

where Y'_ℓ is the matrix of charged lepton Yukawa couplings, with ℓ_R being the charged lepton RH component. It is more convenient to rotate the charged leptons to a basis in which the Yukawa's are diagonal, as well as the RH neutrino fields onto a basis in which the Majorana mass matrix M is diagonal. This choice of basis is also referred to as *flavour basis*. For the charged leptons, we employ the bi-unitary diagonalisation

$$U^\ell_L\,Y'_\ell\,U^{\ell\,\dagger}_R = D^\ell_Y, \tag{2.41}$$

where D^ℓ_Y is a diagonal matrix with real, non-negative entries. The charged lepton fields are transformed as

$$l_{L\alpha} \equiv U^\ell_{L\alpha\beta}\,l'_{L\beta} \tag{2.42}$$

$$\ell_{R\alpha} \equiv U^\ell_{R\alpha\beta}\,\ell'_{R\beta}. \tag{2.43}$$

For the RH neutrinos, we perform the Takagi diagonalisation of M' as

$$V^t_R M' V_R = D_M, \tag{2.44}$$

where V_R is a unitary matrix and D_M a diagonal matrix with diagonal entries M_i, real and non-negative. The RH fields are then rotated as

$$N_{Ri} \equiv V^\dagger_{Rij}\,N'_{Rj}. \tag{2.45}$$

The lagrangian then becomes

$$\mathcal{L} \supset -\sum_\alpha D^\ell_{Y\alpha}\,\overline{l_\alpha}\ell_{R\alpha}\Phi - Y_{\alpha i}\,\overline{l_\alpha}\,N_{Ri}\tilde{\Phi} - \frac{1}{2}\sum_i \overline{N^C_{Ri}}\,D_{M\,i}\,N_{Ri} + \text{h.c.} \tag{2.46}$$

where we have defined the neutrino Yukawa couplings in the flavour basis as

$$Y_{\alpha i} \equiv U^{\ell}_{L\alpha\beta}\, Y'_{\beta j}\, V_{Rji}. \tag{2.47}$$

After EWSSB this lagrangian develops mass terms

$$\mathcal{L} \supset -\sum_{\alpha} D^{\ell}_{m_\alpha} \overline{\ell_{L\alpha}}\, \ell_{R\alpha} - m_{D\alpha i}\, \overline{\nu_{L\alpha}}\, N_{Ri} - \frac{1}{2}\sum_{i} \overline{N_{Ri}^{C}}\, D_{Mi}\, N_{Ri} + \text{h.c.} \tag{2.48}$$

where $D^{\ell}_{m} = v D^{\ell}_{Y}$ is the charged-leptons diagonal mass matrix and $m_D \equiv vY$ is the so-called Dirac mass matrix for neutrinos. It is possible to expand the Dirac term by noticing that

$$\overline{N^{C}_{R\,i}}\nu^{C}_{L\,\alpha} = \left(\mathcal{C}\overline{N_{Ri}}^{t}\right)^{\dagger} \gamma^{0}\mathcal{C}\,\overline{\nu_{L\alpha}}^{t} = \left(\gamma^{0\dagger} N_{Ri}\right)^{t} \mathcal{C}^{-1}\gamma^{0}\mathcal{C}\,\overline{\nu_{L\alpha}}^{t} = -N^{t}_{Ri}\,\overline{\nu_{L\alpha}}^{t} = \overline{\nu_{L\alpha}} N_{R}, \tag{2.49}$$

so that we have

$$\mathcal{L}_{\text{s}} = -\frac{1}{2} m_{D\alpha i}\, \overline{\nu_{L\alpha}}\, N_{Ri} - \frac{1}{2} m_{D\alpha i}\, \overline{N^{C}_{R\,i}}\, \nu^{C}_{L\,\alpha} - \frac{1}{2}\sum_{i} \overline{N_{Ri}^{C}}\, D_{Mi}\, N_{Ri} + \text{h.c.} \tag{2.50}$$

This can then be rewritten more compactly by adopting a matrix notation as

$$\mathcal{L}_{\text{s}} = -\frac{1}{2}\left(\overline{\boldsymbol{\nu}_L}, \overline{\boldsymbol{N}^{C}_{R}}\right) \begin{pmatrix} 0 & m_D \\ m_D^{t} & D_M \end{pmatrix} \begin{pmatrix} \boldsymbol{\nu}^{C}_{L} \\ \boldsymbol{N}_{R} \end{pmatrix} + \text{h.c.} \equiv -\frac{1}{2}\overline{\boldsymbol{n}'_L}\, \mathcal{M}\, \boldsymbol{n}'^{C}_{L} + \text{h.c.}, \tag{2.51}$$

where we defined the six-component vector of fields

$$\boldsymbol{n}'_L \equiv \begin{pmatrix} \boldsymbol{\nu}_L \\ \boldsymbol{N}^{C}_{R} \end{pmatrix}, \tag{2.52}$$

that is LH. The mass term in eq. (2.51) has a Majorana structure, therefore the neutrino fields that arise from the seesaw lagrangian must be Majorana. In order to obtain the mass eigenstates, it is still necessary to diagonalise the matrix $\mathcal{M}$. We can first obtain the two diagonal blocks

$$\lambda_{1,2} = \frac{1}{2}\left(D_M \mp \sqrt{D_M^2 + 4 m_D m_D^{t}}\right). \tag{2.53}$$

Now, if we assume that the M_i are much larger than all the elements of the Dirac mass matrix m_D, we can simplify the expression of the blocks to the leading order in the $D_M^{-1} m_D$ expansion. This is the so called *seesaw limit* and it is indeed naturally realised in several UV completions of the SM. For instance, as we shall see in more detail in the following chapters, in Grand Unified Theories (GUT) such as $SO(10)$-GUT, RH neutrino fields are predicted to complete the representation of the mass fields. In these theories, the scale of the Majorana mass matrix M lies naturally around the GUT scale $\Lambda_{\text{GUT}} \sim 10^{16}\,$GeV. The scale of the matrix m_D is typically the electroweak scale

$\Lambda_{\mathrm{EW}} \sim 10^2\,\mathrm{GeV}$, therefore, in these frameworks, the seesaw limit is naturally realised. In this limit we have

$$\lambda_1 = -m_D\, D_M^{-1}\, m_D^t + \mathcal{O}(D_M^{-1} m_D), \tag{2.54}$$

$$\lambda_2 = D_M + \mathcal{O}(D_M^{-1} m_D), \tag{2.55}$$

while the diagonalising matrix W performing the block diagonalisation is

$$W \simeq \begin{pmatrix} 1 & \left(D_M^{-1} m_D\right)^\dagger \\ -D_M^{-1} m_D & 1 \end{pmatrix} \tag{2.56}$$

Hence, in the seesaw limit we have

$$W^t\, \mathcal{M}\, W \simeq \begin{pmatrix} m_\nu & 0 \\ 0 & D_M \end{pmatrix} \equiv B_{\mathcal{M}}, \tag{2.57}$$

where we defined

$$m_\nu \equiv -m_D\, D_M^{-1}\, m_D^t. \tag{2.58}$$

We can immediately notice that the neutrino mass spectrum splits into two distinct sets. Three neutrinos have masses given by the eigenvalues of m_ν, while three others have masses M_i. We can already say that the first set of fields will be much lighter than the second, due to eq. (2.58). In order to have a clear idea of the final mass eigenstates and the mixing among the neutrino fields, it is still necessary to diagonalise the block matrix $B_{\mathcal{M}}$. To this aim, given that D_M is already diagonal, we can adopt the 6×6 matrix

$$P = \begin{pmatrix} Q & 0 \\ 0 & 1 \end{pmatrix} \tag{2.59}$$

such that

$$P^\dagger\, B_{\mathcal{M}}\, P^* = \begin{pmatrix} -D_m & 0 \\ 0 & D_M \end{pmatrix} \equiv D_{\mathcal{M}}, \tag{2.60}$$

where the diagonal 3×3 matrix D_m is obtained as $Q^\dagger\, m_\nu\, Q^* = -D_m$. Using the 6×6 diagonal matrices $B_{\mathcal{M}}$ and $D_{\mathcal{M}}$ we can rewrite eq. (2.51) as

$$\mathcal{L}_{\mathrm{s}} = -\frac{1}{2}\overline{\boldsymbol{n}'_L}\, W^* B_{\mathcal{M}} W^\dagger \boldsymbol{n}'^C_L + \mathrm{h.c.} = -\frac{1}{2}\overline{\boldsymbol{n}'_L}\, W^* P D_{\mathcal{M}} P^t W^\dagger \boldsymbol{n}'^C_L + \mathrm{h.c.}. \tag{2.61}$$

Hence, the vector of fields $\boldsymbol{n}'_L$ is transformed into

$$\boldsymbol{n}_L \equiv \begin{pmatrix} \boldsymbol{n}_L^{\mathrm{light}} \\ \boldsymbol{n}_L^{\mathrm{heavy}} \end{pmatrix} = P^\dagger\, W^t \boldsymbol{n}'_L \tag{2.62}$$

$$= \begin{pmatrix} Q^\dagger & 0 \\ 0 & 1 \end{pmatrix} \begin{pmatrix} 1 & -\left(D_M^{-1} m_D\right)^t \\ \left(D_M^{-1} m_D\right)^* & 1 \end{pmatrix} \begin{pmatrix} \boldsymbol{\nu}_L \\ \boldsymbol{N}_R^C \end{pmatrix} \tag{2.63}$$

so that the LH components of the final mass eigenstates are

$$\boldsymbol{n}_L^{\text{light}} = Q^\dagger \left[\boldsymbol{\nu}_L - \left(D_M^{-1} m_D\right)^t \boldsymbol{N}_R^C\right], \tag{2.64}$$

$$\boldsymbol{n}_L^{\text{heavy}} = \left(D_M^{-1} m_D\right)^* \boldsymbol{\nu}_L + \boldsymbol{N}_R^C. \tag{2.65}$$

Since all fields are Majorana, we can build the final mass eigenstates as

$$\boldsymbol{n}^{\text{light}} = \boldsymbol{n}_L^{\text{light}} + \left(\boldsymbol{n}_L^{\text{light}}\right)^C, \qquad \boldsymbol{n}^{\text{heavy}} = \boldsymbol{n}_L^{\text{heavy}} + \left(\boldsymbol{n}_L^{\text{heavy}}\right)^C. \tag{2.66}$$

Given the suppression introduced by the factor $D_M^{-1} m_D$, we can notice that the heavy mass eigenstates are almost entirely composed out of the RH neutrino fields N_R, with a tiny mixing with the fields ν_L. Similarly, the LH light mass eigenstates almost coincide with a rotation of the fields $\nu_{L\alpha}$ in the vector $\boldsymbol{\nu}_L$. Thus, neglecting the corrections of order $D_M^{-1} m_D$, we can say

$$\boldsymbol{n}^{\text{light}} \simeq Q^\dagger \boldsymbol{\nu}_L + \left(Q^\dagger \boldsymbol{\nu}_L\right)^C, \tag{2.67}$$

$$\boldsymbol{n}^{\text{heavy}} \simeq \boldsymbol{N}_R^C + \boldsymbol{N}_R. \tag{2.68}$$

Focusing on eq. (2.67), since the lagrangian in eq. (2.46) is already written in a basis in which the charged leptons Yukawa couplings are diagonal, the fields $\nu_{L\alpha}$ correspond to the flavour eigenstates that appear in the charged current interactions. In the seesaw limit, we can identify the matrix Q with the PMNS unitary mixing matrix U. Therefore, we have

$$D_m = -U^\dagger \, m_\nu \, U^*. \tag{2.69}$$

This holds in the seesaw limit approximation, in which the mixing with the N_R fields, that would imply a rectangular mixing matrix, is suppressed. This avoids an unpleasant outcome related to the non-unitarity of the mixing: the failure of the Glashow-Iliopoulos-Maiani (GIM) mechanism [61] and the appearance of flavour changing neutral currents.

It should be now clear how the seesaw mechanism [62–67] works: the heavy RH neutrinos and the LH neutrinos mix in such a way that, due to the different scales involved, the spectrum of the final mass eigenstates splits into two sets. One is composed of light neutrinos, almost entirely made of the LH neutrinos, while the other consisting in heavy neutrinos almost coinciding with the RH neutrinos. The heavy scale of the Majorana mass matrix suppresses the final active neutrino masses so that they can naturally lie around the small experimental values.

2.1.4 Parameters in the seesaw lagrangian

The addition of three new fields in the SM lagrangian necessarily implies an enlargement of the parameter space. Indeed, looking at eq. (2.46), we can see that new Yukawa couplings $Y_{\alpha i}$ and the diagonal Majorana mass matrix D_M are introduced. In general, the 3×3 complex matrix $Y_{\alpha i}$ is specified by 18 real parameters, however, a rephasing of the lepton fields can eliminate 3 of them, reducing the number to 15. D_M includes the three Majorana masses M_i, therefore, in total, the number of parameters introduced by this realisation of the seesaw mechanism is 18. In a particular seesaw model, however, it is not practical to directly specify the Yukawa couplings. Instead, it is possible to input a set of parameters that have a more direct physical meaning. We can notice that combining eq. (2.58) and (2.69) we have

$$D_m = U^\dagger m_D D_M^{-1} m_D^t \, U^*, \tag{2.70}$$

that is

$$1 = D_m^{-1/2} \, U^\dagger m_D D_M^{-1} m_D^t \, U^* \, D_m^{-1/2}. \tag{2.71}$$

By splitting also matrix D_M^{-1} we can see that the seesaw mechanism implies

$$\left(D_m^{-1/2} \, U^\dagger m_D D_M^{-1/2}\right) \left(D_m^{-1/2} \, U^\dagger m_D D_M^{-1/2}\right)^t = 1. \tag{2.72}$$

If we define

$$\Omega = D_m^{-1/2} \, U^\dagger m_D D_M^{-1/2}, \tag{2.73}$$

eq. (2.72) implies that Ω is a *complex orthogonal matrix* [68]. From eq. (2.73) we can express m_D, that is, the Yukawa couplings, as

$$m_D = U D_m^{1/2} \, \Omega \, D_M^{1/2}. \tag{2.74}$$

Therefore, the model is completely specified if we provide

(a) 6 mixing parameters in U: 3 mixing angles and 3 phases,

(b) 3 light neutrino masses m_i in D_m,

(c) 3 heavy neutrino masses M_i in D_M,

(d) 6 real parameters of the complex orthogonal matrix Ω.

The total, clearly, still sums up to 18 parameters, but this parameterisation is quite convenient since (a) and (b) are related to the low-energy scale of the active neutrino physics. Points (c) and (d) are linked to the high-energy physics of the RH Majorana neutrinos. Clearly, while the former set is experimentally accessible, the latter is difficult (if not impossible) to directly measure.
Constraining these sets of free parameters is indeed the aim of the present work.

The Ω matrix entries have also a precise physical meaning. From eq. (2.73) we can easily obtain

$$\Omega_{ij}^2 = \frac{\left(U^\dagger m_D\right)_{ij}^2}{m_i M_j}, \tag{2.75}$$

which satisfy the orthogonality condition

$$\sum_j \Omega_{ij}^2 = 1. \tag{2.76}$$

Therefore, we can write [69]

$$m_i = \sum_j m_i \, \Omega_{ij}^2 = \sum_j \frac{\left(U^\dagger m_D\right)_{ij}^2}{M_j}. \tag{2.77}$$

Each entry Ω_{ij}^2 corresponds to a contribution to m_i proportional to the inverse of the heavy neutrino mass M_j. We can regard then the elements Ω_{ij}^2 as the weights [69, 70] with which the heavy neutrino masses contribute to the determination of the light mass m_i.

2.1.5 Types of seesaw mechanisms

The mechanism we have described in detail in the previous section is actually called *type-I seesaw.* There are indeed other types of seesaw mechanism, all sharing the same idea of different interplaying scales that suppress the neutrino masses. We will very briefly mention the general scheme of the most relevant other types.

Type-II seesaw [71–73]. In this version, an additional Higgs field Δ is introduced, which is a triplet under $SU(2)_L$. This couples both to the leptons and the Higgs doublets, so that, when the neutral component of Δ acquires a VEV, v_Δ, a Majorana mass term is generated. This is of the order $g v_\Delta$, where g is the Higgs triplet-lepton doublets coupling. The triplet VEV is linked by cubic scalar interaction to the EW VEV v so that $v_\Delta \sim \mu v^2/M_\Delta^2$, therefore, the light neutrino mass scale results $m \sim g\mu v^2/M_\Delta^2$. Often, type-II seesaw is found in the so-called *left-right symmetric models*, in which the gauge group is extended to $SU(2)_L \times SU(2)_R \times U(1)_{B-L}$.

Type-III seesaw [74]. In this case, three RH neutrinos are added as in type-I, however they are assumed to be triplets Σ of $SU(2)_L$. They couple via Yukawa couplings Y_Σ the lepton doublets and they are given a Majorana mass term with scale M_Σ. Assuming $M_\Sigma \gg v$, the procedure to obtain the final mass spectrum is the same as in type-I, so that the final light neutrino mass scale is given by $m \sim Y_\Sigma^2 v^2/M_\Sigma$. The most important difference with type-I is given by the triplet nature of the RH neutrino fields, that allows them to couple to the gauge fields and to induce the mixing of the charged leptons with New Physics.

Finally, it is possible to generate a Majorana mass term for the neutrino fields via quantum corrections. This is the feature of the so-called **radiative seesaw** mechanism, whose models usually involve new particles and additional discrete symmetries.

2.2 Leptogenesis

We can now turn to the production of the baryon asymmetry of the Universe and study a mechanism which is indissolubly linked to the seesaw mechanism we have seen in the previous section.
In the framework of the seesaw mechanism, the source of the final asymmetry can be traced back to the new physics represented by the heavy neutrino fields[1] we have introduced. Considering the seesaw lagrangian, eq. (2.46), we must therefore determine if there are all the ingredients needed to satisfy the Sakharov conditions and thus to generate an asymmetry through the interaction term. This term, in form of Yukawa coupling, is responsible for decays and inverse-decays of the heavy neutrinos into lepton and Higgs doublets. However, since only leptons, but no quarks, are involved, we can already understand that an asymmetry is going to be primarily produced among leptons and anti-leptons. Clearly, there must be in addition some other processes that provide the conversion of at least part of this lepton asymmetry into an asymmetry among baryons and anti-baryons, since the experimental evidence refers to a baryon asymmetry. A mechanism in which an asymmetry is originally produced in the lepton sector and partly converted to the baryons takes the name of *leptogenesis* [75]. In this section we shall study the leptogenesis mechanism that naturally arises from the type-I seesaw lagrangian, analysing one by one how the three Sakharov conditions can indeed be satisfied in this framework.

2.2.1 Lepton number violation and baryon asymmetry

Basing on the seesaw lagrangian eq. (2.46), the non-SM physics can be directly source of an asymmetry only in the lepton sector. The conversion of at least part of this asymmetry to the baryons is achieved thanks to the different interactions that take place in the Early Universe and that are in equilibrium at those temperatures. Among these, a crucial role is played by non-perturbative processes, predicted by the SM, that violate the baryon and the lepton numbers: the so-called electroweak *sphalerons*.

In order to obtain a link between the lepton and the baryon asymmetry, we must consider all the relevant interactions that are in equilibrium in the Early Universe [76]. At very high temperatures we can assume that mixing among quark and lepton families

---

[1] From here onwards, we shall call "heavy neutrinos" directly the fields $N_i = N_{R\,i}^C + N_{Ri}$ that appear in the lagrangian eq. (2.46), exploiting the fact that they coincide with the heavy mass eigenstates n_i^{heavy}, eq. (2.68).

is efficient, so that we can identify a single chemical potential for quarks and leptons. Moreover, also $SU(2)_L$ gauge interactions are in equilibrium, so that the components of the same $SU(2)_L$ doublet can be given the same chemical potential. We have therefore the chemical potentials as in tab. 2.1. We can get an expression of the baryon and lepton asymmetries in terms of the chemical potentials. Considering the high temperatures of the Early Universe, and thus $\mu/T \ll 1$, for fermion species we have

μ_{Q_L}	Chemical potential for the quark doublets
μ_{l_L}	Chemical potential for the lepton doublets
μ_{u_R}, μ_{d_R}	Chemical potentials for up and down RH quark fields
μ_{l_R}, μ_{N_R}	Chemical potentials for RH charged lepton and neutrino fields
μ_ϕ	Chemical potential for the Higgs field

Table 2.1: Relevant chemical potentials in the Early Universe.

$$n_X - n_{\bar{X}} = \frac{gT^3}{6}\frac{\mu_X}{T} + \mathcal{O}\left((\mu_X/T)^3\right), \tag{2.78}$$

where $X = B$, L. From tab. 2.1 we have

$$\mu_L = 3\left(2\mu_{l_L} + \mu_{l_R}\right), \tag{2.79}$$

$$\mu_B = 3\left(2\mu_{Q_L} + \mu_{u_R} + \mu_{d_R}\right), \tag{2.80}$$

so that

$$n_B - n_{\bar{B}} = \frac{gT^2}{2}\left(2\mu_{Q_L} + \mu_{u_R} + \mu_{d_R}\right), \qquad n_L - n_{\bar{L}} = \frac{gT^2}{2}\left(2\mu_{l_L} + \mu_{l_R}\right). \tag{2.81}$$

Considering all the processes that are efficient in the Early Universe, we can find relations between these chemical potentials and try to reduce them to fewer independent ones.

Not only $SU(2)_L$ gauge interactions are in equilibrium in the Early Universe, but also Higgs Yukawa interactions. Without considering, for the time being, the RH neutrinos Yukawa couplings, we have a set of equations

$$\begin{cases} \mu_{u_R} - \mu_{Q_L} &= \mu_\phi \\ \mu_{Q_L} - \mu_{d_R} &= \mu_\phi \\ \mu_{l_L} - \mu_{l_R} &= \mu_\phi . \end{cases} \tag{2.82}$$

To these equations, we add the requirement that the total hypercharge of the plasma in the Early Universe vanishes. In terms of chemical potentials we have

$$\mu_{Q_L} + 2\mu_{u_R} - \mu_{d_R} - \mu_{l_L} - \mu_{l_R} + \frac{2}{3}\mu_\phi = 0. \tag{2.83}$$

We can now notice that in the SM the lepton and baryon currents J_L^μ and J_B^μ are conserved *only at the classical level.* Taking into account quantum corrections, these currents are no longer conserved, which ultimately leads to non-perturbative processes, called *sphalerons*, that can efficiently violate both the baryon and the lepton numbers in the Early Universe plasma. We shall now briefly describe how these processes work.

2.2.1.1 Electroweak sphalerons

The pure SM lagrangian is invariant under global $U(1)$ transformations of the lepton and the quark fields respectively. Through the Noether theorem, this invariance leads to the conservation of the lepton and the baryon currents J_L^μ and J_B^μ, so that the lepton and baryon numbers are conserved too. However, this only holds at the classical level. When quantum corrections are considered, these currents are no longer conserved in the SM due to the chiral anomaly [77, 78] and their divergences are non-vanishing

$$\partial_\mu J_L^\mu = \partial_\mu J_B^\mu = \frac{N_f}{32\pi^2}\left(-g^2 {F_L}^a_{\mu\nu}\tilde{F}_L^{a\mu\nu} + g'^2 {F_Y}_{\mu\nu}\tilde{F}_Y^{\mu\nu}\right), \tag{2.84}$$

where ${F_L}^a_{\mu\nu}$ and ${F_Y}_{\mu\nu}$ are the field strengths of $SU(2)_L$ and $U(1)_Y$ respectively. The tilde denotes the dual tensor, i.e. $\tilde{F}_L^{a\mu\nu} = 1/2\, \varepsilon^{\mu\nu\rho\sigma}{F_L}^a_{\rho\sigma}$, g and g' are the gauge couplings and N_f is the number of fermion generations. Clearly eq. (2.84) implies that both the baryon and the lepton number are not conserved anymore at the quantum level. It is very important to notice that we still have

$$\partial_\mu\left(J_B^\mu - J_L^\mu\right) = 0, \tag{2.85}$$

at any order in the quantum theory. Therefore, in the SM the quantum number $B-L$ is exactly conserved. It is interesting to understand how B, L and in general $B+L$ are violated within the SM.
It is possible to re-write eq. (2.84) as

$$\partial_\mu J_L^\mu = \partial_\mu J_B^\mu = N_f\, \partial_\mu K^\mu, \tag{2.86}$$

where we have introduced the new current

$$K^\mu = -\frac{g^2}{32\pi^2}\varepsilon^{\mu\nu\rho\sigma}W_\nu^a\left(\partial_\rho W_\sigma^a + \frac{g}{3}\varepsilon^{abc}W_\rho^b W_\sigma^c\right) + \frac{g'^2}{32\pi^2}\varepsilon^{\mu\nu\rho\sigma}B_\nu {F_Y}_{\rho\sigma}, \tag{2.87}$$

where W_μ^a and B_μ are the gauge fields of $SU(2)_L$ and $U(1)_Y$ respectively. In order to gain information on the variation of the baryon and lepton numbers, the divergences must be integrated on space and time. However, the integral of the divergence of K^μ can be transformed into an integral over a hypersurface at infinity, by Gauss' theorem. It can be shown that for vanishing field strength at infinity, the abelian part vanishes, while the non-abelian term gives

$$\int d^4x\,\partial_\mu K^\mu = \frac{g^3}{96\pi^2}\int_\Sigma d\sigma^\mu \varepsilon_{\mu\nu\rho\sigma}\varepsilon^{abc}W^{a\nu}W^{b\rho}W^{c\sigma}. \tag{2.88}$$

Choosing as integration surface Σ a cylinder with top and bottom at definite time coordinates t_1 and t_0 respectively, and exploiting the gauge invariance of the current in order to pick the temporal gauge $W_0^a = 0$, it is possible to show that the integral over the side surface of the cylinder vanishes and the only contribution is given by the integration over the top and bottom surfaces. We have

$$\int d^4x\,\partial_\mu K^\mu = \frac{g^3}{96\pi^2}\int d^3x\,\varepsilon_{ijk}\varepsilon^{abc}W^{ai}W^{bj}W^{ck}\Big|_{t_0}^{t_1}. \tag{2.89}$$

We can define

$$N_{CS}(t) \equiv \frac{g^3}{96\pi^2}\int d^3x\,\varepsilon_{ijk}\varepsilon^{abc}W^{ai}W^{bj}W^{ck}\Big|_{t}, \tag{2.90}$$

which is the so-called Chern-Simons number, so that in the end we have

$$\Delta B = \Delta L = N_f\left[N_{CS}(t_1) - N_{CS}(t_0)\right] \equiv N_f \Delta N_{CS}. \tag{2.91}$$

The variation in the baryon and lepton number is related to the difference between the Chern-Simons number assigned to the field configurations at t_1 and t_0. The nonabelian group $SU(2)_L$ implies a non-trivial structure of the gauge field vacuum configurations, which can then differ by $\Delta N_{CS} = 0, \pm 1, \pm 2, \ldots$. These vacuum states are separated by a potential barrier. We can therefore say that in the SM, transitions between gauge field configurations with different Chern-Simons number can in principle take place [79], thus implying a non-conservation of the baryon and lepton numbers.

It must be noticed that in perturbation theory, the field fluctuations are small, and oscillate around a well defined vacuum state, without falling into a different one. For this reason, in perturbation theory we always have $\Delta N_{CS} = 0$ and baryon and lepton numbers are conserved at all orders. However, large non-perturbative field configurations that induce the transition between two different topological vacua can exist. The dominant one gives $\Delta N_{CS} = \pm 1$ and therefore a violation of the baryon and lepton number of three units. This can be described by the effective 12-field operator

$$O = \prod_{i=1}^{3}(Q_{Li}Q_{Li}Q_{Li}l_{Li}). \tag{2.92}$$

At zero temperature, these transitions can take place via quantum tunnelling through the potential barrier and we can expect their rate to be exponentially suppressed. These transitions are induced by the anti-instanton [80] and the transition rate can be estimated [79, 81] to be

$$\Gamma_{\text{inst}} \sim \exp\left(-\frac{4\pi}{\alpha_w}\right) \simeq 10^{-164}, \tag{2.93}$$

where $\alpha_w = 4\pi/g^2$. It is clear that the instanton processes are negligible in the SM at zero temperature and so are baryon and lepton number violations.

The situation is different if we consider the thermal effects due to the coupling to a thermal bath, as in the Early Universe. In this case, transitions between different vacua can happen by thermal fluctuations over the potential barrier [82], rather than by tunnelling through it. Two different vacua are separated by a saddle point in the energy which corresponds to a field configuration called *sphalerons*. These have a Chern-Simons number equal to $\pm n/2$ and an energy given by

$$E_s(T) \simeq \frac{8\pi}{g} v(T), \tag{2.94}$$

where $v(T)$ is the VEV of the Higgs field at temperature T. At low temperatures, $T < T_{\mathrm{EW}} \simeq 100\,\mathrm{GeV}$, the $SU(2)_L \times U(1)_Y$ symmetry is broken and $v(T) \neq 0$. Therefore the sphalerons configurations have a finite energy and the transition rate from one vacuum to the other is Boltzmann suppressed. It is possible to compute the rate per unit volume in the broken phase [18, 83, 84]

$$\frac{\Gamma_s}{V} \simeq \frac{m_W^7}{\alpha_w^3 T^3} \exp\left(-\frac{E_s(T)}{T}\right), \tag{2.95}$$

where m_W is the mass of the W boson. This rate is clearly small. However, for high temperatures $T > T_{\mathrm{EW}}$, the electroweak symmetry is restored, the Higgs VEV is zero and the transitions are no longer suppressed by the Boltzmann factor. From eq. (2.95), taking $v(T) = 0$ and employing the W-boson thermal mass $m_W \sim g^2 T$ we could expect that the transition rate per unit volume in the symmetric phase is

$$\frac{\Gamma_s}{V} \simeq \alpha_w^4 T^4. \tag{2.96}$$

However, accounting for thermal effects, the transition rate per unit volume in the symmetric phase is more precisely given by [85, 86]

$$\frac{\Gamma_s}{V} \simeq \alpha_w^5 \log\left(\alpha_w^{-1}\right)\, T^4. \tag{2.97}$$

It is then possible to have a rather high rate and thus efficient B and L violating processes in the Early Universe. Comparing this rate to the Hubble parameter we find that the sphaleron processes are in equilibrium within the temperature range

$$100\,\mathrm{GeV} < T \lesssim 10^{12}\,\mathrm{GeV}. \tag{2.98}$$

These are indeed the temperatures relevant for leptogenesis, as we shall see in the next sections. Therefore, we can consider the sphaleron processes to be in equilibrium at the temperatures we consider.

Efficient sphaleron processes act in a way to minimise the free energy of the plasma in the Early Universe [87]. Indeed, considering the LH quarks and leptons, the free energy is given by

$$F(T) \propto 6\,T^2(3\mu_{Q_L}^2 + \mu_{l_L}^2). \tag{2.99}$$

Since sphalerons preserve $B-L$, the variation in the baryon number must be accompanied by a similar variation in the lepton number, that is $d\mu_{l_L} = d\mu_{Q_L}$. For this reason, we can minimise the free energy as

$$\frac{dF(T)}{d\mu_{l_L}} \propto 12\,T^2(3\mu_{Q_L} + \mu_{l_L}) = 0, \tag{2.100}$$

which gives

$$3\mu_{Q_L} + \mu_{l_L} = 0. \tag{2.101}$$

Clearly, we can obtain the same relation by considering the interactions represented by the operator in eq. (2.92).

Using eqs. (2.82), (2.83) and (2.101) we can rewrite eq. (2.81) in terms of μ_{l_L} as

$$n_B - n_{\bar{B}} = -\frac{2}{3} g T^2 \mu_{l_L}, \qquad n_L - n_{\bar{L}} = \frac{51}{42} g T^2 \mu_{l_L}. \tag{2.102}$$

This clearly shows that in the Early Universe a baryon asymmetry is strictly linked to a lepton asymmetry, through the chemical potential μ_{l_L}[2]. Therefore, the generation of a lepton asymmetry implies the production of a baryon asymmetry at the same time. These relations show that the idea of leptogenesis is indeed viable: the production of a lepton asymmetry is accompanied in the Early Universe by the generation of a baryon asymmetry.

However, since both B and L are violated by SM processes, while $B-L$ is not, we can focus on this quantum number in order to single out the effective contribution of the New Physics through leptogenesis. We have

$$n_{B-L} \equiv n_B - n_{\bar{B}} - (n_L - n_{\bar{L}}) = -\frac{79}{42} g T^2 \mu_{l_L}. \tag{2.103}$$

Hence

$$\begin{align} n_B - n_{\bar{B}} &= \frac{28}{79} n_{B-L}, \tag{2.104}\\ n_L - n_{\bar{L}} &= -\frac{51}{79} n_{B-L}. \tag{2.105}\end{align}$$

Since all the SM processes we have analysed do actively modify both the lepton and the baryon asymmetry, it is more convenient to focus on the $B-L$ asymmetry, rather than on the lepton one. Indeed, $B-L$ is preserved by the SM and eventually broken exclusively by the leptogenesis setup. Therefore, by studying the $B-L$ asymmetry we

---

[2] The choice of μ_{l_L} as independent variable will turn out particularly useful in the following sections.

are allowed to concentrate only on the relevant leptogenesis processes, leaving aside the SM ones, which will then imply the generation of a baryon asymmetry as in eq. (2.104).

We can conclude by observing that the violation of L introduced by the Majorana nature of the heavy neutrinos implies a violation of $B - L$ and the generation of a baryon asymmetry. Therefore, in our setup the first of Sakharov's conditions is satisfied by the violation of the lepton number which implies a final baryon asymmetry through the net of SM processes in equilibrium in the Early Universe.

2.2.2 Violation of C and CP

The C and CP symmetry violation in our model is provided by decays and inverse-decays of the heavy neutrinos into leptons and anti-leptons. We can estimate this asymmetry through the so called *flavoured CP-asymmetry parameters*

$$\varepsilon_{i\alpha} \equiv -\frac{\Gamma_{i\alpha} - \bar{\Gamma}_{i\alpha}}{\Gamma_i + \bar{\Gamma}_i}, \tag{2.106}$$

where we have defined the flavoured decay rates into both components of the $SU(2)_L$ doublets

$$\Gamma_{i\alpha} \equiv \Gamma\left(N_i \rightarrow l_\alpha + \tilde{\Phi}^\dagger\right), \tag{2.107}$$

$$\bar{\Gamma}_{i\alpha} \equiv \Gamma\left(N_i \rightarrow \overline{l_\alpha} + \tilde{\Phi}\right), \tag{2.108}$$

and the unflavoured decay rates

$$\Gamma_i \equiv \sum_\alpha \Gamma_{i\alpha}, \qquad \bar{\Gamma}_i \equiv \sum_\alpha \bar{\Gamma}_{i\alpha}. \tag{2.109}$$

When no dependence in the rates is specified, they are considered as calculated at zero temperature.

The CP asymmetries vanish when the decay rates are computed at tree level. However, taking into account loop corrections they can get a finite value. Indeed, considering the decay process up to one loop, we have a matrix element

$$\mathcal{M}_{i\alpha} = \mathcal{M}^0_{i\alpha} + \mathcal{M}^1_{i\alpha} = y_0 A^0_{i\alpha} + y_1 A^1_{i\alpha}, \tag{2.110}$$

where we have distinguished the coupling parts y_0, y_1 and the amplitudes A^0, A^1 at tree level and 1-loop respectively. For the CP conjugate process we have

$$\overline{\mathcal{M}}_{i\alpha} = y_0^* \overline{A^0}_{i\alpha} + y_1^* \overline{A^1}_{i\alpha}, \tag{2.111}$$

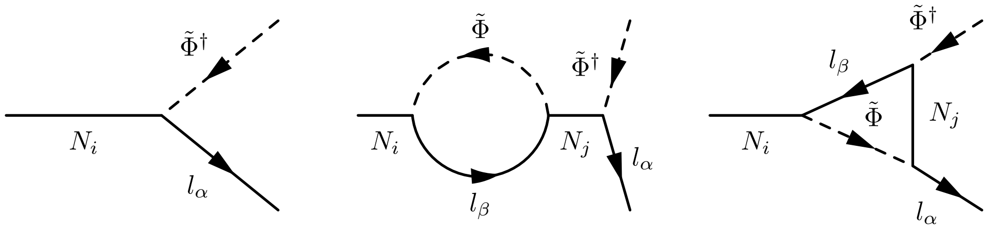

Figure 2.1: Tree-level and 1-loop diagram for the decay $N_i \to l_\alpha \tilde{\Phi}^\dagger$. Majorana neutrinos are depicted with a solid line without arrow, while the arrow on the Higgs dotted line represents the hypercharge flow.

therefore from eq. (2.106) we have

$$\begin{aligned}\varepsilon_{i\alpha} &= -\frac{\int d\Pi_{l,\phi}\,|\mathcal{M}_{i\alpha}|^2 - \left|\overline{\mathcal{M}}_{i\alpha}\right|^2}{\sum_\beta \int d\Pi_{l,\phi}\left(\left|\mathcal{M}^0_{i\beta}\right|^2 + \left|\overline{\mathcal{M}^0}_{i\beta}\right|^2\right)}\\ &= -\frac{\int d\Pi_{l,\phi}\,\left|y_0 A^0_{i\alpha} + y_1 A^1_{i\alpha}\right|^2 - \left|y_0^*\overline{A^0}_{i\alpha} + y_1^*\overline{A^1}_{i\alpha}\right|^2}{\sum_\beta \int d\Pi_{l,\phi}\left(\left|y_0 A^0_{i\beta}\right|^2 + \left|y_0^*\overline{A^0}_{i\beta}\right|^2\right)},\end{aligned} \tag{2.112}$$

where

$$d\Pi_{l,\phi} \equiv (2\pi)^4\delta^4(p_i - p_f)\frac{d^3p_\phi}{(2\pi)^3 2E_\phi}\frac{d^3p_l}{(2\pi)^3 2E_l}, \tag{2.113}$$

is the phase-space integration measure.
Since $\left|A^k\right|^2 = \left|\overline{A^k}\right|^2$, we can write

$$\varepsilon_{i\alpha} = -\frac{2\,\mathrm{Im}\{y_0 y_1^*\}\int d\Pi_{l,\phi}\,\mathrm{Im}\left\{A^0_{i\alpha}{A^1}^*_{i\alpha}\right\}}{\sum_\beta |y_0|^2\int d\Pi_{l,\phi}\left|A^0_{i\beta}\right|^2}. \tag{2.114}$$

It is then clear that the *CP* asymmetry depends on the imaginary part of the couplings and on the interference between the tree-level and the 1-loop decay amplitudes, whose relevant Feynman diagrams are shown in fig. 2.1. It is easy to verify that in order to have non-vanishing *CP* asymmetry, we must have at least two heavy neutrinos. The imaginary part of $A^0_{i\alpha}{A^1}^*_{i\alpha}$ can be computed with cutting rules [88, 89], by cutting the 1-loop diagrams and putting the intermediate particles on shell. For *hierarchical* heavy neutrino masses, $M_1 < M_2 < M_3$, the flavoured *CP* asymmetries are then given by [90]

$$\begin{aligned}\varepsilon_{i\alpha} = \frac{3}{16\pi\,(Y^\dagger Y)_{ii}}\sum_{j\neq i}&\left[\mathrm{Im}\left\{Y^*_{\alpha i}Y_{\alpha j}\left(Y^\dagger Y\right)_{ij}\right\}\frac{\xi\left(M_j^2/M_i^2\right)}{M_j/M_i}\right.\\ &\left.+\frac{2}{3\left(M_j^2/M_i^2 - 1\right)}\mathrm{Im}\left\{Y^*_{\alpha i}Y_{\alpha j}\left(Y^\dagger Y\right)_{ji}\right\}\right],\end{aligned} \tag{2.115}$$

where

$$\xi(x) = \frac{2}{3}x\left[(1+x)\ln\left(\frac{1+x}{x}\right) - \frac{2-x}{1-x}\right]. \tag{2.116}$$

As already mentioned, purely real Yukawa couplings $Y_{\alpha i}$ will result in vanishing *CP* asymmetries.

Using the Dirac neutrino mass matrix $m_D = vY$, it will be useful to define here

$$\widetilde{m}_i \equiv \frac{\left(m_D^\dagger m_D\right)_{ii}}{M_i}, \tag{2.117}$$

and rewrite the *CP* asymmetries as

$$\varepsilon_{i\alpha} = \overline{\varepsilon}(M_i)\sum_{j\neq i}\left\{\mathcal{I}_{ij}^{\alpha}\,\xi\left(\frac{M_j^2}{M_i^2}\right) + \mathcal{J}_{ij}^{\alpha}\,\frac{2}{3(1-M_i^2/M_j^2)}\right\}, \tag{2.118}$$

where

$$\overline{\varepsilon}(M_i) \equiv \frac{3}{16\pi}\frac{M_i\,m_{\rm atm}}{v^2}, \tag{2.119}$$

and

$$\mathcal{I}_{ij}^{\alpha} \equiv \frac{\mathrm{Im}\left\{m_{D\alpha i}^{*}m_{D\alpha j}(m_D^\dagger m_D)_{ij}\right\}}{M_i\,M_j\,\widetilde{m}_i\,m_{\rm atm}}, \tag{2.120}$$

$$\mathcal{J}_{ij}^{\alpha} \equiv \frac{\mathrm{Im}\left\{m_{D\alpha i}^{*}m_{D\alpha j}(m_D^\dagger m_D)_{ji}\right\}}{M_i\,M_j\,\widetilde{m}_i\,m_{\rm atm}}\,\frac{M_i}{M_j}. \tag{2.121}$$

Without distinguishing the flavour of the final lepton doublet, i.e. considering the decay of heavy neutrino N_i into a coherent superposition $|l_i\rangle$ of flavour eigenstates, it is possible to define the *unflavoured CP* asymmetries

$$\varepsilon_i \equiv \sum_{\alpha}\varepsilon_{i\alpha} = \overline{\varepsilon}(M_i)\sum_{j\neq i}\frac{\mathrm{Im}\left\{(m_D^\dagger m_D)_{ij}^2\right\}}{M_i\,M_j\,\widetilde{m}_i\,m_{\rm atm}}\,\xi(M_j^2/M_i^2). \tag{2.122}$$

We can exploit the orthogonal matrix parameterisation and rewrite eq. (2.118) as

$$\begin{aligned}\varepsilon_{i\alpha} =& \frac{3}{16\pi v^2\,\widetilde{m}_i}\\ &\times\sum_{j\neq i}M_j\left[\mathrm{Im}\left\{\left(\sum_k m_k^{1/2}U_{\alpha k}^{*}\Omega_{ki}^{*}\right)\left(\sum_l m_l^{1/2}U_{\alpha l}\Omega_{li}\right)\left(\sum_n m_n\Omega_{ni}^{*}\Omega_{nj}\right)\right\}\frac{\xi\left(M_j^2/M_i^2\right)}{M_j/M_i}\right.\\ &\left.+\frac{2}{3\left(M_j^2/M_i^2-1\right)}\mathrm{Im}\left\{\left(\sum_k m_k^{1/2}U_{\alpha k}^{*}\Omega_{ki}^{*}\right)\left(\sum_l m_l^{1/2}U_{\alpha l}\Omega_{li}\right)\left(\sum_n m_n\Omega_{nj}^{*}\Omega_{ni}\right)\right\}\right],\end{aligned} \tag{2.123}$$

and

$$\widetilde{m}_i = \sum_j m_j \left|\Omega_{ji}\right|^2 . \tag{2.124}$$

It is possible to have non-vanishing flavour *CP* asymmetry also if the orthogonal matrix Ω is purely real[3]. However, in our discussion we will not consider these special cases. We can also notice that, in order to have a sizeable *CP* asymmetry for heavy neutrino N_i, at least one heavier neutrino is needed, so to avoid suppression.

It is worth underlining that in the present work we shall always deal with a hierarchical neutrino spectrum, therefore eq. (2.118) will always be the correct expression for the *CP* asymmetries. In case of degenerate heavy neutrino spectrum, this expression is not valid anymore and it is possible to have sizeable enhancements of the *CP* asymmetry. Leptogenesis scenarios relying on this effect are said to realise *resonant leptogenesis* [91].

2.2.3 Departure from equilibrium

It is important to verify that in this scenario also the last Sakharov's condition is indeed realised. We have seen that, in our seesaw model, the process that violates L, C and *CP*, and therefore is eligible for the production of a final asymmetry, is the decay of the heavy neutrinos into leptons and Higgs doublets. Therefore we must investigate if it is possible that these decays occur out of thermal equilibrium. If equilibrium is enforced, we have

$$N \longleftrightarrow l + \Phi, \tag{2.125}$$

where we have generically indicated the heavy neutrinos, the leptons and the Higgs fields. This means that both the decay and the inverse decay processes take place in equilibrium and we have an additional relation on the relevant chemical potentials

$$\mu_{N_R} - \mu_{l_L} - \mu_\phi = 0. \tag{2.126}$$

Considering the full set of relations given by eqs. (2.82), (2.83), (2.101) and (2.126), we have that the only solution is given by the trivial one, i.e. all the chemical potentials vanish. Therefore, we also have $\mu_{l_L} = 0$ which, through eq. (2.104), implies zero baryon asymmetry. If at least one between the decay and the inverse-decay reactions is not in equilibrium, then we have departure from thermal equilibrium, eq. (2.126) does not hold anymore and a non-vanishing μ_{l_L} can give a sizeable final baryon asymmetry. We must therefore study if and when decays and inverse-decays can take place out of thermal equilibrium.

To understand if this is possible, we can calculate the decay and inverse decay rates and compare them with the Hubble expansion rate $H(T)$. If the rates are larger than the Hubble parameter, then the reaction is in thermal equilibrium [92]. In the temperature

---

[3] Except for permutations of the identity, as we shall see later on.

range of our interest the radiation-dominated expression of the Hubble rate can be used

$$H(T) = \frac{2\pi^{3/2}}{3\sqrt{5}} g_*^{1/2} \frac{T^2}{M_{\rm Pl}} \simeq 1.66\, g_*^{1/2} \frac{T^2}{M_{\rm Pl}}. \tag{2.127}$$

To capture the general picture, we shall consider the *total decay rate*

$$\Gamma_i^{\rm D,tot} \equiv \sum_\alpha (\Gamma_{i\alpha} + \overline{\Gamma}_{i\alpha}) \tag{2.128}$$

and the *total inverse decay rate*

$$\Gamma_i^{\rm ID,tot} \equiv \sum_\alpha (\Gamma_{i\alpha}^{\rm ID} + \overline{\Gamma}_{i\alpha}^{\rm ID}). \tag{2.129}$$

We are interested in studying the ratios

$$\frac{\Gamma_i^{\rm D,tot}(T)}{H(T)}, \qquad \frac{\Gamma_i^{\rm ID,tot}(T)}{H(T)}, \tag{2.130}$$

where the temperature-dependent decay and inverse decay rates appear. The reactions are in equilibrium when

$$\frac{\Gamma_i^{\rm D,tot}(T)}{H(T)} > 2, \qquad \frac{\Gamma_i^{\rm ID,tot}(T)}{H(T)} > 2, \tag{2.131}$$

where we have the factor 2 since in the definitions of $\Gamma_{i\alpha}$ and $\Gamma_{i\alpha}^{\rm ID}$ we consider the decay in the two components of the $SU(2)$ doublets, cf. eq. (2.107).
Taking into account the proper dilation factor, we have [93]

$$\Gamma_i^{\rm D,tot}(T) = \Gamma_i^{\rm D,tot} \frac{\mathcal{K}_1(T)}{\mathcal{K}_2(T)}, \tag{2.132}$$

where $\mathcal{K}_i(T)$ are modified Bessel functions and at tree-level

$$\begin{aligned} \Gamma_i^{\rm D,tot} &\equiv \sum_\alpha (\Gamma_{i\alpha} + \overline{\Gamma}_{i\alpha}) = \sum_\alpha \frac{|m_{Di\alpha}|^2\, M_i}{8\pi v^2} \\ &= \frac{\widetilde{m}_i\, M_i^2}{8\pi v^2}. \end{aligned} \tag{2.133}$$

We can also define the so-called (unflavoured) *decay parameters*

$$K_i \equiv \frac{\Gamma_i^{\rm D,tot}}{H(T = M_i)} = \frac{\Gamma_i + \overline{\Gamma}_i}{H(T = M_i)}, \tag{2.134}$$

so that, using eqs. (2.127) and (2.133), the ratio in eq. (2.130) can be written as

$$\frac{\Gamma_i^{\rm D,tot}(T)}{H(T)} = \frac{\Gamma_i^{\rm D,tot}}{H(T = M_i)} \frac{M_i^2}{T^2} \frac{\mathcal{K}_1(T)}{\mathcal{K}_2(T)} = K_i \frac{M_i^2}{T^2} \frac{\mathcal{K}_1(T)}{\mathcal{K}_2(T)}. \tag{2.135}$$

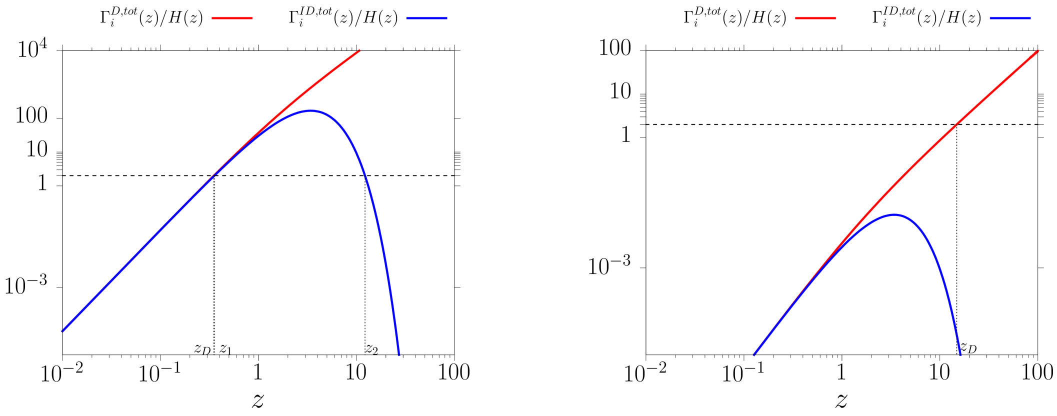

(a) (b)

Figure 2.2: Behaviour of $\Gamma_i^{\mathrm{D,tot}}(z)/H(z)$ (red line) and $\Gamma_i^{\mathrm{ID,tot}}(z)/H(z)$ (blue line) for two different values of K_i: $K_i = 100$ left panel and $K_i = 10^{-2}$ right panel. z_D denotes the value of $z = M_i/T$ such that $\Gamma_i^{\mathrm{D,tot}}(z_D)/H(z_D) = 2$. In (a), $z_{1,2}$ are such that $\Gamma_i^{\mathrm{ID,tot}}(z_{1,2})/H(z_{1,2}) = 2$ and we have $z_1 \simeq z_D$.

It will turn useful to introduce here the variable $z \equiv M_i/T$ so that we have

$$\frac{\Gamma_i^{\mathrm{D,tot}}(z)}{H(z)} = K_i\, z^2 \frac{\mathcal{K}_1(z)}{\mathcal{K}_2(z)}. \tag{2.136}$$

This way, by studying the behaviour of $\Gamma_i(z)/H(z)$, we are able to understand when decays are in equilibrium or out of equilibrium. We can also introduce further useful relations by defining the equilibrium neutrino mass

$$m_* \equiv \frac{8\pi v^2}{M_i^2} H(T = M_i) = \frac{16\pi^{5/2}\sqrt{g_*}}{3\sqrt{5}} \frac{v^2}{M_{\mathrm{Pl}}} \simeq 1.08 \times 10^{-3}\mathrm{eV}, \tag{2.137}$$

so that

$$K_i = \frac{\widetilde{m}_i}{m_*}. \tag{2.138}$$

The total inverse decay rate can be obtained at equilibrium from the decay rate

$$n_l^{\mathrm{eq}}\, \Gamma_i^{\mathrm{ID,tot}} = n_{N_i}^{\mathrm{eq}}\, \Gamma_i^{\mathrm{D,tot}}, \tag{2.139}$$

where n_l^{eq} and $n_{N_i}^{\mathrm{eq}}$ are the equilibrium number densities of lepton doublets and heavy neutrinos. This way we obtain

$$\frac{\Gamma_i^{\mathrm{ID,tot}}(z)}{H(z)} = \frac{1}{2} K_i\, \mathcal{K}_1(z) z^4, \tag{2.140}$$

and it is possible to study the behaviour of $\Gamma_i^{\mathrm{ID,tot}}(z)/H(z)$ to see if the inverse decays drop out of thermal equilibrium. Eqs. (2.136) and (2.140) are plotted in fig. 2.2 for two different values of K_i: $K_i = 100$ in fig. 2.2(a) and $K_i = 10^{-2}$ in fig. 2.2(b).

Studying the red curve in fig. 2.2, we can notice that we always have a value z_D such that

$$\frac{\Gamma_i^{\mathrm{D,tot}}(z_D)}{H(z_D)} = 2, \tag{2.141}$$

so that for $z \geq z_D$ we can say that the decay reaction is in equilibrium.
Studying the blue curve, we can notice two different behaviours in fig. 2.2(a) and 2.2(b), depending on the value of K_i:

- for $K_i \gg 1$ we can find two values z_1, z_2 at which we have

  $$\frac{\Gamma_i^{\mathrm{ID,tot}}(z_{1,2})}{H(z_{1,2})} = 2 \tag{2.142}$$

  and therefore a window $z_1 \leq z \leq z_2$ in which inverse decays reactions are in equilibrium,
- for $K_i \ll 1$ the blue curve never reaches 2, therefore in this case inverse decays are never in equilibrium.

These two situations take the names of *strong washout* and *weak washout* regime respectively.

- In the *strong washout* regime we have a full departure from equilibrium for $z < z_D$, when both decays and inverse decays are out of equilibrium. In this situation the third Sakharov's condition is satisfied and an asymmetry can be generated. For $z_D < z_1 \leq z \leq z_2$ both reactions are in equilibrium and proceed efficiently to erase the asymmetry produced before. Therefore, if thermal equilibrium were maintained, no asymmetry would survive eventually. However, for $z > z_2$ inverse decays drop out of equilibrium, therefore N_i decays take place out of equilibrium, satisfying again the third Sakharov's condition. For this reason, a net asymmetry can be finally produced.
- In the *weak washout* regime inverse decays are never in equilibrium, therefore the third Sakharov's condition is satisfied and an asymmetry can be produced. However, by missing an equilibrium window like that in the strong washout regime, the final asymmetry is sensitive to the initial conditions.

With this analysis of decay and inverse decay rates we have shown that in the framework of leptogenesis the heavy neutrino decays can take place out of thermal equilibrium, thus satisfying also the third Sakharov's condition. In the following section we shall analyse in detail how the asymmetry is actually produced.

2.2.4 Vanilla leptogenesis

Once established that all three Sakharov's conditions can be satisfied within our model, we can study in detail how the asymmetry is generated by the leptogenesis mechanism. In order to point out the key aspects and the fundamentals of the asymmetry production process, it can be more convenient to study the simplest version of leptogenesis, often referred to as *vanilla leptogenesis.* In this framework we shall make the following assumptions.

1. We shall assume a hierarchical heavy neutrino spectrum $M_1 < M_2 < M_3$.
2. We shall assume that the dominant contribution to the final asymmetry comes from the lightest, N_1, while those of N_2 and N_3 are negligible. For this reason, this is called N_1-*dominated leptogenesis.*
3. We shall assume that the leptons originated from the decay of N_1 are produced in a coherent superposition of flavour eigenstates. We are therefore neglecting the effects of lepton flavour, hence the name of *unflavoured* N_1-*dominated leptogenesis* [75, 76, 94]. We shall study flavour effects in the following chapter.
4. We are considering only heavy neutrinos decays and inverse decays, while neglecting the scattering processes predicted by our lagrangian. These violate the lepton number by 1 or 2 units and would in principle concur to the evolution of the asymmetry. We shall comment on their effect in the following section and neglect them in the rest of this work.
5. We shall also neglect other corrective effects such as thermal corrections [95], which in general have a small impact, quantum corrections [96–98], and spectator processes [99, 100]. We will return on the latter effect later in the following chapters when commenting on *flavour coupling.*

As a matter of convention, we can study the evolution of the number density of a species (or asymmetry) X normalised to a comoving volume containing one heavy neutrino in ultra relativistic equilibrium. Therefore we shall use

$$N_X \equiv \frac{n_X(z)}{n_{N_1}^{\rm eq}(z \ll 1)}, \qquad \text{with} \quad z \equiv \frac{M_1}{T}, \tag{2.143}$$

where n_X is the number density of X. This can be easily linked to the abundance, or *yield* $Y_X \equiv n_X/s$ as

$$N_X(z) = \frac{4}{3}\frac{n_X(z)}{n_\gamma^{\rm eq}(z)} = \frac{4}{135}\frac{\pi^4 g_*^s(z)}{\zeta(3)}\frac{n_X(z)}{s(z)} \simeq 2.40\, g_*^s(z) Y_X(z), \tag{2.144}$$

where $g_*^s(T) \equiv \sum_b g_b(T_b/T)^3 + 7/8 \sum_f g_f(T_f/T)^3$. Under the assumption (2), we shall focus on the evolution of the abundance of N_1, which is ruled by the Boltzmann equation

$$\frac{dN_{N_1}}{dz} = -D_1(z)\left(N_{N_1}(z) - N_{N_1}^{\rm eq}(z)\right), \tag{2.145}$$

where only decays and inverse decays are taken into account in the *decay factor* $D_1(z)$, following assumption (4). The decay factor is given by

$$D_1(z) \equiv \frac{\Gamma_1^{\rm D,tot}(z)}{z\,H(z)} = K_1\,z\,\frac{\mathcal{K}_1(z)}{\mathcal{K}_1(z)}, \tag{2.146}$$

where we have used the result in eq. (2.136). The variation in the abundance of N_1 is then determined by how far its distribution is from the equilibrium one.

By what was shown in subsection 2.2.1, it is more convenient to quantify the asymmetry with the $B-L$ term, which is genuinely due to leptogenesis. The $B-L$ asymmetry will then receive a contribution from the decays and inverse-decays of N_1 that takes into account the *CP* asymmetry factor. On top of this, the asymmetry in general will tend to be erased through inverse decay processes that will statistically take place depending on the size of the asymmetry itself. This second contribution is called *washout.* Putting these two terms together we have the following Boltzmann equation for the evolution of the $B-L$ asymmetry

$$\frac{dN_{B-L}^{\rm lep}}{dz} = \varepsilon_1 D_1(z)\left(N_{N_1}(z) - N_{N_1}^{\rm eq}(z)\right) - W_1^{\rm ID}(z)N_{B-L}^{\rm lep}(z). \tag{2.147}$$

Here the washout factor (due to inverse decays into N_1) is defined as

$$W_1^{\rm ID}(z) \equiv \frac{1}{2}\frac{\Gamma_1^{\rm ID,tot}(z)}{z\,H(z)} = \frac{1}{4}K_1 z^3 \mathcal{K}_1(z), \tag{2.148}$$

where we used the result in eq. (2.140). Eq. (2.147) can be integrated giving

$$N_{B-L}^{\rm lep}(z) = N_{B-L}^{\rm p,i}\exp\left[-\int_0^z dz' W_1^{\rm ID}(z')\right] + \varepsilon_1\kappa(z), \tag{2.149}$$

where $N_{B-L}^{\rm p,i}$ is the initial asymmetry and we have defined the *efficiency factor*

$$\kappa(z) \equiv -\int_0^z dz'\,\frac{dN_{N_1}}{dz'}\exp\left[-\int_{z'}^z dz''\,W_1^{\rm ID}(z'')\right]. \tag{2.150}$$

In eq. (2.149), the dependence on the initial asymmetry $N_{B-L}^{\rm p,i}$ is evident. Here we shall consider a *vanishing initial asymmetry* $N_{B-L}^{\rm p,i} = 0$, thus eliminating the first term in the equation and leaving

$$N_{B-L}^{\rm lep}(z) = \varepsilon_1\kappa(z). \tag{2.151}$$

In the strong washout regime the contribution of any initial asymmetry is anyways erased by the intense washout due to $K_1 \gg 1$. We shall here concentrate on this case, giving only some comments on the expressions valid in the weak washout regime.
Assuming vanishing initial abundance of the heavy neutrinos implies that N_1 is thermally produced by inverse decays, which try to reach the equilibrium distribution. Assuming the N_1 distribution reaches the equilibrium distribution

$$N_{N_1}^{\rm eq}(z) = \frac{1}{2} z^2 \mathcal{K}_2(z) \tag{2.152}$$

at z_{eq}, for $z < z_{eq}$ the distribution of N_1 is negligible compared to the equilibrium one, so that we can rewrite eq. (2.145) as

$$\frac{dN_{N_1}}{dz} \simeq D_1(z) N_{N_1}^{\rm eq}(z), \quad z < z_{eq}. \tag{2.153}$$

However, given the detailed balance condition $N_l^{\rm eq}\Gamma_1^{\rm ID} = N_{N_1}^{\rm eq}\Gamma_1$, and $N_l^{\rm eq} = 1$, we also have

$$\frac{dN_{N_1}}{dz} \simeq 2\, W_1^{\rm ID}(z), \quad z < z_{eq}. \tag{2.154}$$

Therefore we obtain

$$\begin{aligned} \kappa^-(z) \equiv \kappa(z < z_{eq}) &= -2 \int_0^z dz'\, W_1^{\rm ID}(z') \exp\left[- \int_{z'}^z dz''\, W_1^{\rm ID}(z'') \right] \\ &\simeq -2 \left(1 - \exp\left[-\frac{1}{12} K_1 z^3 \right] \right). \end{aligned} \tag{2.155}$$

Integrating eq. (2.153), we get

$$N_{N_1}(z < z_{eq}) \simeq \frac{K_1}{6} z^3. \tag{2.156}$$

For $z \to +\infty$ this gives [94]

$$\kappa_f^-(K_1) \equiv \kappa^-(z \to +\infty) \simeq -2 e^{-\frac{1}{2} N(K_1)} \left(\exp\left[\frac{1}{2} \bar{N}(K_1) \right] - 1 \right), \tag{2.157}$$

where

$$N(K_1) \equiv \frac{3\pi}{4} K_1, \qquad \bar{N}(K_1) \equiv \frac{N(K_1)}{\left(1 + \sqrt{N(K_1)}\right)^2}. \tag{2.158}$$

This expression for $\kappa_f^-(K_1)$ is also valid in the weak washout regime. From eq. (2.157) we can see that the strong washout causes an exponential suppression of the asymmetry produced, for $z < z_{eq}$, by the inverse decay processes that build up the N_1 abundance. This implies that around z_{eq} the asymmetry is quickly erased by the strong washout. The final asymmetry must then be produced in the following stage, for $z > z_{eq}$.

For $z > z_{eq}$ the actual distribution $N_{N_1}(z)$ cannot be neglected anymore. We can study the deviation from the equilibrium distribution by defining

$$\Delta(z) \equiv N_{N_1}(z) - N_{N_1}^{\mathrm{eq}}(z), \tag{2.159}$$

and rewriting eq. (2.145) as

$$\Delta(z) = -\frac{1}{D_1(z)}\frac{dN_{N_1}}{dz}. \tag{2.160}$$

Having assumed strong washout, i.e. $K_1 \gg 1$, we can use that $D_1(z) \propto K_1$ and solve eq. (2.145) by perturbatively expanding in $1/K_1$, so that [94]

$$\Delta(z) = -\frac{1}{D_1(z)}\frac{dN_{N_1}^{\mathrm{eq}}(z)}{dz} + \mathcal{O}\left(\frac{1}{K_1^2}\right). \tag{2.161}$$

Using eq. (2.152), (2.148) and the properties of modified Bessel functions, we obtain

$$\Delta(z) = \frac{1}{D_1(z)}\frac{2}{z\,K_1}W_1^{\mathrm{ID}}. \tag{2.162}$$

This can be used in the derivation of the efficiency factor for $z > z_{eq}$

$$\begin{aligned} \kappa^+(z) \equiv \kappa(z > z_{eq}) &= \int_{z_{eq}}^{z} dz' D_1(z')\Delta(z') \exp\left[-\int_{z'}^{z} dz''\, W_1^{\mathrm{ID}}(z'')\right] \\ &= \frac{2}{K_1}\int_{z_{eq}}^{z} dz'\, \frac{W_1^{\mathrm{ID}}(z')}{z'} \exp\left[-\int_{z'}^{z} dz''\, W_1^{\mathrm{ID}}(z'')\right]. \end{aligned} \tag{2.163}$$

This integral can be evaluated by asymptotically expanding around the minimum of the exponent, where the integrand gives the largest contribution. For $z \to +\infty$ this gives [94]

$$\kappa_f^+(K_1) \equiv \kappa^+(z \to +\infty) \simeq \frac{2}{z_L(K_1)\,K_1}\left(1 - \exp\left[-\frac{1}{2}z_L(K_1)\bar{N}(K_1)\right]\right), \tag{2.164}$$

valid also in the weak washout regime, where z_L is such that the exponent in eq. (2.163) has a stationary point and is given by [101]

$$z_L(K_1) \simeq 2 + 4\,K_1^{0.13}\exp\left(-\frac{2.5}{K_1}\right). \tag{2.165}$$

The fact that the efficiency factor receives its largest contribution around this value means that the asymmetry is mostly produced around z_L. Moreover, in the strong washout regime we also have $z_L \simeq z_2$. For these reasons, in the strong washout regime we can take z_L, and the related temperature T_L, as a good estimate for the scale at which leptogenesis takes place.

We can also notice that κ_f^+ and κ_f^- have different sign, which implies that also the asymmetries produced for $z < z_{eq}$ and for $z > z_{eq}$ have different sign as well. We can therefore say that around z_{eq} the asymmetry previously produced is exponentially

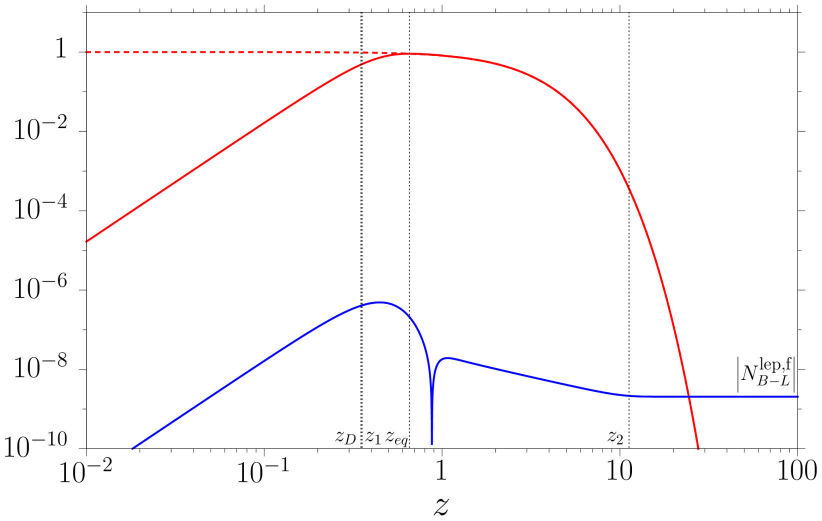

Figure 2.3: Evolution of the N_1 and $|N_{B-L}|$ abundances, in red and blue respectively. The dashed red line marks the N_1 equilibrium distribution. z_D is defined as in eq. (2.141) and $z_{1,2}$ as in eq. (2.142). Here we have $K_1 = 100$

suppressed and on top of it a new asymmetry with different sign is produced. The final asymmetry $N_{B-L}^{\rm lep,f} \equiv N_{B-L}^{\rm lep}(z \to +\infty)$ is then given by

$$N_{B-L}^{\rm lep,f} = \varepsilon_1 \kappa_f(K_1), \tag{2.166}$$

where

$$\kappa_f(K_1) \equiv \kappa_f^-(K_1) + \kappa_f^+(K_1). \tag{2.167}$$

If we assume thermal initial abundance for N_1, the final efficiency factor is given by [94, 102]

$$\kappa_f^{\rm th} \simeq \frac{2}{K_1\, z_L(K_1)} \left[1 - \exp\left(-\frac{1}{2} K_1\, z_L(K_1)\right)\right]. \tag{2.168}$$

It must be noticed that in the strong washout regime the efficiency factors for both vanishing and initial N_1 abundance are given by the same asymptotic expression [103–105]

$$\kappa_f(K_1 \gg 1) \simeq \frac{0.5}{K_1^{1.2}}, \tag{2.169}$$

thus confirming that the strong washout regime is insensitive to the initial conditions.

The evolution of N_1 and $B - L$ abundances in the strong washout case is shown in fig. 2.3. We can notice that for $z \ll 1$ N_1's abundance grows thanks to inverse decays that produce a certain amount of asymmetry $N_{B-L}^{\rm lep}$. At z_D, as in eq. (2.141), the decay processes enter equilibrium and at z_{eq} N_1's distribution reaches the equilibrium one. Around z_{eq} both decays and inverse decays are in equilibrium and the asymmetry generated so far is quickly erased. Decays will then give a new contribution to the asymmetry, with different sign. This would vanish if equilibrium were maintained, however at z_2, as in eq. (2.142), inverse decays drop out of thermal equilibrium, while the heavy neutrino abundance reaches negligible values. Therefore, around $z_2 \simeq z_L$ the asymmetry gets frozen to its final amount $N_{B-L}^{\text{lep,f}}$.

In order to make a comparison with the experimental results, it is necessary to compute the baryon asymmetry that can be obtained from the $B-L$ one produced by leptogenesis. The conversion factor has already been obtained in eq. (2.104), where SM sphalerons and all the processes in equilibrium in the early Universe have been considered. However, as pointed out in the introduction, the experimental evidence we refer to is provided in terms of the baryon-to-photon ratio measured through the CMB, η_B^{CMB}. In order to compare it with the final result of leptogenesis, we must take into account the thermal history of the Universe between the leptogenesis scale $\sim T_L \sim 10^{10}\,\text{GeV}$ and the recombination era $T_0 \sim 0.3\,\text{eV}$. Following the standard picture, during the Universe evolution the baryon-to-photon ratio was diluted by photon production due to the transition to the non-relativistic regime of almost all the particles composing the thermal bath. Therefore, we must obtain the baryon-to-photon ratio produced by leptogenesis and evolve it down to the decoupling temperature, $\eta_B^{\text{lep}}(T_0)$. Considering that after the leptogenesis process, the asymmetry remains stable until present, the asymmetry number density n_{B-L} evolves in a similar way as n_B in eq. (1.12)

$$n_{B-L}^{\text{lep}}(T_0) = \frac{s(T_0)}{s(T_L)} n_{B-L}^{\text{lep}}(T_L), \tag{2.170}$$

Considering the baryon-to-photon ratio, its evolution is similar to eq. (1.13)

$$\eta_B^{\text{lep}} = \frac{n_B - n_{\bar{B}}}{n_\gamma}(T_0) = \frac{28}{79}\frac{n_{B-L}^{\text{lep}}(T_0)}{n_\gamma(T_0)} = \frac{28}{79}\frac{s(T_0)}{s(T_L)}\frac{n_\gamma(T_L)}{n_\gamma(T_0)}\frac{n_{B-L}^{\text{lep}}(T_L)}{n_\gamma(T_L)}, \tag{2.171}$$

where we have used the conversion factor in eq. (2.104). In terms of the N_{B-L} quantity we have

$$\begin{aligned}
\eta_B^{\text{lep}} &= \frac{28}{79}\frac{g_*^s(T_0)}{g_*^s(T_L)}\frac{n_{B-L}^{\text{lep}}(T_L)}{n_\gamma(T_L)} = \frac{28}{79}\frac{g_*^s(T_0)}{g_*^s(T_L)}\frac{N_{B-L}^{\text{lep}}(T_L)}{N_\gamma(T_L)} \\
&= \frac{28}{79}\frac{3}{4}\frac{g_*^s(T_0)}{g_*^s(T_L)} N_{B-L}^{\text{lep}}(T_L) \\
&\equiv d\, N_{B-L}^{\text{lep,f}},
\end{aligned} \tag{2.172}$$

where we have used that $N_\gamma = 4/3$. In the evolution from the high leptogenesis scale T_L down to the recombination era, the count of relativistic degrees of freedom changes sensibly. Indeed, we have $g_*^s(T_L) \simeq 106.75$, while $g_*^s(T_0) \simeq 3.91$, therefore

$$d \simeq 0.96 \times 10^{-2}. \tag{2.173}$$

We are interested in models which are able to produce a final asymmetry compatible with the experimental result η_B^{CMB}, eq. (1.11). In our analysis we shall impose the loose condition

$$\eta_B^{\rm lep} \geq \eta_B^{\rm CMB}. \tag{2.174}$$

Models that are able to satisfy it are said to realised *successful leptogenesis.*

2.2.5 Bounds on vanilla leptogenesis

The simplest leptogenesis scenario we have just discussed is characterised by a lower bound on the mass of the heavy neutrino N_1. We shall now analyse the origin of this important constraint.

Having assumed a hierarchical heavy neutrino spectrum $M_1 \ll M_2 \ll M_3$, we can further simplify the expression of the unflavoured *CP* asymmetry, eq. (2.122), given that

$$\xi(x) = 1 + \frac{5}{9x} + \frac{13}{8x^2} + \mathcal{O}(x^{-3}), \qquad x \to +\infty. \tag{2.175}$$

Taking[4]

$$\xi\left(\frac{M_2^2}{M_1^2}\right) \simeq \xi\left(\frac{M_3^2}{M_1^2}\right) \simeq 1, \tag{2.176}$$

we can rewrite eq. (2.106) for N_1 as [102, 106]

$$\varepsilon_1 \simeq \frac{3\,M_1}{16\pi v^2\,\tilde{m}_1} \sum_j m_j^2 \,\mathrm{Im}\big\{\Omega_{j1}^2\big\}\,. \tag{2.177}$$

It can be immediately noticed that in the degenerate limit, $m_1 \simeq m_2 \simeq m_3 \equiv m$ we have $\varepsilon_1 = 0$ since, given the orthogonality condition $\sum_m \Omega_{lm}\Omega_{km} = \delta_{lk}$ we get $\mathrm{Im}\big\{\Omega_{11}^2 + \Omega_{21}^2 + \Omega_{31}^2\big\} = 0$. By maximising eq. (2.177) we get an upper bound on the unflavoured *CP* asymmetry [102, 107]

$$|\varepsilon_1| \lesssim \varepsilon_1^{\rm max} \equiv \frac{3\,M_1}{16\pi v^2}(m_3 - m_1). \tag{2.178}$$

This gives the maximum value of the final baryon-to-photon ratio

$$\eta_B^{\rm lep,max} = d\varepsilon_1^{\rm max}\,\kappa_f = d\frac{3\,M_1}{16\pi v^2}(m_3 - m_1)\,\kappa_f \geq \eta_B^{\rm CMB}, \tag{2.179}$$

where in the last step we imposed the successful leptogenesis condition. This clearly translates into a condition on M_1

$$M_1 \geq \frac{16\pi v^2}{3d(m_3 - m_1)}\frac{\eta_B^{\rm CMB}}{\kappa_f}. \tag{2.180}$$

---

[4] A detailed study that takes into account the difference between $\xi(M_2^2/M_1^2)$ and $\xi(M_3^2/M_1^2)$ can be found in [102].

Therefore we can say that in the vanilla leptogenesis scenario the mass of the lightest heavy neutrino, producing the asymmetry, is bounded from below [107, 108]. It is possible to show that for the experimental value of m_{atm} and vanishing initial N_1 abundance the bound is given by [94, 102, 108]

$$M_1 \gtrsim 3 \times 10^9\,\mathrm{GeV}. \tag{2.181}$$

In this scenario the successful leptogenesis condition is then able to put a constraint on the heavy neutrino mass spectrum by placing a lower bound on M_1. This is an example of a prediction on the, otherwise inaccessible, high-energy neutrino parameters that is derived indirectly through the requirement that the model reproduces the correct final asymmetry.

2.2.6 Comment on scattering processes

The seesaw lagrangian implies the existence of lepton number violating processes other than the decay of the heavy neutrinos. These are generically scatterings involving the lepton doublets and the heavy neutrinos and can be divided into processes violating L by one or two units [109]. The relevant Feynman diagrams are shown in fig. 2.4. They in general play a role in the thermalisation and modification of the heavy neutrinos

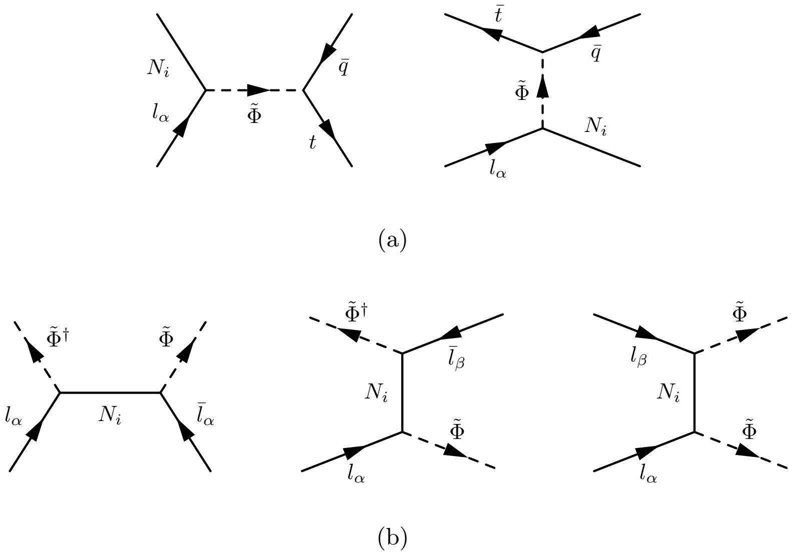

(a)

(b)

Figure 2.4: Feynman diagrams of lepton number violating scattering processes. The full set can be obtained by reversing the fermion/hypercharge arrows. (a) $|\Delta L| = 1$ scattering processes involving the top quark. (b) $|\Delta L| = 2$ scattering processes involving a heavy neutrino in the s and t channel.

abundance and in the generation of the $B-L$ asymmetry, affecting also the washout term. The Boltzmann equations are modified into

$$\frac{dN_{N_1}}{dz} = -\left(D_1(z) + S_1(z)\right)\left(N_{N_1}(z) - N_{N_1}^{\rm eq}(z)\right), \tag{2.182}$$

$$\frac{dN_{B-L}}{dz} = \varepsilon_1\left(D_1(z) + S_1(z)\right)\left(N_{N_1}(z) - N_{N_1}^{\rm eq}(z)\right) - W_1(z)N_{B-L}(z). \tag{2.183}$$

Here the scattering factor S_1 involves the $|\Delta L| = 1$ processes in fig. 2.4(a), that modify the number of heavy neutrinos, and is defined as the decay factor

$$S_1(z) \equiv \frac{\Gamma_1^{|\Delta L|=1}(z)}{z\,H(z)}. \tag{2.184}$$

The washout factor W_1 must take into account also the $|\Delta L| = 2$ processes, in fig. 2.4(b), since these also cause a rebalancing of the asymmetry. The full washout factor is then defined as the sum of three terms

$$W_1(z) \equiv W_1^{\rm ID}(z) + W_1^{|\Delta L|=1}(z) + W_1^{|\Delta L|=2}(z). \tag{2.185}$$

We shall analyse separately the $|\Delta L| = 1$ and the $|\Delta L| = 2$ processes.

2.2.6.1 $|\Delta L| = 1$ scattering

These processes receive the most important contribution from the scattering with top quarks fig. 2.4(a), and gauge bosons. However, here we shall consider only the first case, ignoring the impact of the gauge bosons, which is still rather controversial. It is possible to obtain an expression for the decay plus scattering factor [94]

$$D_1(z) + S_1(z) \simeq K_S\left[1 + \ln\left(\frac{M_1}{m_H}\right) z^2 \ln\left(1 + \frac{a}{z}\right)\right], \tag{2.186}$$

where

$$K_S \equiv \frac{m_*}{m_*^S}K_1, \qquad \text{with} \quad m_*^S \equiv \frac{4\pi^2}{9}\frac{gv^2}{m_t^2}m_*, \tag{2.187}$$

and

$$a \equiv \frac{8\pi^2}{9\ln(M_1/m_H)}, \tag{2.188}$$

with m_H and m_t being respectively the Higgs and the top-quark masses. In eq. (2.186) the scattering term is dominant for $z \lesssim 2$, while for $z \gtrsim 2$ the decay term dominates. This implies that the result of $|\Delta L| = 1$ processes is to favour the heavy neutrino production. Therefore, affecting the the physics before z_{eq} will have an impact mainly in the weak washout regime, which is sensitive to the early stage of leptogenesis. The term $W_1^{|\Delta L|=1}$ can be written as

$$W_1^{|\Delta L|=1}(z) = j_1(z)W_1^{\rm ID}(z), \tag{2.189}$$

where

$$j_1(z) \equiv 1 + \frac{S_1(z)}{D_1(z)} \simeq \left[\frac{z}{a}\ln\left(1+\frac{a}{z}\right) + \frac{K_S}{zK_1}\right]\left(1+\frac{15}{8z}\right). \tag{2.190}$$

It can be shown that, as expected, the final efficiency factor is mildly affected only in the weak washout for vanishing initial abundance. In the strong washout regime the effect of the $|\Delta L| = 1$ scattering processes is negligible [103].

2.2.6.2 $|\Delta L| = 2$ scattering

These processes involve the exchange of a heavy neutrino in the s and t channel. In order to compute the washout factor $W_1^{|\Delta L|=2}$ care must be taken in considering only the non-resonant contribution of the s-channel processes. It is possible to show that these scattering processes are mostly important in the non-relativistic regime and their expression can be approximated as [94]

$$W_1^{|\Delta L|=2} \simeq \frac{\omega}{z^2}\frac{M_1}{10^{10}\,\mathrm{GeV}}\frac{\sum_i m_i^2}{1\,\mathrm{eV}^2}, \tag{2.191}$$

where $\omega \simeq 0.186$. It can be shown [109, 110] that $|\Delta L| = 2$ scatterings give a sizeable contribution only for

$$M_1 \gtrsim 10^{14}\,\mathrm{GeV}\left(\frac{m_{\mathrm{atm}}^2}{\sum_i m_i^2}\right). \tag{2.192}$$

For this reason, we shall safely neglect them in the rest of this work.

Chapter 3

The importance of the N_2-dominated scenario

In the previous chapter we analysed the general setup of the type-I seesaw mechanism and the leptogenesis process linked to it. We described in detail the production of the baryon asymmetry in the particular scenario of *vanilla leptogenesis*. As pointed out, in this case the asymmetry is dominantly produced by the lightest heavy neutrino N_1, while the contributions of N_2 and N_3 are assumed to be negligible. We have shown that this scenario is actually able to reproduce the correct final baryon-to-photon ratio $\eta_B^{\rm CMB}$, thus realising successful leptogenesis. This achievement implies an important constraint on the heavy neutrino sector, imposing a lower bound, eq. (2.181), on the mass of the lightest neutrino that generates the asymmetry. This feature is undoubtedly an interesting prediction on the heavy neutrinos mass spectrum imposed by the successful leptogenesis condition. However, it also represents a drawback of the model. Indeed, when type-I seesaw mechanism is embedded in some larger framework, such as $SO(10)$ GUTs, this bound is typically not respected. The lightest heavy neutrino predicted by grand unification models is sensibly lighter than what required by vanilla leptogenesis. It may therefore seem that the leptogenesis mechanism, though viable on its own, cannot be embedded into a broader and more elegant picture such those proposed by theories like $SO(10)$ GUTs.

Nonetheless, it is possible to find a way to circumvent the lower bound in eq. (2.181). This bound is imposed by the successful leptogenesis condition on the mass of the heavy neutrino that produces the asymmetry. In vanilla leptogenesis this is the lightest one, N_1, which is also subject to opposite restrictions on its mass originating from $SO(10)$ GUT models. A possible way out is to set N_1 free from eq. (2.181) by assigning the leptogenesis task to the next-to-lightest heavy neutrino, N_2. In this way, we can expect successful leptogenesis to impose a bound on M_2, while M_1 can now agree with the lower values predicted by $SO(10)$ GUT models, $M_1 \ll 10^9\,\text{GeV}$. We can try, therefore, to shift leptogenesis from the lightest to the next-to-lightest neutrino, thus introducing the so-called *N_2-dominated leptogenesis* models, in which the final asymmetry is now produced by N_2 and the contribution of N_1 (and N_3) is negligible.

We can make a first attempt to study the asymmetry production in the N_2-dominated models by following the steps explained in the previous chapter. Firstly, we shall consider a hierarchical spectrum, in particular such that

$$M_{i+1} \gtrsim 3\, M_i, \tag{3.1}$$

so to avoid the overlapping of the processes associated to different heavy neutrinos [101]. With this assumption, we can divide the complete leptogenesis process into different stages, depending on the temperature, each one characterised by the interactions involving one particular heavy neutrino. Considering that the heaviest neutrino will have a negligible contribution, we can first concentrate on the processes taking place at $T \sim M_2$, that is on the stage involving the next-to-lightest neutrino, and then on the second stage at $T \sim M_1$, where the lightest neutrino becomes important.

- **Stage I** $T \sim M_2$. Assuming a vanishing initial N_2 abundance and zero initial asymmetry, the situation is totally similar to the vanilla leptogenesis case, but here we are referring to N_2. We have therefore

$$\frac{dN_{N_2}}{dz_2} = -D_2(z_2)\left(N_{N_2}(z_2) - N_{N_2}^{\rm eq}(z_2)\right) \tag{3.2}$$

$$\frac{dN_{B-L}^{\rm lep}}{dz_2} = \varepsilon_2 D_2(z_2)\left(N_{N_2}(z_2) - N_{N_2}^{\rm eq}(z_2)\right) - W_2^{\rm ID}(z_2) N_{B-L}^{\rm lep}(z_2), \tag{3.3}$$

  where $z_2 = M_2/T$. The expression for the asymmetry produced by N_2 at the end of stage I (i.e. $z_2 \gg 1$) will be therefore

$$N_{B-L}^{\rm lep,2} = \varepsilon_2 \kappa_f(K_2) \tag{3.4}$$

- **Stage II** $T \sim M_1$. In this second stage, we can assume again vanishing initial N_1 abundance, however the initial value of the $B-L$ asymmetry is now given by eq. (3.4). Since we are now considering $M_1 \ll 10^9$ GeV, we already know that the asymmetry produced by N_1 will be negligible. For this reason, we can simplify the Boltzmann equations into

$$\frac{dN_{N_1}}{dz_1} = -D_1(z_1)\left(N_{N_1}(z_1) - N_{N_1}^{\rm eq}(z_1)\right), \tag{3.5}$$

$$\frac{dN_{B-L}^{\rm lep}}{dz_1} = -W_1^{\rm ID}(z_1) N_{B-L}^{\rm lep}(z_1), \tag{3.6}$$

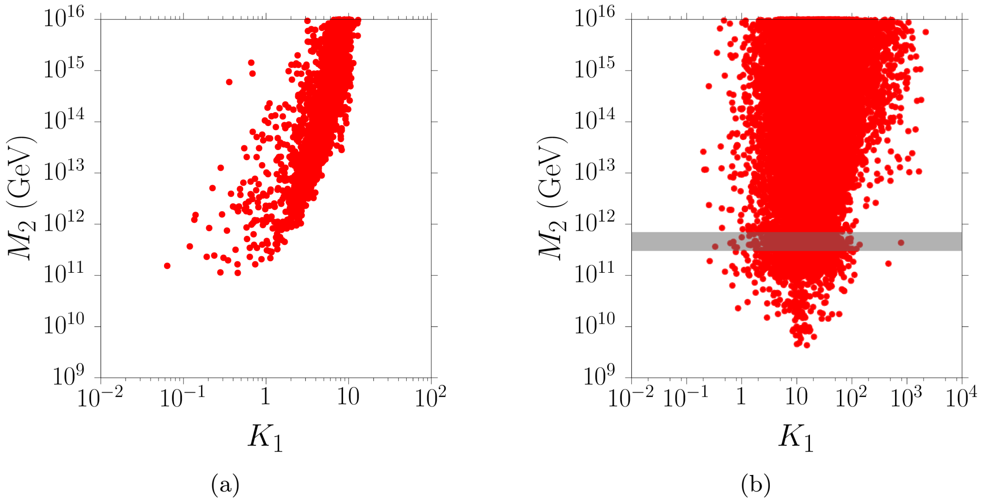

(a) (b)

Figure 3.1: Scatter plots of M_2 vs. K_1 for models realising successful leptogenesis in N_2-dominated models [111]. In the left panel (a) the unflavoured case is considered. In the right panel (b) the flavoured case is studied. Here the shadowed region marks the transition zone around $M_2 \sim 5 \times 10^{11}$ GeV.

where $z_1 = M_1/T$. As we can see, the role of N_1 is now restricted to the washout factor, therefore the expression for the final asymmetry is given by

$$\begin{aligned} N_{B-L}^{\mathrm{lep,f}} &= N_{B-L}^{\mathrm{lep,2}}\, e^{-\frac{3\pi}{8}K_1} \\ &= \varepsilon_2 \kappa_f(K_2)\, e^{-\frac{3\pi}{8}K_1}. \end{aligned} \tag{3.7}$$

In this first attempt to study the asymmetry produced in the N_2-dominated scenario, we can notice that the final asymmetry is produced by N_2 at $T \sim M_2$ and then undergoes the washout due to N_1 at $T \sim M_1$. The washout depends exponentially on K_1. We can therefore expect that for large values of K_1 the final asymmetry is suppressed, so that successful leptogenesis can be achieved only for suitable choices of M_2 and K_1. This can be clearly noticed in fig. 3.1(a) [111]. Here values of M_2 and K_1 realising successful leptogenesis according to eq. (3.7) are plotted. A suitable baryon asymmetry can be produced in this model only for $M_2 \gtrsim 10^{11}$ GeV. Moreover, the value of M_2 increases with K_1 in order to produce an asymmetry large enough to survive the washout. For $K_1 \gtrsim 10$ successful leptogenesis cannot be achieved. This means that for values of $K_1 \sim m_{\mathrm{atm}}/m_* \simeq 50$, successful leptogenesis cannot be realised. We can therefore conclude that in this scenario successful leptogenesis can be achieved only by selecting small values of K_1, and therefore by admitting a certain level of tuning on the parameters.

This analysis may therefore lead us to the conclusion that N_2-dominated leptogenesis is hardly viable. However, it has been pointed out that this study is incomplete, since it neglects very important effects due to *flavour*. We shall then first focus on these new features and then propose an improved model of N_2-dominated leptogenesis.

3.1 Flavour effects

In the analysis previously carried out, the flavour of the produced lepton doublets was completely neglected. However, a more careful study of the model shows that flavour plays a very important role in leptogenesis [112, 113]. In our lagrangian, lepton doublet flavour appears in the Yukawa couplings with the RH neutrinos and with the RH charged-lepton singlets. In general, we have therefore two kinds of flavour effects: *heavy flavour effects* and *light flavour effects*. We shall analyse them separately and then consider how they apply to our N_2-dominated scenario.

3.1.1 Heavy flavour effects

Assuming eq. (3.1), in the thermal window around $T \sim M_i$ the dynamics is ruled by the processes involving the neutrino N_i. In particular, its Yukawa couplings to the lepton and Higgs doublets

$$\mathcal{L} \supset -Y_{\alpha i}\,\overline{l_\alpha}\,N_{Ri}\tilde{\Phi} + \text{h.c.}, \tag{3.8}$$

where $\alpha = e, \mu, \tau$, imply that the lepton doublets are produced in definite quantum states as

$$|N_i\rangle \;\rightarrow\; |l_i\rangle \equiv \sum_\alpha C_{i\alpha}|l_\alpha\rangle, \tag{3.9}$$

$$|N_i\rangle \;\rightarrow\; |\overline{l_i}\rangle \equiv \sum_\alpha \overline{C}_{i\alpha}|\overline{l_\alpha}\rangle, \tag{3.10}$$

that is on coherent superpositions of e-, μ- and τ-flavoured lepton doublets. The superposition is specified by the coefficients $C_{i\alpha}$ and $\overline{C}_{i\alpha}$ such that

$$\sum_\alpha |C_{i\alpha}|^2 = 1, \qquad \sum_\alpha \left|\overline{C}_{i\alpha}\right|^2 = 1. \tag{3.11}$$

Due to loop corrections, we have in general $\overline{C}_{i\alpha} \neq C^*_{i\alpha}$ and therefore $CP|l_i\rangle \neq |\overline{l_i}\rangle$. The flavour states $|l_i\rangle$ and $|\overline{l_i}\rangle$ are not in general CP conjugated. Moreover, the lepton doublets produced by the different heavy neutrinos do not generally respect orthogonality conditions. That is, in general, we have [113]

$$\langle l_i|l_j\rangle \neq \delta_{ij}. \tag{3.12}$$

This has remarkable consequences on our N_2-dominated model.

- **Stage I** $T \sim M_2$. Here lepton doublets are produced by the decay of N_2 in the flavour states $|l_2\rangle$, $|\overline{l_2}\rangle$.
- **Stage II** $T \sim M_1$. At these temperatures N_1 becomes relevant, i.e. its decays and inverse decays are efficient. These processes would involve lepton doublets in the

flavour states $|l_1\rangle$, $|\overline{l_1}\rangle$, which are, in general, different from the states produced earlier by N_2. However, since heavy flavour states are not, generally, orthogonal, N_1 interactions measure the projection of states $|l_2\rangle$, $|\overline{l_2}\rangle$ along the flavour direction imposed by N_1. This means that N_1 interactions will break the coherence of state $|l_2\rangle$ into a $|l_1\rangle$ component and an orthogonal component $|l_{1_2^\perp}\rangle$. Similarly happens for states $|\overline{l_2}\rangle$. Only states $|l_1\rangle$ and $|\overline{l_1}\rangle$ will now be involved in the dynamics of N_1, while the orthogonal states $|l_{1_2^\perp}\rangle$, $|\overline{l_{1_2^\perp}}\rangle$ will not be touched by N_1. Out of the asymmetry produced by N_2, only the projection onto the flavour $|l_1\rangle$, $|\overline{l_1}\rangle$ will then be affected by the processes involving N_1, and undergo the washout. The orthogonal component will survive stage II unmodified.

We can define the probabilities

$$p_{ij} \equiv |\langle l_j|l_i\rangle|^2 = \left|\sum_\alpha C^*_{j\alpha} C_{i\alpha}\right|^2, \qquad \overline{p}_{ij} \equiv |\langle \overline{l_j}|\overline{l_i}\rangle|^2 = \left|\sum_\alpha \overline{C}^*_{j\alpha} \overline{C}_{i\alpha}\right|^2, \tag{3.13}$$

such that

$$p_{ij} + p_{ij_i^\perp} = 1, \qquad \overline{p}_{ij} + \overline{p}_{ij_i^\perp} = 1. \tag{3.14}$$

Neglecting here[1], for simplicity, the differences in flavour composition between $|l_i\rangle$ and $|\overline{l_i}\rangle$, at tree-level $\overline{C}^0_{i\alpha} = C^{0\,*}_{i\alpha}$, so that $p^0_{ij} = \overline{p}^0_{ij}$. This way, eq. (3.7) can be rewritten as

$$\begin{aligned} N^{\rm lep,f}_{B-L} &= N^{\rm lep,f}_{\Delta_1} + N^{\rm lep,f}_{\Delta_{1\perp}} \\ &\simeq p^0_{21}\,\varepsilon_2 \kappa_f(K_2)\, e^{-\frac{3\pi}{8}K_1} + (1 - p^0_{21})\varepsilon_2\kappa_f(K_2), \end{aligned} \tag{3.15}$$

where N_{Δ_1} and $N_{\Delta_{1\perp}}$ are, respectively, the components of the lepton asymmetry along the flavour $|l_1\rangle$ and its orthogonal state.

We can already notice that flavour effects, in this case heavy flavour effects, introduce significant modifications to our initial picture. In particular, it is very important to notice that part of the asymmetry produced can actually escape N_1's washout [114].

It is also interesting to obtain an expression for the probabilities in eq. (3.13). At tree level we have [115, 116]

$$p^0_{ij} = \frac{\left|(m_D^\dagger m_D)_{ij}\right|^2}{(m_D^\dagger m_D)_{ii}\,(m_D^\dagger m_D)_{jj}} = \frac{1}{\widetilde{m}_i\,\widetilde{m}_j}\left|\sum_k m_k\,\Omega^*_{ki}\Omega_{kj}\right|^2. \tag{3.16}$$

When $p^0_{ij} = 0$ it means that the flavour compositions of the lepton states produced by neutrinos N_i and N_j are orthogonal in the flavour space. Therefore, a lepton state produced by N_i cannot interact with N_j and this can be the case of the lepton states exchanged in the 1-loop neutrino decay, fig. 2.1. Therefore, $p^0_{ij} = 0$ implies that the

---

[1] We shall consider this feature in the following sections.

interference of neutrino N_i with N_j does not occur and the relative term in the *CP* asymmetry vanishes. This can be easily seen since $p^0_{ij} = 0$ implies $(m_D^\dagger m_D)_{ij} = 0$, which can then be plugged in eq. (2.118).
From eq. (3.16) it is also interesting to notice that if the orthogonal matrix is $\Omega = 1$ or one of the 5 permutations that can be obtained from the identity, we have $p^0_{ij} = 0 \; \forall i, j$, so that the flavour compositions of the lepton states produced by the heavy neutrinos are all orthogonal. In this case it is easy to realise that the heavy neutrinos do not interfere and therefore all the *CP* asymmetries vanish. We can therefore conclude that the particular seesaw models in which the complex orthogonal matrix Ω is the identity, or one of its permutation, are not able to provide any *CP* asymmetry, hence they cannot realise leptogenesis.

3.1.2 Light flavour effects

The flavour of lepton doublets plays a role in the Yukawa interactions with Higgs doublets and charged-lepton singlets as well

$$\mathcal{L} \supset -\sum_\alpha D^\ell_{Y\alpha}\, \overline{l_\alpha} \ell_{R\alpha} \Phi + \text{h.c.} \tag{3.17}$$

This implies that, beside the leptogenesis processes, interactions involving the charged singlets take place in the Early Universe involving definite flavour lepton doublets. Since, as we have seen, the heavy neutrino decays produce lepton doublets in a coherent superposition of flavour states, in principle the interaction given by (3.17) could act as a quantum measurement of the flavour components of the lepton doublet states $|l_i\rangle$, $|\overline{l_i}\rangle$. We must therefore understand when these interactions are efficient enough to break the coherence of the heavy flavour states produced by heavy neutrino decays.
Given the interaction term in eq. (3.17), the reaction rates can be estimated as [117]

$$\Gamma_\alpha(T) \simeq 5 \times 10^{-3} \left(D^\ell_{Y\alpha}\right)^2 T, \tag{3.18}$$

so that, comparing it to the Hubble rate and using eq. (2.127), we can expect that these interactions enter thermal equilibrium while temperature drops. The exact temperature depends on the Yukawa coupling $D^\ell_{Y\alpha}$, therefore we have different thresholds at which different flavour interactions enter equilibrium: for $T \lesssim 10^{12}\,\text{GeV}$ τ-interactions are in equilibrium, while for $T \lesssim 10^9\,\text{GeV}$ also μ-interactions enter equilibrium. Finally, for $T \lesssim 10^6\,\text{GeV}$ also e-interaction are in thermal equilibrium.

The light flavour interactions given by eq. (3.17) are then competing with the heavy flavour interactions in eq. (3.8). If light flavour interactions are "faster", the lepton doublets produced by the heavy neutrinos will be measured along the light flavour directions, otherwise they will be projected onto the heavy flavour ones. It is possible to say [118] that if the charged-lepton Yukawa interactions are in equilibrium and we also have

$$\Gamma_\alpha \gtrsim \sum_i \Gamma_i^{\mathrm{ID,tot}}, \tag{3.19}$$

the light flavour effects dominate and the coherence of the produced lepton doublets is broken accordingly. This is easily understood considering that in these situations a lepton doublet produced by a heavy neutrino decay interacts on average with a charged-lepton singlet before scattering with a Higgs doublet back to the heavy neutrino. Thus the coherence of the heavy flavour state is broken and the temperature regions in which this occurs take the name of *fully-flavoured regimes.*
In the temperature intervals in which this situation is not realised and neither of the two kinds of Yukawa interactions dominates, the full decoherence of the lepton doublet quantum states is not achieved. In these cases a detailed density matrix formalism must be employed [116, 119–121]. In this work we shall not deal with these situations, and we will always consider the full decoherence limit.

We can therefore consider the dynamics involving the heavy neutrino N_i. From the discussion in chapter 2, we can focus on a temperature window around its mass M_i, since it is in this range that the relevant processes (decays and inverse decays) are mostly effective. From the condition eq. (3.19) and comparing the interaction rates with the Hubble parameter eq. (2.127), we can define three different regimes in which the dynamics take place

1. $M_i \gtrsim 5 \times 10^{11}\,\mathrm{GeV}$. At temperatures $T \simeq M_i \gtrsim 5 \times 10^{11}\,\mathrm{GeV}$ charged-lepton Yukawa interactions are not in equilibrium, therefore the coherence of the lepton doublet produced by N_i decays is not broken. Heavy neutrino flavour dynamics dominates. This regime is often called *unflavoured*, in the sense of light flavour effects.

2. $5 \times 10^{8}\,\mathrm{GeV} \lesssim M_i \lesssim 5 \times 10^{11}\,\mathrm{GeV}$. At temperatures $T \simeq M_i$ in this case the τ Yukawa interactions are in equilibrium and efficient enough to measure the τ component of the lepton doublets. The heavy flavour quantum states are therefore broken into

   $$|l_i\rangle \to |l_\tau\rangle,\, |l_{\tau_i^\perp}\rangle, \tag{3.20}$$

   $$|\overline{l}_i\rangle \to |\overline{l}_\tau\rangle,\, |\overline{l}_{\tau_i^\perp}\rangle, \tag{3.21}$$

   that is in a component along the τ flavour direction and a component orthogonal to τ obtained from the heavy flavour direction $|l_i\rangle$. We have a *two fully-flavoured regime.* The splitting in the two components can be quantified by introducing the probabilities

   $$P_{i\alpha} \equiv |\langle l_\alpha | l_i\rangle|^2\,, \qquad \overline{P}_{i\alpha} \equiv \left|\langle \overline{l}_\alpha | \overline{l}_i\rangle\right|^2 \tag{3.22}$$

where $\alpha = \tau, \tau_i^{\perp}$. These expressions account for loop corrections. We can write [116]

$$P_{i\alpha} = P^0_{i\alpha} + \delta P_{i\alpha}, \tag{3.23}$$

$$\overline{P}_{i\alpha} = P^0_{i\alpha} + \delta \overline{P}_{i\alpha}, \tag{3.24}$$

where we extract the tree level expression $P^0_{i\alpha}$, equal in both cases:

$$P^0_{i\alpha} = \frac{1}{\widetilde{m}_i} \left| \sum_j \sqrt{m_j} U_{\alpha j} \Omega_{ji} \right|^2 . \tag{3.25}$$

The tree-level expressions satisfy as well

$$\sum_\alpha P^0_{i\alpha} = 1, \tag{3.26}$$

so that we have

$$\sum_\alpha \delta P_{i\alpha} = \sum_\alpha \delta \overline{P}_{i\alpha} = 0. \tag{3.27}$$

The full probabilities eq. (3.22) can be derived from the decay rates of the heavy neutrinos, so that

$$P_{i\alpha} = \frac{\Gamma_{i\alpha}}{\Gamma_i}, \qquad \overline{P}_{i\alpha} = \frac{\overline{\Gamma}_{i\alpha}}{\overline{\Gamma}_i}. \tag{3.28}$$

Hence

$$\varepsilon_{i\alpha} = -\frac{P_{i\alpha}\Gamma_i - \overline{P}_{i\alpha}\overline{\Gamma}_i}{\Gamma_i + \overline{\Gamma}_i} = P^0_{i\alpha}\varepsilon_i + \frac{\delta P_{i\alpha} + \delta \overline{P}_{i\alpha}}{2}\varepsilon_i - \frac{\Delta P_{i\alpha}}{2}, \tag{3.29}$$

where $\Delta P_{i\alpha} \equiv P_{i\alpha} - \overline{P}_{i\alpha}$.

3. $M_i \lesssim 5 \times 10^8$ GeV. At temperatures $T \simeq M_i$ now also the μ Yukawa interactions are in equilibrium and efficient enough to measure also the μ component of the heavy flavour state. Given that e, μ and τ flavours form an orthonormal basis, also the e-component is measured. This implies

$$|l_i\rangle \rightarrow |l_\tau\rangle, |l_\mu\rangle, |l_e\rangle, \tag{3.30}$$

$$|\overline{l_i}\rangle \rightarrow |\overline{l_\tau}\rangle, |\overline{l_\mu}\rangle, |\overline{l_e}\rangle. \tag{3.31}$$

We have therefore a *three fully-flavoured regime*. Here, similar probability definitions as in the previous point hold, with $\alpha = e, \mu, \tau$.

In the regions around $M_i \sim 5 \times 10^{11}$ GeV and $M_i \sim 5 \times 10^8$ GeV we do not have full decoherence and density matrices must be employed. As already stated, we shall always avoid this situation or approximate the behaviour with an instantaneous transition.

We can now employ these new features to study how the N_2-dominated leptogenesis process must be modified to account for them. Always assuming a hierarchical spectrum eq. (3.1) and $M_1 \ll 10^9\,\mathrm{GeV}$ we shall also consider a very heavy N_3, $M_3 \gg 10^{12}\,\mathrm{GeV}$, and two cases

a) $5 \times 10^8\,\mathrm{GeV} < M_2 < 5 \times 10^{11}\,\mathrm{GeV}$,

b) $M_2 > 5 \times 10^{11}\,\mathrm{GeV}$.

3.1.2.1 Case (a): $5 \times 10^8\,\mathbf{GeV} < M_2 < 5 \times 10^{11}\,\mathbf{GeV}$

We can identify two stages through which the leptogenesis process will proceed.

Stage I: production. Since leptogenesis takes place at temperatures $T \sim M_2$, the asymmetry will be produced in the two fully-flavoured regime. The lepton doublets produced by the decay of N_2 in the heavy flavour states $|l_2\rangle$, $|\overline{l_2}\rangle$ will be broken by τ-Yukawa interactions into the projection onto the τ flavour direction, giving $|l_\tau\rangle$, $|\overline{l_\tau}\rangle$, and along the direction given by N_2 on the plane orthogonal to τ, giving $|l_{\tau_2^\perp}\rangle$, $|\overline{l_{\tau_2^\perp}}\rangle$. Therefore, the relevant quantities will be the asymmetries $\Delta_\tau \equiv B/3 - L_\tau$ and $\Delta_{\tau_2^\perp} \equiv B/3 - L_{\tau_2^\perp}$. Defining here $z_2 \equiv M_2/T$, the Boltzmann equations will be

$$\frac{dN_{\Delta_{\tau_2^\perp}}}{dz_2} = \varepsilon_{2\tau_2^\perp} D_2(z_2)\left(N_{N_2}(z_2) - N_{N_2}^{\mathrm{eq}}(z_2)\right) - P^0_{2\tau_2^\perp} W_2^{\mathrm{ID}}(z_2)\left(N_{L_{\tau_2^\perp}} + N_\Phi\right), \tag{3.32}$$

$$\frac{dN_{\Delta_\tau}}{dz_2} = \varepsilon_{2\tau} D_2(z_2)\left(N_{N_2}(z_2) - N_{N_2}^{\mathrm{eq}}(z_2)\right) - P^0_{2\tau} W_2^{\mathrm{ID}}(z_2)\left(N_{L_\tau} + N_\Phi\right), \tag{3.33}$$

together with eq. (3.2). Here we can notice what follows.

- The *CP* asymmetries involved are $\varepsilon_{2\tau}$ and $\varepsilon_{2\tau_2^\perp} = \varepsilon_{2e} + \varepsilon_{2\mu}$.
- The washout factor is reduced by the factors $P^0_{2\tau}$ and $P^0_{2\tau_2^\perp}$ to account for the fact that here we are considering its action only on the respective flavour component. We are considering the tree-level probabilities since we can safely neglect terms $\mathcal{O}(\delta P_{2\alpha}\, N_{\Delta_\alpha})$. We have
$$P^0_{2\tau_2^\perp} = P^0_{2e} + P^0_{2\mu}. \tag{3.34}$$
- The washout factor is expressed now only in terms of the asymmetries in the Higgs and lepton doublets of the relevant flavour. This is a peculiar difference from eq. (2.147), where we summed over all flavours.

It is possible to relate the asymmetries in the Higgs and lepton doublets to the $B/3-L_\alpha$ asymmetries N_{Δ_α} by exploiting the network of efficient reactions in the Early Universe, as in section 2.2.1. Employing the so-called *flavour-coupling* matrices [99, 103, 112, 113, 119, 122, 123], in the two fully-flavoured regime we have

$$N_{L_\alpha} + N_\Phi = C^{(2)}_{\alpha\beta} N_{\Delta_\beta}. \tag{3.35}$$

For $\alpha = \tau,\, \tau_2^{\perp}$ we have

$$\frac{dN_{\Delta_{\tau_2^{\perp}}}}{dz_2} = \varepsilon_{2\tau_2^{\perp}} D_2(z_2)\left(N_{N_2}(z_2) - N_{N_2}^{\rm eq}(z_2)\right) - P^0_{2\tau_2^{\perp}} W_2^{\rm ID}(z_2)\sum_{\beta} C^{(2)}_{\tau_2^{\perp}\beta} N_{\Delta_\beta}(z_2), \quad (3.36)$$

$$\frac{dN_{\Delta_\tau}}{dz_2} = \varepsilon_{2\tau} D_2(z_2)\left(N_{N_2}(z_2) - N_{N_2}^{\rm eq}(z_2)\right) - P^0_{2\tau} W_2^{\rm ID}(z_2)\sum_{\beta} C^{(2)}_{\tau\beta} N_{\Delta_\beta}(z_2). \quad (3.37)$$

And the flavour coupling matrix in the two fully-flavoured regime is [123]

$$C^{(2)} = \begin{pmatrix} C^{(2)}_{\tau_2^{\perp}\tau_2^{\perp}} & C^{(2)}_{\tau_2^{\perp}\tau} \\ C^{(2)}_{\tau\tau_2^{\perp}} & C^{(2)}_{\tau\tau} \end{pmatrix} = \begin{pmatrix} 581/589 & 104/589 \\ 194/589 & 614/589 \end{pmatrix}. \quad (3.38)$$

If we now assume $C^{(2)} \simeq 1$, thus neglecting flavour coupling[2], we can easily solve these equations, together with that ruling the abundance of N_2. Indicating with $T_{L2} \gtrsim 5 \times 10^8$ GeV the temperature scale at which the asymmetry production by N_2 is completed, we get, at the end of stage I:

$$N_{\Delta_{\tau_2^{\perp}}}(T_{L2}) \simeq \varepsilon_{2\tau_2^{\perp}}\, \kappa_f(K_{2\tau_2^{\perp}}), \quad (3.39)$$

$$N_{\Delta_\tau}(T_{L2}) \simeq \varepsilon_{2\tau}\, \kappa_f(K_{2\tau}), \quad (3.40)$$

where $K_{i\alpha}$ are the *flavoured decay parameters* defined as

$$K_{i\alpha} \equiv \frac{\Gamma_{i\alpha} + \overline{\Gamma}_{i\alpha}}{H(T = M_i)}. \quad (3.41)$$

We also have

$$K_{i\alpha} = P^0_{i\alpha} K_i, \quad (3.42)$$

so that, using eqs. (3.25) and (2.138), we obtain the expression of the flavoured decay parameters in the orthogonal matrix parameterisation

$$K_{i\alpha} = \frac{1}{m_*}\left|\sum_j \sqrt{m_j}\, U_{\alpha j}\Omega_{ji}\right|^2. \quad (3.43)$$

We have $K_{2\tau_2^{\perp}} = P^0_{2\tau_2^{\perp}} K_2$, therefore, from eq. (3.34), we get

$$K_{2\tau_2^{\perp}} = K_{2e} + K_{2\mu}. \quad (3.44)$$

The efficiency factors in eq. (3.40) and (3.39) are given by eqs. (2.157), (2.164) and (2.167).

---

[2] In the following chapter we shall analyse in some detail the effects of flavour coupling.

Stage II: washout. Below T_{L2}, the asymmetry stays constant. However, for temperatures $T \lesssim 5 \times 10^8\,\mathrm{GeV}$ the μ Yukawa interactions are in equilibrium. This implies that the coherence of the quantum states $|l_{\tau_2^\perp}\rangle$, $|\overline{l_{\tau_2^\perp}}\rangle$ is broken. At temperatures $M_1 < T' \lesssim 5 \times 10^8\,\mathrm{GeV}$ the asymmetry $N_{\Delta_{\tau_2^\perp}}$ gets projected onto the e and μ flavour directions. We might expect this projection to be

$$N_{\Delta_e}(T') = \frac{P^0_{2e}}{P^0_{2\tau_2^\perp}} N_{\Delta_{\tau_2^\perp}}(T_{L2}), \qquad N_{\Delta_\mu}(T') = \frac{P^0_{2\mu}}{P^0_{2\tau_2^\perp}} N_{\Delta_{\tau_2^\perp}}(T_{L2}). \tag{3.45}$$

However, this simple projection does not consider the effects due to the different flavour composition of $|l_{\tau_2^\perp}\rangle$ and $|\overline{l_{\tau_2^\perp}}\rangle$. For this reason, the asymmetry in the e and μ flavours is not simply the projection of the asymmetry in $\tau_2^\perp$, but must take into account the fact that additional asymmetry between each light flavour and its *CP* conjugate is stored in $|l_{\tau_2^\perp}\rangle$ and $|\overline{l_{\tau_2^\perp}}\rangle$. This is a consequence of the fact that in general $|\overline{l_{\tau_2^\perp}}\rangle \neq CP|l_{\tau_2^\perp}\rangle$. It is possible to show that, taking correctly into account also flavour-blind gauge interactions [116] the projection is given by

$$N_{\Delta_e}(T') = \frac{P^0_{2e}}{P^0_{2\tau_2^\perp}} N_{\Delta_{\tau_2^\perp}}(T_{L2}) + p_{2e}\,\kappa(K_{2\tau_2^\perp}/2), \tag{3.46}$$

$$N_{\Delta_\mu}(T') = \frac{P^0_{2\mu}}{P^0_{2\tau_2^\perp}} N_{\Delta_{\tau_2^\perp}}(T_{L2}) + p_{2\mu}\,\kappa(K_{2\tau_2^\perp}/2). \tag{3.47}$$

Here $p_{2\delta}$, with $\delta = e, \mu$, are the so-called *phantom terms* and can be obtained from the flavoured *CP* asymmetries as

$$p_{2\delta} = \varepsilon_{2\delta} - \frac{P^0_{2\delta}}{P^0_{2\tau_2^\perp}} \varepsilon_{2\tau_2^\perp}, \qquad \delta = e, \mu. \tag{3.48}$$

In the three fully-flavoured regime the action of N_1 will take place along the three flavour directions e, μ, τ. Considering that the asymmetry produced by N_1 can be safely neglected we can write the three-flavoured Boltzmann equations as

$$\frac{dN_{\Delta_\alpha}}{dz_1} = -P^0_{1\alpha} \sum_\beta C^{(3)}_{\alpha\beta}\, W_1^{\mathrm{ID}}(z_1) N_{\Delta_\beta}(z_1), \qquad \text{with} \quad \alpha, \beta = e, \mu, \tau, \tag{3.49}$$

where $z_1 \equiv M_1/T$. The role of N_1 is again essentially to apply a washout on the asymmetry produced by N_2. Here $C^{(3)}$ is the flavour coupling matrix in the three fully-flavoured regime [123]

$$C^{(3)} \equiv \begin{pmatrix} C^{(3)}_{ee} & C^{(3)}_{e\mu} & C^{(3)}_{e\tau} \\ C^{(3)}_{\mu e} & C^{(3)}_{\mu\mu} & C^{(3)}_{\mu\tau} \\ C^{(3)}_{\tau e} & C^{(3)}_{\tau\mu} & C^{(3)}_{\tau\tau} \end{pmatrix} = \begin{pmatrix} 188/179 & 32/179 & 32/179 \\ 49/358 & 500/537 & 142/537 \\ 49/358 & 142/537 & 500/537 \end{pmatrix}. \tag{3.50}$$

Neglecting again flavour coupling, $C^{(3)} \simeq 1$, and taking as initial conditions eqs. (3.46), (3.47) and (3.40), the Boltzmann equations can be solved giving the total final asymmetry produced by leptogenesis [102, 116, 123–125]

$$\begin{aligned} N_{B-L}^{\rm lep,f} &= \sum_\alpha N_{\Delta_\alpha}^{\rm lep,f} \\ &\simeq \left[\frac{P_{2e}^0}{P_{2\tau_2^\perp}^0}\varepsilon_{2\tau_2^\perp}\kappa_f(K_{2\tau_2^\perp}) + \left(\varepsilon_{2e} - \frac{P_{2e}^0}{P_{2\tau_2^\perp}^0}\varepsilon_{2\tau_2^\perp}\right)\kappa_f(K_{2\tau_2^\perp}/2)\right] e^{-\frac{3\pi}{8}K_{1e}} \\ &+ \left[\frac{P_{2\mu}^0}{P_{2\tau_2^\perp}^0}\varepsilon_{2\tau_2^\perp}\kappa_f(K_{2\tau_2^\perp}) + \left(\varepsilon_{2\mu} - \frac{P_{2\mu}^0}{P_{2\tau_2^\perp}^0}\varepsilon_{2\tau_2^\perp}\right)\kappa_f(K_{2\tau_2^\perp}/2)\right] e^{-\frac{3\pi}{8}K_{1\mu}} \\ &+ \varepsilon_{2\tau}\kappa_f(K_{2\tau})e^{-\frac{3\pi}{8}K_{1\tau}}. \end{aligned} \tag{3.51}$$

It is possible to notice that the final asymmetry is obtained from the sum of the final asymmetries in the flavours e, μ and τ, each of them affected by N_1's washout depending on $K_{1\alpha}$. This implies that, in general, the final asymmetry can escape N_1's washout along at least one particular flavour direction, in which the decay parameter is small $K_{1\alpha} \lesssim 1$. Therefore, due to flavour effects, the condition imposed by successful leptogenesis changes from the rather stringent $K_1 \lesssim 1$ to the milder condition on at least one flavoured decay parameter.

3.1.2.2 Case (b): $M_2 > 5 \times 10^{11}$ GeV

In this case, the asymmetry is produced by N_2 in the unflavoured regime. Indeed, for $T \gtrsim 5 \times 10^{11}$ GeV charged-lepton Yukawa interaction are all out of equilibrium, therefore the coherence of the lepton doublets produced by N_2 is not spoilt.

Stage I: production. As observed, the production takes place in the unflavoured regime, therefore we employ eq. (2.147) suitably modified for N_2. We get a final asymmetry at the end of the production process

$$N_{B-L}(T_{L2}) \simeq \varepsilon_2 \kappa_f(K_2). \tag{3.52}$$

Stage II: washout. For $T \lesssim 5 \times 10^8$ GeV, the μ-Yukawa interactions are in equilibrium and the asymmetry is projected onto the three flavours e, μ and τ. Following the previous discussion, at $M_1 < T' \lesssim 5 \times 10^8$ GeV we get

$$N_{\Delta_e}(T') = P_{2e}^0\, N_{B-L}(T_{L2}) + p_{2e}\, \kappa_f(K_2/2), \tag{3.53}$$

$$N_{\Delta_\mu}(T') = P_{2\mu}^0\, N_{B-L}(T_{L2}) + p_{2\mu}\, \kappa_f(K_2/2), \tag{3.54}$$

$$N_{\Delta_\tau}(T') = P_{2\tau}^0\, N_{B-L}(T_{L2}) + p_{2\tau}\, \kappa_f(K_2/2), \tag{3.55}$$

where the phantom terms are given by

$$p_{2\alpha} = \varepsilon_{2\alpha} - P^0_{2\alpha}\,\varepsilon_2, \qquad \alpha = e, \mu, \tau. \tag{3.56}$$

It is important to notice that in this case also the τ flavour gets a phantom term, since we are projecting a fully unflavoured asymmetry onto the three light flavours. Similarly to the previous case, these asymmetries undergo the washout by N_1 each one along its flavour direction, so that we eventually obtain

$$\begin{aligned} N^{\rm lep,f}_{B-L} &= \sum_\alpha N^{\rm lep,f}_{\Delta_\alpha} \\ &\simeq \left[P^0_{2e}\,\varepsilon_2\kappa_f(K_2) + \left(\varepsilon_{2e} - P^0_{2e}\,\varepsilon_2\right)\kappa_f(K_2/2)\right] e^{-\frac{3\pi}{8}K_{1e}} \\ &+ \left[P^0_{2\mu}\,\varepsilon_2\kappa_f(K_2) + \left(\varepsilon_{2\mu} - P^0_{2\mu}\,\varepsilon_2\right)\kappa_f(K_2/2)\right] e^{-\frac{3\pi}{8}K_{1\mu}} \\ &+ \left[P^0_{2\tau}\,\varepsilon_2\kappa_f(K_2) + \left(\varepsilon_{2\tau} - P^0_{2\tau}\,\varepsilon_2\right)\kappa_f(K_2/2)\right] e^{-\frac{3\pi}{8}K_{1\tau}}. \end{aligned} \tag{3.57}$$

Considerations similar to the previous case hold here as well, since again it is possible that the final asymmetry escape N_1's suppression along a flavour direction in which the washout is particularly mild.

Considering flavour effects, then, the N_2-dominated scenario of leptogenesis dramatically changes from the first attempt considered at the beginning, see eq. (3.7). To show the important modifications brought about by flavour effects, we can consider fig. 3.1(b). Here, each point in the plane $M_2 - K_1$ marks an N_2-dominated model able to realise successful leptogenesis. The final asymmetry is computed using eqs. (3.51) and (3.57), depending on the value of M_2. We have assumed an instantaneous transition between the unflavoured and the two fully-flavoured regimes at $M_2 = 5 \times 10^{11}\,\text{GeV}$. The shaded band marks the actual transition region in which a fuller treatment with density matrices must be employed. Comparing fig. 3.1(a) and 3.1(b), we can notice that, in the latter, successful leptogenesis can be achieved also for high values of K_1, which are forbidden in the unflavoured case. Moreover, lower values of M_2 are accessible, since the asymmetry produced does not have to be high in order to survive the strong washout by K_1 as in the unflavoured case. We can find a lower bound

$$M_2 \gtrsim 3 \times 10^9\,\text{GeV}. \tag{3.58}$$

In conclusion, flavour effects greatly help the N_2-dominated scenario by making it possible to realise successful leptogenesis much more easily than in the unflavoured case. For this reason, flavoured N_2-dominated leptogenesis can indeed be regarded as a promising mechanism for producing the baryon asymmetry of the Universe, while complying with the bounds on the lightest heavy neutrino mass.

We shall now analyse in detail two theoretical frameworks that significantly draw the attention on the N_2-dominated scenario: *strong thermal leptogenesis* and $SO(10)$*-inspired* *leptogenesis.*

3.2 Strong thermal leptogenesis

In chapter 2, we saw that, in principle, the conditions imposed on the initial value of the asymmetry can actually play a role, cf. eq. (2.149). The initial value of the asymmetry directly depends on the detailed history of the Early Universe before the leptogenesis stage and, in general, there are no theoretical reasons to assume it to be vanishing, as in eq. (2.151). On the contrary, if we assume a vanishing initial abundance of the heavy neutrinos, in order to produce enough neutrinos and consequently enough asymmetry, we get that the reheating temperature of the Universe must be at least of the order of the mass of the neutrino producing the asymmetry. Therefore, we can in general expect rather high reheating temperatures $T_{\rm RH} \gtrsim 10^{10}\,\mathrm{GeV}$.
With these rather high reheating temperatures, it is possible that other mechanisms are able to produce a sizeable amount of asymmetry before leptogenesis takes place. For instance, in the late stages of inflation we can have Affleck-Dine [126] or gravitational baryogenesis [127, 128], while after inflation, but before the onset of leptogenesis, more standard GUT baryogenesis [93, 129–132] can take place. For these reasons, we can expect that the initial value of the asymmetry is not zero, and a sizeable value of *initial pre-existing asymmetry*, $N^{\rm p,i}_{B-L}$, must be taken into account. After the leptogenesis process, we are therefore left with a total asymmetry given by

$$N^{\rm f}_{B-L} = N^{\rm lep,f}_{B-L} + N^{\rm p,f}_{B-L}, \tag{3.59}$$

where the first term is the asymmetry genuinely produced by leptogenesis, while the second represents the remnants of the initial pre-existing asymmetry after it undergoes leptogenesis. It is possible that, due to mechanisms such as those mentioned before, the *final pre-existing asymmetry*, $N^{\rm p,f}_{B-L}$, is even larger than the contribution of leptogenesis itself. Since these processes actually escape the experimental probes, the fact that the final baryon asymmetry of the Universe can heavily depend on the initial conditions and the detailed history of the Early Universe poses a serious theoretical problem. The value of $N^{\rm p,i}_{B-L}$ is difficult to estimate since it depends on the precise state of the Universe at the inflation era, so that also the final value of the baryon asymmetry remains difficult to explain. Moreover, the experimental evidences on the baryon asymmetry of the Universe cannot be employed to constrain our leptogenesis model, since the final asymmetry can in general receive a large, unknown contribution from other mechanisms.

For these reasons, we can require that leptogenesis is able to erase any pre-existing contribution, while producing the correct amount of baryon asymmetry. We can therefore require

$$\left|N^{\rm p,f}_{B-L}\right| \ll \left|N^{\rm lep,f}_{B-L}\right| \qquad \text{and} \qquad N^{\rm lep,f}_{B-L} \simeq N^{\rm exp}_{B-L}, \tag{3.60}$$

where $N^{\rm exp}_{B-L}$ is obtained from the experimental observations, eq. (1.11). Leptogenesis models that satisfy the conditions (3.60) are said to realise *strong thermal leptogenesis* [115]. This way, the final asymmetry is entirely produced by leptogenesis processes and full independence of the initial conditions is ensured.

The key of strong thermal leptogenesis is to rely on strong washout in the thermal production of the heavy neutrinos. We can analyse first the unflavoured vanilla leptogenesis case. Here we assume that only N_1 thermalises. Starting from eq. (2.149), we assume now a non-vanishing initial pre-existing asymmetry $N^{\rm p,i}_{B-L}$, so that the total final $B-L$ asymmetry is given by

$$\begin{aligned} N^{\rm f}_{B-L} &= N^{\rm p,f}_{B-L} + N^{\rm lep,f}_{B-L} \\ &= N^{\rm p,i}_{B-L} e^{-\frac{3\pi}{8}K_1} + \varepsilon_1 \kappa_f(K_1). \end{aligned} \tag{3.61}$$

Strong thermal leptogenesis requires that the final pre-existing asymmetry be smaller than the final asymmetry produced by leptogenesis. Adopting the CMB measurement of the baryon-to-photon ratio, eq. (1.11), we can quantify this requirement as

$$\left|\eta^{\rm p,f}_B\right| \lesssim 0.1\, \eta^{\rm lep,f}_B \simeq 0.1\, \eta^{\rm CMB}_B, \tag{3.62}$$

with $\eta^{\rm p,f}_B = d\, N^{\rm p,f}_{B-L}$. Therefore, from eq. (3.61) we get the condition

$$K_1 \gtrsim K_{\rm st}(N^{\rm p,i}_{B-L}), \tag{3.63}$$

where [1]

$$K_{\rm st}(N^{\rm p,i}_{B-L}) \equiv \frac{8}{3\pi}\left[\ln\left(\frac{0.1}{\eta^{\rm CMB}_B}\right) + \ln\left|N^{\rm p,i}_{B-L}\right|\right] \simeq 16 + 0.85 \ln\left|N^{\rm p,i}_{B-L}\right|. \tag{3.64}$$

We can therefore see that strong thermal leptogenesis implies strong washout that is able to erase the pre-existing asymmetry. The amount of washout depends on the size of the initial pre-existing asymmetry.

When flavour is considered, the scenario becomes in general more involved. This is due to the fact that now the pre-existing asymmetry can in principle escape the washout of the heavy neutrinos along a certain flavour direction. It is possible to show [115] that, taking into account light flavour effects, strong thermal leptogenesis can be achieved only if the heavy neutrino spectrum is hierarchical and

$$5\times 10^9\,{\rm GeV} \lesssim M_2 \lesssim 5\times 10^{11}\,{\rm GeV}, \tag{3.65}$$

$$M_1 \ll 10^9\,{\rm GeV}. \tag{3.66}$$

Since N_1 is too light, and the *CP* asymmetries of N_3 are suppressed, the asymmetry must be produced dominantly by N_2. Therefore we can conclude that strong thermal leptogenesis can be realised only in a N_2-dominated leptogenesis scenario.

The asymmetry produced by leptogenesis is then given by eq. (3.51), while the final pre-existing asymmetry is obtained in the following ways.

3.2.1 Case $M_3 \gtrsim 5 \times 10^{11}$ GeV

In this case, the heaviest neutrino is either not thermalised or, in general, cannot wash out completely the pre-existing asymmetry. Indeed, for $M_3 \gtrsim 5 \times 10^{11}$ GeV the washout by N_3 would take place in the unflavoured (in the sense of light flavours) regime, therefore the component of the asymmetry orthogonal to the heavy flavour direction $|l_3\rangle$, $|\overline{l_3}\rangle$ would escape washout. We can therefore neglect its presence. The washout by N_2 will then take place in the two fully-flavoured regime, while the washout by N_1 will be in the three fully-flavoured regime. Eventually we get a final pre-existing asymmetry given by $N^{\rm p,f}_{B-L} = \sum_\alpha N^{\rm p,f}_{\Delta_\alpha}$ where $\alpha = e, \mu, \tau$ and [115]

$$\begin{aligned}
N^{\rm p,f}_{\Delta_e} = & \left\{ \left(1 - P^0_{p\tau}\right) \left[\frac{P^0_{2e}}{P^0_{2\tau_2^\perp}} P^0_{p\tau_2^\perp} e^{-\frac{3\pi}{8}(K_{2e}+K_{2\mu})} + \left(1 - \frac{P^0_{2e}}{P^0_{2\tau_2^\perp}}\right) \left(1 - P^0_{p\tau_2^\perp}\right) \right] \right. \\
& \left. + \Delta P_{pe} \right\} e^{-\frac{3\pi}{8}K_{1e}} \, N^{\rm p,i}_{B-L}, \qquad (3.67) \\
N^{\rm p,f}_{\Delta_\mu} = & \left\{ \left(1 - P^0_{p\tau}\right) \left[\frac{P^0_{2\mu}}{P^0_{2\tau_2^\perp}} P^0_{p\tau_2^\perp} e^{-\frac{3\pi}{8}(K_{2e}+K_{2\mu})} + \left(1 - \frac{P^0_{2\mu}}{P^0_{2\tau_2^\perp}}\right) \left(1 - P^0_{p\tau_2^\perp}\right) \right] \right. \\
& \left. + \Delta P_{p\mu} \right\} e^{-\frac{3\pi}{8}K_{1\mu}} \, N^{\rm p,i}_{B-L}, \qquad (3.68) \\
N^{\rm p,f}_{\Delta_\tau} = & \left(P^0_{p\tau} + \Delta P_{p\tau}\right) e^{-\frac{3\pi}{8}(K_{1\tau}+K_{2\tau})} N^{\rm p,i}_{B-L}. \qquad (3.69)
\end{aligned}$$

Here $P^0_{p\tau}$ and $P^0_{p\tau_2^\perp}$ are the fractions of the pre-existing asymmetry in the τ and $\tau_2^\perp$ components. The quantities $\Delta P_{p\alpha}$, with $\sum_\alpha \Delta P_{p\alpha} = 0$, take into account the possibility of different flavour composition of the initial pre-existing asymmetry. Similarly to what was discussed in the previous section, the pre-existing asymmetry along the e, μ and τ directions is not simply a fraction of the initial pre-existing asymmetry, but possible difference in the flavour composition of the leptons and anti-leptons states must be accounted for.

In order to have successful strong thermal leptogenesis, we must combine eqs. (3.67), (3.68) and (3.69) with eq. (3.51) to account for the asymmetry production. Taking all these equations together, it is possible to notice that successful strong thermal leptogenesis can be realised only if [1, 115]

$$K_{1e},\, K_{1\mu} \gtrsim K_{\rm st}(N^{\rm p,i}_{\Delta_{e,\mu}}), \qquad K_{2\tau} \gtrsim K_{\rm st}(N^{\rm p,i}_{\Delta_\tau}), \qquad K_{1\tau} \lesssim 1. \qquad (3.70)$$

Here, the first condition ensures that the pre-existing asymmetry along e and μ directions is washed-out by the action of N_1 in the three fully-flavoured regime. The second condition implies that the pre-existing asymmetry in the τ flavour is washed out by N_2 in the two fully-flavoured regime. In order to produce at the same time the suitable asymmetry through leptogenesis itself, and given the conditions on K_{1e} and $K_{1\mu}$, the final asymmetry must necessarily be produced by N_2 in the τ flavour. Hence, the last condition on $K_{1\tau}$ ensures that the contribution of leptogenesis, in the τ flavour, is not washed out by N_1.

This scenario realising a *tauon N_2-dominated leptogenesis* is the only possibility to achieve successful strong thermal leptogenesis [115].

3.2.2 Case $M_3 \lesssim 5 \times 10^{11}$ GeV

If $M_3 \lesssim 5 \times 10^{11}$ GeV, the dynamics of N_3 takes place in the two-fully flavoured regime, as for N_2. Therefore, the contribution of N_3 adds up to the washout operated by the next-to-lightest. We therefore have [1]

$$\begin{aligned}
N_{\Delta_\delta}^{\mathrm{p,f}} = \Bigg\{ \left(1 - P_{p\tau}^0\right) \Bigg[& P_{p\tau_3^\perp}^0 \frac{P_{2\tau_2^\perp}^0}{P_{3\tau^\perp}^0} \frac{P_{2\delta}^0}{P_{2\tau_2^\perp}^0} P_{p\tau_2^\perp}^0 e^{-\frac{3\pi}{8}(K_{3\tau^\perp} + K_{2\tau_2^\perp})} \\
& + \left(1 - P_{p\tau_3^\perp}^0\right) \left(1 - \frac{P_{2\tau_2^\perp}^0}{P_{3\tau^\perp}^0} \frac{P_{2\delta}^0}{P_{2\tau_2^\perp}^0} e^{-\frac{3\pi}{8} K_{2\tau_2^\perp}}\right) \\
& + P_{p\tau_3^\perp}^0 \left(1 - P_{p\tau_2^\perp}^0\right) \left(1 - \frac{P_{2\delta}^0}{P_{2\tau_2^\perp}^0}\right) \Bigg] + \Delta P_{p\delta} \Bigg\} e^{-\frac{3\pi}{8} K_{1\delta}} N_{B-L}^{\mathrm{p,i}}, \qquad (3.71) \\
N_{\Delta_\tau}^{\mathrm{p,f}} = {} & (P_{p\tau}^0 + \Delta P_{p\tau}) e^{-\frac{3\pi}{8}(K_{3\tau} + K_{2\tau} + K_{1\tau})} N_{B-L}^{\mathrm{p,i}}, \qquad (3.72)
\end{aligned}$$

where $\delta = e, \mu$ and $K_{3\tau^\perp} \equiv K_{3e} + K_{3\mu}$. Clearly, the addition of the washout by N_3 tends to relax the strong thermal conditions eq. (3.70), replacing the second one with $K_{2\tau} + K_{3\tau} \gtrsim K_{\mathrm{st}}(N_{\Delta_\tau}^{\mathrm{p,i}})$. In this way one can have strong thermal leptogenesis with lower values of $K_{2\tau}$ and so the condition of successful leptogenesis can be more easily satisfied.

We can therefore conclude that strong thermal leptogenesis, by solving the problem of the initial conditions of the asymmetry abundance, has very important implications and consequences in the leptogenesis setup.

It necessarily selects a hierarchical spectrum of the heavy neutrinos that realises N_2-dominated leptogenesis and selects a final asymmetry dominantly produced in the τ flavour. It is noticeable that the requirement of full independence of the initial conditions is able to fix the heavy neutrino mass spectrum, thus giving a prediction in the otherwise almost unattainable realm of the high-energy neutrino parameters. This requirement provides also an additional theoretical reason for shifting the leptogenesis paradigm from the N_1 to the N_2-dominated scenario.

Moreover, the conditions implied by strong thermal leptogenesis, eq. (3.70), can be regarded as further constraints on the seesaw parameter space, beyond the requirement of successful leptogenesis eq. (2.174). We shall see in the following chapter how these constraints are able to provide us with interesting predictions on the low-energy neutrino parameters as well.

3.3 $SO(10)$-inspired leptogenesis

The attractive feature of the seesaw mechanism, able to provide a solution to the problems of neutrino masses and asymmetry of the Universe, relies on the addition of extra particles. These particles, the RH neutrinos introduced in eq. (2.46), are somehow added by hand to the SM lagrangian and so is their high mass scale. A more elegant and attractive origin of the RH neutrinos and their mass scale can be found in GUT. In particular, it can be noticed that theories based on $SO(10)$ as grand unification group [133–135], naturally include three RH neutrinos in the same irreducible representation together with quarks and leptons. In particular, RH neutrinos precisely fit in the 16-dimensional spinor representation of $SO(10)$. Moreover, in $SO(10)$ GUTs interesting links between quark and lepton parameters arise, as well as relations between charged leptons and neutrinos.

We shall analyse here a large class of leptogenesis models based on the seesaw lagrangian eq. (2.46) that enjoy additional conditions on the parameters which are inspired to those realised in $SO(10)$ GUTs. For this reason, we shall call these models $SO(10)$-*inspired* [136–141].

The type-I seesaw mass lagrangian eq. (2.48) is written in the *flavour basis*, in which both the charged leptons and the RH neutrinos mass matrices, D^{ℓ}_{m} and D_M respectively, are diagonal. It is possible to rotate both the LH and the RH neutrino fields to a basis in which the Dirac mass matrix m_D is diagonal. This basis is called *Yukawa basis.* The transformation can be performed via a bi-unitary transformation

$$m_D = V_L^{\dagger} D_{m_D} U_R, \tag{3.73}$$

where V_L and U_R are unitary matrices acting respectively on the LH and RH neutrino fields. Matrix D_{m_D} is then diagonal with real, non-negative entries m_{Di}. The matrix U_R, in particular, defines the RH neutrino Majorana mass matrix in the Yukawa basis

$$M = U_R^{*}\, D_M\, U_R^{\dagger}. \tag{3.74}$$

Inserting eq. (3.73) in the seesaw relation eq. (2.70), we can obtain the expression of the Majorana mass matrix M in terms of V_L, D_m, U and D_{m_D}:

$$M = D_{m_D}\, V_L^{*} U^{*}\, D_m^{-1}\, U^{\dagger} V_L^{\dagger} D_{m_D}. \tag{3.75}$$

Eq. (3.74) performs the Takagi diagonalisation of M, thus it is possible to obtain also the matrix U_R and the diagonal matrix D_M in terms of D_m, V_L, U and D_{m_D}.
More in detail, the procedure goes as follows [2]. First, we can diagonalise, according to the standard procedure, the hermitian matrix $M^\dagger M$ with a unitary matrix $\tilde{U}_R$:

$$M^\dagger M = \tilde{U}_R D_M^2 \tilde{U}_R^\dagger. \tag{3.76}$$

Using matrix $\tilde{U}_R$ in eq. (3.74) would diagonalise M up to a diagonal matrix of phases. We can solve the phase ambiguities in $\tilde{U}_R$ by fixing the phases matrix

$$D_\phi \equiv \text{diag}\left(e^{-i\frac{\phi_1}{2}}, e^{-i\frac{\phi_2}{2}}, e^{-i\frac{\phi_3}{2}}\right), \tag{3.77}$$

to

$$D_\phi = \sqrt{D_M\, \tilde{U}_R^\dagger M^{-1} \tilde{U}_R^*}. \tag{3.78}$$

Finally, the matrix

$$U_R \equiv \tilde{U}_R\, D_\phi, \tag{3.79}$$

performs the Takagi diagonalisation of M as in eq. (3.74).

The bi-unitary transformation eq. (3.73) therefore allows us to express several quantities in terms of a definite set of parameters. This introduces a parameterisation of the seesaw space alternative to the orthogonal matrix one, eq. (2.74). The set of free parameters now is

- 3 Dirac masses in D_{m_D},
- 3 mixing angles and 3 phases in the unitary matrix V_L,
- 3 mixing angles and 3 phases in the PMNS matrix U,
- 3 active neutrino masses in D_m.

Clearly, the total always sums up to 18 free parameters. On these parameters, additional conditions inspired to those realised in $SO(10)$ GUT theories can be placed. We define $SO(10)$*-inspired leptogenesis models* those respecting the following conditions.

1. The entries of the Dirac mass matrix D_{m_D} can be parameterised in terms of the up-type quark masses as

$$m_{D1} = \alpha_1\, m_u, \qquad m_{D2} = \alpha_2\, m_c, \qquad m_{D3} = \alpha_3\, m_t. \tag{3.80}$$

In $SO(10)$-inspired models we have

$$\alpha_i = \mathcal{O}(0.1 \div 10). \tag{3.81}$$

This condition implies a natural hierarchy $m_{D1} < m_{D2} < m_{D3}$ that traces the quark masses hierarchy. In what follows, we shall assume

$$m_u = 1\,\mathrm{MeV}, \qquad m_c = 400\,\mathrm{MeV}, \qquad m_t = 100\,\mathrm{GeV}, \tag{3.82}$$

as reference values of the up-type quark masses at the leptogenesis scale [142].

2. The unitary matrix V_L is bounded by the Cabibbo-Kobayashi-Maskawa (CKM) quark mixing matrix

$$1 \leq V_L \lesssim V_{CKM}. \tag{3.83}$$

By labelling the three mixing angles in V_L as θ^L_{13}, θ^L_{12}, θ^L_{23}, as in the usual PDG parameterisation, this condition implies that the θ^L_{ij} are not too larger than the corresponding mixing angles in CKM and in particular $\theta^L_{12} \lesssim \theta^{CKM}_{12} \equiv \theta_C \simeq 12°$.

It is worth mentioning that these conditions can be also satisfied beyond traditional $SO(10)$-models. For instance, in the cases of the examples discussed in [143], in the 5D-$SO(10)$ model [144], in the 'tetra-model' [145] or in the 'A to Z' model [146]. Vice-versa not all $SO(10)$-models necessarily respect them. For example, $SO(10)$ GUT models could give rise to a type II see-saw contribution for the neutrino masses (e.g. [141, 147]) and to alternative leptogenesis scenarios than those considered here. It should also be said that traditional (4D, no flavour symmetries) $SO(10)$ models that have been explored as viable realistic models able to fit both quarks and leptons parameters also usually respect these conditions (see discussion in [125]).

3.3.1 Heavy neutrino masses and *CP* asymmetries

By exploiting the bi-unitary parameterisation and applying the two defining conditions, it is possible to obtain analytical expressions for the heavy neutrino masses and their *CP* asymmetries [2]. These expressions can be obtained by means of some further assumptions and approximations:

(a) considering $m_{Di} \ll m_{Dj}$ for $j > i$, we shall assume we can always make an expansion in m_{Di}/m_{Dj} and neglect subheading terms with $m_{Di}/m_{Dj} < 1$, regardless of their factor;

(b) we shall assume $V_L = 1$.

We will comment later on the impact of assumption (a), while the discussion about assumption (b) is postponed to chapter 5, where we shall present our results.

In the following, the ordering of the light neutrino mass spectrum is not specified and all results are valid both for NO and IO, if the suitable expressions of m_2 and U are employed.

For $V_L = 1$ we have

$$U_R^* D_M U_R^\dagger = D_{m_D} U^* D_m^{-1} U^\dagger D_{m_D}, \tag{3.84}$$

and using eq. (2.69) we have

$$M = U_R^* D_M U_R^\dagger = -D_{m_D} m_\nu^{-1} D_{m_D}. \tag{3.85}$$

We can now notice that $M_{i3}/M_{33} = M_{3i}/M_{33} \propto m_{Di}/m_{D3}$, therefore, according to the assumptions mentioned above, we can say that the matrix M is in a block-diagonal form. Neglecting terms $\mathcal{O}(m_{D1}/m_{D3})$ and $\mathcal{O}(m_{D2}/m_{D3})$ we get

$$M_3 \simeq m_{D3}^2 \left|(m_\nu^{-1})_{\tau\tau}\right| = m_{D3}^2 \left|\frac{(U_{\tau 1}^*)^2}{m_1} + \frac{(U_{\tau 2}^*)^2}{m_2} + \frac{(U_{\tau 3}^*)^2}{m_3}\right| \propto \alpha_3^2 m_t^2, \tag{3.86}$$

where, from eq. (2.69), we have used

$$(m_\nu^{-1})_{\alpha\beta} = -\sum_i m_i^{-1}\, U_{\alpha i}^* U_{\beta i}^*. \tag{3.87}$$

The phase ϕ_3 in D_ϕ is simply given by

$$\phi_3 = \mathrm{Arg}\left[-(m_\nu^{-1})_{\tau\tau}\right]. \tag{3.88}$$

Similar procedure can be employed with matrix M^{-1}. In this case we have

$$M^{-1} = U_R D_M^{-1} U_R^t = -D_{m_D}^{-1} m_\nu D_{m_D}^{-1}, \tag{3.89}$$

and we can notice that $M_{i1}^{-1}/M_{11}^{-1} = M_{1i}^{-1}/M_{11}^{-1} \propto m_{D1}/m_{Di}$, so that the largest M^{-1} eigenvalue, $1/M_1$ can be obtained as $1/M_1 \simeq |m_{\nu ee}|/m_{D1}^2$. Hence we have

$$M_1 \simeq \frac{m_{D1}^2}{|m_{\nu ee}|} = \frac{m_{D1}^2}{\left|m_1 U_{e1}^2 + m_2 U_{e2}^2 + m_3 U_{e3}^2\right|} \propto \alpha_1^2 m_u^2, \tag{3.90}$$

where we have used

$$m_{\nu\alpha\beta} = -\sum_i m_i\, U_{\alpha i} U_{\beta i}. \tag{3.91}$$

We can also obtain

$$\phi_1 = \mathrm{Arg}[-m_{\nu ee}^*]. \tag{3.92}$$

From eq. (2.70), and taking the determinant of both sides, we have

$$m_1 m_2 m_3 = \frac{m_{D1}^2\, m_{D2}^2\, m_{D3}^2}{M_1\, M_2\, M_3}\, e^{i(2\tilde{\Phi}_R - 2\Phi_U - \sum_i \phi_i)}, \tag{3.93}$$

where $\Phi_R \equiv \mathrm{Arg}\Big[\det\Big(\tilde{U}_R\Big)\Big]$ and $\Phi_U \equiv \mathrm{Arg}[\det(U)] = \rho + \sigma$. Hence we get

$$\begin{aligned} M_2 &\simeq \frac{m_{D2}^2}{m_1\, m_2\, m_3} \frac{|m_{\nu ee}|}{\left|(m_\nu^{-1})_{\tau\tau}\right|} = m_{D2}^2 \frac{\left|m_1 U_{e1}^2 + m_2 U_{e2}^2 + m_3 U_{e3}^2\right|}{\left|m_2 m_3 {U_{\tau 1}^*}^2 + m_1 m_3 {U_{\tau 2}^*}^2 + m_1 m_2 {U_{\tau 3}^*}^2\right|} \\ &\propto \alpha_2^2 m_c^2. \end{aligned} \tag{3.94}$$

We can also notice that $\sum_i \phi_i = 2\tilde{\Phi}_R - 2\Phi_U$, and therefore

$$\begin{aligned} \phi_2 &= 2(\tilde{\Phi}_R - \Phi_U) - \phi_3 - \phi_1 \\ &= \mathrm{Arg}\left[\frac{m_{\nu ee}}{(m_\nu^{-1})_{\tau\tau}}\right] + 2\tilde{\Phi}_R - 2(\rho + \sigma). \end{aligned} \tag{3.95}$$

From eqs. (3.90), (3.94) and (3.86) we notice that the heavy neutrinos mass spectrum is hierarchical with approximately

$$M_1 \,:\, M_2 \,:\, M_3 = \alpha_1^2 m_u^2 \,:\, \alpha_2^2 m_c^2 \,:\, \alpha_3^2 m_t^2, \tag{3.96}$$

thus implying

$$M_1 \ll 10^9\,\mathrm{GeV}, \tag{3.97}$$

$$10^9\,\mathrm{GeV} \lesssim M_2 \lesssim 10^{12}\,\mathrm{GeV}, \tag{3.98}$$

$$M_3 \gg 10^{12}\,\mathrm{GeV}. \tag{3.99}$$

This spectrum is precisely the one realising N_2-dominated leptogenesis, since, as we have already seen, the lightest heavy neutrino is too light to contribute significantly to the asymmetry, and the heaviest also gives negligible contribution since it is either non thermalised or its *CP* asymmetries are in general suppressed. In this way, we can notice that $SO(10)$-inspired conditions naturally select a heavy neutrino mass spectrum compatible only with N_2-dominated leptogenesis.

It is really important to comment on approximation (a) stated above. The obtained expressions are only valid within the range of applicability of this approximation. It is possible to find [140] particular configurations of the low-energy neutrino parameters in which one cannot adopt approximation (a) and safely expand in m_{Di}/m_{Dj}, $j > i$. In these situations, called *crossing level solutions*, the heavy neutrino spectrum does not follow eq. (3.96) anymore and two or even all three heavy neutrinos become degenerate. Our analytical expressions are not valid in the vicinity of these solutions. It must be noted that crossing level solutions involve in general a rather high level of fine tuning, taking place only for some special values of the low-energy parameters.

In fig. 3.2 we compare the analytical expressions of the heavy neutrino masses (cf. eqs. (3.90), (3.94) and (3.86)) with the numerical solutions in the four sets of parameters yielding level crossings for special values of m_1 as discussed in [140] (note that for simplicity $\theta_{13} = 0$ and $\theta_{23} = \pi/4$). It can be noticed that the analytical solutions

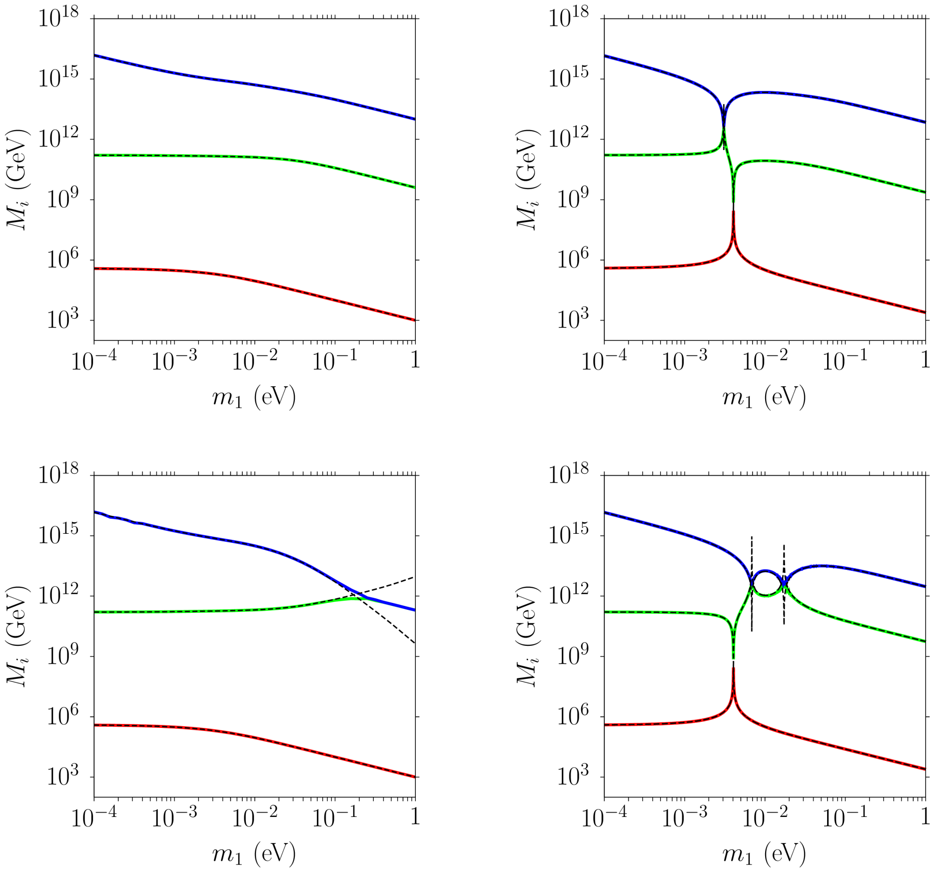

Figure 3.2: Comparison between the numerical solutions for the heavy neutrino masses (solid lines) and the analytical solutions eqs. (3.90), (3.94) and (3.86) (dashed lines), [2]. The solutions are obtained for $\theta_{13} = 0$, $\theta_{23} = 45°$, $\theta_{12} = 33°$, $\delta = 0$, $\alpha_1 = \alpha_2 = \alpha_3 = 1$, $V_L = 1$ and for $(\rho, \sigma) = (0, 0), (\pi/2, 0), (0, \pi/2), (\pi/2, \pi/2)$ from top left to bottom right respectively.

(dashed black lines) perfectly track the numerical ones (solid coloured lines) except in the close vicinity of those values of m_1 where the heavy neutrino masses become quasi-degenerate and the validity of the adopted approximations breaks down.

Sticking to assumption (a), we shall bar regions around the crossing level solutions in the rest of this work.

In fig. 3.3 we show a comparison between the analytical expressions of M_1, M_2, M_3 and the values obtained numerically. Here we chose three particular setups with physical meaning. These three choices of parameters are able, as we shall see in chapter 5, to realise successful leptogenesis around the indicated values of m_1. As we can see, there are no level crossings and the analytical solutions perfectly track the numerical values.

It is also possible to find an analytical approximate expression for the RH neutrino mixing matrix U_R. From the discussions that led to the expressions of M_3 and M_1 it should be clear that U_R is of the form $U_R = 1 + \xi$, where $\xi_{ii} = 0$ and the $\xi_{i \neq j}$ leading

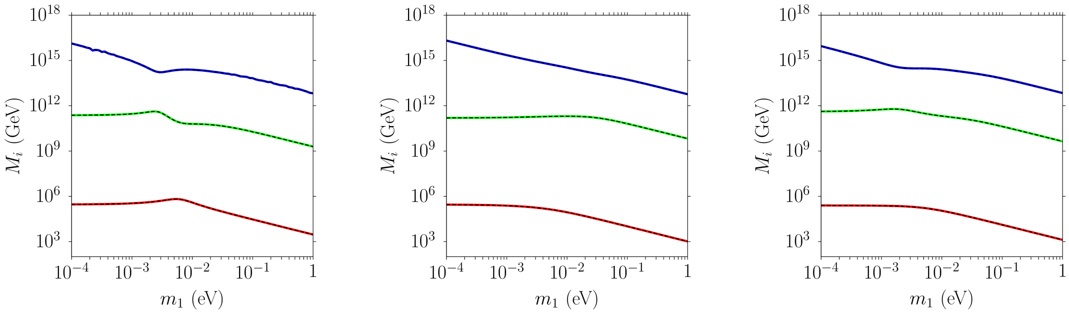

Figure 3.3: Comparison of the analytical expressions for the RH neutrino masses eqs.(3.86), (3.94), (3.90) (dashed lines) with the numerical solutions (solid lines) versus m_1 for the three following sets of parameters: $V_L = 1$, $(\alpha_1, \alpha_2, \alpha_3) = (1, 5, 1)$, $\theta_{13} = (7.55°, 8.14°, 9.2°)$, $\theta_{12} = (35.2°, 34.75°, 35.0°)$, $\theta_{23} = (46.2°, 42.1°, 40.0°)$, $\delta/\pi = (0.275, 0.067, -0.24)$, $\rho/\pi = (0.54, 1.080, 0.24)$, $\sigma/\pi = (1.14, 0.94, 0.80)$. These three solutions are examples of τ_A, τ_B and strong thermal solutions respectively and realise successful leptogenesis for $m_1 \simeq (2.5, 300, 10)\,\mathrm{meV}$. All three cases are for NO, [2].

terms are suppressed $\propto m_{Di}/m_{Dj}$ with $j > i$. Here we shall compute the matrix $\tilde{U}_R$, while the matrix D_ϕ can be obtained afterwards from eqs. (3.92), (3.95) and (3.88). From the unitarity condition $\tilde{U}_{Rik}\tilde{U}^\dagger_{Rkj} = \delta_{ij}$ we get

$$\tilde{U}_{R12} \simeq -\tilde{U}^*_{R21}, \qquad \tilde{U}_{R32} \simeq -\tilde{U}_{R23}, \tag{3.100}$$

while

$$\tilde{U}^*_{R31} \simeq -\tilde{U}_{R13} - \tilde{U}_{R12}\tilde{U}^*_{R32}. \tag{3.101}$$

From eq. (3.89) we also have

$$D^{-1}_M = -\tilde{U}^\dagger_R D^{-1}_{m_D} m_\nu D^{-1}_{m_D} \tilde{U}^*_R, \tag{3.102}$$

which, for the matrix entries, translates to

$$\frac{\delta_{ij}}{M_i} = -\tilde{U}^*_{Rki}\left(D^{-1}_{m_D} m_\nu D^{-1}_{m_D}\right)_{kl}\tilde{U}^*_{Rlj}. \tag{3.103}$$

For $(i, j) = (1, 2)$ this gives

$$\tilde{U}_{R21} \simeq \frac{m_{D1}}{m_{D2}}\frac{m_{\nu e\mu}}{m_{\nu ee}}. \tag{3.104}$$

Plugged into eq. (3.103), with the help of eq. (3.101) and (3.100), for $(i, j) = (3, 1)$ we have

$$\tilde{U}_{R31} \simeq \frac{m_{D1}}{m_{D3}}\frac{m_{\nu e\tau}}{m_{\nu ee}}. \tag{3.105}$$

From eq. (3.103) for $(i, j) = (2, 3)$ and using eq. (3.100) in order to write $\tilde{U}^*_{R23}$ in terms of $\tilde{U}^*_{R13}$ and $\tilde{U}_{R31}$ we find

$$\tilde{U}_{R13} \simeq \frac{m_{D1}}{m_{D3}}\frac{(m^{-1}_\nu)^*_{e\tau}}{m_\nu{}^*_{\tau\tau}}. \tag{3.106}$$

Finally, from eq. (3.100) and (3.101) we obtain

$$\tilde{U}_{R23} \simeq \frac{\tilde{U}_{R13} + \tilde{U}^{*}_{R31}}{\tilde{U}_{R12}} \simeq \frac{m_{D2}}{m_{D3}} \frac{(m_\nu^{-1})^{*}_{\mu\tau}}{(m_\nu^{-1})^{*}_{\tau\tau}}. \tag{3.107}$$

Putting everything together, we can approximate the U_R matrix as

$$U_R \simeq \begin{pmatrix} 1 & -\frac{m_{D1}}{m_{D2}} \frac{m^{*}_{\nu e\mu}}{m^{*}_{\nu ee}} & \frac{m_{D1}}{m_{D3}} \frac{(m_\nu^{-1})^{*}_{e\tau}}{(m_\nu^{-1})^{*}_{\tau\tau}} \\ \frac{m_{D1}}{m_{D2}} \frac{m_{\nu e\mu}}{m_{\nu ee}} & 1 & \frac{m_{D2}}{m_{D3}} \frac{(m_\nu^{-1})^{*}_{\mu\tau}}{(m_\nu^{-1})^{*}_{\tau\tau}} \\ \frac{m_{D1}}{m_{D3}} \frac{m_{\nu e\tau}}{m_{\nu ee}} & -\frac{m_{D2}}{m_{D3}} \frac{(m_\nu^{-1})_{\mu\tau}}{(m_\nu^{-1})_{\tau\tau}} & 1 \end{pmatrix} \cdot D_\phi. \tag{3.108}$$

We can notice now that, given the expression of the $\tilde{U}_R$ matrix, we have $\tilde{\Phi}_R \simeq 0$, therefore

$$\phi_2 \simeq \mathrm{Arg}\left[\frac{m_{\nu ee}}{(m_\nu^{-1})_{\tau\tau}}\right] - 2(\rho + \sigma), \tag{3.109}$$

so that the matrix D_ϕ, eq. (3.77) is now entirely determined.

Once the matrix U_R is expressed in terms of the input parameters through the matrix m_ν and its inverse m_ν^{-1}, we can obtain an analytical expression for the *CP* asymmetries as well. Considering that, by barring the crossing level solutions, the relevant *CP* asymmetries are related to N_2 and that the spectrum is hierarchical, we can concentrate on $\varepsilon_{2\alpha}$ and consider only the interference with N_3 by taking $j = 3$ in eq. (2.118). Indeed, the contribution of the interference with N_1 given by $j = 1$ is heavily suppressed by the mass hierarchy. We get

$$\varepsilon_{2\alpha} \simeq \overline{\varepsilon}(M_2) \left\{ \mathcal{I}_{23}^{\alpha}\, \xi\left(\frac{M_3^2}{M_2^2}\right) + \mathcal{J}_{23}^{\alpha} \frac{2}{3(1 - M_2^2/M_3^2)} \right\}, \tag{3.110}$$

where, specialising eqs. (2.120) and (2.121),

$$\mathcal{I}_{23}^{\alpha} \equiv \frac{\mathrm{Im}\left\{ m^{*}_{D\alpha 2} m_{D\alpha 3} (m_D^{\dagger} m_D)_{23} \right\}}{M_2\, M_3\, \widetilde{m}_2\, m_{\mathrm{atm}}}, \qquad \mathcal{J}_{23}^{\alpha} \equiv \frac{\mathrm{Im}\left\{ m^{*}_{D\alpha 2} m_{D\alpha 3} (m_D^{\dagger} m_D)_{32} \right\}}{M_2\, M_3\, \widetilde{m}_2\, m_{\mathrm{atm}}} \frac{M_2}{M_3}. \tag{3.111}$$

Moreover, since also $M_3 \gg M_2$ we can approximate $\xi(M_3^2/M_2^2) \simeq 1$ and neglect the term $\mathcal{J}_{23}^{\alpha}$, so that we get the simpler expression

$$\varepsilon_{2\alpha} \simeq \overline{\varepsilon}(M_2)\, \mathcal{I}_{23}^{\alpha}, \tag{3.112}$$

It must be noticed that this result is a feature of any N_2-dominated leptogenesis scenario. The additional constraints and relations typical of $SO(10)$-inspired models will be employed in what follows.

Always considering $V_L = 1$, we can use our previous results to find a final approximated analytical expression for the flavoured CP asymmetries

$$\varepsilon_{2\alpha} \simeq \bar{\varepsilon}(M_2) \frac{m_{D\alpha}^2}{m_{D3}^2 \left|U_{R32}^2\right|^2 + m_{D2}^2} \frac{\left|(m_\nu^{-1})_{\tau\tau}\right|^{-1}}{m_{\rm atm}} {\rm Im}\{U_{R\alpha 2}^* U_{R\alpha 3} U_{R32}^* U_{R33}\}\,. \tag{3.113}$$

Using the expressions in eq. (3.108), we find that also the CP asymmetries follow a hierarchical pattern

$$\varepsilon_{2\tau} \,:\, \varepsilon_{2\mu} \,:\, \varepsilon_{2e} \;\simeq\; \alpha_3^2 m_t^2 \,:\, \alpha_2^2 m_c^2 \,:\, \alpha_1^2 m_u^2 \frac{\alpha_3 m_t}{\alpha_2 m_c} \frac{\alpha_1^2 m_u^2}{\alpha_2^2 m_c^2}. \tag{3.114}$$

As one can see, while $\varepsilon_{2\mu}$ is suppressed by about four orders of magnitude ($\sim m_c^2/m_t^2$) compared to $\varepsilon_{2\tau}$, the electronic CP asymmetry is suppressed even by about seven orders of magnitude compared to $\varepsilon_{2\mu}$. For this reason, for $V_L = 1$ and avoiding the crossing level solutions, the electron contribution to the final asymmetry is always completely negligible. With respect to ε_{2e}, it is worth noticing that, since the contribution from the interference with N_3 is so suppressed, actually it becomes comparable to the term coming from the interference with N_1 that we are neglecting in eq. (3.113).

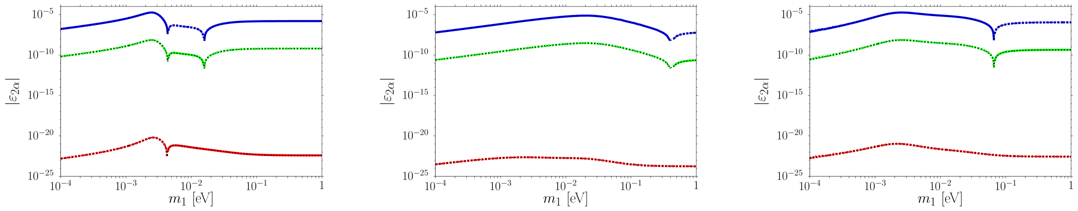

Figure 3.4: Plots of the CP flavoured asymmetries corresponding respectively to the same three sets of parameters of fig. 3.3, [2]. The solid coloured lines are the numerical curves (blue, green and red lines correspond respectively to τ, μ and e flavours). The dashed lines are the analytical expressions eqs. (3.113).

The hierarchy among the CP asymmetries and the goodness of the analytical expression eq. (3.113) are well shown in fig. 3.4. Here, for the same four sets of parameters of fig. 3.3, the flavoured CP asymmetries are plotted versus m_1, comparing the numerical result (solid lines) with the analytic expressions (dashed lines).

It is possible to obtain an analytical expression for the flavoured decay parameters as well. From the definition eq. (3.41) and eq. (2.133), we get an expression of $K_{i\alpha}$ in terms of the Dirac mass matrix m_D

$$K_{i\alpha} = \frac{\left|m_{D\alpha i}\right|^2}{m_* M_i}. \tag{3.115}$$

Therefore, using the relations found above, for $V_L = 1$ we have

$$K_{i\alpha} = \frac{m_{D\alpha}^2}{m_* M_i} \left|U_{R\alpha i}\right|^2. \tag{3.116}$$

We can finally employ the analytical expressions of M_i and U_R in order to obtain also the expression of the orthogonal matrix Ω in $SO(10)$-inspired models. From eq. (2.73) and (3.73) we have

$$\Omega = D_m^{-1/2}\, U^\dagger V_L^\dagger\, D_{m_D}\, U_R D_M^{-1/2}, \tag{3.117}$$

therefore, for $V_L = 1$ we have

$$\Omega_{ij} = \frac{1}{\sqrt{m_i\, M_j}} \sum_k m_{Dk}\, U^*_{ki}\, U_{Rkj}, \qquad \text{with} \quad V_L = 1. \tag{3.118}$$

Using eqs. (3.90), (3.94), (3.86) and (3.108) we get

$$\Omega \simeq \begin{pmatrix} -\frac{\sqrt{m_1\,|m_{\nu ee}|}}{m_{\nu ee}} U_{e1} & \sqrt{\frac{m_2 m_3 |(m_\nu^{-1})_{\tau\tau}|}{|m_{\nu ee}|}} \left(U^*_{\mu 1} - U^*_{\tau 1}\frac{(m_\nu^{-1})_{\mu\tau}}{(m_\nu^{-1})_{\tau\tau}}\right) & \frac{U^*_{\tau 1}}{\sqrt{m_1 |(m_\nu^{-1})_{\tau\tau}|}} \\ -\frac{\sqrt{m_2\,|m_{\nu ee}|}}{m_{\nu ee}} U_{e2} & \sqrt{\frac{m_1 m_3 |(m_\nu^{-1})_{\tau\tau}|}{|m_{\nu ee}|}} \left(U^*_{\mu 2} - U^*_{\tau 2}\frac{(m_\nu^{-1})_{\mu\tau}}{(m_\nu^{-1})_{\tau\tau}}\right) & \frac{U^*_{\tau 2}}{\sqrt{m_2 |(m_\nu^{-1})_{\tau\tau}|}} \\ -\frac{\sqrt{m_3\,|m_{\nu ee}|}}{m_{\nu ee}} U_{e3} & \sqrt{\frac{m_1 m_2 |(m_\nu^{-1})_{\tau\tau}|}{|m_{\nu ee}|}} \left(U^*_{\mu 3} - U^*_{\tau 3}\frac{(m_\nu^{-1})_{\mu\tau}}{(m_\nu^{-1})_{\tau\tau}}\right) & \frac{U^*_{\tau 3}}{\sqrt{m_3 |(m_\nu^{-1})_{\tau\tau}|}} \end{pmatrix} \cdot D_\phi . \tag{3.119}$$

We have therefore shown that, barring crossing level solutions, the $SO(10)$-inspired conditions eqs. (3.81) and (3.83) give a hierarchical heavy neutrino mass spectrum with $M_1 \ll 10^9\,\text{GeV}$, $10^9\,\text{GeV} \lesssim M_2 \lesssim 10^{12}\,\text{GeV}$ and $M_3 \gg 10^{12}\,\text{GeV}$. Therefore, we can conclude that in $SO(10)$-inspired models the N_2-dominated scenario of leptogenesis is naturally realised.

Moreover, the hierarchy in the *CP* asymmetries, eq. (3.114), suggests that the final asymmetry is dominantly produced in the τ flavour. Therefore, we can say that the $SO(10)$-inspired leptogenesis setup can naturally favour the τ N_2-dominated leptogenesis scenario that is requested by strong thermal leptogenesis. We can then expect that the condition of strong thermal leptogenesis can be imposed and successfully realised also in $SO(10)$-inspired models, thus providing additional constraints on the parameter space. In chapter 5, we shall consider the impact on the parameter space of the $SO(10)$-inspired conditions and the additional strong thermal leptogenesis requirement.

Part II

Understanding and predicting neutrino parameters

Chapter 4

Strong thermal leptogenesis and the absolute neutrino mass scale

In chapter 2 we explained the basic mechanism of leptogenesis and laid out our formalism. In particular, we have noticed that, in the minimal setup, the type-I seesaw lagrangian has a total of 18 free parameters. Leptogenesis generally implies the additional condition that the asymmetry produced is compatible with the experimental observation. Therefore, by requiring successful leptogenesis, eq. (2.174), we can impose a constraint over the parameters. This condition is able to provide us with some information on the heavy neutrino spectrum, see eqs. (2.180) and (2.181). However, this is in the form of a generic lower bound. Moreover, no additional information is given on the other parameters such as the mixing angles or the light neutrino masses.
In chapter 3 we showed that both strong thermal leptogenesis and $SO(10)$-inspired leptogenesis are able to provide us with important predictions on the heavy neutrino spectrum: in both cases a hierarchical spectrum that favours N_2-dominated leptogenesis is required. This is a remarkable prediction that draws attention to the N_2-dominated scenario, providing solid theoretical reasons for this leptogenesis paradigm. However, the consequences of both strong thermal leptogenesis and $SO(10)$-inspired leptogenesis are much richer than that. In this chapter we shall study what are the consequences on the leptogenesis mechanism of imposing strong thermal leptogenesis. We shall focus in particular on the constraints on neutrino parameters that are entailed by this scenario and on the predictions that can be derived. As we shall see, these will turn out to be quite robust so that the idea of strong thermal leptogenesis can be put to test especially by forthcoming cosmological observations.

We shall analyse here how the strong thermal leptogenesis condition (3.62) can imply interesting constraints, in particular on the absolute neutrino mass scale m_1 [1]. We shall discuss first the more significant case $M_3 \gtrsim 5 \times 10^{11}\,\mathrm{GeV}$, so that the final pre-existing asymmetry is given by eqs. (3.67), (3.68) and (3.69). As we have seen, this implies the conditions on the flavoured decay parameters eq. (3.70). Let us study first the case with normally ordered light neutrino masses.

4.1 Normal Ordering

Our aim is to show that the conditions $K_{1\tau} \lesssim 1$ and $K_{1e}, K_{1\mu} \gtrsim K_{\rm st} \gg 1$ can be satisfied simultaneously, without fine-tuned conditions, only if m_1 is sufficiently large. Let us start by analysing $K_{1\tau}$. The general eq. (3.43) for the $K_{i\alpha}$'s specialises into

$$K_{1\tau} = \left|\sqrt{\frac{m_1}{m_*}}U_{\tau 1}\Omega_{11} + \sqrt{\frac{m_2}{m_*}}U_{\tau 2}\Omega_{21} + \sqrt{\frac{m_3}{m_*}}U_{\tau 3}\Omega_{31}\right|^2 . \tag{4.1}$$

From this expression, anticipating that the lower bound falls in a range of values $m_1 \lesssim m_{\rm sol}$, we can approximate $m_2 \simeq m_{\rm sol}$ and $m_3 \simeq m_{\rm atm}$, and write

$$\sqrt{\frac{m_{\rm atm}}{m_*}}U_{\tau 3}\Omega_{31} = -\sqrt{\frac{m_1}{m_*}}U_{\tau 1}\Omega_{11} - \sqrt{\frac{m_{\rm sol}}{m_*}}U_{\tau 2}\Omega_{21} + \sqrt{K_{1\tau}}\, e^{i\varphi}, \tag{4.2}$$

where φ is some generic phase. Adopting our assumption on m_i, the expression of K_{1e} and $K_{1\mu}$ can be similarly obtained from eq. (3.43) as

$$K_{1\alpha} = \left|\sqrt{\frac{m_1}{m_*}}U_{\alpha 1}\Omega_{11} + \sqrt{\frac{m_{\rm sol}}{m_*}}U_{\alpha 2}\Omega_{21} + \sqrt{\frac{m_{\rm atm}}{m_*}}U_{\alpha 3}\Omega_{31}\right|^2 , \tag{4.3}$$

where $\alpha = e, \mu$. By using eq. (4.2), we get

$$K_{1\alpha} = \left|\Omega_{11}\sqrt{\frac{m_1}{m_*}}\left(U_{\alpha 1} - \frac{U_{\tau 1}}{U_{\tau 3}}U_{\alpha 3}\right) + \Omega_{21}\sqrt{\frac{m_{\rm sol}}{m_*}}\left(U_{\alpha 2} - \frac{U_{\tau 2}}{U_{\tau 3}}U_{\alpha 3}\right) + \frac{U_{\alpha 3}}{U_{\tau 3}}\sqrt{K_\tau}e^{i\varphi}\right|^2 . \tag{4.4}$$

We can define $K^0_{1\alpha} \equiv K_{1\alpha}(m_1 = 0)$ and φ_0 such that

$$\sqrt{K^0_{1\alpha}}\, e^{i\varphi_0} \equiv \Omega_{21}\sqrt{\frac{m_{\rm sol}}{m_*}}\left(U_{\alpha 2} - \frac{U_{\tau 2}}{U_{\tau 3}}U_{\alpha 3}\right) + \frac{U_{\alpha 3}}{U_{\tau 3}}\sqrt{K_{1\tau}}\, e^{i\varphi}, \tag{4.5}$$

this way eq. (4.4) can be rewritten as

$$K_{1\alpha} = \left|\Omega_{11}\sqrt{\frac{m_1}{m_*}}\left(U_{\alpha 1} - \frac{U_{\tau 1}}{U_{\tau 3}}U_{\alpha 3}\right) + \sqrt{K^0_{1\alpha}}\, e^{i\varphi_0}\right|^2 . \tag{4.6}$$

Imposing the strong thermal leptogenesis conditions $K_{1\alpha} > K_{\rm st}(N^{\rm p,i}_{\Delta_\alpha})$, $\alpha = e, \mu$, we get

$$\left|\Omega_{11}\sqrt{\frac{m_1}{m_*}}\left(U_{\alpha 1} - \frac{U_{\tau 1}}{U_{\tau 3}}U_{\alpha 3}\right) + \sqrt{K^0_{1\alpha}}\, e^{i\varphi_0}\right|^2 > K_{\rm st}(N^{\rm p,i}_{\Delta_\alpha}). \tag{4.7}$$

Taking the square root of both sides and maximising the left-hand side, we obtain a lower bound on m_1 ($\alpha = e, \mu$),

$$m_1 > m_1^{\rm lb} \equiv m_* \max_\alpha \left[\left(\frac{\sqrt{K_{\rm st}(N_{\Delta_\alpha}^{\rm p,i})} - \sqrt{K_{1\alpha}^{0,\rm max}}}{\max[|\Omega_{11}|] \left| U_{\alpha 1} - \frac{U_{\tau 1}}{U_{\tau 3}} U_{\alpha 3} \right|} \right)^2 \right], \tag{4.8}$$

when $K_{1\alpha}^{0,\rm max} < K_{\rm st}(N_{\Delta_\alpha}^{\rm p,i})$, where

$$\sqrt{K_{1\alpha}^{0,\rm max}} \equiv \max[|\Omega_{21}|] \sqrt{\frac{m_{\rm sol}}{m_*}} \left| U_{\alpha 2} - \frac{U_{\tau 2}}{U_{\tau 3}} U_{\alpha 3} \right| + \left| \frac{U_{\alpha 3}}{U_{\tau 3}} \right| \sqrt{K_{1\tau}^{\rm max}}. \tag{4.9}$$

Because of the smallness of the reactor mixing angle θ_{13} there are two consequences: firstly, the maximum is found for $\alpha = e$ and secondly, imposing $K_{1\tau}^{\rm max} \lesssim 1$ as prescribed by the strong thermal leptogenesis condition, both the two terms in $K_{1e}^{0,\rm max}$ proportional to U_{e3} are suppressed and in this way there is indeed a lower bound for a sufficiently small value of $\max[|\Omega_{21}|]$. Assuming in general $|\Omega_{ij}|^2 \leq M_\Omega$, we can study the dependence of the lower bound $m_1^{\rm lb}$ on the maximum values of $|\Omega_{11}|$ and $|\Omega_{21}|$, by putting $\max\left[|\Omega_{11}|^2\right] = \max\left[|\Omega_{21}|^2\right] = M_\Omega$.

We can study more in detail an intermediate situation in which $M_\Omega = 2$. In fig. 4.1(a) we plotted, with a solid red line, the lower bound $m_1^{\rm lb}$ for $N_{B-L}^{\rm p,i} = 0.1$ as a function of the Dirac phase δ and at 95% C.L. on the mixing angles. Here θ_{13} and θ_{12} were drawn from a Gaussian distribution as reported in tab. 1.1. For the atmospheric mixing angle we have employed the Gaussian distribution $s_{23}^2 = 0.5 \pm 0.1$, centred on the maximal value, in order to account for the current experimental instabilities. At $\delta = 0$ we find (top-left panel) $m_1^{\rm lb} \simeq 0.7\,\text{meV}$ while for $\delta = \pm\pi$ we obtain $m_1^{\rm lb} \simeq 2\,\text{meV}$, showing how a future determination of the Dirac phase δ could tighten the lower bound. The lower bound becomes more stringent for $M_\Omega = 1$ and we find $m_1^{\rm lb}(\delta = 0) \simeq 6\,\text{meV}$. On the other hand for $M_\Omega = 3$ the lower bound gets relaxed and we obtain $m_1^{\rm lb}(\delta = 0) \simeq 0.13\,\text{meV}$. For $M_\Omega \gtrsim 4$ the condition $K_{1\alpha}^{0,\rm max} < K_{\rm st}$ is not verified anymore and hence the lower bound vanishes.

In order to verify the existence of the lower bound, to test the validity of the analytical estimation and to show in more detail the level of fine tuning involved in order to saturate the lower bound, we performed a scatter plot analysis in the space of the 13 parameters (m_1, 6 in U, 6 in Ω). For the scatter plots, the mixing angles were uniformly extracted on their experimental 3σ ranges. The orthogonal matrix Ω was also randomly generated, with the constraint $|\Omega_{ij}|^2 \leq M_\Omega$. For each set of extracted parameters, the final produced asymmetry $N_{B-L}^{\rm lep,f}$ was computed according to eq. (3.51), while the final pre-existing asymmetry was obtained from eqs. (3.67), (3.68) and (3.69). We assumed flavour-blindness of the initial pre-existing asymmetry by taking

$$\frac{P^0_{p\tau_2^\perp}}{2} = P^0_{p\tau} = \Delta P_{pe} = \Delta P_{p\mu} = \frac{1}{3}. \tag{4.10}$$

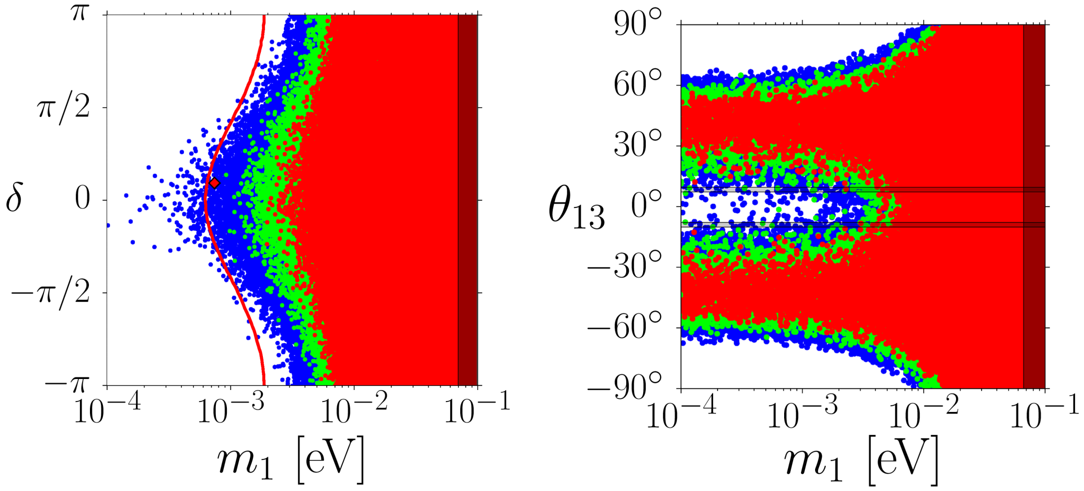

(a) (b)

Figure 4.1: Scatter plot points in the plane $\delta - m_1$ (a) and $\theta_{13} - m_1$ (b) satisfying successful strong thermal leptogenesis for $N^{\rm p,i}_{B-L} = 10^{-1}$, $10^{-2}\,10^{-3}$ in red, green and blue respectively, and $M_\Omega = 2$, [1]. The vertical grey band marks the experimental upper bound from Planck on m_1 for NO. In figure (a), the mixing angles are extracted according to their experimental Gaussian distribution, except for θ_{23} which is obtained from the Gaussian distribution of $s^2_{23} = 0.5 \pm 0.1$. The solid red band is the analytic lower bound $m_1^{\rm lb}$ at 95% C.L. on the mixing angles. In figure (b) the mixing angles are uniformly extracted over $[-\pi/2, \pi/2]$. The shadowed bands mark the experimental 3σ range for θ_{13}.

This corresponds to the most general choice and provides us with the most conservative results. We shall discuss later the situation without phantom terms $\Delta P_{p\alpha}$ in the flavoured initial pre-existing asymmetries. It must be noticed, anyways, that the results depend only logarithmically on these parameters, so the final analysis is rather insensitive to a precise choice. Each set of parameters is accepted if satisfies the successful strong thermal leptogenesis conditions

$$\eta_B^{\rm lep,f} \gtrsim \eta_B^{\rm CMB} \qquad \text{and} \qquad \eta_B^{\rm p,f} \leq 0.1\,\eta_B^{\rm lep,f}, \tag{4.11}$$

and is represented in the scatter plot as a point coloured according to the pre-existing initial asymmetry: $N^{\rm p,i}_{B-L} = 10^{-1}, 10^{-2}, 10^{-3}$ respectively in red, green and blue.

The points in fig. 4.1(a) represent models realising successful strong thermal leptogenesis in the plane $\delta - m_1$ for $M_\Omega = 2$. One can see that for $N^{\rm p,i}_{B-L} = 10^{-1}$ the minimum values of m_1 at different values of δ are much higher than the analytic estimation given by the solid red line. The reason is due to the fact that the lower bound is saturated for very special choices of Ω such that $|\Omega_{11}|^2$ and $|\Omega_{21}|^2$ are as close as possible to the maximum value M_Ω, but at the same time are such that the *CP* asymmetry $\varepsilon_{2\tau}$, given by eq. (3.112), is not too suppressed and successful leptogenesis can be realised. This is confirmed by fig. 4.2 where in the three panels we plotted $\mathcal{I}^\tau_{23}$, $|\Omega_{11}|^2$ and $|\Omega_{22}|^2$ for $M_\Omega = 2$. We made a focused search (by fine-tuning the parameters) managing to find a point (the red

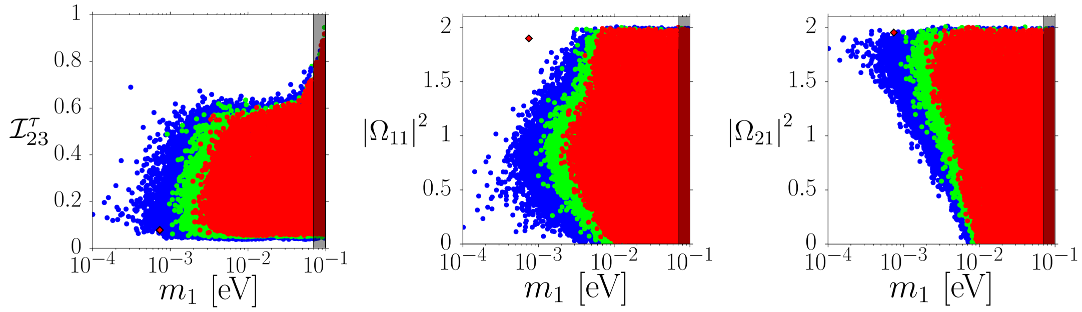

Figure 4.2: Scatter plots for $M_\Omega = 2$ of $\mathcal{I}_{23}^{\tau}$, $|\Omega_{11}|^2$ and $|\Omega_{21}|^2$ versus m_1, [1].

diamond) where m_1 is very close to the lower bound. The same red diamond is shown in fig. 4.1(a). For this point $\mathcal{I}_{23}^{\tau}$ gets considerably reduced since it corresponds to a situation where the term $\propto \sqrt{m_1}$ in the flavoured decay parameters becomes negligible and the strong thermal condition is satisfied for a very special condition. Indeed, plugging into the expression of $\mathcal{I}_{23}^{\tau}$ the results of eq. (4.2) when the terms on the right-hand side $\propto \sqrt{m_1}, \sqrt{K_{1\tau}}$ are neglected and $|\Omega_{11}|, |\Omega_{21}|$ become maximal, we obtain that the final *CP* asymmetry is suppressed.

In order to show the importance of the smallness of the reactor mixing angle in the determination of the lower bound, we also performed a scatter plot with the same procedure, but letting the mixing angles vary within the whole range of physical values with no experimental constraints. They were randomly extracted uniformly over $[-\pi/2, \pi/2]$. In fig. 4.1(b) we show the results in the plane $m_1 - \theta_{13}$. One can see that the smallness of θ_{13} is crucial for the existence of the lower bound. For larger values, such as $\theta_{13} \sim 45°$ the lower bound disappears irrespectively of the size of the pre-existing asymmetry. This can be well understood analytically considering that in the expression for $K_{1e}^{0,\max}$, eq. (4.9), there are two terms $\propto |U_{e3}|^2$.

In fig. 4.3 we also show the values of the four relevant decay parameters $K_{1\alpha}$ and $K_{2\tau}$ for $M_\Omega = 2$. Firstly, we can see that the values of the flavoured decay parameters respect the strong thermal conditions eq. (3.70). From the plot of K_{1e} vs. m_1, bottom-right panel, we can notice that for values $m_1 \lesssim 10\,\text{meV}$ the maximum value of K_{1e} gets considerably reduced until it falls below K_{st}, indicated by the horizontal dashed line for $N_{B-L}^{\text{p,i}} = 0.1$. It is also clear that already below $m_1 \sim 10\,\text{meV}$ the possibility to realise strong thermal leptogenesis requires a high fine tuning in the parameters since in this case $K_{1e} \lesssim K_{1e}^{0,\max} \simeq 4\,M_\Omega \lesssim K_{\text{st}}$ for large asymmetries and not too unreasonably high values of M_Ω.

In order to quantitatively show that it is actually very difficult to saturate the analytical lower bound, thus demonstrating that it requires some level of fine-tuning of the parameters, we have plotted the distributions of the values of m_1 obtained from the scatter plots. These are shown in fig. 4.4 for $M_\Omega = 1,\, 2,\, 5, 10$ and for $N_{B-L}^{\text{p,i}} = 10^{-1},\, 10^{-2},\, 10^{-3}$ (red, green and blue lines respectively). One can see that there is a clear peak around $m_1 \simeq m_{\text{atm}}$ and that the distributions rapidly tend to zero when $m_1 \lesssim m_{\text{sol}} \simeq 10\,\text{meV}$.

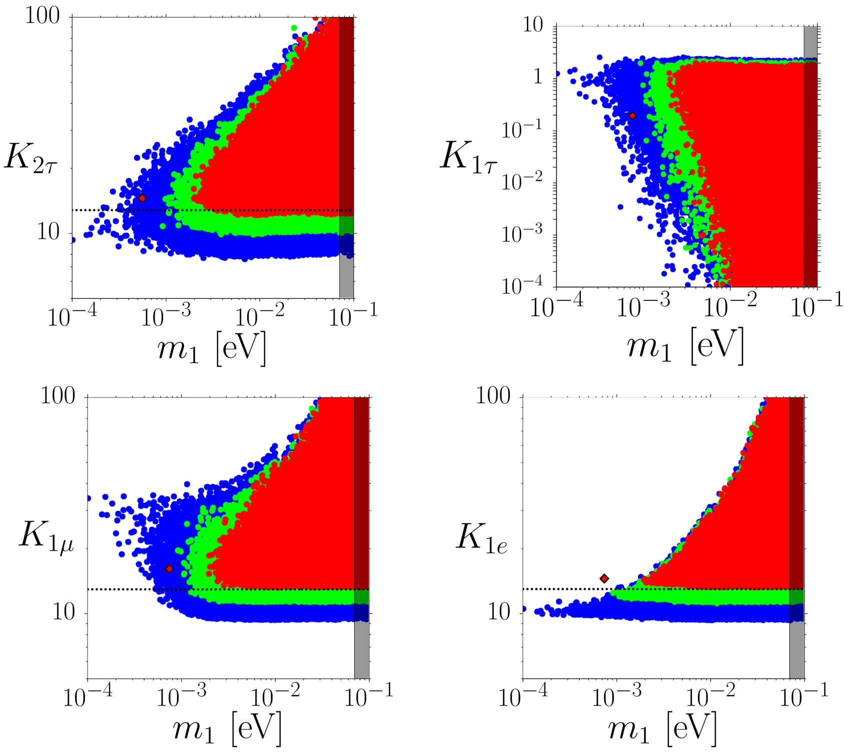

Figure 4.3: Results of the scatter plots of $K_{2\tau}$, $K_{1\tau}$, $K_{1\mu}$, K_{1e} versus m_1 for $M_\Omega = 2$, [1]. The horizontal dashed line indicates the value $K_{\rm st}(N^{\rm p,i}_{\Delta_\alpha} = 0.03) \simeq 13$.

For instance, for $M_\Omega = 2$ and $N^{\rm p,i}_{B-L} = 10^{-1}$, top-right panel, it can be noticed that in more than 99% we have $m_1 \gtrsim 10\,\text{meV}$.

For $M_\Omega = 5$ the analytical lower bound vanishes, however we still have that 95% of points satisfying successful strong thermal leptogenesis are found for $m_1 \gtrsim 6\,\text{meV}$. For $M_\Omega = 10$ one obtains that 95% of points fall at $m_1 \gtrsim 1\,\text{meV}$ while for $M_\Omega = 100$, which is not shown in fig. 4.4, this limit decreases at the untestable values $m_1 \gtrsim 0.4\,\text{meV}$.

This provides another example of how, more generally, leptogenesis neutrino mass bounds tend to disappear in the limit $M_\Omega \gg 1$ [102, 148]. However, considering eq. (2.77), we can notice that large values of $|\Omega_{ij}|^2$ imply high cancellations in the seesaw formula, so that the lightness of the active neutrino masses becomes a combined effect of these cancellations with the actual seesaw mechanism. Therefore, barring these special situations in which the seesaw mechanism is not genuinely realised, we can expect $M_\Omega \lesssim \mathcal{O}(1)$.

4.2 Inverted Ordering

We shall now discuss the IO case. The analytical procedure shown before for NO can be applied to the IO case to find an expression similar to eq. (4.8) with the replacements $m_{\rm sol} \to m_{\rm atm}$ and $U \to U^{\rm IO}$. These replacements have a significant impact on the results. Firstly, replacing $m_{\rm sol} \to m_{\rm atm}$ tends to push all $K_{1\alpha}$ values to much higher values. If

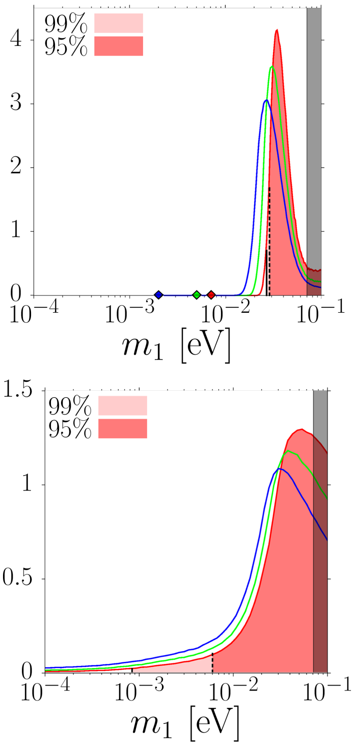

Figure 4.4: Distributions of the values of m_1 from the scatter plots of successful strong thermal leptogenesis models, [1]. From left to right, top to bottom: $M_\Omega = 1,\ 2,\ 5,\ 10$. The coloured lines correspond to $N_{B-L}^{\mathrm{p,i}} = 10^{-1},\ 10^{-2},\ 10^{-3}$ in red, green and blue respectively. The diamonds mark the m_1 minimum values if found. For $N_{B-L}^{\mathrm{p,i}} = 10^{-1}$ light and dark red filling indicate regions where, respectively, 99% and 95% of points accumulate.

one considers again the quantity $K_{1e}^{0,\max}$ in eq. (4.9), it is possible to check that now we always have $K_{1e}^{0,\max} \gg K_{\mathrm{st}}$ for $N_{B-L}^{\mathrm{p,i}} \lesssim 0.1$. On the other hand, this time the value of $K_{1\mu}$ has to be tuned in order to be larger than K_{st}. The reason is that for IO there is now a cancellation in the quantity

$$U_{\mu 2}^{\mathrm{IO}} - U_{\tau 2}^{\mathrm{IO}} \frac{U_{\mu 3}^{\mathrm{IO}}}{U_{\tau 3}^{\mathrm{IO}}}, \tag{4.12}$$

that suppresses $K_{1\mu}^{0,\max}$, though not as strongly as K_{1e} in NO. Indeed one finds now that $K_{1\mu}^{0,\max} < K_{\mathrm{st}}$, implying the existence of the lower bound, holds only for $M_\Omega \lesssim 0.9$. Therefore, the lower bound on m_1 for IO is much looser than for the NO case. This result is again confirmed by a scatter plot analysis. The results are shown in fig. 4.5 directly in the form of the distribution of probabilities for m_1. The distributions were obtained in the same way as for the NO case, by simply adopting the IO expressions for the light neutrino mass spectra and the mixing matrix U. We can notice that, in the IO case, there is no analytical lower bound for $M_\Omega = 1,\ 2,\ 5,\ 10$ and successful strong thermal leptogenesis could be realised with arbitrarily small m_1. However, we still find a peak in the distributions and a rapid decrease towards small values of m_1. Indeed,

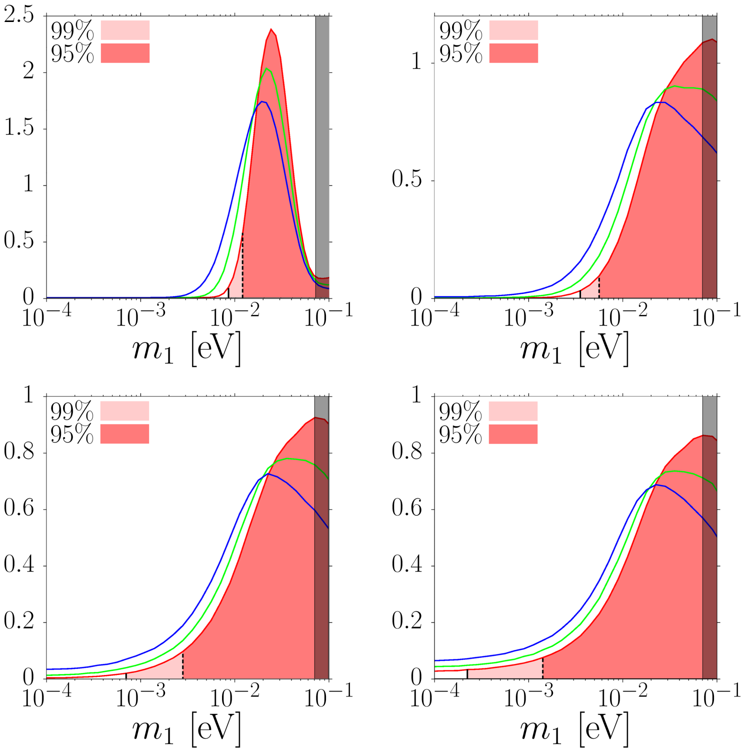

Figure 4.5: IO case. Distributions of the values of m_1 from the scatter plots of successful strong thermal leptogenesis models, [1]. From left to right, top to bottom: $M_\Omega = 1, 2, 5, 10$. The coloured lines correspond to $N^{\rm p,i}_{B-L} = 10^{-1}, 10^{-2}, 10^{-3}$ in red, green and blue respectively. For $N^{\rm p,i}_{B-L} = 10^{-1}$ light and dark red filling indicate regions where, respectively, 99% and 95% of points accumulate.

the fact that $K^{0,\rm max}_{1\mu}$ is suppressed implies that one has to fine tune the parameters in the orthogonal matrix in order to maximise $K_{1\mu}$ so that it can get slightly higher than $K_{\rm st}(N^{\rm p,i}_{\Delta_\mu})$. This still acts in a way that, in the limit $m_1/m_{\rm atm} \to 0$, the density of points drops quickly. For instance, we can see that for $M_\Omega = 2$ we still have that 99% of the solutions are found for values $m_1 \gtrsim 3\,\rm meV$. The tuning on $K_{1\mu}$ can be noticed from the panel in fig. 4.6. Here, values of $K_{1e} \gg K_{\rm st} \sim 13$ can be easily found even for small values of m_1. On the other hand, the maximum value of $K_{1\mu}$ for small values $m_1 \ll m_{\rm atm}$ is just a little larger than $K_{\rm st}$. Therefore, in the IO case, the leading role in constraining the absolute neutrino mass scale m_1 is played by $K_{1\mu}$, instead of K_{1e} as in NO.

For completeness, we can now turn to analyse the case in which $M_3 \lesssim 5 \times 10^{11}$ GeV. In this case, the final pre-existing asymmetry is given by eq. (3.71) and, as already pointed out, the condition $K_{2\tau} \gtrsim K_{\rm st}(N^{\rm p,i}_{\Delta_\tau})$ becomes $K_{2\tau} + K_{3\tau} \gtrsim K_{\rm st}(N^{\rm p,i}_{\Delta_\tau})$. Potentially, this condition can be much more easily satisfied and, in particular, the value of $K_{2\tau}$ has not to be necessarily very large. However, this does not substantially change the results on the absolute neutrino mass scale obtained before for $M_3 \gtrsim 5 \times 10^{11}$ GeV. Indeed, as

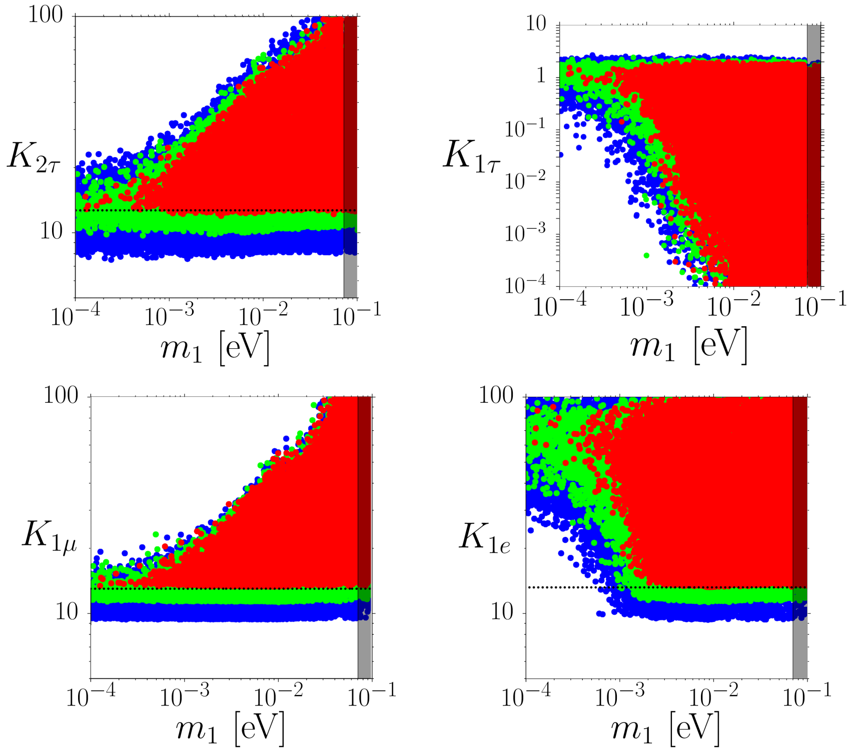

Figure 4.6: IO case. Results of the scatter plots of $K_{2\tau}$, $K_{1\tau}$, $K_{1\mu}$, K_{1e} versus m_1 for $M_\Omega = 2$, [1]. The horizontal dashed line indicates the value $K_{\rm st}(N^{\rm p,i}_{\Delta_\alpha} = 0.03) \simeq 13$.

we have shown, these results depend only on the the $K_{1\alpha}$'s rather than on $K_{2\tau}$ and in particular on the fact that in the NO (IO) case the value of $K_{1e}^{\rm -0,max}$ ($K_{1\mu}^{\rm -0,max}$) is very close to $K_{\rm st}$.

In fig. 4.7 we show $K_{2\tau}$ and the $K_{1\alpha}$'s for $M_3 \lesssim 5 \times 10^{11}$ GeV in the NO case. We can compare these results with those obtained for the case of large M_3, fig. 4.3, and notice that now $K_{2\tau}$ can also be smaller than $K_{\rm st}$. Nonetheless, the scatter plot for K_{1e} is substantially the same, so that the conclusions drawn above are essentially still valid. In general, for $M_3 \lesssim 5 \times 10^{11}$ GeV the success rate of successful strong thermal leptogenesis becomes higher, since the conditions are less restrictive, but still the possibility to get values $m_1 \lesssim 10\,$meV relies on a tuned choice of the orthogonal matrix.

4.3 Comments on the results

The results shown before were all obtained with some assumptions and present some features that are worth discussing with some detail. Here we shall comment on the most relevant issues.

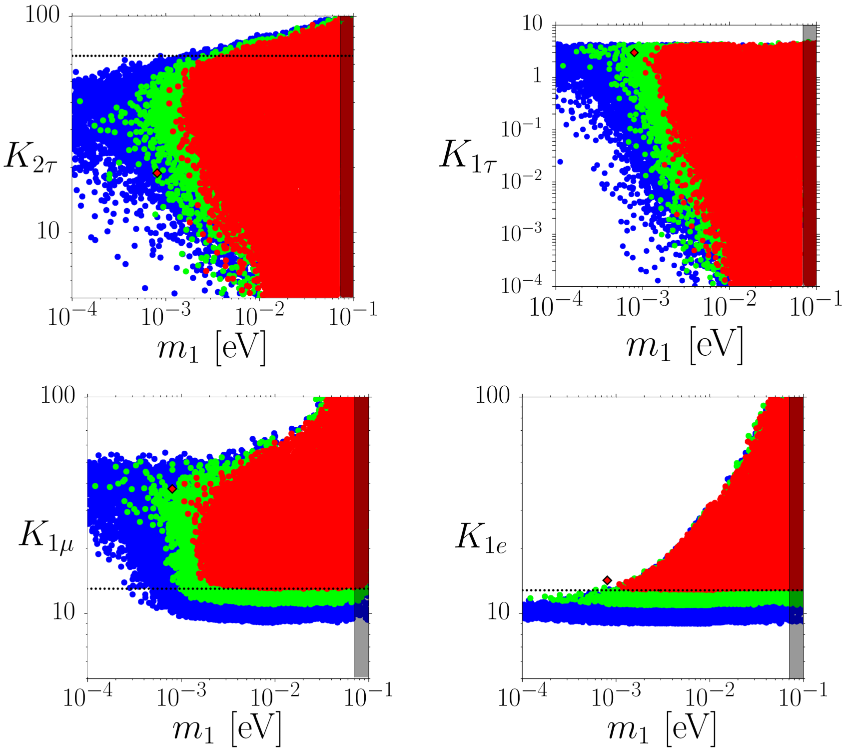

Figure 4.7: NO case with $M_3 \lesssim 5 \times 10^{11}$ GeV, [1]. Results of the scatter plots of $K_{2\tau}$, $K_{1\tau}$, $K_{1\mu}$, K_{1e} versus m_1 for $M_\Omega = 2$. The horizontal dashed line indicates the value $K_{\rm st}(N^{\rm p,i}_{\Delta_\alpha} = 0.03) \simeq 13$.

4.3.1 Neutrino oscillation data

The results we obtained rely on the smallness of $K^{0,\rm max}_{1e}$ and $K^{0,\rm max}_{1\mu}$ for NO and IO respectively, once $K_{1\tau} \lesssim 1$ is imposed. As we have seen, the condition $K^{0,\rm max}_{1e} < K_{\rm st}(N_{\Delta_e})$, which allows for the existence of the lower bound in NO, is enforced by the current measured value of the PMNS matrix entries, in particular $|U_{e3}|^2 \ll 1$. Similarly, in IO we have $K^{0,\rm max}_{1\mu} < K_{\rm st}(N_{\Delta_\mu})$ thanks to $\left|U^{\rm IO}_{\mu 3} - U^{\rm IO}_{\tau 2}\, U^{\rm IO}_{\mu 3}/U^{\rm IO}_{\tau 3}\right|^2 \ll 1$. It is then quite remarkable that the strong thermal leptogenesis conditions realise an interesting interplay between low-energy neutrino data and leptogenesis predictions.

4.3.2 Pre-existing asymmetry phantom terms

In the derivation of our results we have assumed eq. (4.10). It is possible to study how the results would vary if the initial pre-existing asymmetry had the same flavour composition for leptons and anti-leptons, so that $\Delta P_{p\alpha} = 0$. In this case there is no lower bound for any value of M_Ω, since now, for instance, the strong thermal condition is also satisfied if

$$\left(1 - \frac{P^0_{2e}}{P^0_{2\tau_2^\perp}}\right) \lesssim 10^{-7} \tag{4.13}$$

in eq. (3.67) (without $\Delta P_{p\alpha}$), independently of the value of K_{1e}, which depends on m_1. From eqs. (3.34), (3.44) and (3.42) we obtain

$$\frac{P^0_{2e}}{P^0_{2\tau_2^\perp}} = \frac{K_{2e}}{K_{2e}+K_{2\mu}} \sim 1 \quad \Rightarrow \quad K_{2\mu} \simeq 0, \tag{4.14}$$

therefore this situation is realised only for very special models where N_2 essentially decays into leptons without a muon component. Clearly, this is a very special case, though not excluded by experimental data. However, even though the lower bound on m_1 can be evaded, the m_1 distributions are not modified by these very special solutions.

4.3.3 Flavour coupling

It is important to remark here that in our analysis we have fully neglected flavour coupling of the Boltzmann equations. This effect would generally imply modifications of the results, since it would open new ways for the pre-existing asymmetry to escape N_1's washout [123]. For this reason, accounting for flavour coupling would then make strong thermal leptogenesis conditions more strict, so tightening the lower bound on m_1.
We can briefly analyse how the strong thermal leptogenesis setup would change if these effects were taken into account [111]. We shall always consider the heavy neutrino mass spectrum as in eqs. (3.65), (3.66) and, for simplicity take $M_3 \gtrsim 5 \times 10^{11}$ GeV. In this case, as we have seen, N_2's dynamics take place in the two fully-flavoured regime, while N_1's washout happens in the three fully-flavoured one.

Let us start by analysing the production stage in the two fully-flavoured regime. When flavour coupling is considered, the relevant Boltzmann equations for the asymmetry production are given by eqs. (3.37) and (3.36). We can notice that the asymmetries in each flavour $\alpha = \tau$, $\tau_2^\perp$ are coupled by means of the two-flavour coupling matrix $C^{(2)}$ in eq. (3.38). We can solve the system of Boltzmann equations in a basis (τ', ${\tau_2^\perp}'$) in which the equations are uncoupled [123]. The basis change is performed by the unitary matrix Q that diagonalises the matrix

$$P_2^0 \equiv \begin{pmatrix} P^0_{2\tau_2^\perp} & 0 \\ 0 & P^0_{2\tau} \end{pmatrix} \cdot C^{(2)}, \tag{4.15}$$

as

$$Q\, P_2^0\, Q^{-1} = P^0_{2'} \equiv \text{diag}\Big(P^0_{2{\tau_2^\perp}'},\, P^0_{2\tau'}\Big)\,. \tag{4.16}$$

Using eq. (3.42) we can rewrite

$$P_2^0 = \begin{pmatrix} K_{2\tau_2^\perp}/K_2 & 0 \\ 0 & K_{2\tau}/K_2 \end{pmatrix} \cdot C^{(2)}. \tag{4.17}$$

If $K_{2\tau_2^\perp} \neq K_{2\tau}$, a perturbative expansion in the off-diagonal terms of $C^{(2)}$ can be performed and it is easy to obtain an expression of the entries of Q and Q^{-1}:

$$Q \equiv \begin{pmatrix} Q_{\tau_2^\perp{}'\tau_2^\perp} & Q_{\tau_2^\perp{}'\tau} \\ Q_{\tau'\tau_2^\perp} & Q_{\tau'\tau} \end{pmatrix} \simeq \begin{pmatrix} 1 & C^{(2)}_{\tau_2^\perp\tau}\frac{K_{2\tau_2^\perp}}{K_{2\tau_2^\perp}-K_{2\tau}} \\ C^{(2)}_{\tau\tau_2^\perp}\frac{K_{2\tau}}{K_{2\tau}-K_{2\tau_2^\perp}} & 1 \end{pmatrix}, \tag{4.18}$$

$$Q^{-1} \equiv \begin{pmatrix} Q^{-1}_{\tau_2^\perp\tau_2^\perp{}'} & Q^{-1}_{\tau_2^\perp\tau'} \\ Q^{-1}_{\tau\tau_2^\perp{}'} & Q^{-1}_{\tau\tau'} \end{pmatrix} \simeq \begin{pmatrix} 1 & -C^{(2)}_{\tau_2^\perp\tau}\frac{K_{2\tau_2^\perp}}{K_{2\tau_2^\perp}-K_{2\tau}} \\ -C^{(2)}_{\tau\tau_2^\perp}\frac{K_{2\tau}}{K_{2\tau}-K_{2\tau_2^\perp}} & 1 \end{pmatrix}. \tag{4.19}$$

From eq. (4.16) and the expressions of Q and Q^{-1} we obtain that the primed decay parameters are $K_{2\tau_2^\perp{}'} \simeq K_{2\tau_2^\perp}$and $K_{2\tau'} \simeq K_{2\tau}$. Solving the Boltzmann equations in the uncoupled basis and then rotating back to the $(\tau,\, \tau_2^\perp)$ one we can replace eqs. (3.39) and (3.40) with

$$N_{\Delta_{\tau_2^\perp}}(T_{L2}) \simeq \varepsilon_{2\tau_2^\perp}\kappa_f\Big(K_{2\tau_2^\perp}\Big) + C^{(2)}_{\tau_2^\perp\tau}\frac{K_{2\tau_2^\perp}}{K_{2\tau_2^\perp}-K_{2\tau}}\varepsilon_{2\tau}\left[\kappa_f\Big(K_{2\tau_2^\perp}\Big) - \kappa_f(K_{2\tau})\right], \tag{4.20}$$

$$N_{\Delta_\tau}(T_{L2}) \simeq \varepsilon_{2\tau}\kappa_f\left(K_{2\tau}\right) + C^{(2)}_{\tau\tau_2^\perp}\frac{K_{2\tau}}{K_{2\tau_2^\perp}-K_{2\tau}}\varepsilon_{2\tau_2^\perp}\left[\kappa_f\Big(K_{2\tau_2^\perp}\Big) - \kappa_f(K_{2\tau})\right]. \tag{4.21}$$

The pre-existing asymmetry in the two fully-flavoured regime is ruled by equations similar to eqs. (3.36), (3.37) but without the production term, i.e.

$$\frac{dN^{\rm p}_{\Delta_{\tau_2^\perp}}}{dz_2} = -P^0_{2\tau_2^\perp}W_2^{\rm ID}(z_2)\sum_\beta C^{(2)}_{\tau_2^\perp\beta}N^{\rm p}_{\Delta_\beta}(z_2), \tag{4.22}$$

$$\frac{dN^{\rm p}_{\Delta_\tau}}{dz_2} = -P^0_{2\tau}W_2^{\rm ID}(z_2)\sum_\beta C^{(2)}_{\tau\beta}N^{\rm p}_{\Delta_\beta}(z_2). \tag{4.23}$$

Therefore we get

$$N^{\rm p}_{\Delta_{\tau_2^\perp}} \simeq N^{\rm p,i}_{\Delta_{\tau_2^\perp}}e^{-\frac{3\pi}{8}K_{2\tau_2^\perp}} + C^{(2)}_{\tau_2^\perp\tau}\frac{K_{2\tau_2^\perp}}{K_{2\tau_2^\perp}-K_{2\tau}}\left(e^{-\frac{3\pi}{8}K_{2\tau_2^\perp}} - e^{-\frac{3\pi}{8}K_{2\tau}}\right)N^{\rm p,i}_{\Delta_\tau}, \tag{4.24}$$

$$N^{\rm p}_{\Delta_\tau} \simeq N^{\rm p,i}_{\Delta_\tau}e^{-\frac{3\pi}{8}K_{2\tau}} + C^{(2)}_{\tau\tau_2^\perp}\frac{K_{2\tau}}{K_{2\tau_2^\perp}-K_{2\tau}}\left(e^{-\frac{3\pi}{8}K_{2\tau_2^\perp}} - e^{-\frac{3\pi}{8}K_{2\tau}}\right)N^{\rm p,i}_{\Delta_{\tau_2^\perp}}, \tag{4.25}$$

where $N^{\rm p,i}_{\Delta_{\tau_2^\perp}} = P^0_{p\tau_2^\perp}(1-P^0_{p\tau})N^{\rm p,i}_{B-L}$ and $N^{\rm p,i}_{\Delta_\tau} = (P^0_{p\tau}+\Delta P_{p\tau})N^{\rm p,i}_{B-L}$. It is important to stress that these approximated expressions hold only in the case of non-degenerate decay parameters. If $K_{2\tau_2^\perp} \simeq K_{2\tau}$ the perturbative expansion is not reliable anymore [149] and the full formulae must be adopted. We can notice, however, that these degenerate cases require quite a high level of fine tuning in the leptogenesis setup, therefore in what follows we will always bar them, without loss of generality.

The impact of flavour-coupling at N_2's decay is plotted in fig. 4.8(a). Here we consider flavour coupling *only* in the two fully-flavoured regime, while we neglect the coupling in the three fully-flavoured one, $C^{(3)} = 1$. The asymmetries in eqs. (4.20), (4.21) and (4.24), (4.25) will then undergo N_1's washout as shown in the previous chapter, in the uncoupled regime. Here a random extraction of leptogenesis parameters is performed and

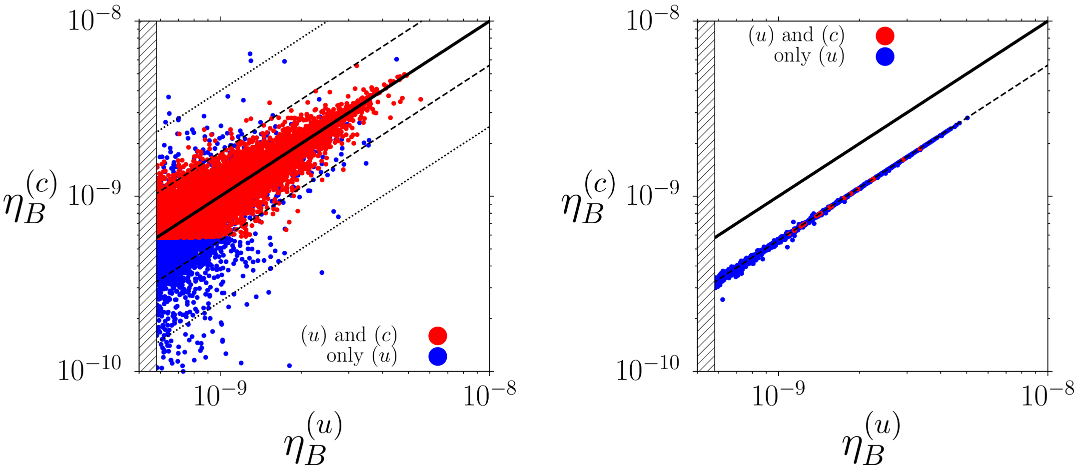

(a) (b)

Figure 4.8: Plot of the final baryon-to-photon ratio $\eta_B^{(c)}$ computed in flavour-coupled strong thermal leptogenesis versus $\eta_B^{(u)}$, computed from the same setup, but in the unflavoured regime. The initial pre-existing asymmetry we required to washout is $N_{B-L}^{\rm p,i} = 10^{-3}$ and we have $M_\Omega = 2$, $10^9\,\text{GeV} \leq M_2 \leq 5\times10^{11}\,\text{GeV}$ and NO, [111].
(a) Flavour coupling at N_2's decay only is considered,
(b) Flavour coupling at N_1's washout only is considered.
Blue dots indicate models in which strong thermal leptogenesis is successful only in the uncoupled regime, while red points denote models in which strong thermal leptogenesis is realised both in the uncoupled and in the coupled regimes. The solid line represents $\eta_B^{(c)} = \eta_B^{(u)}$, the dashed lines $\eta_B^{(c)} = (1 - C_{e\tau}^{(3)} - C_{\mu\tau}^{(3)})\,\eta_B^{(u)}$, while the dotted lines in (a) are $\eta_B^{(c)} = 4^{\pm1} \times \eta_B^{(u)}$. We hatched out the part of the plot corresponding to $\eta_B^{(u)} \leq 5.8 \cdot 10^{-10}$, the 3σ lower bound, eq. (1.11)

the final baryon-to-photon ratio is computed both in the flavour-uncoupled, $\eta_B^{(u)}$, and in the coupled, $\eta_B^{(c)}$, regimes. A NO spectrum of the light neutrino masses is considered. At the same time, the efficient washout of an initial pre-existing $N_{B-L}^{\rm p,i} = 10^{-3}$ is required. We selected a standard setup with $M_\Omega = 2$ and with M_2 logarithmically extracted between $10^9\,\text{GeV} \leq M_2 \leq 5 \times 10^{11}\,\text{GeV}$. In fig. 4.8(a) the blue dots represent models in which strong thermal leptogenesis is successful only in the uncoupled regime, while red points indicate models in which strong thermal leptogenesis is successful in both regimes. The solid line represents a baryon-to-photon ratio equal in the coupled and uncoupled regimes, i.e. no significant effect from flavour coupling. The two dotted lines indicate an enhancement/suppression of the final asymmetry in the coupled regime of a factor 4. The dashed lines represent an enhancement/suppression of 40%, which is shown for an easier comparison with the case with flavour coupling at N_1's washout, discussed below. From fig. 4.8(a) it can also be noticed that the number of red points is comparable with the number of blue points. This shows that strong thermal leptogenesis, when flavour coupling at N_2's decay is considered, is not harder to realise than in the uncoupled case. This can be explained by noticing that the flavour coupling in the two-flavoured regime does not modify significantly the strong thermal leptogenesis conditions found in the uncoupled case. As it can be seen from eq. (4.25), flavour coupling here adds the requirement

$$K_{2\tau_2^\perp} \gg 1, \tag{4.26}$$

in order to suppress the additional term proportional to $N^{\rm p,i}_{\Delta_{\tau_2^\perp}}$. Nevertheless, this is not particularly difficult to realise together with the conditions (3.70). A rough estimate of the bounds given by the two dotted lines can be obtained if the ratio of the two terms in eq. (4.21) is taken. We can consider the limit case $K_{2\tau_2^\perp}$, $K_{2\tau} \gg 1$ and the fact that the *CP* asymmetries are bounded from above $\varepsilon_{2\alpha} \lesssim 10^{-6} M_2/(10^{10}\,{\rm GeV})\sqrt{K_{2\alpha}/K_2}$ [123]. Considering $M_2 \simeq 5\times 10^{11}$ GeV and the strong thermal leptogenesis conditions, we obtain a value for this ratio ~ 3, in absolute value. The sign depends on the sign of $\varepsilon_{2\tau_2^\perp}$, which can be negative. Therefore, in the coupled regime, the final asymmetry given by $N^{\rm lep,f}_{\Delta_\tau}$ can be at most approximately four times larger (or smaller) than the uncoupled case.

We can now turn to study the dynamics in the three fully-flavoured regime. We shall first study flavour coupling *only* at N_1's washout, thus assuming $C^{(2)} = 1$. This way it will be possible to analyse separately the effects on the final asymmetry produced by flavour coupling in each regime. Finally, we will combine the two effects.

Both the produced and the pre-existing asymmetries undergo N_1's washout. In both cases, we have to solve eq. (3.49) with the coupling matrix $C^{(3)}$ in eq. (3.50). Since the treatment is the same for both the produced and the pre-existing asymmetry, we shall generally indicate with N_{Δ_α} the former as well as the latter.

The Boltzmann equations can be solved in an uncoupled, double-primed basis (e'', μ'', τ'') which is reached thanks to the unitary matrix V that diagonalises the matrix

$$P_1^0 \equiv \begin{pmatrix} P^0_{1e} & & \\ & P^0_{1\mu} & \\ & & P^0_{1\tau} \end{pmatrix} \cdot C^{(3)}, \tag{4.27}$$

as

$$V\, P_1^0\, V^{-1} = P^0_{1''} \equiv {\rm diag}\big(P^0_{1e''},\, P^0_{1\mu''},\, P^0_{1\tau''}\big)\,. \tag{4.28}$$

The final pre-existing asymmetry will have a general form given by [123]

$$N^{\rm f}_{\Delta_\alpha} = \sum_{\alpha''} V^{-1}_{\alpha\alpha''} e^{-\frac{3\pi}{8}K_{1\alpha''}} \left[\sum_\beta V_{\alpha''\beta} N_{\Delta_\beta}(T_{L2}) \right] , \tag{4.29}$$

where, as already mentioned, N_{Δ_α} stands for both the pre-existing and the produced asymmetries.

In order to obtain approximated expressions for the final asymmetries, and thus also for the entries of V and V^{-1}, it is convenient to directly consider here the conditions imposed by strong thermal leptogenesis in the uncoupled case. Indeed, in the flavour-coupled regime, the final asymmetry in each flavour will be composed of the terms already present in the uncoupled case, plus terms proportional to the asymmetries in the other flavours. Therefore, we can say that a necessary condition for successful strong thermal leptogenesis in the flavour-coupled case is given by the conditions obtained in the uncoupled one, eq. (3.70). Hence, we can perturbatively expand in the off diagonal terms of $C^{(3)}$ and in $\exp(-3\pi/8K_{1\delta})$, with $\delta = e, \mu$. Attention must be paid here as well to the degenerate cases that, given the conditions in eq. (3.70), can occur if $K_{1e} \simeq K_{1\mu}$. Barring these cases without loss of generality, we end with the set of equations for the final asymmetry

$$N^{\rm f}_{\Delta_e} \simeq N_{\Delta_e}(T') e^{-\frac{3\pi}{8}K_{1e}} - C^{(3)}_{e\tau} N_{\Delta_\tau}(T') e^{-\frac{3\pi}{8}K_{1\tau}} , \tag{4.30}$$

$$N^{\rm f}_{\Delta_\mu} \simeq N_{\Delta_\mu}(T') e^{-\frac{3\pi}{8}K_{1\mu}} - C^{(3)}_{\mu\tau} N_{\Delta_\tau}(T') e^{-\frac{3\pi}{8}K_{1\tau}} , \tag{4.31}$$

$$N^{\rm f}_{\Delta_\tau} \simeq N_{\Delta_\tau}(T') e^{-\frac{3\pi}{8}K_{1\tau}} - \left[C^{(3)}_{\tau e} \frac{K_{1\tau}}{K_{1e}} N_{\Delta_e}(T') + C^{(3)}_{\tau\mu} \frac{K_{1\tau}}{K_{1\mu}} N_{\Delta_\mu}(T') \right] e^{-\frac{3\pi}{8}K_{1\tau}} , \tag{4.32}$$

where $M_1 \lesssim T' \lesssim 5 \times 10^8\,{\rm GeV}$ as in the previous chapter, and, again, the N_{Δ_α}'s mean both the pre-existing and the produced asymmetries.

Since we are here considering flavour coupling only at N_1's washout, for the produced asymmetry, $N_{\Delta_e}(T')$ and $N_{\Delta_\mu}(T')$ are given by eqs. (3.46), (3.47) and (3.39), (3.40).

Always ignoring flavour coupling in the two fully-flavoured stage, for the pre-existing asymmetry we have ($\delta = e$, μ), as in the uncoupled regime

$$\begin{aligned} N^{\rm p}_{\Delta_\delta}(T') = \Bigg\{ & \left(1 - P^0_{p\tau}\right) \left[\frac{P^0_{2\delta}}{P^0_{2\tau_2^\perp}} P^0_{p\tau_2^\perp} e^{-\frac{3\pi}{8}K_{2\tau_2^\perp}} + \left(1 - \frac{P^0_{2\delta}}{P^0_{2\tau_2^\perp}}\right) \left(1 - P^0_{p\tau_2^\perp}\right) \right] \\ & + \Delta P_{p\delta} \Bigg\} N^{\rm p,i}_{B-L} , \end{aligned} \tag{4.33}$$

$$N^{\rm p}_{\Delta_\tau}(T') = \left(P^0_{p\tau} + \Delta P_{p\tau}\right) e^{-\frac{3\pi}{8}K_{2\tau}} N^{\rm p,i}_{B-L} . \tag{4.34}$$

It is interesting to notice that, given the strong thermal leptogenesis conditions eq. (3.70), the final asymmetry produced by leptogenesis in the flavour-coupled regime is [5]

$$N^{\rm lep,f}_{B-L} = \sum_\alpha N^{\rm lep,f}_{\Delta_\alpha} \simeq N_{\Delta_\tau}(T_{L2}) \left(1 - C^{(3)}_{e\tau} - C^{(3)}_{\mu\tau}\right) e^{-\frac{3\pi}{8}K_{1\tau}} . \tag{4.35}$$

Considering flavour coupling in the three fully-flavoured regime only, $N_{\Delta_\tau}(T_{L2})\, e^{-\frac{3\pi}{8}K_{1\tau}}$, with $N_{\Delta_\tau}(T_{L2})$ given by eq. (3.40), is the final asymmetry produced in the uncoupled case. We can immediately notice that, when flavour coupling at the washout only is taken into account, the final asymmetry produced is *reduced* by a factor $(-C^{(3)}_{e\tau} - C^{(3)}_{\mu\tau})$. This amounts to a reduction of around 40% with respect to the uncoupled case and can be seen in fig. 4.8(b). Here we plotted points realising successful strong thermal leptogenesis only in the uncoupled regime (blue dots) and points that realise successful strong thermal leptogenesis also when flavour coupling at N_1's washout is considered (red dots). In the generation of this plot we adopted the same procedure described for fig. 4.8(a). It is evident the reduction of the final asymmetry due to flavour coupling. Points tend to cluster around the dashed line that marks $\eta^{(c)}_B = (1 - C^{(3)}_{e\tau} - C^{(3)}_{\mu\tau})\eta^{(u)}_B$. At the same time, it is interesting to notice that here, unlike in the previous case, the red dots are fewer than the blue ones. This means that successful strong thermal leptogenesis with flavour coupling in the three fully-flavoured regime is much more difficult to realise than in the uncoupled regime. This can be understood by looking at eq. (4.32), where the contribution of $N_{\Delta_\delta}(T')$, $\delta = e, \mu$, must be suppressed by the power law $K_{1\tau}/K_{1\delta}$, and not exponentially as usual, thus forcing

$$K_{1\tau} \ll 1. \tag{4.36}$$

We can now turn to consider together both cases analysed so far.

In the fully-coupled regime, when both the flavour coupling in the two and in the three fully-flavoured regimes are considered, the final produced asymmetry is given by eqs. (4.30), (4.31) and (4.32) with $N_{\Delta_e}(T')$ and $N_{\Delta_\mu}(T')$ given by eqs. (3.46), (3.47) and (4.20), (4.21).

The final pre-existing asymmetry is always given by eqs. (4.30), (4.31) and (4.32), but now we have

$$N^{\rm p}_{\Delta_\delta}(T') = \frac{P^0_{2\delta}}{P^0_{2\tau_2^\perp}} N^{\rm p}_{\Delta_{\tau_2^\perp}}(T_{L2}) + \left[\left(1 - P^0_{p\tau}\right)\left(1 - \frac{P^0_{2\delta}}{P^0_{2\tau_2^\perp}}\right)\left(1 - P^0_{p\tau_2^\perp}\right) + \Delta P_{p\delta}\right] N^{\rm p,i}_{B-L}, \tag{4.37}$$

$$N^{\rm p}_{\Delta_\tau}(T') = N^{\rm p}_{\Delta_\tau}(T_{L2}), \tag{4.38}$$

where $N^{\rm p}_{\Delta_{\tau_2^\perp}}(T_{L2})$ and $N^{\rm p}_{\Delta_\tau}(T_{L2})$ are given by eqs. (4.24) and (4.25). The results in the fully-coupled regime are shown in fig. 4.9. Here the same conventions as for fig. 4.8 apply. As expected, the results in the fully-coupled case show the combination of the effects of the previous cases. From fig. 4.9 we can notice that the points show the spreading we found already in fig. 4.8(a) for the washout in the two fully-flavoured regime only, while at the same time they tend to cluster around $\eta^{(c)}_B = \left(1 - C^{(3)}_{e\tau} - C^{(3)}_{\mu\tau}\right)\eta^{(u)}_B$ as in fig. 4.8(b), where the flavour coupling at N_1's washout only was considered. We can

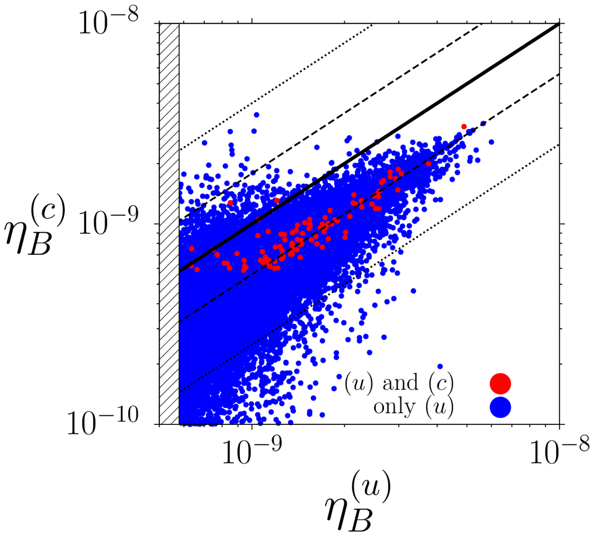

Figure 4.9: (a) Plot of the final baryon-to-photon ratio $\eta_B^{(c)}$ in fully-coupled strong thermal leptogenesis versus $\eta_B^{(u)}$, computed from the same setup, but in the uncoupled regime, [111]. In the fully-coupled regime flavour coupling is considered both at N_2's decay and at N_1's washout. The same setup and legend as in fig. 4.8 applies.

summarise the overall effect of flavour coupling by saying that coupling in the two-flavoured regime causes a spreading of the points around the line $\eta_B^{(c)} = \eta_B^{(u)}$, while the coupling in the three-flavoured regime translates downwards this line, reducing the final asymmetry produced by leptogenesis by a factor $\sim 40\%$.

A comparison between red and blue points shows that when successful strong thermal leptogenesis in the fully-coupled case is required, the dominant effect is given by the coupling at N_1's washout. Indeed, in fig. 4.9 we can see that the red points tend to cluster around $\eta_B^{(c)} = \left(1 - C_{e\tau}^{(3)} - C_{\mu\tau}^{(3)}\right) \eta_B^{(u)}$, as in fig. 4.8(b), and their number is much smaller than the number of blue points. The dominance of the coupling in the three-flavoured regime can be explained if we recall that, unlike the coupling in the two-fully flavoured regime, strong thermal leptogenesis with flavour coupling at N_1's washout requires the very stringent condition $K_{1\tau} \ll 1$, as discussed above, eq. (4.36). On the contrary, the condition $K_{2\tau_2^{\perp}} \gg 1$ imposed, as we have seen, by the coupling in the two-fully flavoured regime eq. (4.26), is easier to be realised and, together with eq. (3.70), forces the final asymmetry to be close to what is found with flavour coupling at N_1's washout alone. For this reason, it is a good approximation to neglect flavour coupling in the two fully-flavoured regime and consider only coupling in the three fully-flavoured one [5].

We can now comment on the changes that these effects imply on the lower bound $m_1^{\rm lb}$. In the derivation of the analytical bound, eq. (4.8), we employed $K_{1\tau} \simeq 0$. This is indeed the case we have described when flavour coupling at N_1's washout is considered, that

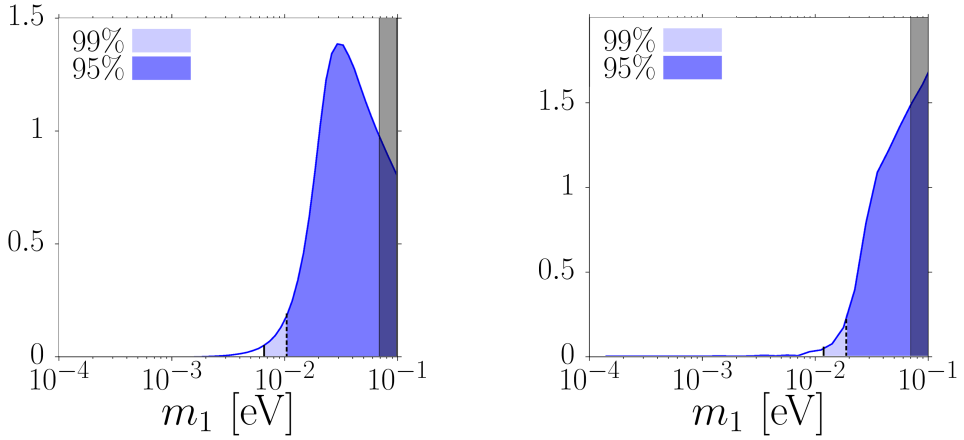

(a) (b)

Figure 4.10: Distribution of probability of m_1 for $M_\Omega = 2$ and $N^{\rm p,i}_{B-L} = 10^{-3}$, [111]. In the right column, flavour coupling is taken into account, while in the left column the uncoupled case is shown. NO case.

implies eq. (4.36). Therefore we can conclude that flavour coupling does not change the analytical lower bound in eq. (4.8).

Nonetheless, flavour coupling severely strengthen the condition on $K_{1\tau}$, that must now be very small. From the top-right panel in fig. 4.3, the $K_{1\tau}$ vs. m_1 scatter plot, we can see that low values of $K_{1\tau}$ can be obtained much more easily for high values of m_1, since this allows for cancellations in the formula of $K_{1\tau}$. It is possible to obtain quite a low $K_{1\tau}$ also for smaller values of m_1, as can be seen in the case of the red diamond corresponding to the saturation of the analytical lower bound, but this can happen, as already discussed, only at the expense of fine-tuning in the decay parameters and in the seesaw formula. For this reason, a good tool to understand the modifications caused by flavour coupling is again given by the distribution of the values of m_1. As an example, in fig. 4.10 we show the distributions of m_1 both in the uncoupled and in the coupled cases, for $M_\Omega = 2$ and $N^{\rm p,i}_{B-L} = 10^{-3}$. For simplicity, we have considered NO light neutrino spectrum. Here we can notice that the values of m_1 above which we have 95% and 99% of points are shifted towards higher values when flavour coupling is considered. In particular, for $N^{\rm p,i}_{B-L} = 10^{-3}$ we can notice that in the uncoupled case $m_1 > 11.8\,\rm meV$ for 95% of points, while in the coupled regime $m_1 > 18.8\,\rm meV$ for 95% of points. Similarly, in the uncoupled case we have $m_1 > 6.7\,\rm meV$ for 99% of points, while in the coupled one we get $m_1 > 11.1\,\rm meV$.

We can conclude that, as we could expect since the beginning of this detailed study, flavour coupling tends to tighten the bounds on m_1, pushing them towards higher values that are approximately a factor 2 larger than in the uncoupled case. As we have seen, this is explained by the need of strong thermal leptogenesis in the coupled regime for high values of m_1 that allow $K_{1\tau}$ to be very small.

4.4 Experimental implications of the lower bound

We have seen that the strong thermal leptogenesis conditions imply, for not too large values of M_Ω, a lower bound on m_1. In general, we have noticed a preference for rather high values of m_1 also for those cases (such as IO) in which the analytical lower bound was not present. In particular, referring to a standard case with $M_\Omega = 2$ we have $m_1 \gtrsim 10\,\mathrm{meV}$ for 99% of points in NO and $m_1 \gtrsim 3\,\mathrm{meV}$ for 99% of points in IO.

This conclusion can be regarded as quite robust, and we can speculate on the power of different experimental observations to test the strong thermal leptogenesis scenario by providing some results on the absolute neutrino mass scale. Clearly, the NO case can be more easily tested since it favours values of m_1 sufficiently large to produce sizeable deviations from the fully hierarchical case. Therefore, it is very important that in the next years neutrino experiments will be able to solve the ambiguity between NO and IO neutrino masses.

We shall discuss here the implication of the obtained lower bounds on some important experimental observations.

4.4.1 Cosmological observations

As mentioned in section 1.2.2.3, cosmological observations are sensitive to neutrino masses and are able to place an upper bound on their sum. Future observations could potentially reach a precision of $\delta(\sum_i m_i) \simeq 10\,\mathrm{meV}$ [150]. In the case of NO, assuming that experiments would be able to measure the hierarchical lower limit finding $\sum_i m_i = (60 \pm 10)\,\mathrm{meV}$, it would be possible to place a 2σ upper bound $m_1 \lesssim 10\,\mathrm{meV}$. From our results, this means that future cosmological observations will be potentially able to severely constrain strong thermal leptogenesis. On the other hand, a measurement $\sum_i m_i \gtrsim (95 \pm 10)\,\mathrm{meV}$ would correspond to $m_1 \gtrsim (20 \pm 5)\,\mathrm{meV}$, allowing to place a 2σ lower bound $m_1 \gtrsim 10\,\mathrm{meV}$. This would be in agreement with the expectations from strong thermal leptogenesis.

In the case of IO, expected values $m_1 \gtrsim 3\,\mathrm{meV}$ would correspond to measurements $\sum_i m_i \gtrsim (100 \pm 10)\,\mathrm{meV}$, generally not distinguishable from the inverted hierarchical limit. As already mentioned, this shows that NO would be a much more favourable option than IO for a significant test of strong thermal leptogenesis, since it more strongly favours detectable deviations from the hierarchical limit. It should be noticed that normally ordered neutrino masses with $m_1 \simeq 20\,\mathrm{meV}$ would also yield $\sum_i m_i \simeq 100\,\mathrm{meV}$ as for IO hierarchical neutrino masses ($m_1 \ll m_{\mathrm{sol}}$) thus providing another reason why it is important that neutrino oscillation experiments will be able to solve the NO-IO ambiguity independently of absolute neutrino mass experiments.

We can in any case notice that the cosmological observations, especially when combined, are becoming able to put more and more stringent upper bounds. We can mention, in particular the promising results obtained when the data from CMB anisotropies are combined with those from the Lyman-α forest. Combining Planck13 plus a low-l WMAP+Planck polarisation likelihood, the high-l likelihood from the Atacama Cosmology Telescope and the South Pole Telescope (SPT) ground-based experiments with the measurement of the BAO scale by the BOSS collaboration and the BOSS Lyman-α likelihood, it is possible to place an upper bound $\sum_i m_i < 140\,\mathrm{meV}$ at 95% C.L. [151]. Combining the BOSS Lyman-α likelihood with the full Planck mission polarisation likelihood, the upper bound is improved to $\sum_i m_i < 120\,\mathrm{meV}$ at 95% C.L. [152]. Considering the CMB data from Planck15, BAO and data from luminous red galaxies it is possible to tighten even more the upper bound to $\sum_i m_i < 110\,\mathrm{meV}$ at 95% C.L. [153]. It is interesting to notice that if cosmological observations become able to place an upper bound $\sum_i m_i < 100\,\mathrm{meV}$ at a reliable significance level, they would also be able to exclude the IO neutrino spectrum.

While these analyses are improving, but are still placing an upper bound which allows for the fully hierarchical limit, some results pointing at a non-vanishing absolute neutrino mass scale have already been published. We can mention, in particular, the results obtained by the Planck collaboration in 2013 when the Sunyaev-Zel'dovich effect [154] is taken into account. Adding the constraints imposed by the Sunyaev-Zel'dovich effect to the CMB and BAO data, the Planck collaboration obtained for the sum of the neutrino masses $\sum_i m_i = (0.22\pm0.09)\,\mathrm{eV}$ [155], thus pointing at nonzero m_1. More recently, combining CMB datasets with low-redshift growth of structure measurements from BOSS provided a tighter prediction on the sum of the neutrino masses $\sum_i m_i = (0.36\pm0.10)\,\mathrm{eV}$ at 3.4σ [156]. Though these results are susceptible of large improvements and modifications, they can be nonetheless regarded with some interests as an indication of a deviation of the light neutrino spectrum from the fully hierarchical limit, as favoured by strong thermal leptogenesis.

4.4.2 Neutrinoless double-beta decay

In fig. 4.11, we plotted the results of successful strong thermal leptogenesis on the $0\nu\beta\beta$ decay effective mass m_{ee}, eq. (1.39). The yellow points correspond to vanishing pre-existing initial abundance, i.e. strong thermal leptogenesis conditions not imposed. It can be seen that for NO the effective neutrino mass m_{ee} can be well below m_1 thanks to phase cancellations [157]. Imposing the 99% statistical lower bound on the absolute neutrino mass scale $m_1 \simeq 10\,\mathrm{meV}$, the effective neutrino mass falls around $m_1 \simeq 1\,\mathrm{meV}$, as indicated by the solid horizontal and vertical lines in fig. 4.11. This implies that strong thermal leptogenesis is not able to produce effective constraints on m_{ee}. Vice versa, a future measurement of $m_{ee} \gtrsim 10\,\mathrm{meV}$ would imply necessarily $m_1 \gtrsim 10\,\mathrm{meV}$, providing an interesting support to the strong thermal leptogenesis expectations.

Similarly, in the IO case, imposing the statistical lower bound on m_1 does not give any useful information on m_{ee}, since its corresponding value coincides with that obtained in the fully hierarchical limit.

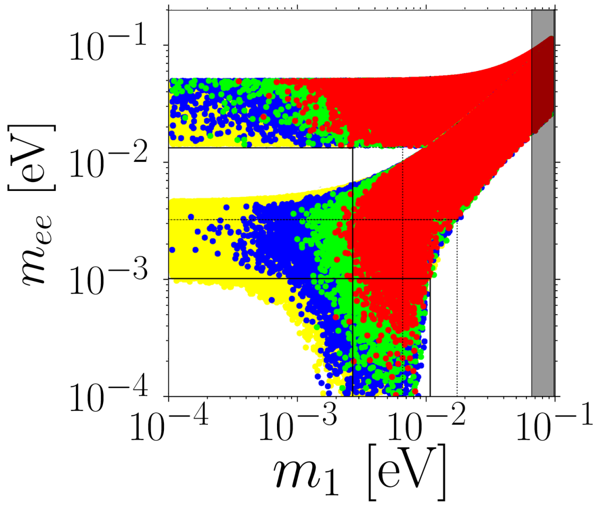

Figure 4.11: Scatter plot [1] of the neutrinos double-beta decay effective mass m_{ee} in strong thermal leptogenesis, for $M_\Omega = 2$ and $N_{B-L}^{\rm p,i} = 10^{-1}$, 10^{-2}, 10^{-3}, 0 respectively in red, green, blue and yellow. The solid and dashed vertical lines indicate the values of m_1 above which respectively 99% and 95% of the points are found.

4.4.3 Tritium beta decay

As mentioned in section 1.2.2.1, in case of absence of signal, the KATRIN experiment will be able to place an upper bound on the effective electron neutrino mass $m_\beta \lesssim 0.2\,\text{eV}$ [49]. This translates into a similar upper bound on m_1. Therefore, it will not be able to place severe constraints on strong thermal leptogenesis. In the PROJECT 8 experimental proposal [158], the energy of electrons emitted in tritium beta decay is determined from the frequency of cyclotron radiation and the upper bound could be improved to $m_\beta \lesssim 50\,\text{meV}$. This would translate again into a similar upper bound on m_1, providing a more stringent constraint. Nonetheless, this is still not able to severely corner strong thermal leptogenesis.

We can therefore conclude that the lower bounds imposed by strong thermal leptogenesis, in particular the more stringent statistical ones, are remarkably interesting in relation to forthcoming cosmological observations. This kind of experimental evidence results, at the moment, far more compelling than other neutrino mass experiments.

Chapter 5

$SO(10)$-inspired leptogenesis and neutrino parameters

In chapter 3, we mentioned that, in general, it is possible to resort to viable embeddings of the seesaw mechanism in larger theoretical frameworks. This is what is done when referring to $SO(10)$-*inspired leptogenesis*. We shall now consider this possibility by studying the constraints on the neutrino parameters originating from the $SO(10)$-inspired conditions, when imposing successful leptogenesis as well as the successful strong thermal leptogenesis.

In section 3.3 we introduced the two conditions that define $SO(10)$-inspired leptogenesis and derived analytical expressions for the quantities relevant to leptogenesis, within the assumption $V_L = 1$. We also showed that these analytical relations very well reproduce the numerical results, away from some special, fine-tuned regions called crossing level solutions. As already mentioned, we shall avoid these particular situations and deal with hierarchical, non-resonant leptogenesis.
We can now impose successful leptogenesis, and, later, successful strong thermal leptogenesis, on the $SO(10)$-inspired framework and see what constraints on the parameters arise. In this respect, we shall extend the results found in the hierarchical limit of the light neutrino masses [125, 159] to arbitrary values of m_1.

5.1 Successful leptogenesis condition

The final produced asymmetry should be calculated using eq. (3.51). However, from eq. (3.114) we noticed that, in the approximation $V_L = 1$, the tauon CP asymmetry is by far the dominant one and the inclusion of the washout at the production cannot change the τ-dominance as a contribution to the final $B-L$ asymmetry. We can therefore neglect the contribution of the other flavours and retain only the term proportional to

$\varepsilon_{2\tau}$ in eq. (3.51)

$$N_{B-L}^{\rm lep,f} \simeq \varepsilon_{2\tau}\,\kappa_f(K_{2\tau})\,e^{-\frac{3\pi}{8}K_{1\tau}}. \tag{5.1}$$

It should be stressed that this result holds in the $V_L = 1$ approximation. As we shall see later on, if we relax this approximation, a μ-dominated solution appears for $m_1 \gtrsim 10\,\text{meV}$ [159, 160]. For the time being, we shall assume $V_L = 1$ and stick to the approximation eq. (5.1). Using the explicit expressions eqs. (3.108), (3.94) and (3.116), we are now able to express the final $B-L$ asymmetry in $SO(10)$-inspired models in terms of the α_i and the neutrino parameters.

We can specialise eq. (3.113) to the case $\alpha = \tau$, obtaining

$$\varepsilon_{2\tau} \simeq \frac{3M_2}{16\pi v^2}\,\frac{m_{D3}^2}{m_{D3}^2\,|U_{R32}|^2 + m_{D2}^2}\,\frac{1}{\left|(m_\nu^{-1})_{\tau\tau}\right|}\,\mathrm{Im}\big\{(U_{R32}^\star\,U_{R33})^2\big\}\,. \tag{5.2}$$

Using the expressions of U_R and M_2, we get

$$\varepsilon_{2\tau} \simeq \frac{3}{16\,\pi}\,\frac{\alpha_2^2\,m_c^2}{v^2}\,\frac{|m_{\nu ee}|\left(\left|(m_\nu^{-1})_{\tau\tau}\right|^2 + \left|(m_\nu^{-1})_{\mu\tau}\right|^2\right)^{-1}}{m_1\,m_2\,m_3}\,\frac{\left|(m_\nu^{-1})_{\mu\tau}\right|^2}{\left|(m_\nu^{-1})_{\tau\tau}\right|^2}\,\sin\alpha_L, \tag{5.3}$$

where α_L is the effective $SO(10)$-inspired leptogenesis phase, in the approximation $V_L = 1$. It is given by

$$\alpha_L \equiv 2\,\mathrm{Arg}\big[(m_\nu^{-1})_{\tau\tau}\big] - 2\,\mathrm{Arg}\big[(m_\nu^{-1})_{\mu\tau}\big] + \phi_2 - \phi_3. \tag{5.4}$$

From eqs. (3.88) and (3.109) we have

$$\phi_2 - \phi_3 = \mathrm{Arg}[m_{\nu ee}] - 2\,\mathrm{Arg}\big[(m_\nu^{-1})_{\tau\tau}\big] + \pi - 2(\rho+\sigma), \tag{5.5}$$

so that we obtain

$$\alpha_L = \mathrm{Arg}[m_{\nu ee}] - 2\,\mathrm{Arg}\big[(m_\nu^{-1})_{\mu\tau}\big] + \pi - 2(\rho+\sigma). \tag{5.6}$$

We can also obtain analytical expressions of $K_{2\tau}$ and $K_{1\tau}$. From eq. (3.116) we get

$$K_{2\tau} \simeq \frac{m_{D3}^2}{m_\star M_2}\,|U_{R32}|^2 \simeq \frac{m_1\,m_2\,m_3}{m_\star}\,\frac{\left|(m_\nu^{-1})_{\mu\tau}\right|^2}{|m_{\nu ee}|\,\left|(m_\nu^{-1})_{\tau\tau}\right|}, \tag{5.7}$$

and

$$K_{1\tau} \simeq \frac{m_{D3}^2}{m_\star M_1}\,|U_{R31}|^2 \simeq \frac{|m_{\nu e\tau}|^2}{m_\star\,|m_{\nu ee}|}. \tag{5.8}$$

From this equation and using eq. (3.91), we can obtain an explicit expression in terms of the mixing angles and phases that will prove useful

$$
\begin{aligned}
K_{1\tau} &\simeq \frac{\left|m_1 U_{e1} U_{\tau 1} + m_2 U_{e2} U_{\tau 2} + m_3 U_{e3} U_{\tau 3}\right|^2}{m_* \left|m_1 U_{e1}^2 + m_2 U_{e2}^2 + m_3 U_{e3}^2\right|} \\
&= \frac{\left|c_{13} c_{12} s_{12} s_{23} (m_1 e^{2i\rho} - m_2) + s_{13} c_{13} c_{23} \left(m_3\, e^{i(2\sigma-\delta)} - m_2\, s_{12}^2 e^{i\delta} - m_1\, c_{12}^2 e^{i(2\rho+\delta)}\right)\right|^2}{m_* \left|m_1\, c_{12}^2 c_{13}^2 e^{2i\rho} + m_2\, s_{12}^2 c_{13}^2 + m_3\, s_{13}^2 e^{2i(\sigma-\delta)}\right|} .
\end{aligned}
\tag{5.9}
$$

Putting everything together we can find an explicit expression for the final $B-L$ asymmetry[1] [2]

$$
\begin{aligned}
N_{B-L}^{\mathrm{lep,f}} \simeq\ & \frac{3}{16\pi} \frac{\alpha_2^2 m_c^2}{v^2} \frac{|m_{\nu ee}| \left(\left|(m_\nu^{-1})_{\tau\tau}\right|^2 + \left|(m_\nu^{-1})_{\mu\tau}\right|^2\right)^{-1}}{m_1\, m_2\, m_3} \frac{\left|(m_\nu^{-1})_{\mu\tau}\right|^2}{\left|(m_\nu^{-1})_{\tau\tau}\right|^2} \sin\alpha_L \\
& \times \kappa_f \left(\frac{m_1\, m_2\, m_3}{m_*} \frac{\left|(m_\nu^{-1})_{\mu\tau}\right|^2}{|m_{\nu ee}|\left|(m_\nu^{-1})_{\tau\tau}\right|}\right) \\
& \times \exp\left(-\frac{3\pi}{8} \frac{|m_{\nu e\tau}|^2}{m_* \, |m_{\nu ee}|}\right) .
\end{aligned}
\tag{5.10}
$$

It is interesting to notice that in this expression the asymmetry does not depend on α_1 and α_3 [125]. The only left non-observable parameter is α_2, which, however, given eq. (3.81), cannot be in any case too large. This shows the power of the $SO(10)$-inspired conditions to severely restrict the set of free parameters. The final asymmetry is indeed

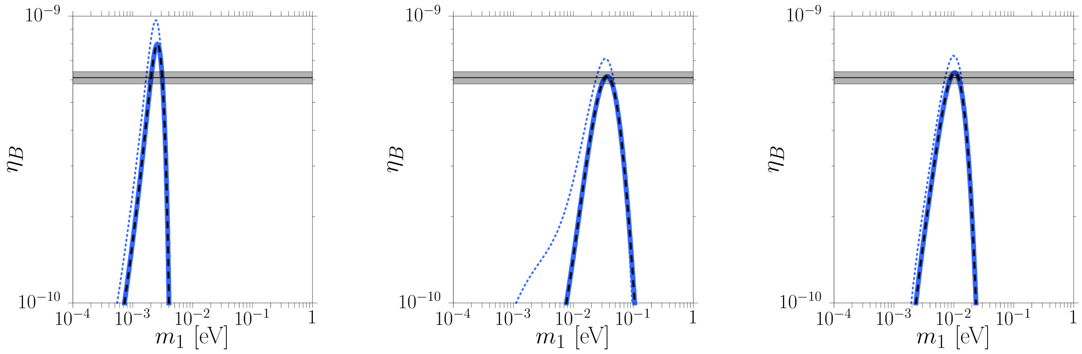

Figure 5.1: Plots of the final η_B for the same three sets of parameters of figs. 3.3 and 3.4, [2]. The numerical results (blue solid lines) are compared with the analytical results (black dashed lines) obtained using eq. (5.10). The dotted lines are obtained for $V_L \neq 1$. From left to right, we have $\theta_{12}^L = (0.79°, 4.1°, 0.1°)$, $\theta_{13}^L = (0, 0.05°, 0.07°)$, $\theta_{23}^L = (2.3°, 2.3°, 2.3°)$, $\delta_L/\pi = (0.2, 0.63, 1.22)$, $\rho_L/\pi = (1.65, 0.85, 0.79)$ and $\sigma_L/\pi = (1.05, 1.1, 0.94)$. The shaded band marks the 3σ interval around the experimental measure, eq. (1.11).

---

[1] Here we correct a typo in [3], where, instead of $\left|(m_\nu^{-1})_{\mu\tau}\right|^2 / \left|(m_\nu^{-1})_{\tau\tau}\right|^2$ there is, incorrectly, its inverse.

strictly linked to the low-energy neutrino parameters, which are constrained to lie on a hypersurface determined by the only theoretical parameter left, α_2.

Moreover, we can also notice that the effective $0\nu\beta\beta$ decay mass $m_{ee} \equiv |m_{\nu ee}|$ plays a direct role in eq. (5.10) and, as we shall see, the successful leptogenesis condition will be able to interestingly constrain it.

In fig. 5.1 we have plotted η_B vs. m_1 for the same three sets of parameters of figs. 3.3 and 3.4, comparing the numerical results (blue solid lines) with the analytical results (black dashed lines) obtained from eq. (5.10). We can see that the analytical results perfectly match the numerical ones.

We also made a more general comparison between the constraints derived from the analytical expression eq. (5.10) and the numerical constraints (for $V_L = 1$). In fig. 5.2 we show, with orange points, the results of a scatter plot for $V_L = 1$ imposing successful $SO(10)$-inspired leptogenesis for $\alpha_2 = 5$. The asymmetry is computed from eq. (3.51), in which the heavy neutrino masses and mixing matrix U_R are calculated numerically. The mixing angles are randomly extracted according to a uniform distribution over the following ranges

$$0 \leq \theta_{13} \leq 11.5^\circ, \qquad 35^\circ \leq \theta_{23} \leq 52^\circ, \qquad 31.3^\circ \leq \theta_{12} \leq 36.3^\circ. \tag{5.11}$$

The phases are uniformly extracted over their full variability ranges as

$$\delta \in [-\pi,\, \pi), \qquad \sigma, \rho \in [0,\, 2\pi). \tag{5.12}$$

The value of the next-to-lightest neutrino mass is imposed to be $M_2 < 5 \times 10^{11}$ GeV in order to ensure the production in the two fully-flavoured regime and avoid the transition region. Moreover, in the numerical simulation we fixed

$$\alpha_1 = \alpha_3 = 1, \tag{5.13}$$

even though, as already mentioned, these parameters do not play a role in the determination of the final produced asymmetry, eq. (5.10). In general, the results in fig. 5.2 confirm those obtained in [125, 159], but here a much larger (about thousand times) amount of points was obtained and the constraints are much sharper.

For comparison with fig. 5.2, we have produced the corresponding scatter plots using directly the analytical expression for the final asymmetry, eq. (5.10). The results are shown in fig. 5.3. We can notice that they perfectly reproduce the numerical results given by the orange points in fig. 5.2. We can then conclude that eq. (5.10) provides a very precise analytical way to calculate the final asymmetry in $SO(10)$-inspired models when $V_L = 1$ and crossing level solutions are avoided. Indeed it can be reliably applied in all models where $SO(10)$-inspired conditions hold, in order impose the successful leptogenesis condition using directly input on the low-energy neutrino parameters. In these cases, the only additional parameter that has to be introduced is α_2.

Once established that eq. (5.10) precisely reproduces the final leptogenesis asymmetry

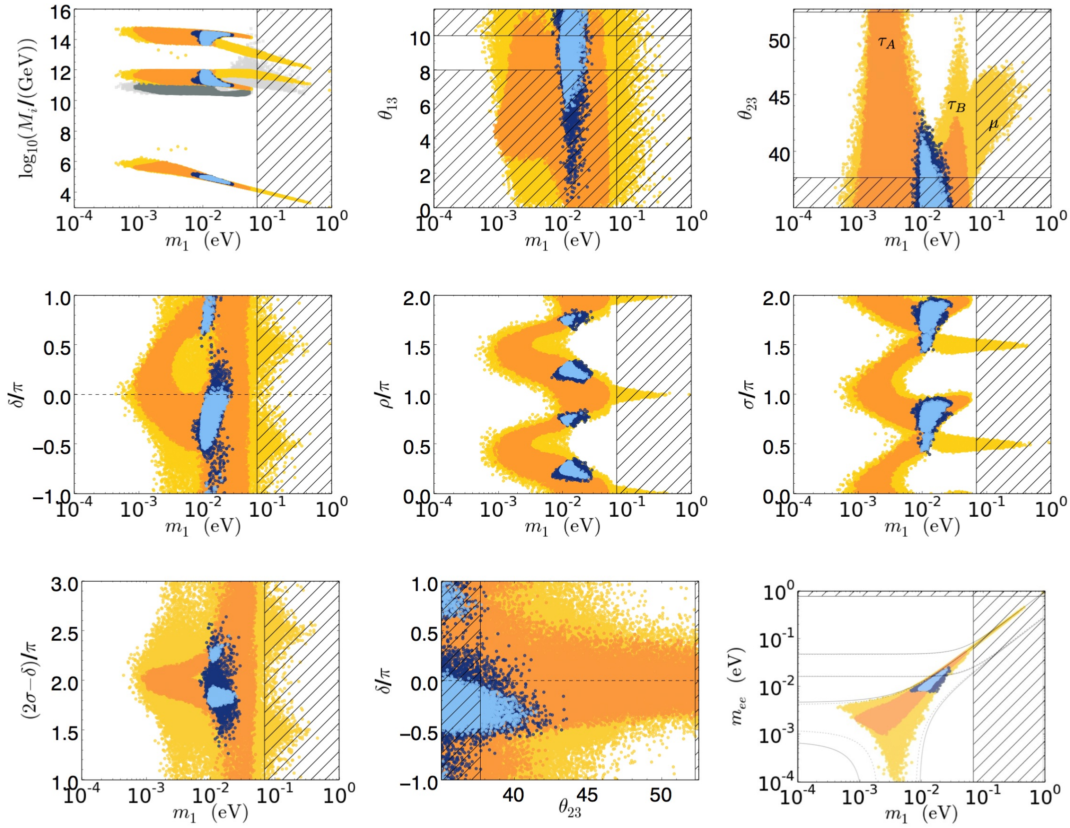

Figure 5.2: Scatter plots [2] in the neutrino parameter space projected on different selected planes for NO and $\alpha_2 = 5$. We imposed the bound $M_2 < 5 \times 10^{11}$ GeV. The orange points respect the successful leptogenesis condition $\eta_B^{\text{lep,f}} > \eta_B^{\text{CMB}} > 5.9 \times 10^{-10}$ for $V_L = 1$ where $\eta_B^{\text{lep,f}}$ is calculated from eq. (3.51) using a numerical determination of heavy neutrino masses, U_R matrix, mixing matrix and phases. The mixing angles vary within the ranges eq. (5.11). The blue points are those respecting the additional successful strong thermal leptogenesis condition for $V_L = 1$ (light blue) or for $1 \leq V_L \leq V_{CKM}$ (dark blue). The vertical hatched regions mark the cosmological upper bound on of m_1, eq. (1.43), in all panels except for the bottom-central one, where the 3σ experimental lower bound on θ_{23} is showed (see tab. 1.1). In the top-central panel the horizontal hatched regions mark the experimentally excluded values of θ_{13} at 3σ. In the bottom-right panel the horizontal hatched region marks the values of m_{ee} excluded by $0\nu\beta\beta$ experiments, while the dashed (solid) black lines indicate the generally allowed bands, both for NO and IO, for θ_{13} in the range in eq. (5.11).

for $V_L = 1$, we can proceed further and safely employ eq. (5.10) to derive analytical constraints on the neutrino parameters, when successful leptogenesis is imposed.

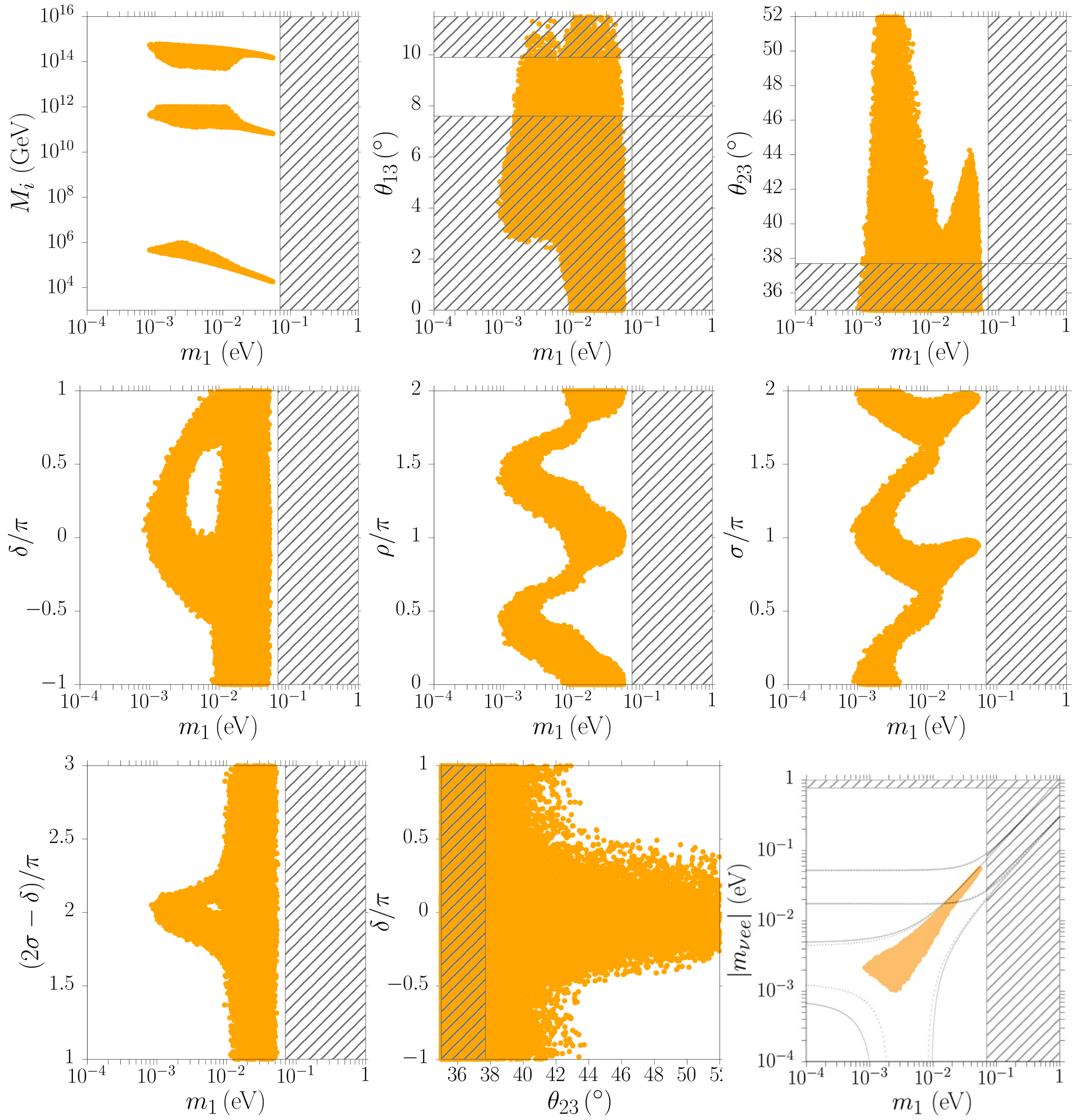

Figure 5.3: Scatter plots [2] in the neutrino parameter space projected on different selected planes for NO and $\alpha_2 = 5$, respecting the successful leptogenesis condition $\eta_B^{\rm lep} > \eta_B^{\rm CMB} > 5.9\times10^{-10}$ and obtained from the analytical expression eq. (5.10) for the final asymmetry. Same ranges and conventions as in fig. 5.2 are adopted. These analytical results should be compared with the numerical results of fig. 5.2 (orange points).

5.1.1 Lower bound on m_1

Using eq. (5.10), we can calculate the final asymmetry in the limit $m_1 \to 0$ showing that this tends to vanish. Therefore, successful $SO(10)$-inspired leptogenesis implies a lower bound on the absolute neutrino mass scale. It is convenient to start from the expression of $K_{1\tau}$, eq. (5.9). In the limit $m_1/m_{\rm sol} \to 0$ we have

$$K_{1\tau} \simeq \frac{\left|m_{\rm atm}\, s_{13}c_{13}c_{23}e^{i(2\sigma-\delta)} - m_{\rm sol}\, c_{13}s_{12}c_{12}s_{23}\right|^2}{m_\star \left|m_{\rm sol}\, s_{12}^2c_{13}^2 + m_{\rm atm}\, s_{13}^2 e^{2i(\sigma-\delta)}\right|}, \tag{5.14}$$

and we can notice that the condition $K_{1\tau} \lesssim 1$ can be realised for $2\sigma - \delta \simeq 2n\pi$ and

$$s_{13} \gtrsim \frac{m_{\rm sol}}{m_{\rm atm}} s_{12} c_{12} \tan\theta_{23} \gtrsim 0.06. \tag{5.15}$$

This implies a lower bound on θ_{13} given by

$$\theta_{13} \gtrsim 3^\circ \qquad m_1/m_{\rm sol} \to 0, \tag{5.16}$$

confirmed by the scatter plots in [125] and by the top-central panel of figs. 5.2 and 5.3. The asymptotic limit of $K_{2\tau}$ can be obtained from eq. (5.7) giving

$$K_{2\tau} \simeq \frac{c_{23}^2 m_{\rm atm}}{m_*} \simeq 25, \tag{5.17}$$

thus showing that, in the low m_1 limit, the washout at the production is strong. We can therefore employ the simple approximation (see eq. (2.169))

$$\kappa_f(K_{2\tau}) \simeq \frac{0.5}{K_{2\tau}^{1.2}} \simeq 0.01, \tag{5.18}$$

for the final efficiency factor.

We can now turn to the $m_1 \to 0$ limit of the *CP* asymmetry $\varepsilon_{2\tau}$. From eq. (5.3) we have

$$\begin{aligned}\varepsilon_{2\tau} &\simeq \frac{3}{16\pi}\frac{\alpha_2^2 m_c^2}{v^2}\frac{m_1}{m_{\rm sol}\,m_{\rm atm}}\frac{\left|m_{\rm sol}\,U_{e2}^2 + m_{\rm atm}\,U_{e3}^2\right| |U_{\mu 1}|^2}{|U_{\tau 1}|^4\left(|U_{\tau 1}|^2 + |U_{\mu 1}|^2\right)}\sin\alpha_L \\ &\simeq \frac{3}{16\pi}\frac{\alpha_2^2 m_c^2}{v^2}\frac{m_1}{m_{\rm sol}\,m_{\rm atm}}\frac{\left|m_{\rm sol}\,s_{12}^2 c_{13}^2 + m_{\rm atm}\,s_{13}^2 e^{2i(\sigma-\delta)}\right| c_{23}^2}{s_{12}^4 s_{23}^4}\sin\alpha_L, \end{aligned}\tag{5.19}$$

and the asymptotic limit of the effective leptogenesis phase is given by

$$\alpha_L \simeq 2(\rho - \sigma), \qquad m_1/m_{\rm sol} \to 0. \tag{5.20}$$

The expression for $\varepsilon_{2\tau}$ is maximised for $\sigma - \delta \simeq n\pi$ and for $\sin\alpha_L = 1$, so that

$$\varepsilon_{2\tau} \lesssim \frac{75}{16\pi}\frac{m_c^2}{v^2}\left(\frac{\alpha_2}{5}\right)^2 \frac{m_1}{m_{\rm atm}}\frac{c_{23}^2}{s_{12}^2 s_{23}^4}\left(1 + \frac{m_{\rm atm}\,s_{13}^2}{m_{\rm sol}\,s_{12}^2}\right). \tag{5.21}$$

Combining all these expressions together, we find that, in the limit $m_1 \to 0$, the baryon-to-photon ratio is maximised by

$$\begin{aligned}\eta_B^{\rm lep,f} < \eta_B^{\max} &\simeq m_1\left(\frac{\alpha_2}{5}\right)^2 10^{-4}\frac{75}{16\pi}\frac{m_c^2}{v^2}\frac{c_{23}^2}{m_{\rm atm}\,s_{12}^2 s_{23}^4}\left(1 + \frac{m_{\rm atm}\,s_{13}^2}{m_{\rm sol}\,s_{12}^2}\right) \\ &\equiv m_1\left(\frac{\alpha_2}{5}\right)^2 f(\theta_{12},\theta_{13},\theta_{23}). \end{aligned}\tag{5.22}$$

If we now impose the successful leptogenesis condition $\eta_B^{\max} \gtrsim \eta_B^{\rm CMB}$, we obtain a lower bound on the absolute neutrino mass scale

$$m_1 \gtrsim m_1^{\min} \equiv \frac{6 \times 10^{-10}}{f(\theta_{12},\theta_{13},\theta_{23})} \left(\frac{5}{\alpha_2}\right)^2 \gtrsim 0.8\,{\rm meV} \left(\frac{5}{\alpha_2}\right)^2 , \tag{5.23}$$

where the last step is obtained for the values of the mixing angles, within the ranges in eq. (5.11), that maximise $f(\theta_{12},\theta_{12},\theta_{23})$. This result is in very good agreement with the scatter plots in figs. 5.2 and 5.3.

Eventually, we can also notice that the three conditions for maximal asymmetry on the phases, i.e. $2\sigma - \delta \simeq 2m\pi$, $\sigma - \delta \simeq n\pi$ and $\sin[2(\rho-\sigma)] \simeq 1$ with $n, m \in \mathbb{Z}$, imply that, always for $m_1/m_{\rm sol} \to 0$, we have

$$\sigma \simeq k\pi, \qquad \delta \simeq 2l\,\pi, \qquad \text{with} \quad k, l \in \mathbb{Z}. \tag{5.24}$$

This is confirmed by the scatter plots in the two panels of figs. 5.2 and 5.3 for σ and δ vs. m_1.

One also finds $\rho = \pi/4 + q\,\pi$, with $q \in \mathbb{Z}$. However, from the scatter plots it can be noticed that at small m_1 the value of ρ is actually $\rho \simeq 0.35\,\pi + q\,\pi$. The reason for this shift can be understood from the complete expression of $K_{1\tau}$ in eq. (5.9). For $\rho = \pi/2$ the term $m_1\,e^{2i\pi\rho} = -m_1$ adds to the term $-m_2$ in a way that $K_{1\tau} \lesssim 1$ for slightly lower values of s_{23}. However, because of the strong dependence $\varepsilon_{2\tau} \propto s_{23}^{-4}$, a shift of ρ towards $\pi/2$ maximises the asymmetry even though the phase α_L is not maximal. This interplay results in an intermediate solution $\rho \simeq 0.35\,\pi \pm q\,\pi$.

5.1.2 Upper bound on m_1

As can be seen from figs. 5.2 and 5.3, together with a lower bound on m_1, there is also an upper bound. We can work in the quasi-degenerate neutrino limit $m_1 \simeq m_2 \simeq m_3$ and then check whether the upper bound does indeed fall in this regime. We can obtain the expressions of the quantities relevant to the final asymmetry, i.e. $\varepsilon_{2\tau}$, $K_{2\tau}$ and $K_{1\tau}$, in the quasi-degenerate limit.

Starting from $K_{1\tau}$, from eq. (5.9) for $\rho = n\pi$ we have

$$K_{1\tau} \simeq s_{13} c_{23}^2 \frac{m_1}{m_*} \left| e^{i(2\sigma-\delta)} - s_{12}^2 - c_{12}^2 e^{i\delta} \right|^2 \lesssim 0.015 \frac{m_1}{m_*} \left| e^{i(2\sigma-\delta)} - s_{12}^2 - c_{12}^2 e^{i\delta} \right|^2 , \tag{5.25}$$

so that for $m_1 \lesssim 0.1\,$eV we always have $K_{1\tau} \lesssim 4$. The maximum is obtained for $\sigma = 2m\pi$ and $\delta = \pi/2 + k\pi$. Hence, $K_{1\tau}$ is never too large and, in general, it can always be made vanish.

Always taking $\rho = n\pi$, we can compute the limit of $\varepsilon_{2\tau}$. To this aim, we can separately study the behaviour of the m_ν and (m_ν^{-1}) entries, neglecting all the subdominant terms

$\propto s_{13}^2$. This way, the dependence on δ cancels out. In the quasi degenerate limit we have

$$m_{ee} \equiv |m_{\nu ee}| \simeq m_1, \tag{5.26}$$

as can be seen from bottom-right panel of figs. 5.2 and 5.3. Moreover, we have

$$\left|(m_\nu^{-1})_{\tau\tau}\right|^2 \simeq \frac{1}{m_1^2}\left|s_{23}^2 + c_{23}^2 e^{-2i\sigma}\right|^2, \tag{5.27}$$

$$\left|(m_\nu^{-1})_{\mu\tau}\right|^2 \simeq \frac{s_{23}^2 c_{23}^2}{m_1^2}\left|e^{-2i\sigma} - 1\right|^2. \tag{5.28}$$

Using these results, from eq. (5.3) we get the quasi degenerate limit of $\varepsilon_{2\tau}$

$$\varepsilon_{2\tau} \simeq \frac{3}{16\pi}\frac{\alpha_2^2 m_c^2}{v^2}\frac{\left|e^{-2i\sigma}-1\right|^2}{\left|s_{23}^2 + c_{23}^2 e^{-2i\sigma}\right|^2}\frac{s_{23}^2 c_{23}^2}{\left|s_{23}^2 + c_{23}^2 e^{-2i\sigma}\right|^2 + s_{23}^2 c_{23}^2\left|e^{-2i\sigma}-1\right|^2}\sin\alpha_L, \tag{5.29}$$

where the asymptotic limit of α_L is given by $\alpha_L \simeq -4\sigma$.
Finally, from eq. (5.7) we get

$$K_{2\tau} \simeq \frac{m_1}{m_*}\frac{s_{23}^2 c_{23}^2\left|e^{-2i\sigma}-1\right|^2}{\left|s_{23}^2 + c_{23}^2 e^{-2i\sigma}\right|}. \tag{5.30}$$

We can now obtain the expression of the baryon-to-photon ratio in the quasi-degenerate limit. Approximating the efficiency factor as $\kappa_f(K_{2\tau}) \simeq (1 + 2K_{2\tau}^{1.2})^{-1}$, we have

$$\begin{aligned}\eta_B^{\rm lep,f} \simeq{}& 0.01\frac{3}{16\pi}\frac{\alpha_2^2 m_c^2}{v^2}\frac{\left|e^{-2i\sigma}-1\right|^2}{\left|s_{23}^2 + c_{23}^2 e^{-2i\sigma}\right|^2}\frac{s_{23}^2 c_{23}^2}{\left|s_{23}^2 + c_{23}^2 e^{-2i\sigma}\right|^2 + s_{23}^2 c_{23}^2\left|e^{-2i\sigma}-1\right|^2}\\ &\times\frac{\sin\alpha_L}{1+2K_{2\tau}^{1.2}}e^{-\frac{3\pi}{8}K_{1\tau}},\end{aligned} \tag{5.31}$$

where we always have $\rho = n\pi$, so that $K_{1\tau} \lesssim 1$. We can notice that the asymptotic limit mainly depends on σ, since ρ is fixed and the dependence on δ is very weak and negligible. We can therefore assume that $K_{2\tau}$ is minimised by $2\sigma \simeq 2n\pi$, so that, simply using $\sin\alpha_L \lesssim 1$, we have that $\eta_B^{\rm lep,f}$ is maximised by

$$\eta_B^{\rm lep,f} \lesssim \eta_B^{\rm max} \equiv 0.01\frac{3}{16\pi}\frac{\alpha_2^2 m_c^2}{v^2}\frac{x}{1+2\left(\frac{m_1}{m_*}\right)^{1.2}x^{1.2}} \lesssim \frac{0.01}{192\pi}\frac{\alpha_2^2 m_c^2}{v^2}\frac{m_*}{m_1}, \tag{5.32}$$

where

$$x \equiv s_{23}^2 c_{23}^2\left|e^{-2i\sigma}-1\right|^2. \tag{5.33}$$

Eq. (5.32) is maximised for

$$x = 2.5^{1.2}\frac{m_*}{m_1}, \tag{5.34}$$

which indeed implies $\sigma \simeq n\pi$ as guessed. Imposing successful leptogenesis $\eta_B^{\rm max} \gtrsim \eta_B^{\rm CMB}$ we obtain the upper bound

$$m_1 \lesssim m_1^{\rm max} \equiv m_\star \frac{2.5^{1.2} \times 10^8}{192\pi} \frac{\alpha_2^2 m_c^2}{v^2} \lesssim 52\,{\rm meV}. \tag{5.35}$$

This very well reproduces the result from the scatter plots in figs. 5.2 and 5.3. In the top-left panel of fig. 5.4 a scatter plot of $K_{2\tau}$ vs. m_1 (orange points) confirms that for $m_1 \gtrsim 10\,{\rm meV}$ the value of $K_{2\tau}$ becomes smaller and smaller for growing m_1, in order to minimise the washout at the production that would suppress the asymmetry. The upper bound on m_1 is saturated for an analytical minimum value of $K_{2\tau} \simeq 2.5$ well in agreement with the numerical result.

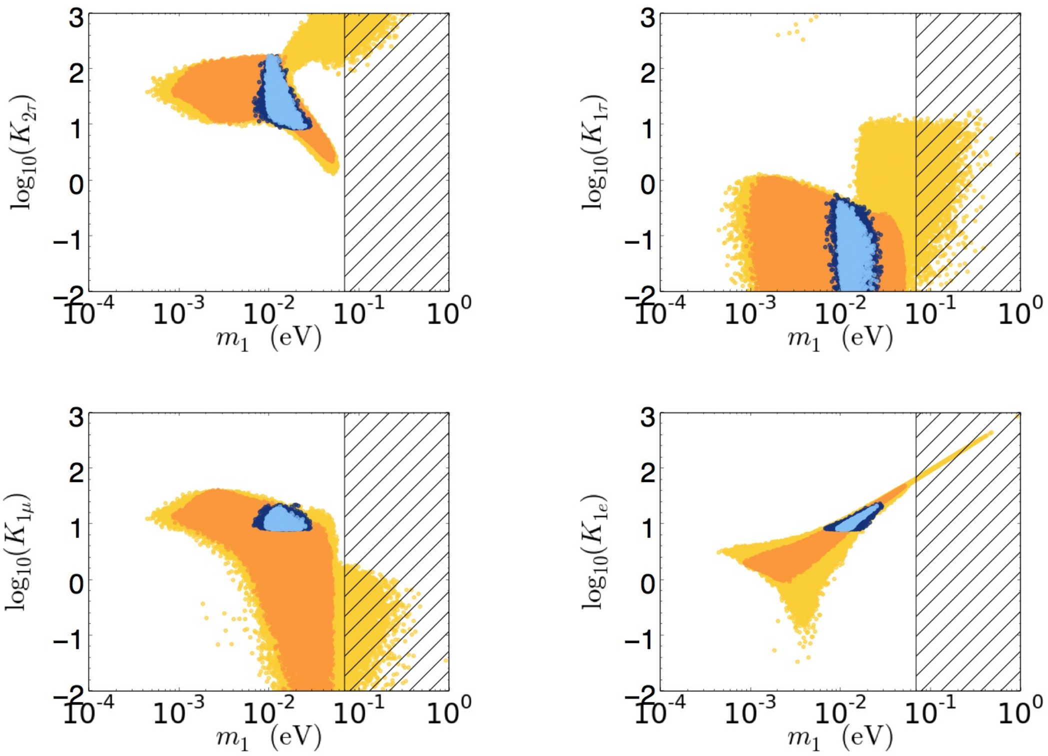

Figure 5.4: Scatter plots [2] for the four flavoured decay parameters $K_{2\tau}$, $K_{1\tau}$, $K_{1\mu}$, K_{1e} vs. m_1. The colour code is the same as in fig. 5.2.

5.1.3 τ_A solution: $m_1 \lesssim m_{\rm sol}$

We can now study the behaviour for intermediate values of m_1, between the lower and the upper bound. From this point of view, as we shall see, the value of $m_{\rm sol} \simeq 10\,{\rm meV}$ will represent a sort of border between two different solutions, the so-called τ_A and τ_B.

It is clear that the labels of these two different solutions emphasise the fact that the final asymmetry is dominantly produced in the τ-flavour. These two kinds of solutions, anyways, are not precisely distinct, but there is an overlap around $m_1 \simeq 10\,\text{meV}$. This distinction will be useful when we will discuss the strong thermal leptogenesis solution in the next section. We shall start considering values $m_1 \lesssim m_{\rm sol}$.

In the case of low values of $m_1 \lesssim m_{\rm sol}$, imposing $K_{1\tau} \lesssim 1$ has an important consequence on the atmospheric mixing angle. Indeed, from eq. (5.14), taking into account the dominant term $\propto m_1 e^{2\,i\,\rho}$, that was previously discarded, and approximating $\rho \simeq \pi/2$, we obtain the upper bound

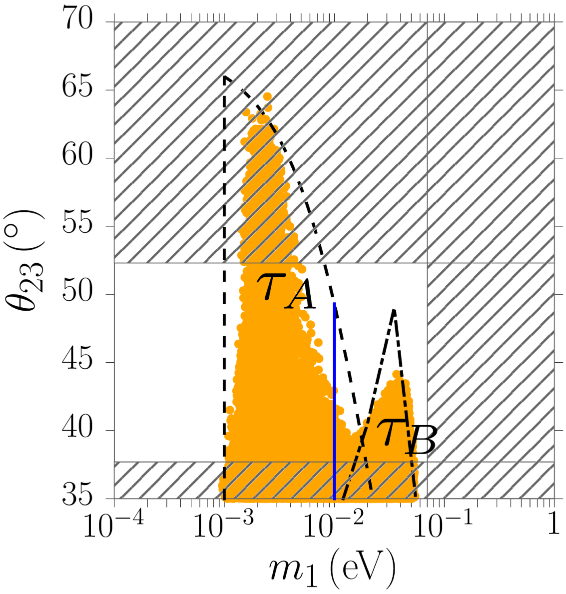

Figure 5.5: Scatter plot [2] in the plane $m_1 - \theta_{23}$ obtained imposing successful leptogenesis with the asymmetry calculated from the analytical expression eq. (5.10). Here we have $35^\circ \lesssim \theta_{23} \lesssim 70^\circ$ uniformly distributed. The dashed lines indicate the lower bound on m_1 eq. (5.23) and the upper bound on θ_{23} at low m_1 eq. (5.36). The dot-dashed lines indicate the upper bound on m_1 eq. (5.35) and the upper bound on θ_{23} at high m_1. The solid line is the lower bound on m_1 from the strong thermal leptogenesis condition for $N_{B-L}^{\rm p,i} = 10^{-3}$, eq. (5.48).

$$\theta_{23} \lesssim \arctan\left(\frac{m_{\rm atm} - m_{\rm sol}\,s_{12}^2}{m_{\rm sol} + m_1}\,\frac{s_{13}}{c_{12}s_{12}}\right) \lesssim 65^\circ, \tag{5.36}$$

where the maximum value in the last step is obtained in the hierarchical limit. In fig. 5.5 we show the results of a specific scatter plot obtained from the analytical expression in eq. (5.10), with $V_L = 1$, in the plane $m_1 - \theta_{23}$. The mixing angles are extracted as previously specified, but here we have $35^\circ \lesssim \theta_{23} \lesssim 70^\circ$, uniformly distributed. It can be seen that the analytical upper bound eq. (5.36), given by the dashed line, well reproduces the numerical result.

It is interesting to study the link between the values of the mixing phases δ, ρ, σ and the final produced asymmetry, in particular its sign.
We have seen that for $m_1 \ll m_{\rm sol}$ we have to impose $2\sigma - \delta \simeq 2m\pi$ to minimise $K_{1\tau}$, $\sigma - \delta \simeq n\pi$ to maximise the *CP* asymmetry, while the effective leptogenesis phase is given by $\alpha_L \simeq 2(\rho - \sigma)$. In order to maximise, in magnitude, $\sin\alpha_L$ we have

$$\sin\alpha_L = \pm 1 \quad \Longrightarrow \quad \rho = \frac{\pi}{4} + q\pi, \quad \vee \quad \rho = \frac{3\pi}{4} + q\pi. \tag{5.37}$$

Since the sign of the asymmetry is determined by the sign of $\sin\alpha_L$, the second possibility must be discarded because, even though maximal, it would give a negative final asymmetry. Therefore, the sign of the asymmetry selects $\rho \simeq \pi/4 + q\pi$. However, as already mentioned, for low m_1 we actually have $\rho \simeq 0.35\pi + q\pi$. This is originated by a compromise that maximises the *CP* asymmetry ($\rho \to \pi/2$) and minimises $K_{1\tau}$ ($\rho \to \pi/4$) at the same time.
When m_1 increases, we can understand the values taken by the phases by looking at eq. (5.9). For growing m_1, the first term in the numerator $\propto m_1 e^{2i\rho}$ becomes non negligible. Since, as said, we have $\rho \neq \pi/2$, this term gives an imaginary part that must be cancelled out in order to keep $K_{1\tau}$ sufficiently small. At low m_1, since $\theta_{13} \neq 0$, this imaginary part is cancelled by the term $\propto m_3\, e^{i(2\sigma-\delta)}$, with $2\sigma - \delta < 0$. For larger values of m_1 we must have the cancellation $m_1\, e^{2i\rho} - m_2 \simeq 0$ in the first term, therefore ρ has necessarily to tend to $\rho \simeq n\pi$. There are two possibilities: either $\rho > \pi/2$ and so $2\sigma - \delta > 0$, or $\rho < \pi/2$ with $2\sigma - \delta < 0$. The latter solution is the dominant case, since at very low m_1 we already have $\rho \simeq 0.35\pi < \pi/2$ with small $K_{1\tau}$ and maximal leptogenesis phase. The other solution is forbidden for small m_1, due to the sign of the asymmetry, as said before, and exists only for intermediate values of m_1, though being very subdominant, since α_L cannot be maximised.
In order to better show these results in the scatter plots, we produced new plots constraining the reactor mixing angle in the current 3σ experimental range, fig. 5.6. In the top-left panel we show the ρ vs. m_1 scatter plot. We can notice that, due to the more restricted θ_{13} range, many points disappear compared to the corresponding plot in figs. 5.2 and fig. 5.3. The behaviour is then much cleaner. At the lower bound $m_1 \simeq 1\,{\rm meV}$ we can see that indeed $\rho \simeq 0.35\,\pi$. For increasing values of m_1 there are two branches for ρ: in a first "high" branch the value of ρ increases to π, while in a second "low" branch it decreases to 0, where the two branches actually merge because of the π periodicity. It is clearly noticeable that the low branch dominates, since it corresponds to values of ρ that produce the correct sign of the asymmetry and to maximal leptogenesis phase already at minimum m_1 values. The high-ρ branch is suppressed since it corresponds to non-maximal α_L values.
In the top-right panel we show the $2\sigma - \delta$ scatter plot. This clearly shows that the

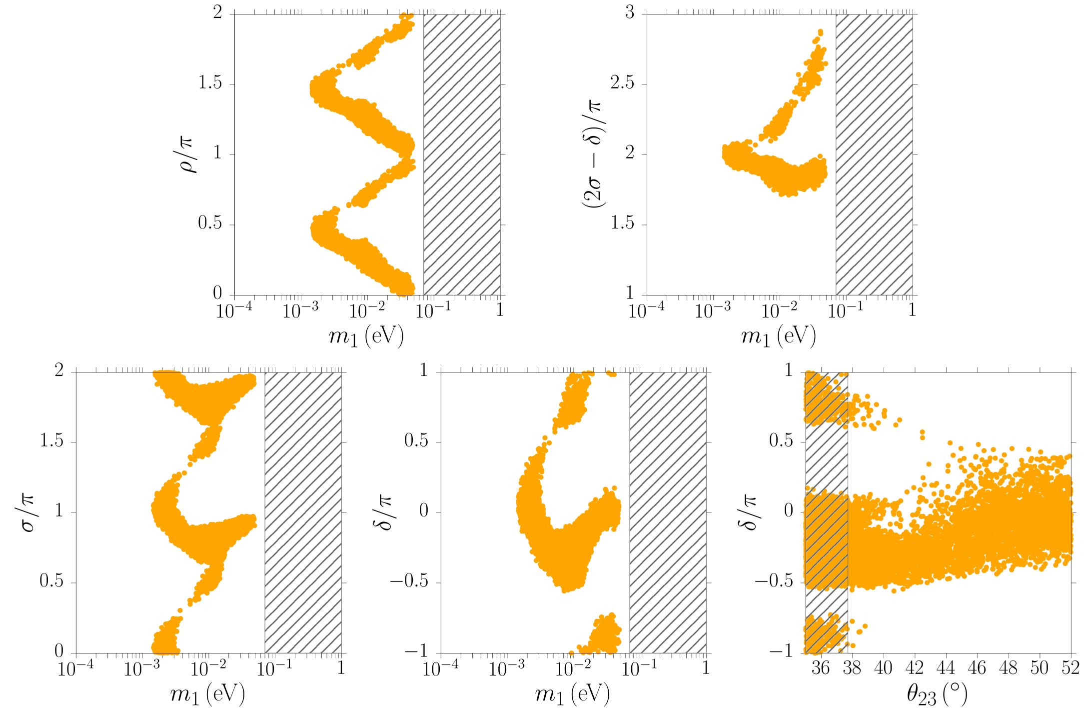

Figure 5.6: Scatter plots [2] of points satisfying successful leptogenesis generated using the analytical expression eq. (5.10) for the final asymmetry. The mixing angle θ_{13} is uniformly randomly generated within the $3\,\sigma$ allowed experimental range. Panels should be compared with the corresponding ones in fig. 5.3, in particular the last one for δ vs. θ_{23}.

low-ρ branch corresponds to dominant $2\sigma-\delta$ values below $2n\pi$, while the high-ρ branch corresponds to sub-dominant $2\sigma-\delta$ values larger than $2n\pi$.

From these results, we can also obtain the corresponding values of σ. In the bottom-left panel of fig. 5.6 we show σ vs. m_1. Since $\alpha_L \simeq 2(\rho-\sigma)$ for $m_1 \ll m_{\rm sol}$, the subdominant $\rho > \pi/2$ values branch corresponds to a sub-dominant σ branch $\sigma > n\pi$. The dominant low-ρ values branch corresponds to a dominant $\sigma < n\pi$ branch.

Finally, combining the results on σ with the results on $2\sigma-\delta$, we can deduce the behaviour of δ. For the dominant low-ρ values branch, corresponding to a dominant $\sigma < n\pi$ values branch and values of $2\sigma-\delta \lesssim 2m\pi$ we can conclude that δ shifts towards negative values. Vice versa, for the sub-dominant high-ρ values branch, corresponding to $2\sigma-\delta > 2n\pi$ and $\sigma > n\pi$, we have positive δ values. These results are shown in the bottom-right panel. Here we can see the clear dominance of values of δ in the fourth quadrant. This conclusion is supported by the scatter plot of δ vs. θ_{23}, showing that actually positive values of δ are even more constrained if one imposes the current 3σ lower bound $\theta_{23} \gtrsim 38^\circ$. This result shows that within $SO(10)$-inspired leptogenesis the sign of the asymmetry yields asymmetric constraints between positive and negative $\sin\delta$ values, favouring $\delta < 0$. We must, nevertheless, remind that this discussion is valid when $V_L = 1$. Relaxing this assumption will also relax this link.

5.1.4 τ_B solution: $m_1 \gtrsim m_{\rm sol}$

For $m_1 \gtrsim m_{\rm sol}$ and given the upper bound eq. (5.35), we can approximate $m_1 \simeq m_2$ and $m_3 \simeq m_{\rm atm}$, so that eq. (5.9) can be rewritten as

$$K_{1\tau} \simeq \frac{\left|c_{13}c_{12}s_{12}s_{23}\, m_1\big(e^{2i\rho}-1\big) + s_{13}c_{13}c_{23}\, e^{i\delta}\big[m_{\rm atm}\, e^{i2(\sigma-\delta)} - m_1\left(s_{12}^2 + c_{12}^2\, e^{2i\rho}\right)\big]\right|^2}{m_*\left|m_1\, c_{13}^2\left(c_{12}^2 e^{2i\rho} + s_{12}^2\right) + m_{\rm atm}\, s_{13}^2 e^{2i(\sigma-\delta)}\right|}. \tag{5.38}$$

It is clear that if $s_{13}=0$, having $\rho = n\pi$ gives $K_{1\tau}=0$. However, with the experimental value $s_{13}\simeq 0.15$ we need a non-vanishing first term in the numerator in order to cancel the second one. The exact value of ρ depends on the value of m_1. The value of δ must then be able to cancel the imaginary part of $e^{2i\rho}$ while, at the same time, being such to keep $\sigma-\delta\simeq n\pi$, in order to maximise m_{ee} in $\varepsilon_{2\tau}$. Moreover, since $\alpha_L \simeq -4\,\sigma$, σ has to be negative, which also leads to negative values of δ and hence favours positive values of ρ. This is confirmed by the first panel of fig. (5.6) showing a scatter plot of ρ vs. m_1 with θ_{13} in its experimental 3σ range. It can be seen that now, compared to the analogous plot of fig. 5.3, where $0 \leq \theta_{13} \leq 11.54^\circ$, we have $\rho = n\pi$ only when m_1 saturates its upper bound. Indeed, in this case the first term in the numerator of eq. (5.38) vanishes, while, since $m_1 \simeq m_{\rm atm}$, we have a sizeable cancellation within the second one. We can anyway set $\rho = n\pi$ even for $m_1 \simeq m_{\rm sol} \ll m_{\rm atm}$ and take $\sigma-\delta = n\pi$ in order to maximise $|m_{\nu ee}|$ in $\varepsilon_{2\tau}$, obtaining

$$K_{1\tau} \lesssim \frac{s_{13}^2 c_{23}^2\,(m_{\rm atm}-m_1)^2}{m_*\, m_{\rm atm}\big(1+s_{13}^2\big)} \simeq 2. \tag{5.39}$$

Considering the *CP* asymmetry, we can still approximate $|m_{\nu ee}| \simeq m_1$, but now we have

$$\left|(m_\nu^{-1})_{\tau\tau}\right| \simeq \frac{1}{m_1}\left|s_{23}^2 + \frac{m_1}{m_3}c_{23}^2\right|, \tag{5.40}$$

$$\left|(m_\nu^{-1})_{\mu\tau}\right| \simeq \frac{s_{23}c_{23}}{m_1}\left|1-\frac{m_1}{m_3}\right|, \tag{5.41}$$

where $\sigma \simeq n\pi$. With these expressions we obtain again that $\eta_B^{\rm lep,f} \propto s_{23}^4$, which implies a strong suppression of the final asymmetry for increasing s_{23}. This originates a tight upper bound on θ_{23} for $m_1 \gtrsim m_{\rm sol}$. We also have $\eta_B^{\rm lep,f} \propto m_1/m_3$. This implies that the upper bound on θ_{23} gets relaxed at higher values of m_1, reaching a maximum at $m_1 \simeq 35\,{\rm meV}$. For higher values of m_1 the term $\left|(m_\nu^{-1})_{\mu\tau}\right| \propto 1 - m_1/m_3$ suppresses the asymmetry.

For intermediate values of m_1 and for the τ_B region we also have

$$K_{2\tau} \simeq \frac{m_3}{m_*}\frac{s_{23}^2 c_{23}^2\,(1-m_1/m_3)^2}{s_{23}^2 + c_{23}^2\, m_1/m_3}. \tag{5.42}$$

Combining together all these results, and imposing the successful leptogenesis condition, we can find an implicit expression for the upper bound of s_{23} vs. m_1. In fig. 5.5 we have plotted with the dot-dashed line the result. As we can see, it overestimates the allowed region, a consequence of the crude approximations used for the phases. In any case, these results well explain the existence of an upper bound on θ_{23} also for values $m_1 \gtrsim m_{\rm sol}$ and how this gets relaxed for increasing values of m_1 up to a peak value that is reached for $m_1 \simeq 35\,{\rm meV}$. For values $m_1 \gtrsim 35\,{\rm meV}$ the upper bound on θ_{23} vs m_1 becomes more stringent and $\theta_{23}^{\rm max} \to 0$ when $m_1 \to m_1^{\rm max}$, given by eq. (5.35).

It should be noticed that the regions for the τ_A and for the τ_B solutions overlap to some extent for $m_1 \simeq 10\,{\rm meV}$. This is not contradictory since they are realised for different values of the phases, in particular in the case of the τ_A solution we have $\rho \simeq \pi/2$ for $m_1 \simeq 0$, while for the τ_B solution one has $\rho \simeq \pi$ for $m_1 \simeq m_1^{\rm max}$.

5.2 Strong thermal leptogenesis condition

We can now impose the successful strong thermal leptogenesis condition on our $SO(10)$-inspired model and derive analytical expressions for the features already discussed in [160]. However, we shall consider here always $V_L = 1$.

We have already seen that in $SO(10)$-inspired models, with $V_L = 1$, the final asymmetry is dominantly produced in the τ flavour and that $K_{1\tau} \lesssim 1$. This is perfectly in line with what is required by strong thermal leptogenesis, therefore we only have to impose the conditions eq. (3.70) on $K_{2\tau}$, K_{1e} and $K_{1\mu}$

5.2.1 Ruling out the τ_B solution

From eq. (5.42), in the τ_B case, we can check that for $m_1 \simeq m_{\rm sol}$ we have $K_{2\tau} \simeq 13$. Using eq. (3.64), we can conclude that this would be sufficient to wash out a pre-existing asymmetry as large as about 10^{-2}. Starting from eq. (3.116) for $K_{i\alpha}$ and using eq. (3.90) and $|U_{R11}| \simeq 1$ as in eq. (3.108), one immediately obtains, in general and therefore also for τ_B solutions

$$K_{1e} \simeq \frac{m_{ee}}{m_*} \simeq \frac{m_1}{m_*}, \tag{5.43}$$

where, as we have already discussed, the last approximation can be accepted both in the low and high m_1 regimes. This is sufficient to wash out electronic pre-existing asymmetries as large as 10^{-3} for $m_1 \gtrsim 10\,{\rm meV}$ and even larger if m_1 increases. However, considering $K_{1\mu}$, in the τ_B case we have

$$K_{1\mu} \simeq \frac{m_{\rm atm}^2}{m_*} \frac{s_{13}^2 s_{23}^2}{\left|m_1 + s_{13}^2\, m_{\rm atm}\right|} \lesssim 4. \tag{5.44}$$

As we can see, $K_{1\mu}$ is then too small to provide an efficient washout of a sizeable pre-existing asymmetry in the μ flavour, therefore successful strong thermal leptogenesis cannot be realised by τ_B solutions. This confirms in a general analytical way the numerical examples shown in [125, 159, 160]. For this reason, from now on we shall focus on the τ_A solutions.

5.2.2 Lower bounds on m_{ee} and m_1

From eq. (5.43), the requirement $K_{1e} \gtrsim K_{\rm st}(N_{\Delta_e}^{\rm p,i})$ translates into a constraint over the $0\nu\beta\beta$ decay effective mass m_{ee}. Using the expression eq. (3.64) we immediately have

$$m_{ee} \gtrsim 8\,{\rm meV}\left(1+0.095\ln\left|\frac{N_{\Delta_e}^{\rm p,i}}{1.5\times10^{-4}}\right|\right). \tag{5.45}$$

This is rather interesting since it predicts that, despite neutrino masses are NO, next generation $0\nu\beta\beta$ experiments, such as MAJORANA and GERDA as mentioned in section 1.2.2.2, should be able to find a signal.

Using eq. (3.91), we can better approximate m_{ee} as

$$m_{ee} = \left|m_1\, c_{12}^2 c_{13}^2 e^{2i\rho} + m_2\, s_{12}^2 c_{13}^2 + m_3\, s_{13}^2 e^{2i(\sigma-\delta)}\right| \simeq m_1 \left|c_{12}^2 e^{2i\rho} + s_{12}^2\right|, \tag{5.46}$$

where, already assuming $m_1 \simeq m_{\rm sol}$, we have approximated $m_1 \simeq m_2$ and neglected the term $\propto m_3 s_{13}^2$. Considering that in the τ_A solution we have $\pi/4 \lesssim \rho \lesssim \pi/2$ (plus π periodicity), we can choose $\rho = \pi/4$, that corresponds to lower values of m_1. This way

$$\frac{m_{ee}}{m_1} \simeq \sqrt{c_{12}^4 + s_{12}^4} \simeq 0.75. \tag{5.47}$$

From this result and eq. (5.45) we obtain

$$m_1 \gtrsim 10\,{\rm meV}\left(1+0.095{\rm ln}\left|\frac{N_{\Delta_e}^{\rm p,i}}{1.5\times10^{-4}}\right|\right). \tag{5.48}$$

This is perfectly in line with the general feature of strong thermal leptogenesis for NO, that we analysed in the previous chapter. As seen, it is the washout of the electronic pre-existing asymmetry that imply a lower bound on m_1, eq. (4.8). When $SO(10)$-inspired conditions are also considered, this lower bound becomes more stringent, yielding eq. (5.48). This result totally agrees with the numerical simulations in fig. 5.2, where the successful strong thermal leptogenesis solutions for $V_L = 1$ are represented by light blue points. The lower bound on m_1 obtained by successful strong thermal leptogenesis for $N_{\Delta_e}^{\rm p,i} = 10^{-3}$ is also shown in fig. 5.5 by the solid blue line.

5.2.3 Atmospheric mixing angle and upper bounds on m_{ee} and m_1

The lower bound on m_1 given by successful strong thermal leptogenesis, eq. (5.48), can be used to further constrain the atmospheric mixing angle. Plugging eq. (5.48) in eq. (5.36), we obtain that, for $N_{\Delta_e}^{\rm p,i} = 10^{-3}$, the atmospheric mixing angle is $\theta_{23} \lesssim 40°$. This is well in agreement with the numerical results in the top-right panel of fig. 5.2 (light blue points). Successful strong thermal leptogenesis therefore remarkably requires θ_{23} to lie in the first octant.
Since eq. (5.42) is valid also for intermediate values of m_1, we can impose $K_{2\tau} \gtrsim K_{\rm st}(N_{\Delta_\tau}^{\rm p,i})$. Plugging the minimum experimental value of $\theta_{23} \simeq 35°$, we can obtain an upper bound $m_1 \lesssim 20\,{\rm meV}$. This in turn implies an upper bound on m_{ee} given by $m_{ee} \lesssim 0.8\, m_1 \lesssim 16\,{\rm meV}$, which is in fair agreement with the results in fig. 5.2.

5.2.4 Lower bound on the reactor mixing angle

From eq. (3.116), we can obtain an expression of $K_{1\mu}$ valid for intermediate values of m_1

$$K_{1\mu} \simeq \frac{c_{13}^2 \left| s_{12} c_{12} c_{23}\, m_1 (1 - e^{2i\rho}) + m_3\, s_{13} s_{23} \right|^2}{m_* \left| m_1 + m_3 s_{13}^2 \right|}, \tag{5.49}$$

where we used $m_1 \simeq m_2$, $2\sigma - \delta \simeq 2n\pi$ and we retained the terms $\propto m_3\, s_{13}$ and $\propto m_3\, s_{13}^2$. For $s_{13}^2 = 0$ the strong thermal leptogenesis condition $K_{1\mu} \gtrsim K_{\rm st}(N_{\Delta_\mu}^{\rm p,i} \simeq 10^{-3})$ would imply $m_1 \gtrsim 30\,{\rm meV}$, which contradicts the upper bound $m_1 \lesssim 20\,{\rm meV}$. However, for non vanishing values of the reactor mixing angle this incompatibility can be overcome. Indeed, for $s_{13}^2 \gtrsim 0.1$, that is $\theta_{13} \gtrsim 5°$, we can have $K_{1\mu} \gtrsim 10$ and $m_1 \lesssim 20\,{\rm meV}$ at the same time. This confirms the result obtained in [160], that successful strong thermal leptogenesis predicts a non vanishing reactor mixing angle, as now firmly established by neutrino oscillation experiments.

5.2.5 Dirac phase

While discussing the τ_A solution, we noticed that the Dirac phase δ preferably takes negative values. The Dirac phase was linked to σ by the condition $2\sigma - \delta < 0$ that suppresses $K_{1\tau}$ when θ_{13} is non vanishing. The more stringent lower bound on θ_{13} imposed by strong thermal leptogenesis strengthens the preference for negative values of δ. This is well shown in the bottom-right panel in fig. 5.6, where θ_{13} lies in its 3σ experimental range, tab. 1.1. It is also possible to notice that for $38° < \theta_{23} \lesssim 42°$ the phase δ is basically constrained in the fourth quadrant. This is indeed the situation realised in strong thermal leptogenesis, where, as seen, we have the upper bound $\theta_{23} < 40°$. Therefore, by constraining the atmospheric mixing angle between its 3σ experimental lower bound $\theta_{23} > 38°$ and the upper bound imposed by strong thermal leptogenesis $\theta_{23} \lesssim 40°$, we obtain that the Dirac phase δ lies necessarily in the fourth quadrant, i.e. $-\pi/2 \lesssim \delta \lesssim 0$. This can be clearly seen in the bottom-central panel of fig. 5.2, where the highest value $\theta_{23} \simeq 41^\circ$ is obtained for $\delta \simeq -\pi/3$ (light blue points). The constraint of δ in the fourth quadrant is particularly interesting in light of the experimental hint at $\sin\delta < 0$. More precisely, the $SO(10)$-inspired strong thermal leptogenesis solution implies $\sin\delta < 0$ and $\cos\delta > 0$.

5.3 Inverted ordering

We shall now study $SO(10)$-inspired leptogenesis in case the light neutrino masses follow the IO spectrum. As in the previous discussion, we shall first analyse the results obtained by imposing the successful leptogenesis condition and later consider strong thermal leptogenesis.

The analytical expression of the final $B-L$ asymmetry, eq. (5.10) is valid in the IO case as well, if we employ the correct expressions of m_2, and the IO mixing matrix $U^{\rm IO}$, eq. (1.29). In fig. 5.7 we repeated the scatter plots made in fig. 5.3 for the NO case. The analytical expressions for IO are able to reproduce the numerical results of [159] for $V_L = 1$. In particular, we can notice that IO is only marginally allowed, since it requires a very narrow range of values $20\,\mathrm{meV} \lesssim m_1 \lesssim 40\,\mathrm{meV}$. Moreover, from the top-right panel of fig. 5.7, we clearly have now a lower bound on the atmospheric mixing angle $\theta_{23} \gtrsim 48^\circ$, that falls in the second octant. For $V_L = 1$, values $\alpha_2 \lesssim 4.5$ are not allowed. From eq. (3.116), we can compute $K_{1\tau}$ and using now $m_2 \simeq m_3$ we get that it is minimised for $\rho = n\pi$ with

$$K_{1\tau} \gtrsim \frac{m_1^2\, s_{13}^2 c_{23}^2}{m_* m_2}. \tag{5.50}$$

Imposing $K_{1\tau} \lesssim 1$ we have the upper bound

$$m_1 \lesssim 0.1\,\mathrm{eV}\,\frac{0.01}{s_{13}^2 c_{23}^2}. \tag{5.51}$$

We can also obtain

$$K_{2\tau} \simeq \frac{m_3}{m_*} s_{23}^2, \tag{5.52}$$

so that again we can employ the strong washout approximation $\kappa_f(K_{2\tau}) \simeq 0.5 K_{2\tau}^{-1.2}$ for the efficiency factor.

Considering the CP asymmetry $\varepsilon_{2\tau}$, in the approximation $m_2 \simeq m_3 \simeq m_{\rm atm}$, $m_1 \ll m_{\rm atm}$ and taking $\rho = n\pi$ we have

$$m_{ee} \simeq m_2, \tag{5.53}$$

$$\left|(m_\nu^{-1})_{\tau\tau}\right| \simeq \frac{c_{23}^2}{m_1}, \tag{5.54}$$

$$\left|(m_\nu^{-1})_{\mu\tau}\right| \simeq \frac{s_{23} c_{23}}{m_1}. \tag{5.55}$$

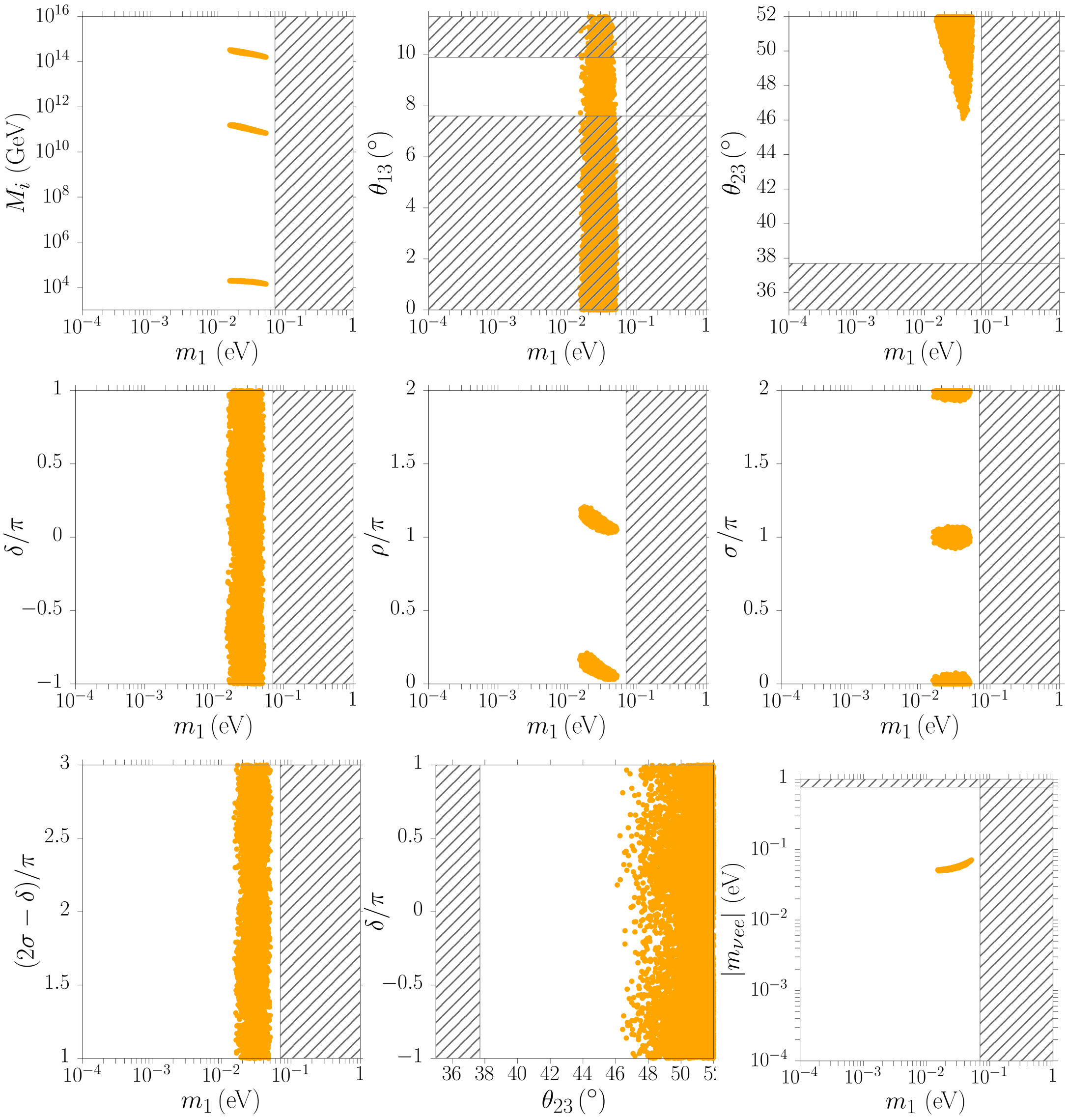

Figure 5.7: Scatter plots [2] in the neutrino parameter space projected on different selected planes for IO and $\alpha_2 = 5$, respecting the successful leptogenesis condition $\eta_B^{\rm lep} > \eta_B^{\rm CMB} > 5.9\times 10^{-10}$ and obtained from the analytical expression eq. (5.10) for the final asymmetry. Same ranges and conventions as in fig. 5.3 are adopted.

This way we obtain

$$\varepsilon_{2\tau} \simeq \frac{3}{16\pi}\,\frac{\alpha_2^2 m_c^2}{v^2}\,\frac{s_{23}^2}{c_{23}^4}\,\frac{m_1}{m_{\rm atm}}\,\sin\alpha_L\,. \tag{5.56}$$

With respect to the effective leptogenesis phase, here we have

$$\alpha_L \simeq 2\rho - {\rm Arg}\big[c_{12}^2 e^{2i\rho} + s_{12}^2\big]\,. \tag{5.57}$$

Hence, for $\rho = n\pi$ the *CP* asymmetry would vanish. Therefore, we must have a small positive displacement from $\rho = n\pi$, so that the upper bound eq. (5.51) actually becomes more stringent. The shift from $\rho = n\pi$ is clearly visible in the central panel of fig. 5.7.

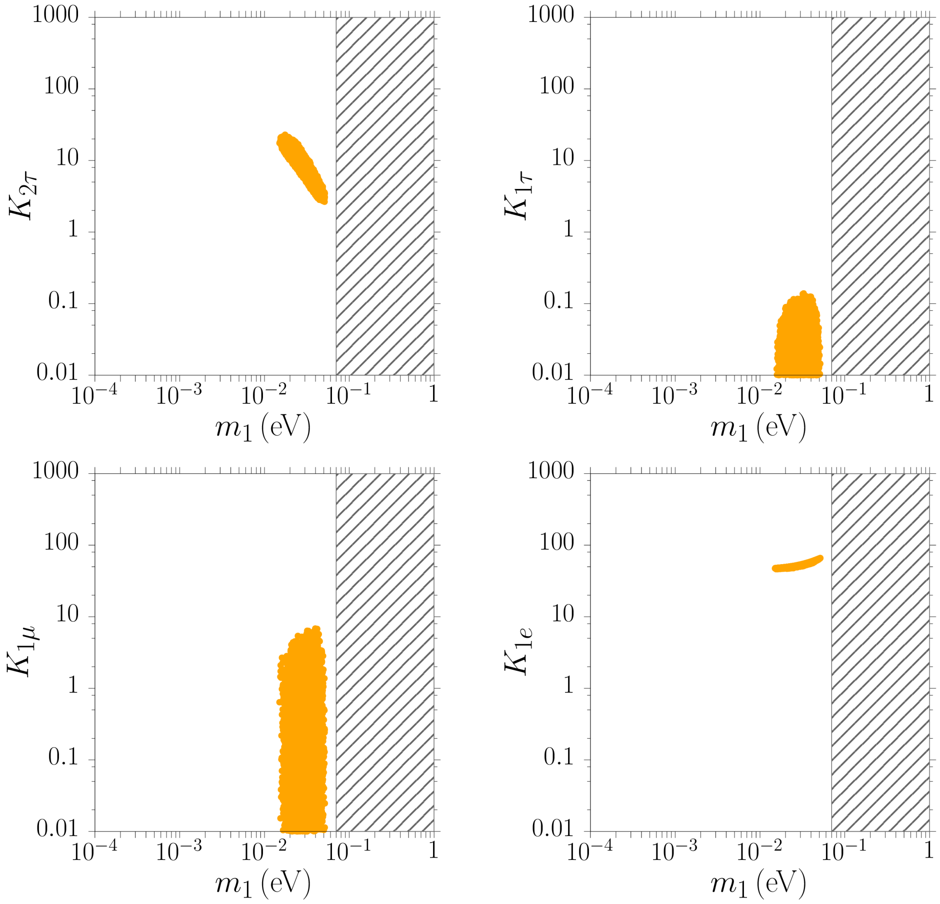

Figure 5.8: Scatter plots [2] for the four flavoured decay parameters $K_{2\tau}$, $K_{1\tau}$, $K_{1\mu}$, K_{1e} vs. m_1, IO case.

Combining all these results together and imposing successful leptogenesis, we obtain a lower bound on m_1

$$m_1 \gtrsim 32\pi\, 10^{-8}\, \frac{m_{\rm atm}\, v^2}{\alpha_2^2 m_c^2}\, \frac{c_{23}^4}{s_{23}^2}\, \left[\kappa_f(K_{2\tau})\, \sin\alpha_L\right]^{-1} . \tag{5.58}$$

When this lower bound is combined with the result of eq. (5.51), we obtain a lower bound on $\theta_{23} \gtrsim 45°$ for $\sin\alpha_L \simeq 0.5$. The phase cannot be maximal since, otherwise, we would not have $K_{1\tau} \lesssim 1$ anymore.

Considering the strong thermal leptogenesis conditions, we can notice that the washout of the pre-existing asymmetry along the e flavour does not pose any problem. Indeed, $K_{1e} = m_{ee}/m_* \simeq 50$. However, for the μ-flavour from the third panel of fig. 5.8, we can notice that $K_{1\mu} \lesssim 9 < K_{\rm st}(N^{\rm p,i}_{\Delta_\mu})$. Therefore, in IO it is not possible to efficiently wash out a sizeable pre-existing asymmetry along the μ flavour.

5.4 Beyond the $V_L = 1$ approximation

The assumption $V_L = 1$ greatly reduces the number of free parameters so that, as already mentioned, the neutrino parameters lie on a hypersurface described by the only free theoretical parameter left: α_2. This allowed us to obtain several interesting results on the neutrino parameters by imposing successful leptogenesis or, even more strictly, successful strong thermal leptogenesis. We can now ask what happens when this assumption is relaxed and the more general $SO(10)$-inspired condition $1 \leq V_L \lesssim V_{CKM}$, eq. (3.83), is enforced.

In fig. 5.2 we have included the results of a scatter plot, for $\alpha_2 = 5$ and NO, of points respecting successful leptogenesis for $1 \leq V_L \leq V_{CKM}$, in yellow. In particular, for these points we uniformly extracted the angles in V_L from

$$0^\circ \leq \theta_{12}^L \leq 13^\circ, \qquad 0^\circ \leq \theta_{23}^L \leq 2.5^\circ, \quad 0^\circ \leq \theta_{13}^L \leq 0.2^\circ, \tag{5.59}$$

while the phases δ^L, ρ^L and σ^L are kept varying on $[0,\, 2\pi)$.

The results in fig. 5.2 confirm once more what previously obtained in [159, 160]. Comparing the results with varying V_L, in yellow, with those obtained for $V_L = I$, in orange, we can see that some constraints do not get strongly modified, such as the lower bound on m_1. On the contrary, some other constraints are more sizeably affected, as in the case of the upper bound on m_1. The most remarkable difference can be noticed in the top-right panel, θ_{23} vs. m_1. Here a complete new region at large values $m_1 \gtrsim m_{\rm sol}$ appears. This region corresponds to a μ-dominated solution that is now possible since, when deviations from $V_L = 1$ are taken into account, the strong hierarchy in the *CP* asymmetries, eq. (3.114), gets relaxed and a muonic solution is allowed [159].

We can also notice that for the τ_B solution the upper bound on θ_{23} is much more relaxed when $1 \leq V_L \leq V_{CKM}$. On the other hand, the constraints for the τ_A solution do not change dramatically, a part from the disappearance of the lower bound on θ_{13}.

Imposing successful strong thermal leptogenesis for $1 \leq V_L \leq V_{CKM}$, in the same setup, produced the dark blue points in fig. 5.2. We can see that the constraints obtained for $V_L = 1$ (light blue points) get moderately relaxed. The lower bound on θ_{13} gets relaxed from $\theta_{13} \gtrsim 5^\circ$ to $\theta_{13} \gtrsim 2^\circ$. The upper bound on θ_{23} changes from $\theta_{23} \lesssim 41.5^\circ$ to $\theta_{23} \lesssim 43^\circ$. This can likely be regarded as the most important effect in light of the current experimental constraints on θ_{23} that tend to favour $\theta_{23} \gtrsim 40^\circ$, at least at 2σ [40].

It is then clear that relaxing the $V_L = 1$ assumption acts to enlarge the parameter space allowed by successful leptogenesis as well as by successful strong thermal leptogenesis. This is also due to the enhancement of the final produced asymmetry that $V_L \neq 1$ brings about. In fig. 3.4 we plotted $\eta_B^{\rm lep,f}$ vs. m_1 in three examples with $V_L \neq 1$ (dotted lines). This clearly shows that turning on the angles and phases in V_L can significantly enhance the final asymmetry, though not generally more than a factor 2.

Nevertheless, it is interesting to notice that the modifications on the constraints on the neutrino parameters are not dramatic, so that the analytical bounds obtained for $V_L = 1$ can often represent a good approximation.

As we have shown, overimposing the successful leptogenesis condition or the successful strong thermal leptogenesis conditions on $SO(10)$-inspired models determines the appearance of several interesting constraints on the neutrino parameters. It also allows us to make predictions on the value of some of them. In particular, on the ranges of the absolute neutrino mass scale m_1 and on the octant of the atmospheric mixing angle θ_{23}. In view of the forthcoming neutrino experiments and cosmological observations, these results become particularly fascinating, since they will allow compelling tests of the $SO(10)$-inspired scenario, as well as of the strong thermal leptogenesis assumptions. In order to get a better insight on these features and obtain quantitative results that can be compared to the experimental observations, we can now proceed to a first statistical analysis of the scatter plots.

5.5 A statistical analysis of the $SO(10)$-inspired leptogenesis results

Our aim is now to gain some information on the free parameters of the model through the analysis of the numerical simulations. Important results were found in the previous discussion, imposing successful leptogenesis and even more when combining the $SO(10)$-inspired conditions with the successful strong thermal leptogenesis one. Together, these conditions were able to constrain several parameters to narrow regions in the parameter space. Nevertheless, the scatter plots in fig. 5.2 do not consider the statistical significance of the different regions, so that, as we have seen, it is only possible to derive lower and upper bounds. We now propose to extract more information from the simulations through a statistical analysis of the numerical results, constraining the parameters to intervals with a precise statistical meaning [161].

The $SO(10)$-inspired models rely on a set of input parameters $\boldsymbol{\lambda} \equiv \{m_1, \theta_{ij}, \delta, \dots\}$, in which we do not include $m_{\rm sol}$ and $m_{\rm atm}$, given the great precision of their measurements. In the simulations that give the scatter plots, the parameters in $\boldsymbol{\lambda}$ are randomly extracted according to some *prior* Probability Density Function (PDF) $\pi(\boldsymbol{\lambda})$. Given a set $\boldsymbol{\lambda}$ of parameters, a value $\eta_B^{\rm lep,f}$ of the final asymmetry produced by leptogenesis can be obtained and compared to the experimental value $\eta_B^{\rm CMB}$. Following a bayesian approach, the comparison of the final produced asymmetry with the experimental value provides additional information that allows us to update the PDFs of the input parameters to the so-called *posterior* functions. These can then be used to obtain credible regions and intervals in the parameter space.
According to Bayes' theorem [162–164], the probability density $f(\boldsymbol{\lambda}\,|\,\eta_B^{\rm lep,f} = \eta_B)$ of having a parameter set $\boldsymbol{\lambda}$, given that the final produced asymmetry $\eta_B^{\rm lep,f}$ fully explains the

baryon asymmetry of the Universe η_B, is

$$f(\boldsymbol{\lambda}\,|\,\eta_B^{\rm lep,f}=\eta_B)=\frac{f(\eta_B^{\rm lep,f}=\eta_B\,|\,\boldsymbol{\lambda})\,\pi(\boldsymbol{\lambda})}{\int d\boldsymbol{\lambda}\,f(\eta_B^{\rm lep,f}=\eta_B\,|\,\boldsymbol{\lambda})\,\pi(\boldsymbol{\lambda})} \tag{5.60}$$

where $f(\eta_B^{\rm lep,f}=\eta_B\,|\,\boldsymbol{\lambda})$ is the probability of reproducing the baryon asymmetry of the Universe η_B with the asymmetry produced by leptogenesis with the given input parameters $\boldsymbol{\lambda}$. It is possible to rewrite $f(\eta_B^{\rm lep,f}=\eta_B\,|\,\boldsymbol{\lambda})$ in a simpler way, assuming the baryon-to-photon ratio η_B of the Universe is normally distributed around the experimental value $\eta_B^{\rm CMB}$, so that

$$f(\eta_B^{\rm lep,f}=\eta_B\,|\,\boldsymbol{\lambda})=f_\eta(\eta_B^{\rm lep,f}(\boldsymbol{\lambda}))\equiv\frac{1}{\sigma_\eta\sqrt{2\pi}}\exp\left\{-\frac{\left[\eta_B^{\rm lep,f}(\boldsymbol{\lambda})-\eta_B^{\rm CMB}\right]^2}{2\sigma_\eta^2}\right\}, \tag{5.61}$$

where $\eta_B^{\rm CMB}=6.1\times10^{-10}$ and $\sigma_\eta=0.1\times10^{-10}$, as given by eq. (1.11). The posterior PDF, $f(\boldsymbol{\lambda}\,|\,\eta_B^{\rm lep,f}=\eta_B)$, can then be marginalised in order to obtain a PDF for each parameter λ_i

$$f(\lambda_i\,|\,\eta_B^{\rm lep,f}=\eta_B)=\int\left(\prod_{j\neq i}d\lambda_j\right)f(\boldsymbol{\lambda}\,|\,\eta_B^{\rm lep,f}=\eta_B), \tag{5.62}$$

which updates the prior PDF $\pi(\lambda_i)$. The function $f(\boldsymbol{\lambda}\,|\,\eta_B^{\rm lep,f}=\eta_B)$ and the marginalised PDFs $f(\lambda_i\,|\,\eta_B^{\rm lep,f}=\eta_B)$ enclose information about the parameters and show the regions of the parameter space preferred by the model, together with their likelihood.
In order to obtain a posterior PDF $f(\boldsymbol{\lambda}\,|\,\eta_B^{\rm lep,f}=\eta_B)$ it is necessary to specify the priors of the input parameters.

- **Absolute neutrino mass scale.** m_1 is randomly extracted according to a uniform logarithmic distribution on $[10^{-4},\,10^{-1}]\,$eV.
- **Solar and reactor mixing angles.** These two mixing angles are well determined by the current neutrino global analyses and they are assumed as normally distributed as in tab. 1.1.
- **Atmospheric mixing angle.** This angle is still poorly constrained by neutrino global fits, which are not yet able to pin down the octant. To account for these large uncertainties we have chosen to *uniformly* extract θ_{23} in its 3σ range as in eq. (5.11). With this flat prior it is also possible to clearly notice the preference determined by leptogenesis itself.
- ***CP*-violating phases.** Given the little knowledge on the Dirac phase δ, this is chosen to be uniformly extracted on its full variability range, i.e. $\delta\in[-\pi,\,\pi)$. Similarly, the Majorana phases are uniformly extracted on $\rho,\sigma\in[0,\,2\pi)$.

- V_L **unitary matrix.** The V_L matrix parameters are uniformly extracted on the ranges in eq. (5.59).

The input parameter set $\boldsymbol{\lambda}$ is therefore determined according to these priors and the generated asymmetry $\eta_B^{\rm lep,f}(\boldsymbol{\lambda})$ is then weighted according to eq. (5.61). In addition, we shall take $\alpha_2 = 5$.

Being particularly interested in the tight constraints originating by imposing successful strong thermal leptogenesis, and considering the marginal role of the IO case in $SO(10)$-inspired models, we shall focus our statistical study to the NO case only.
The results obtained for the different parameters and in different setups are shown in the following paragraphs. Firstly, we shall analyse the $SO(10)$-inspired and strong thermal $SO(10)$-inspired scenarios with $V_L = 1$. We shall then relax this assumption and consider more general models with $1 \leq V_L \leq V_{CKM}$.

5.5.1 Results for $V_L = 1$

Here we describe the results of the statistical analysis of the numerical simulations with $V_L = 1$. For clearness, we have separately studied the two scenarios: the $SO(10)$-inspired successful leptogenesis solution and the successful strong thermal $SO(10)$-inspired one. In the former we have not taken into account any pre-existing asymmetry, while in the latter we have considered the washout of an initial pre-existing asymmetry $N_{B-L}^{\rm p,i} = 10^{-3}$. As expected from our previous discussion, the allowed regions for the parameters are quite tight for $V_L = 1$. At the same time, they are narrower when the strong thermal conditions are imposed on the $SO(10)$-inspired scenario.

5.5.1.1 Successful $SO(10)$-inspired leptogenesis with $V_L = 1$

Here we summarise the results obtained when only the successful leptogenesis condition is imposed on the $SO(10)$-inspired model. We show a set of planes cutting the parameter space along definite directions and for each 2-dimensional slice we plot the 68% and 95% credible regions obtained following the procedure described above. The 2-dimensional plots are shown in fig. 5.9 [161]. The statistical analysis points out the preferred subregions within the allowed ones that were found in [159, 160] and in the previous discussion [2]. In particular, the top-central panel confirms that $V_L = 1$ $SO(10)$-inspired successful leptogenesis introduces a net asymmetry between positive and negative values of the Dirac *CP*-violating phase δ. Negative values are favoured with respect to positive ones. The top-right and bottom-left panels, respectively showing ρ and σ versus m_1 confirm the analytical results discussed in the previous section. The maximal values at low and high m_1 are connected by branches, and we can notice that the lower branches are dominant. This provides us with a clear confirmation of what was analytically derived

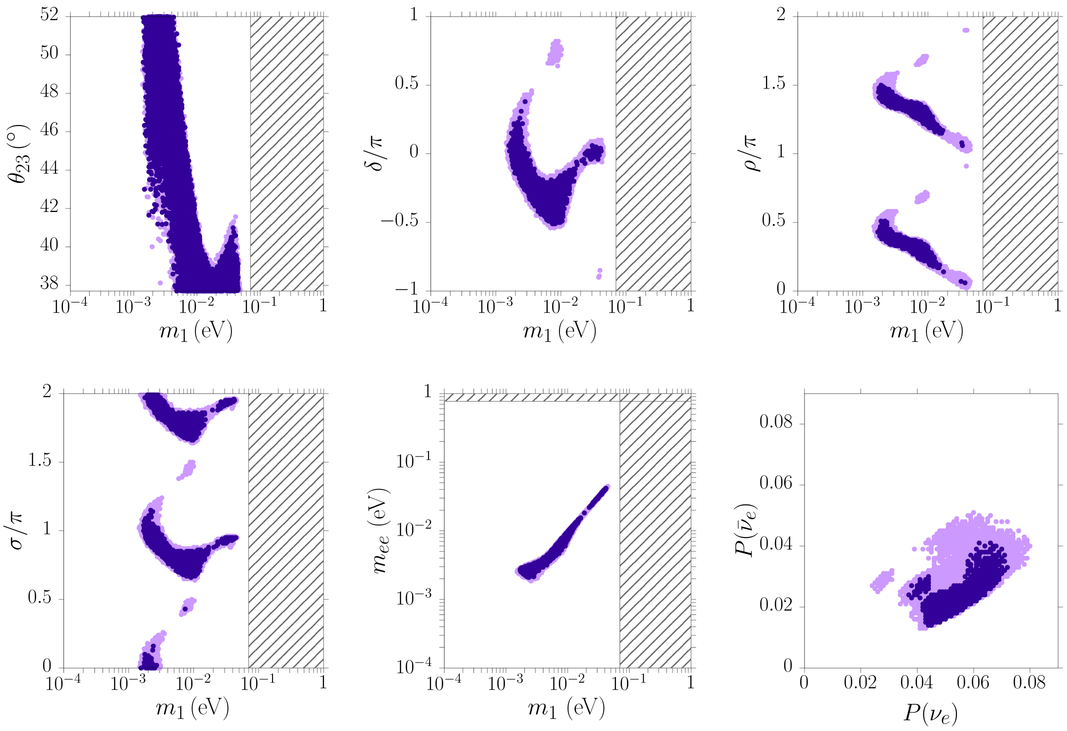

Figure 5.9: 2-dimensional credible regions for different sections of the parameter space (first four panels) plus effective $0\nu\beta\beta$ decay mass m_{ee} and oscillation bi-probability plot (bottom centre and right panels) for $SO(10)$-inspired successful leptogenesis with $\alpha_2 = 5$ and $V_L = 1$, [161]. In dark purple the 68% credible region, while in light purple the 95% one. The hatched regions are currently excluded by the experimental observations, in particular, the upper bound on m_1 imposed by cosmology, eq. (1.43).

before, quantitatively showing the preference for particular values of the phases.

From the top-left panel it is not possible to obtain clear information about the atmospheric mixing angle. All values of θ_{23} in its 3σ range are allowed both at 68% and 95% probability.

The bottom-right panel shows the oscillation probability $P(\bar{\nu}_\mu \to \bar{\nu}_e)$ versus the probability $P(\nu_\mu \to \nu_e)$. This can be a useful way to compare the predictions of the models with the next results coming from long-baseline oscillation experiments such as NOνA [43, 165]. These experiments will be able, in the coming future, to place confidence regions on this plane, which can then be compared with the region shown in the panel of fig. 5.9, and corresponding to the $SO(10)$-inspired successful leptogenesis solution, with $V_L = 1$. To this aim, these probabilities are computed taking into account matter effects as [166]

$$
\begin{aligned}
P\left(\overset{(-)}{\nu_\mu} \to \overset{(-)}{\nu_e}\right) &\simeq \sin^2(2\theta_{13})\,\sin^2\!\theta_{23}\frac{\sin^2[(A-1)\Delta]}{(A-1)^2} \\
&+ 2\alpha\,\sin\!\theta_{13}\cos\!\delta\,\sin(2\theta_{12})\,\sin(2\theta_{23})\frac{\sin(A\Delta)}{A}\frac{\sin[(A-1)\Delta]}{A-1}\cos\Delta \\
&- 2\alpha\,\sin\!\theta_{13}\sin\!\delta\,\sin(2\theta_{12})\,\sin(2\theta_{23})\frac{\sin(A\Delta)}{A}\frac{\sin[(A-1)\Delta]}{A-1}\sin\Delta, \qquad (5.63)
\end{aligned}
$$

where $\Delta \equiv \frac{\Delta m^2_{31}}{4E}\frac{10^{19}L}{1.97}$ with L being the distance in km (for NOνA, $L = 810\,\text{km}$), $\alpha \equiv \frac{\Delta m^2_{21}}{\Delta m^2_{31}}$ and $A = \pm E/(11\,\text{GeV})$ for NO, with + or − respectively for neutrinos and antineutrinos and $E = 2\,\text{GeV}$ for NOνA.

5.5.1.2 Successful strong thermal $SO(10)$-inspired leptogenesis with $V_L = 1$

Along the lines of the previous analysis, we show in fig. 5.10 the results obtained when the strong thermal leptogenesis condition is imposed on the $SO(10)$-inspired model. Here we considered an initial pre-existing asymmetry $N^{\rm p,i}_{B-L} = 10^{-3}$. We can notice that the regions are compatible with what found in fig. 5.2 (light blue points). As expected, the regions are dramatically narrower than in the successful $SO(10)$-inspired leptogenesis case. Strong thermal $SO(10)$-inspired leptogenesis with $V_L = 1$ realises the most predictive scenario, with the tightest bounds on the low-energy neutrino parameters.

From the top-left panel it is possible to notice that the atmospheric mixing angle is constrained to a very narrow region in the first octant. Similarly, from the top-central panel we can see that the Dirac phase δ can only take negative values in its fourth quadrant, i.e. around $\delta = -\pi/4$. The top-right and bottom-left panel show that the Majorana phases are constrained to very small regions, with π periodicity.

Moreover, in the bottom-centre panel the $0\nu\beta\beta$ decay effective mass is allowed to vary in a tight region around 15 meV.

In the bi-probability plot (bottom-right panel) the region corresponding to the strong thermal $SO(10)$-inspired leptogenesis solution, with $V_L = 1$, is quite small, which is a direct consequence of the predictivity of the model.

For a better understanding of the statistical significance of these intervals, it is convenient to obtain the single parameter PDFs by marginalisation, as in eq. (5.62). The results are shown in fig. 5.11, where the 68% and 95% intervals are plotted in dark and light blue respectively. Each parameter shown in fig 5.11 had a flat uniform prior on the allowed 3σ range. As can be seen from the panels, the posterior PDFs are greatly changed and show pronounced peaks around particular values. From the top-left panel we can notice that the absolute neutrino mass scale is constrained to a very narrow range, in particular $m_1 \in [12, 15]\,\text{meV}$ with 95% probability. At the same time, the effective $0\nu\beta\beta$ mass is $m_{ee} \in [10, 13]\,\text{meV}$ with 95% probability. Due to the precise values assumed by the Majorana phases (see bottom-centre and bottom-right panels)

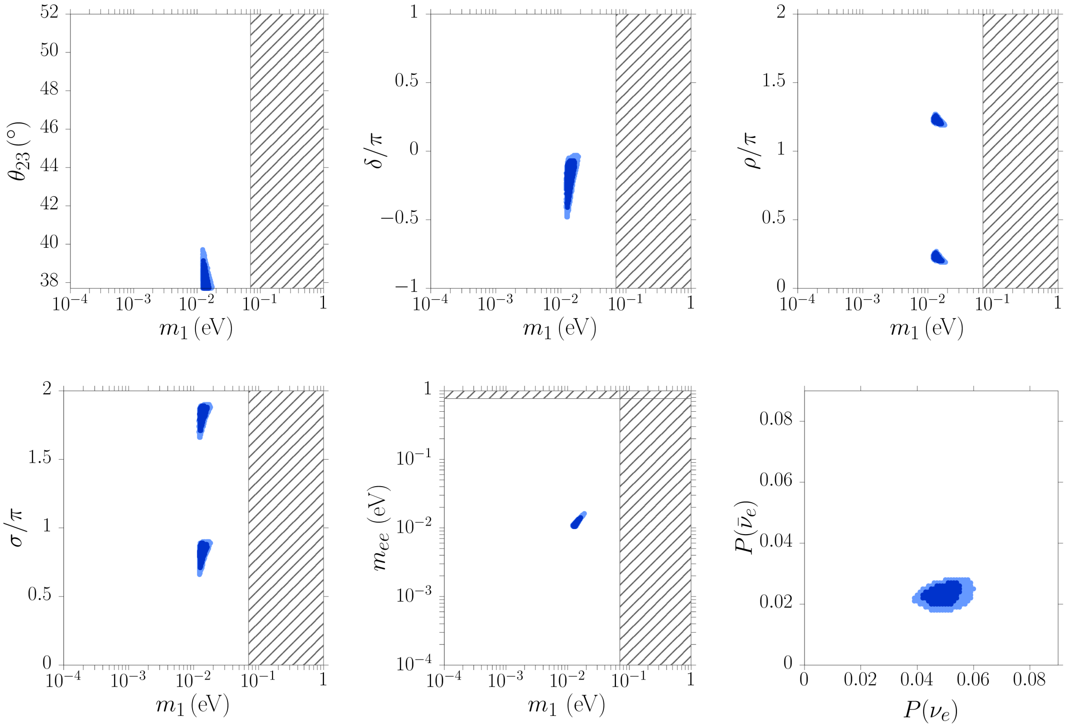

Figure 5.10: 2-dimensional credible regions for different sections of the parameter space (first four panels) plus effective $0\nu\beta\beta$ decay mass m_{ee} and oscillation bi-probability plot (bottom centre and right panels) for $SO(10)$-inspired successful strong thermal leptogenesis with $\alpha_2 = 5$, $V_L = 1$ and $N^{\rm p,i}_{B-L} = 10^{-3}$, [161]. In dark blue is the 68% credible region, while in light blue is the 95% one. The hatched regions are currently excluded by the experimental observations, in particular, the upper bound on m_1 imposed by cosmology, eq. (1.43).

the cancellations in m_{ee} are very mild, so that we have $m_{ee} \sim m_1$.

The top-right panel shows the PDF of the atmospheric mixing angle. As we can see, we have $\theta_{23} \leq 39^\circ$ with 95% probability and $\theta_{23} \leq 40.5^\circ$ at 99.99994%, corresponding to 5σ in a frequentist approach. This clearly shows that strong thermal $SO(10)$-inspired leptogenesis, with $V_L = 1$, strongly disfavours maximal atmospheric mixing angle, and constrains it to the first octant.

In the bottom-left panel the PDF of δ is plotted and we have $\delta/\pi \in [-0.36, -0.08]$ with 95% probability. All the δ values are negative, and it is also possible to compute the '5σ' range: $-0.5 \leq \delta/\pi \leq -0.01$ with 99.99994% probability. This confirms once again the discussion of the previous section, and we can conclude that $V_L = 1$ strong thermal $SO(10)$-inspired leptogenesis strongly favours δ in the fourth quadrant, thus implying $\sin\delta < 0$ and $\cos\delta > 0$.

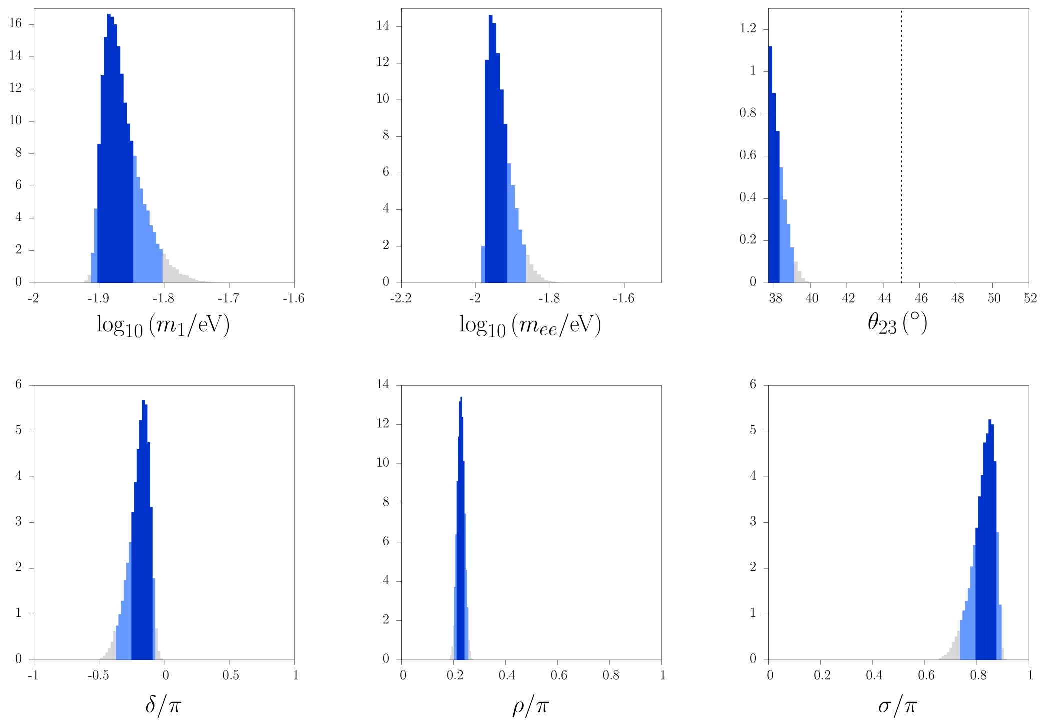

Figure 5.11: Single parameter posterior PDFs for $SO(10)$-inspired successful strong thermal leptogenesis with $\alpha_2 = 5$, $V_L = 1$ and $N^{\rm p,i}_{B-L} = 10^{-3}$, [161]. In dark blue the 68% credible region, while in light blue the 95% one. The ranges of m_1 and m_{ee} are restricted to the intervals of interest in the first and second panels. The Majorana phases ρ and σ show π-periodicity which is not plotted. The dashed line in the top-right panel marks the maximal solution $\theta_{23} = 45^\circ$.

5.5.2 Results for $1 \leq V_L \leq V_{CKM}$

We can now statistically analyse the $SO(10)$-inspired models imposing successful leptogenesis and successful strong thermal leptogenesis when the assumption $V_L = 1$ is relaxed. These models are clearly more general than those analysed so far, therefore we can regarded the results obtained in this case as the most important ones. Indeed they provide predictions which are more general, encompassing all the $SO(10)$- and strong thermal $SO(10)$-inspired leptogenesis models. The range of the mixing angle and phases in V_L can be found in eq. (5.59). We shall follow the same guidelines as in the previous section, dealing with successful leptogenesis first and then adding the strong thermal condition.

5.5.2.1 Successful $SO(10)$-inspired leptogenesis with varying V_L

The 2-dimensional plots are shown in fig. 5.12. Here we can notice that the statistically significant regions are almost coinciding with what found in fig. 5.2 (dark blue points), and it is not possible to improve the bounds already obtained thereby.

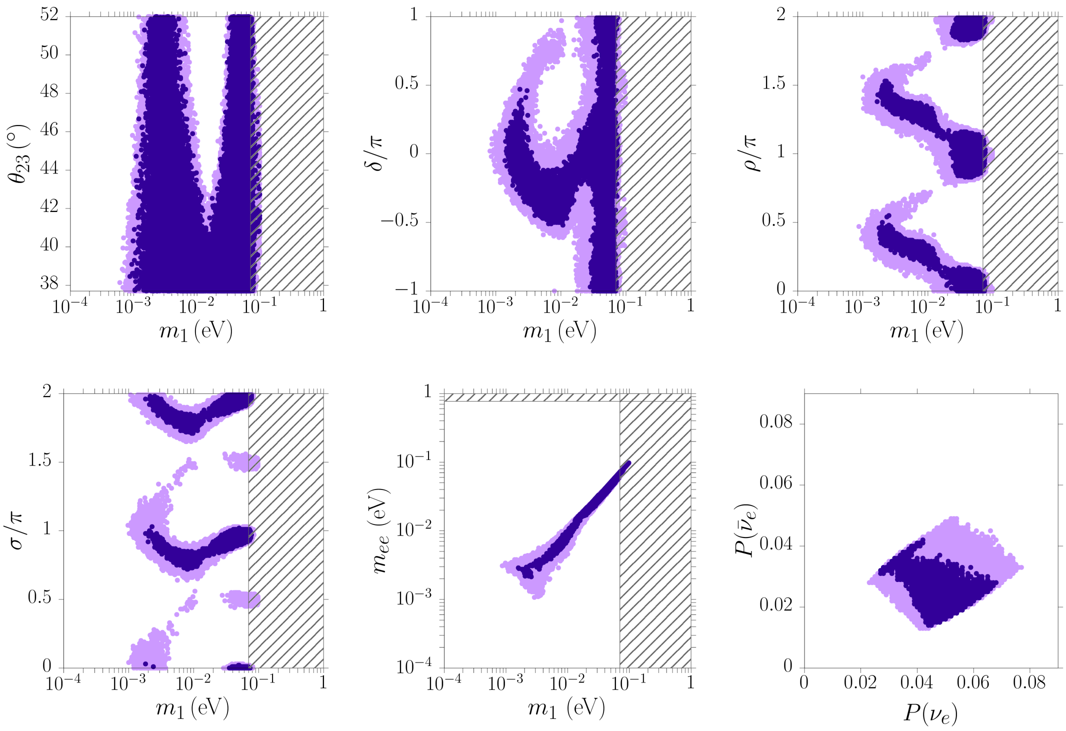

Figure 5.12: 2-dimensional credible regions for $SO(10)$-inspired successful leptogenesis with $\alpha_2 = 5$ and $1 \leq V_L \leq V_{CKM}$, [161]. Panels and conventions as in fig. 5.9.

It is possible, however, to notice an asymmetry between positive and negative values of δ, as in the $V_L = 1$ case. Here again, for low values of the lightest neutrino mass, i.e. $m_1 \lesssim m_{\mathrm{sol}}$, positive values of δ are statistically disfavoured, being scarcely included in the 95% credible region.

Similarly, the Majorana phases keep showing preferences for some branches, as already pointed out in the $V_L = 1$ case. With varying V_L, however, the favourable zones are larger and slightly less evident.

An analysis of the one-dimensional PDFs does not allow us to obtain any interesting predictions on the values of the unknown parameters, other than the bounds already found. In the case of successful $SO(10)$-inspired leptogenesis with varying V_L, therefore, the statistical analysis is not particularly powerful in constraining the low-energy parameters to tight intervals with definite statistical meaning.

5.5.2.2 Successful strong thermal $SO(10)$-inspired leptogenesis with varying V_L

When imposing the successful strong thermal leptogenesis condition on an $SO(10)$-inspired model, the allowed regions in the parameter space are largely reduced. The statistical analysis performed on this scenario enables us to provide the intervals with a statistical significance. As before, we have considered an initial pre-existing asymmetry

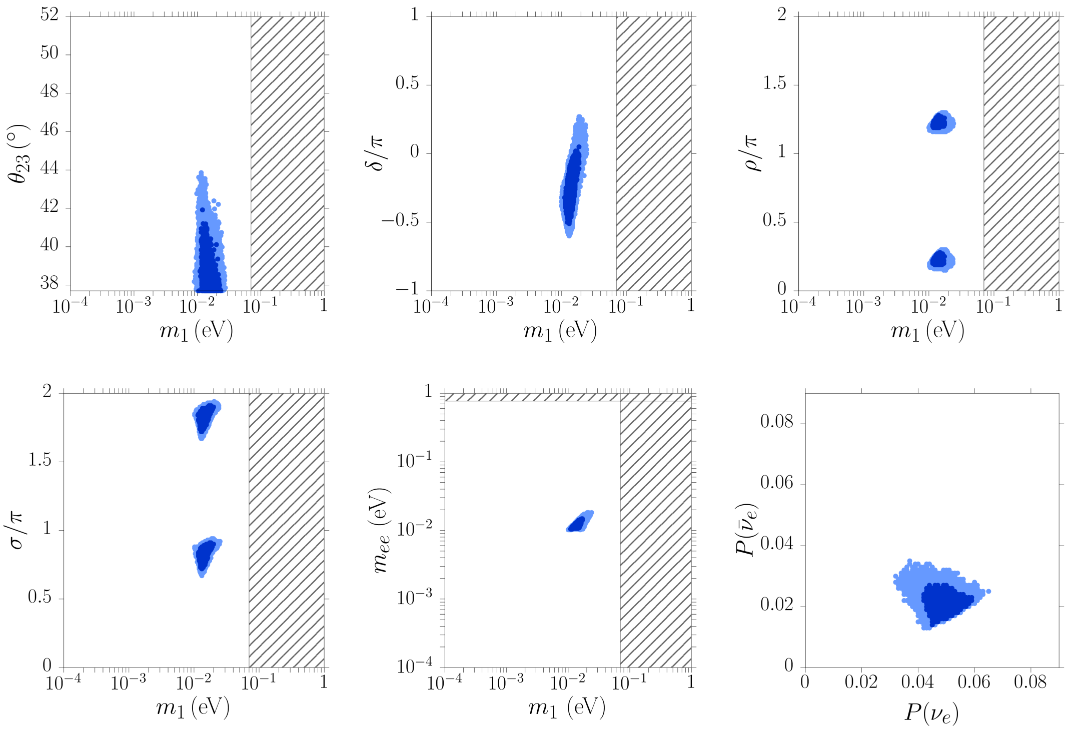

Figure 5.13: 2-dimensional credible regions for $SO(10)$-inspired successful strong thermal leptogenesis with $\alpha_2 = 5$, $1 \leq V_L \leq V_{CKM}$ and $N^{\rm p,i}_{B-L} = 10^{-3}$, [161]. Panels and conventions as in fig. 5.10.

$N^{\rm p,i}_{B-L} = 10^{-3}$. In fig. 5.13 we show the 2-dimensional sections of the parameter space. The allowed regions are much smaller than in the varying V_L successful leptogenesis only case, but larger than the successful strong thermal $SO(10)$-inspired case with $V_L = 1$. The comparison between fig. 5.13 and 5.10 shows how much the bounds relax when the $V_L = 1$ assumption is removed. The most important differences between the two cases can be found in the top-left and top-central panels. The 95% contour of θ_{23} extends up to 44°, while for δ it goes up to about $\pi/2$. For a better understanding of the statistical significance of these intervals, it is convenient to obtain the single parameter PDFs by marginalisation, as in eq. (5.62). The results are shown in fig. 5.14, where the 68% and 95% intervals are plotted in dark and light blue respectively. As for the $V_L = 1$ case, we can get precise predictions on the parameters.

In table 5.1, [161], we have summarised the posterior 68% and 95% credible regions for the free low-energy neutrino parameters, the effective $0\nu\beta\beta$ decay mass m_{ee} and the sum of the neutrino masses $\sum_i m_i$. Very precise statements can then be made on the basis of table 5.1. In particular, the following can be noticed.

- **Atmospheric mixing angle.** The second octant of θ_{23} is highly disfavoured. More precisely, $\theta_{23} \leq 43.7^\circ$ with 99.99994% probability (corresponding to 5σ in a frequentist approach), which clearly excludes the maximal value $\theta_{23} = 45^\circ$.

  It must be noticed that the intervals in tab. 5.1 are bounded from below by the

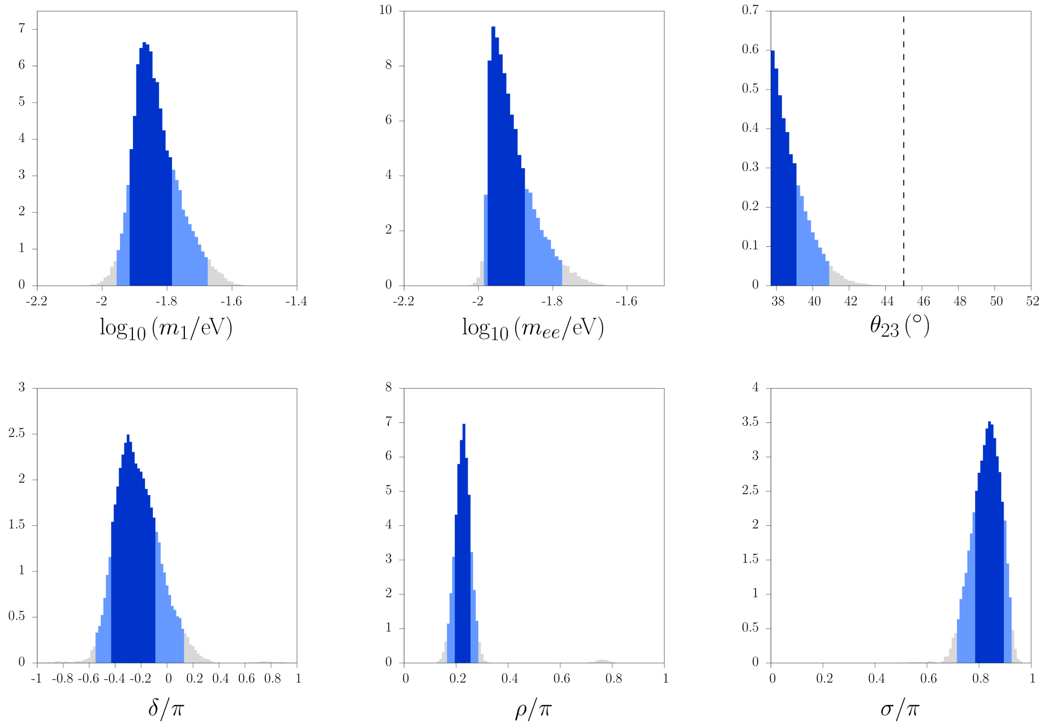

Figure 5.14: Single parameter posterior PDFs for $SO(10)$-inspired successful strong thermal leptogenesis with $\alpha_2 = 5$, $1 \leq V_L \leq V_{CKM}$ and $N^{\mathrm{p,i}}_{B-L} = 10^{-3}$, [161]. Panels and conventions as in fig. 5.11.

choice of the prior distribution. This is due to the feature of $SO(10)$-inspired models, in which the final asymmetry $\eta_B^{\mathrm{lep,f}} \propto \sin^{-4}(\theta_{23})$ as shown in the previous discussion. Therefore low values of the atmospheric angle are preferred.

We shall comment on the choice of the priors in the following paragraph.

- **Dirac *CP*-violating phase.** Negative values of δ are preferred, positive values are marginally allowed, since we have $\delta \leq 0.31\,\pi$ with 99.99994% probability (5σ).
- **Absolute neutrino mass scale.** m_1 shows preferred values which are not compatible with the hierarchic limit ($m_1 \to 0$). More in detail, $m_1 \geq 8.78\,\mathrm{meV}$ with 99.99994% probability (5σ).

  Neglecting the errors on m_{sol} and m_{atm} it is possible to give a credible interval to the sum of the neutrino masses, which is particularly interesting for cosmology and reported in the last row of tab. 5.1.
- **Majorana phases and m_{ee}.** The values of the Majorana phases are strongly constrained to small regions. This implies mild cancellations in the expression of the effective $0\nu\beta\beta$ decay mass, which falls around $12\,\mathrm{meV}$, a region within the reach of forthcoming experiments.

	Prior range	Posterior ranges	
		68%	95%
m_1	$[10^{-4},\, 10^{-1}]$ eV (log)	[12, 16] meV	[11, 21] meV
θ_{23}	[37.7°, 52°]	[37.7°, 39°]	[37.7°, 40.8°]
δ	$[-1,\, 1]\pi$	$[-0.13,\, -0.031]\pi$	$[-0.17,\, -0.038]\pi$
ρ	$[0,\, 2]\pi$	$[0.063,\, 0.079]\pi$	$[0.054,\, 0.089]\pi$
σ	$[0,\, 2]\pi$	$[0.25,\, 0.28]\pi$	$[0.23,\, 0.29]\pi$
m_{ee}		[11, 13] meV	[10, 17] meV
$\sum_i m_i$		[76, 85] meV	[75, 97] meV

Table 5.1: Credible intervals at 68% and 95% for the low-energy parameters, effective $0\nu\beta\beta$ mass m_{ee} and sum of the neutrino masses $\sum_i m_i$ for $SO(10)$-inspired successful strong thermal leptogenesis with $\alpha_2 = 5$, $1 \leq V_L \leq V_{CKM}$ and $N^{\rm p,i}_{B-L} = 10^{-3}$, [161]. The Majorana phases ρ and σ show π-periodicity, while δ has a 2π period.

These considerations build up a very definite pattern of predictions, as shown in tab. 5.1, which precisely characterises the strong thermal $SO(10)$-inspired leptogenesis solution, making it possible to put it to the experimental test, at least in part, in the next future.

5.5.3 Comments and remarks

As in any Bayesian analysis, these results are dependent on the choice of the priors and this can often be a source of controversy. However, as pointed out in the previous section, the parameter priors have been chosen on the basis of solid experimental evidences, that constrain the variability ranges to narrow intervals. When the experimental results are not well grounded, we have adopted a conservative approach, accounting for the current uncertainties with flat distributions over 3σ ranges, as in the case of θ_{23}, or the full variability ranges, as for δ, ρ, and σ.

As mentioned in the previous paragraph, the prior of the atmospheric mixing angle can raise some concern. Indeed, the posterior distribution is bounded from below by the lower limit of the prior, thus showing a sizeable impact of this on the final result. We have considered a more generic, though experimentally not supported, case with θ_{23} over its full variability range, i.e. $\theta_{23} \in [0°,\, 90°]$. This is shown in fig. 5.15. Here, all the other input parameters are extracted as described above, while the atmospheric mixing angle is extracted uniformly over [0°, 90°]. From this figure we can notice that $SO(10)$-inspired leptogenesis indeed tends to prefer low values of θ_{23}. However they do not saturate the range accumulating around 0°, rather they show a definite peak around 25°. In particular, it is possible to identify the credible intervals $\theta_{23} \in [21.6°,\, 32°]$ with 68% probability and $\theta_{23} \in [17.6°,\, 36°]$ with 95% probability. It is possible to notice that the leptogenesis-favoured θ_{23} values marginally encompass the experimentally allowed band, the shadowed region in the figure. In this setup, with wide variability range for

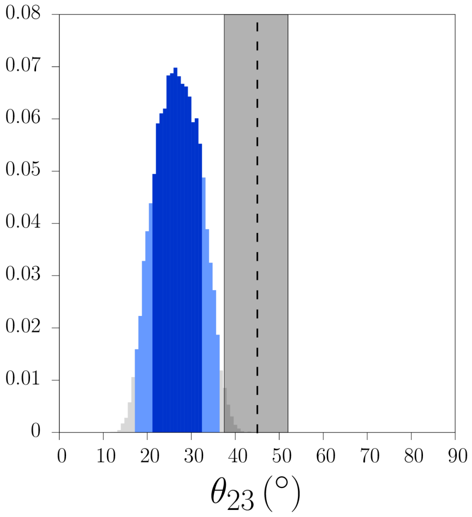

Figure 5.15: PDF histogram of the atmospheric mixing angle θ_{23} with uniform prior on [0°, 90°], [161]. All the other input parameters have their usual prior distributions. The shadowed region corresponds to the current 3σ experimental range. The dashed lines marks the maximal solution $\theta_{23} = 45°$.

the atmospheric mixing angle, the probability that leptogenesis picks a θ_{23} value in the 3σ experimental region is about 1%. This is quite small, however it is not sufficient to rule out the model. It must also be noticed that the Dirac phase δ is free to vary on its entire variability range. Values around $\delta \sim -2\pi/3$, as hinted by recent best-fits, make large values of θ_{23} much more likely.

We have also studied the strong thermal $SO(10)$-inspired scenario with a different choice of priors. In order to be extremely general, we have considered the case in which all the mixing angles are randomly extracted from a PDF uniform over the full variability range [0°, 90°]. For simplicity, we shall refer to this choice of priors as prior π'. We can thus make comparison with the choice of priors described and used in the previous paragraphs, and that we shall call *base prior* π^0. Firstly, it is possible to study the global sensitivity to the prior choice, via standard range analysis, by comparing the outcomes of the two choices. Focusing on the main parameters m_1, θ_{13}, θ_{12} and θ_{23} the range analysis implies a study of the variation of their expectation values from the base prior π^0 to π'. In table 5.2 we have reported the expectation values for the two cases. The

	m_1 (meV)	θ_{13} (°)	θ_{12} (°)	θ_{23} (°)
π^0	14.5	8.8	33.7	38.8
π'	8	37.0	45.5	67.6
R_π	0.88	2.04	2.07	1.18

Table 5.2: Range of the expectation values of the parameters in the case of prior π^0 and π'. In the last row we show the relative sensitivity.

priors π^0 and π' do not belong to a continuous class and the difference between them is rather big (e.g. θ_{13} goes from a peaked gaussian distribution to a flat uniform distribution over a finite range [0, 90°]), therefore we could expect significant variations in the expected values and so quite a wide range. This is indeed the case in tab. 5.2, where the comparison between the first two rows shows a large change of the expected values between π^0 and π'. We may conclude that our analysis is sensitive to the prior choice and, in general, lacks of robustness. Other sensitivity analyses, e.g. the study of relative sensitivity [167], can be carried out, in general confirming this situation. However, this high prior sensitivity is not worrying in our case, since we have solid reasons to prefer the prior π^0 to the extreme case π', so that they are not considered *a priori* equally plausible. On the contrary, it can be shown that our analysis is actually robust with respect to a neighbourhood class of priors around π^0.

We can conclude in any case that the priors described in the previous section and employed in the analysis can be considered as the most reasonable and accurate, therefore more suitable than other possible prior choices.

Finally, it is possible to reproduce an analysis in the lines of what already carried out in [160]. We can compute the fraction of the total parameter space that allows successful strong thermal leptogenesis, in the π^0 and π' setups. We shall consider only the parameter space related to the mixing angles. Computing the volume $\Omega_{\pi^0}^{\mathrm{STlep}}$ of the region corresponding to successful strong thermal leptogenesis, its ratio to the total volume $\Omega_{\pi^0}^{\mathrm{tot}}$ is

$$r_{\pi^0} \equiv \frac{\Omega_{\pi^0}^{\mathrm{STlep}}}{\Omega_{\pi^0}^{\mathrm{tot}}} = 93.0\%. \tag{5.64}$$

As for the prior π', the mixing angles are all uniformly extracted on [0°, 90°], and computing the ratio of the successful strong thermal leptogenesis volume to the total volume we get

$$r_{\pi'} \equiv \frac{\Omega_{\pi'}^{\mathrm{STlep}}}{\Omega_{\pi'}^{\mathrm{tot}}} = 5.7\%. \tag{5.65}$$

We can conclude that, considering just the mixing angles and marginalising on the other free parameters, the probability to have successful strong thermal leptogenesis from a randomly picked triplet of mixing angles is just 5% in the generic π' case. This probability raises up to 93% when the parameter space is restricted to the experimentally allowed range. It is important to recall that this restriction is made independently of leptogenesis and only on the basis of current neutrino oscillation experiment. For this reason, we can conclude that the experimental data from neutrino oscillations are in good agreement with strong thermal $SO(10)$-inspired leptogenesis and seem to represent a valid support.

It must be mentioned that a fully detailed analysis would require the derivation of the PDFs of the parameters directly from the experimental data, by fitting the relevant datasets and then marginalising the joint PDF. This would also take correctly into account the correlations between the different neutrino parameters. Our aim was to provide a first analysis of the numerical leptogenesis results. We have therefore adopted prior distributions based on the information currently available from global neutrino fits. In a first approximation, then, we have neglected the correlation between the different oscillation parameters. This can be considered sufficient for our goal of showing the constraining power of the strong thermal solution and providing predictions that can be used for comparison with the forthcoming experimental measurements.

In this regard, it is important to recall that these results are obtained for an initial pre-existing asymmetry $N_{B-L}^{\rm p,i} = 10^{-3}$. Lower values of $N_{B-L}^{\rm p,i}$ imply looser bounds, while higher ones give narrower intervals. The chosen value $N_{B-L}^{\rm p,i} = 10^{-3}$ can be regarded as a good estimation of the large pre-existing asymmetry that can be generated by different primordial mechanisms. In general, it is possible to verify the compatibility of the ranges shown in the previous section with the experimental results, thus allowing to either support or severely corner the assumptions of the models. However, we can also reverse the perspective and employ the new experimental data to put an upper bound on the magnitude of the pre-existing asymmetry that is possible to efficiently wash out. Clearly, if the parameter values only allow the washout of negligible pre-existing asymmetries, the strong thermal condition will lose its interest.

Chapter 6

A supersymmetric extension

We can now consider the supersymmetric extension of the $SO(10)$-inspired models we have studied so far. Supersymmetric extensions are important since they offer a traditional way to address naturalness, while at the same time they can help improving the goodness of fits of lepton and quark parameters in GUTs [168–170]. In this respect, it is worth noticing that in [170] good fits of the fermion parameters have been obtained within supersymmetric $SO(10)$ models with hierarchical RH neutrino masses and, interestingly, IO light neutrino masses. Moreover, the found values of m_{ee} are well in the reach of next generation $0\nu\beta\beta$ decay experiments. This can motivate an analysis of leptogenesis within the supersymmetric framework.

Care must be taken since supersymmetry is typically implemented as a local symmetry, leading to supergravity. In this case one has to worry whether successful thermal leptogenesis can be achieved with values of the reheating temperature $T_{\rm RH}$ compatible with the upper bound imposed by the solution of the gravitino problem [171–174]. A quite conservative and model independent upper bound, $T_{\rm RH} \lesssim 10^{10}\,{\rm GeV}$, is obtained in order to avoid DM over abundance [174], where the DM particle can be either the neutralino or the gravitino itself or some other hidden sector lighter particle, depending whether the gravitino is the lightest supersymmetric particle. There exist, however, different ways to circumvent this upper bound. For example, considering entropy production diluting the DM abundance [175] or in models with mixed axion/axino DM [176]. Another possibility is that the gravitino is heavier than $\sim 10^7\,{\rm GeV}$ so that its lifetime is so short to decay before neutralino dark matter freeze-out [177].

Here we will extend $SO(10)$-inspired leptogenesis to the supersymmetric case, studying how the constraints derived in the non-supersymmetric case (in the previous chapter) change [3]. We shall also consider with attention the lower bound on $T_{\rm RH}$.

For what explained in the previous sections, we already know that $SO(10)$-inspired models naturally realise the N_2-dominated scenario, and this feature is preserved in the supersymmetric extension. In the following section we shall then analyse how the key ingredients of leptogenesis in the N_2-dominated scenario are modified by the introduction of supersymmetry.

6.1 Calculation of the asymmetry within supersymmetric N_2-dominated leptogenesis

In this section we will extend the calculation of the asymmetry in the N_2-dominated scenario, as rising from $SO(10)$-inspired conditions, to a supersymmetric framework. The supersymmetric extension of the seesaw lagrangian eq. (2.46) is given by the superpotential [178, 179]

$$\mathcal{W}_{\ell+\nu+N} = \sum_{\alpha} D^{\ell}_{Y\,\alpha}\, \overline{l_\alpha} \epsilon H_d \ell_{R\alpha} + Y_{\alpha i}\, \overline{l_\alpha}\, \epsilon H_u N_{Ri} + \frac{1}{2}\sum_i \overline{N_{Ri}^{C}}\, D_{M\,i}\, N_{Ri} + \text{h.c.}, \tag{6.1}$$

where where l_α and $\ell_{R\alpha}$ are respectively the $SU(2)$ doublets and singlets lepton superfields, H_u and H_d are the Higgs superfields and ϵ is the total antisymmetric tensor. After spontaneous symmetry breaking the two neutral Higgs field VEVs, v_u and v_d, generate the Dirac masses for the charged leptons and for the neutrinos, respectively

$$m_\ell = v_d\, D^{\ell}_{Y} \qquad \text{and} \qquad m_D = v_u\, Y\,, \tag{6.2}$$

with $\tan\beta \equiv v_u/v_d$ and $v = \sqrt{v_u^2 + v_d^2} \simeq 174.6\,\text{GeV}$, the usual SM Higgs VEV.
The supersymmetric extension of the model implies modifications in the expression of the parameters related to leptogenesis, in particular of the decay parameters and of the CP asymmetries.

The flavoured decay parameters are given by

$$K_{i\alpha} = \frac{|m_{D\alpha i}|^2}{m_*^{MSSM}\, M_i}, \tag{6.3}$$

where the equilibrium neutrino mass is [105]

$$m_*^{MSSM} \equiv \frac{8\pi^{5/2}\sqrt{g_*^{MSSM}}}{3\sqrt{5}}\,\frac{v_u^2}{M_{\rm Pl}} = \frac{1}{2}\sqrt{\frac{g_*^{MSSM}}{g_*}}\, m_* \sin^2\beta \simeq 0.78\times 10^{-3}\sin^2\beta\,\text{eV}, \tag{6.4}$$

where m_* and g_* are the parameters in the SM. This difference is due to the fact that the number of decay channels into leptons is now double than in the SM and that, because of the presence of superpartners, the number of relativistic degrees of freedom is now $g_*^{MSSM} = 915/4$. We shall assume that g_*^{MSSM} does not change between the N_2 production and N_1 washout. The overall effect is to reduce the final value of m_*^{MSSM}, so that the decay factors are about $\sqrt{2}$ times larger than in the SM.

The CP asymmetries are different in the supersymmetric extension, due to the presence of additional interference terms. We shall focus on N_2's flavoured CP asymmetries, which are given by [178]

$$\varepsilon_{2\alpha} = \frac{3}{8\pi}\frac{M_2\, m_{\rm atm}}{v^2}\sum_{j\neq 2}\left(\mathcal{I}_{2j}^{\alpha}\,\xi\big(M_j^2/M_i^2\big) + \frac{2}{3}\mathcal{J}_{2j}^{\alpha}\frac{M_j/M_2}{M_j^2/M_2^2-1}\right), \tag{6.5}$$

where $\mathcal{I}_{2j}^{\alpha}$ and $\mathcal{J}_{2j}^{\alpha}$ are obtained from eqs. (2.120) and (2.121) respectively, but now

$$\xi(x) = \frac{x}{3}\left[\ln\left(\frac{1+x}{x}\right) - \frac{2}{1-x}\right]. \tag{6.6}$$

Neglecting here as well the interference with N_1, we obtain

$$\varepsilon_{2\alpha} \simeq \frac{3}{8\pi}\frac{M_2\, m_{\rm atm}}{v^2}\mathcal{I}_{23}^{\alpha}, \tag{6.7}$$

which is double compared to the SM case, eq. (3.112).

Finally, also the conversion factor of the $B-L$ asymmetry to the baryon-to-photon ratio, defined in eq. (2.172), is modified in the supersymmetric extension. Indeed it is $\eta_B = d^{MSSM}\, N_{B-L}^{\rm lep,f}$ where, following eq. (2.172) we have [105]

$$d^{MSSM} = 2\, a_{\rm sph}^{MSSM}\frac{3}{4}\frac{g_*^s(T_0)}{(g_*^s(T))^{MSSM}} \simeq 0.89\times 10^{-2}, \tag{6.8}$$

where $a_{\rm sph}^{MSSM} = 8/23$ [180, 181] and $(g_*^s)^{MSSM} = g_*^{MSSM} = 915/4$.
With these relations we shall compute the final $B-L$ asymmetry along the lines explained in the previous chapters. We will neglect again flavour coupling effects, which, in the supersymmetric extension, must receive a dedicated treatment [182]. We will also not consider the possibility given by soft leptogenesis, that offers a way to lower the leptogenesis scale, thus avoiding the gravitino problem [183–186].
The standard high scale leptogenesis scenario we have shown before gets modified when supersymmetry is introduced and light flavour effects are considered. Due to the structure of the superpotential eq. (6.1), the charged lepton masses are now given by

$$m_\alpha = (D_{Y_\alpha}^{\ell})^{MSSM} v_d, \tag{6.9}$$

where the VEV v_d appears, in place of v as in the SM. Therefore, to ensure the matching of the charged lepton masses we must have

$$(D_{Y_\alpha}^{\ell})^{MSSM} = (D_{Y_\alpha}^{\ell})^{SM}\frac{1}{\cos\beta}. \tag{6.10}$$

Using this relation in eq. (3.19) and in the discussion of section 3.1.2, we obtain that the thresholds of the fully-flavoured regimes are modified by a factor $(1+\tan^2\beta)$ [113, 187].

Considering, in our case, asymmetry production from the next-to-lightest, N_2, the three fully-flavoured production regimes are now given by

- $M_2 \gg 5\times10^{11}\,\text{GeV}(1+\tan^2\beta)$: unflavoured regime. The final asymmetry is given by eq. (3.57), where the different terms are computed in their supersymmetric version.
- $5\times10^{11}\,\text{GeV}(1+\tan^2\beta) \gg M_2 \gg 5\times10^{8}\,\text{GeV}(1+\tan^2\beta)$: two fully-flavoured regime. The asymmetry is computed from eq. (3.51).
- $M_2 \ll 5\times10^{8}(1+\tan^2\beta)$: three fully-flavoured regime. The asymmetry is computed as

  $$N_{B-L}^{\text{lep,f}} \simeq \varepsilon_{2e}\kappa(K_{2e})e^{-\frac{3\pi}{8}K_{1e}} + \varepsilon_{2\mu}\kappa(K_{2\mu})e^{-\frac{3\pi}{8}K_{1\mu}} + \varepsilon_{2\tau}\kappa(K_{2\tau})e^{-\frac{3\pi}{8}K_{1\tau}}. \quad (6.11)$$

  In the SM framework, this case is never realised in N_2-dominated leptogenesis, given the lower bound eq. (3.58). However, in the supersymmetric extension, large values of $\tan\beta$ can raise the threshold above this lower bound and cause the asymmetry production to take place in the three fully-flavoured regime.

As already discussed, in the transition regimes around $M_2 \simeq 5\times10^{11}\,\text{GeV}(1+\tan^2\beta)$ and $M_2 \simeq 5\times10^{8}\,\text{GeV}(1+\tan^2\beta)$ the asymmetry should be calculated using density matrix equations. We will not consider these particular regimes and we shall describe the transitions by switching sharply from one fully-flavoured regime to the other, depending on the value of M_2.

We can also study the evolution of a pre-existing asymmetry in the supersymmetric extension, taking into consideration the three different regimes described above.

- If $M_2 \gg 5\times10^{11}\,\text{GeV}(1+\tan^2\beta)$ it is impossible to realise successful strong-thermal leptogenesis, since N_2's washout cannot suppress the pre-existing asymmetry in any of the three light flavours. The pre-existing asymmetry can then be erased only by N_1's washout, occurring in the three fully-flavoured regime. However, this would also washout the produced asymmetry, thus making it impossible to realise successful leptogenesis.
- If $5\times10^{11}\,\text{GeV}(1+\tan^2\beta) \gg M_2 \gg 5\times10^{8}\,\text{GeV}(1+\tan^2\beta)$ successful strong thermal leptogenesis can be realised as in the SM case. The final pre-existing asymmetry is given by eqs. (3.67), (3.68) and (3.69) and can be efficiently washed out by imposing the conditions in eq. (3.70).
- If $M_2 \ll 5\times10^{8}\,\text{GeV}(1+\tan^2\beta)$ N_2's dynamics take place in the three fully-flavoured regime so that also the washout by N_2 occurs along the three light flavours. Eqs. (3.67), (3.68) and (3.69) are thus modified by the replacements

$K_{1e} \to K_{1e} + K_{2e}$ and $K_{1\mu} \to K_{2\mu} + K_{1\mu}$ in the exponentials. The conditions in eq. (3.70) are then modified to

$$K_{1e} + K_{2e},\, K_{1\mu} + K_{2\mu} \gtrsim K_{\rm st}(N^{\rm p,i}_{\Delta_{e,\mu}}), \qquad K_{2\tau} \gtrsim K_{\rm st}(N^{\rm p,i}_{\Delta_{\tau}}), \qquad K_{1\tau} \lesssim 1. \quad (6.12)$$

Hence, it is possible to have successful strong-thermal leptogenesis also with $K_{1\mu} \lesssim 1$, if $K_{2\mu} \gg 1$. This way, $K_{2\mu}$ will provide the washout of the pre-existing asymmetry along the μ-flavour, while small values of $K_{1\mu}$ will allow the final produced asymmetry to be dominated by the muon flavour, instead of tauon. Therefore, in the supersymmetric scenario it is possible to have a μ-dominated successful strong-thermal leptogenesis scenario.

We can now study how these modifications impact on the results on the low-energy neutrino parameters that we have derived in the previous chapter.

6.2 Low-energy neutrino parameters

In order to study the constraint imposed by successful leptogenesis and successful strong thermal leptogenesis on the low-energy parameters in supersymmetric $SO(10)$-inspired leptogenesis, we have numerically calculated the asymmetry and produced scatter plots as in the SM $SO(10)$-inspired case. Again, we have considered $(\alpha_1, \alpha_2, \alpha_3) = (1, 5, 1)$ and checked that, as in the SM case, the final results do not depend on α_1 and α_3. We also imposed the hierarchy condition $M_3 > 3M_2$, eq. (3.1). In the supersymmetric extension we have to distinguish between "small $\tan\beta$ values", in which the production takes place in the two fully-flavoured regime as in the non-supersymmetric case, and "large $\tan\beta$ values" for which the asymmetry is produced in the three-fully flavoured regime. Since for successful $SO(10)$-inspired leptogenesis, barring crossing level solutions, we typically have $M_2 \gtrsim 10^{11}\,{\rm GeV}$, and given the threshold $M_2 \simeq 5 \times 10^8\,{\rm GeV}(1 + \tan^2\beta)$, for $\tan\beta \gtrsim 15$ the production mainly occurs in the three fully-flavoured regime, while for $\tan\beta \lesssim 15$ it takes place in the two fully-flavoured one. On the other hand, since there are no solutions for $M_2 \gtrsim 3 \times 10^{12}\,{\rm GeV}$, we can conclude that for $\tan\beta \gtrsim 80$ all solutions fall in the three fully-flavoured regime. For definiteness, we considered two representative cases: $\tan\beta = 5$, in which the production occurs almost entirely in the two flavoured regime, and $\tan\beta = 50$ in which the asymmetry is mainly produced in the three fully-flavoured regime.

As in the SM case, we also distinguished between NO and IO light neutrino mass spectrum, so that we studied 4 cases in total.

All the parameter values were taken as described in the previous chapter for the non-supersymmetric case.

6.2.1 Normal ordering

We shall first deal with normally ordered light neutrino masses. As mentioned. we will separately discuss the $\tan\beta = 5$ and the $\tan\beta = 50$ cases.

6.2.1.1 **Small** $\tan\beta$ **values:** $\tan\beta = 5$

The value $\tan\beta = 5$ gives a threshold between the two-fully flavoured and the three fully flavoured regimes $M_2 \simeq 10^{10}\,\mathrm{GeV}$. This is sufficiently small to ensure that almost all values of M_2 fall in the two fully-flavoured regime. We present the results in fig. 6.1. As in the non-supersymmetric case, yellow points correspond to successful leptogenesis with $1 \leq V_L \leq V_{CKM}$, while orange points have $V_L = 1$. Here we consider thermal initial N_2 abundance.

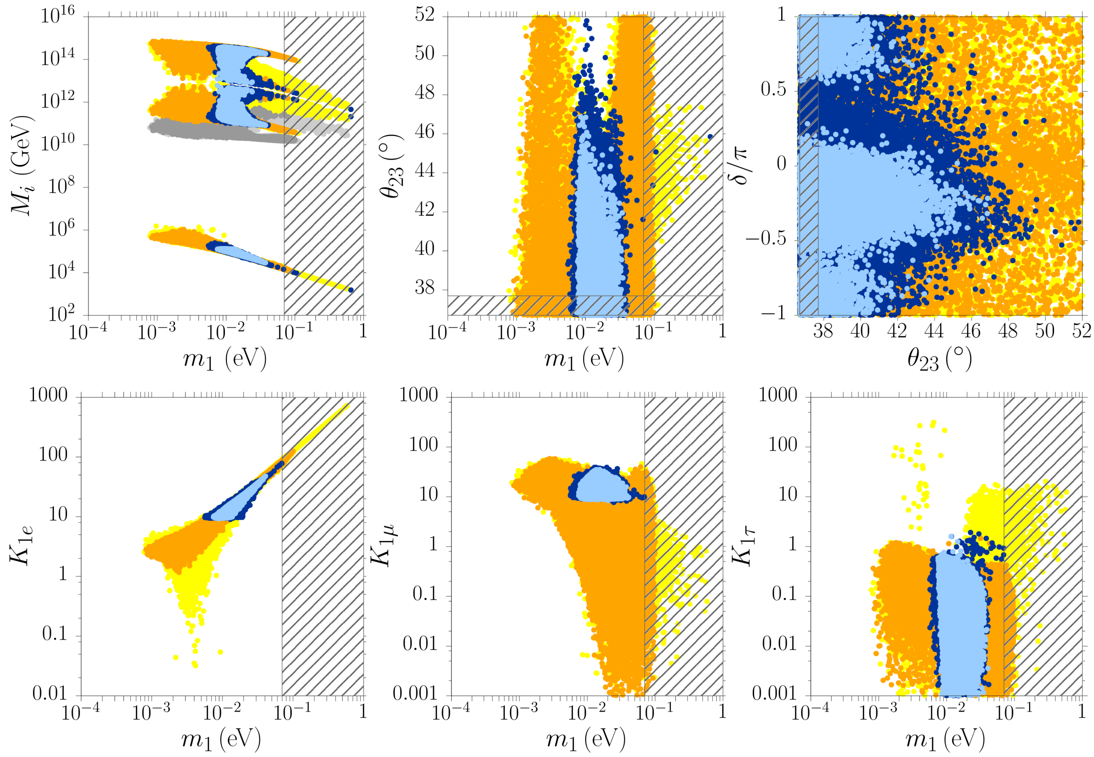

Figure 6.1: Scatter plots [3] in the low-energy neutrino parameter space projected on different selected planes for NO, in supersymmetric $SO(10)$-inspired leptogenesis. Here we have tan =5, $\alpha_2 = 5$ and thermal initial N_2 abundance. The yellow (orange) points realise successful leptogenesis for $1 \leq V_L \leq V_{\mathrm{CKM}}$ ($V_L = I$). The dark (light) blue points realise successful $SO(10)$-inspired strong thermal leptogenesis for $1 \leq V_L \leq V_{\mathrm{CKM}}$ ($V_L = I$) for an initial value of the pre-existing asymmetry $N^{\mathrm{p,i}}_{B-L} = 10^{-3}$. The hatched regions indicate either the cosmological upper bound eq. (1.43), or the values of θ_{23} excluded by current data at 3σ, eq. (5.11). The grey points indicate the minimum value of T_{RH}.

The results for $\tan\beta = 5$ are similar to those obtained in the non-supersymmetric case, fig. 5.2. It must be noticed that, even if they are obtained with thermal initial N_2 abundance, they are very little dependent on the initial N_2 abundance, since both for the τ-dominated and the μ-dominated solutions we have $K_{2\tau} \gg 1$ and $K_{2\tau_2^\perp} \gg 1$ respectively (except for very few points with $K_{2\tau_2^\perp} \simeq 1$). In principle, due to the smaller value of m_*^{MSSM} compared to m_*, the washout is stronger and therefore it should be more difficult to obtain $K_{1\tau} \lesssim 1$. However, from the analytical expression of $K_{1\tau}$, eq. (5.9) with $V_L = 1$, we know that $K_{1\tau} \lesssim 1$ produces conditions on the phases that are only marginally dependent on m_*^{MSSM}. The overall effect introduced by supersymmetry is an increase of the asymmetry at the production of a factor $\sim\sqrt{2}$, due to the doubling of the *CP* asymmetries partly compensated by the stronger washout. This causes the allowed range of m_1 to be slightly larger compared to the non-supersymmetric case. In particular, the upper bound moves from $0.06\,\text{eV}$ to $0.1\,\text{eV}$.

When studying successful strong thermal leptogenesis, we can notice that the most significant difference with respect to the non-supersymmetric case is given by the larger θ_{23} allowed range. In particular, we now have $\theta_{23} \lesssim 46^\circ$, more relaxed than the upper bound derived in the SM. We can understand this relaxation by considering the analytical description of the $V_L = 1$ case. The upper bound on θ_{23} is obtained by plugging the lower bound on m_1 in eq. (5.36). In strong thermal leptogenesis, the lower bound on m_1 is derived from the lower bound on m_{ee}, eq. (5.45), which is originated by the requirement $K_{1e} \gg 1$. Since in the supersymmetric case all $K_{1\alpha}$ are about $\sqrt{2}$ larger, the condition on K_{1e} is more easily satisfied, resulting in a relaxation of the lower bounds on m_{ee} and m_1. Indeed we now have $m_{ee} \gtrsim 6\,\text{meV}$, giving $m_1 \gtrsim 7\,\text{meV}$, as can be seen from the bottom-left panel in fig. 6.1. This in turn implies $\theta_{23} \lesssim 46^\circ$.

We can also study the dependence of the asymmetry on the value of α_2. To this aim, in fig. 6.2 we show the scatter plots of M_i vs. m_1 for integer values $\alpha_2 = 1, \ldots, 10$ and $1 \leq V_L \leq V_{CKM}$. Here we also plot the minimum requested value of T_{RH} and highlight the flavour that dominates the final asymmetry: red, green and blue colours correspond to electron-, muon- and tauon-domination respectively. It is possible to notice that, beyond τ- and μ-dominated, also e-dominated solutions appear. At low values, $\alpha_2 = 1, 2$, these are the only solutions found for $m_1 \lesssim 20\,\text{meV}$. As shown in section 3.3.1, for $V_L = 1$ the electron *CP* asymmetry ε_{2e} is many orders of magnitude suppressed compared to $\varepsilon_{2\mu}$ and, even more, to $\varepsilon_{2\tau}$ (see eq. (3.114) and fig. 3.4). However, when $V_L \neq 1$ this strict hierarchy does not hold anymore. In the non-supersymmetric case electron-dominated solutions can indeed be found, but are extremely marginal and were not mentioned in the previous discussion. They are obtained for very special conditions and the maximum possible asymmetry produced in these solutions is slightly above the observed value. In the supersymmetric case, since the produced asymmetry is increased by about a factor $\sqrt{2}$, these marginal e-dominated solutions can be realised more easily than in the SM case.

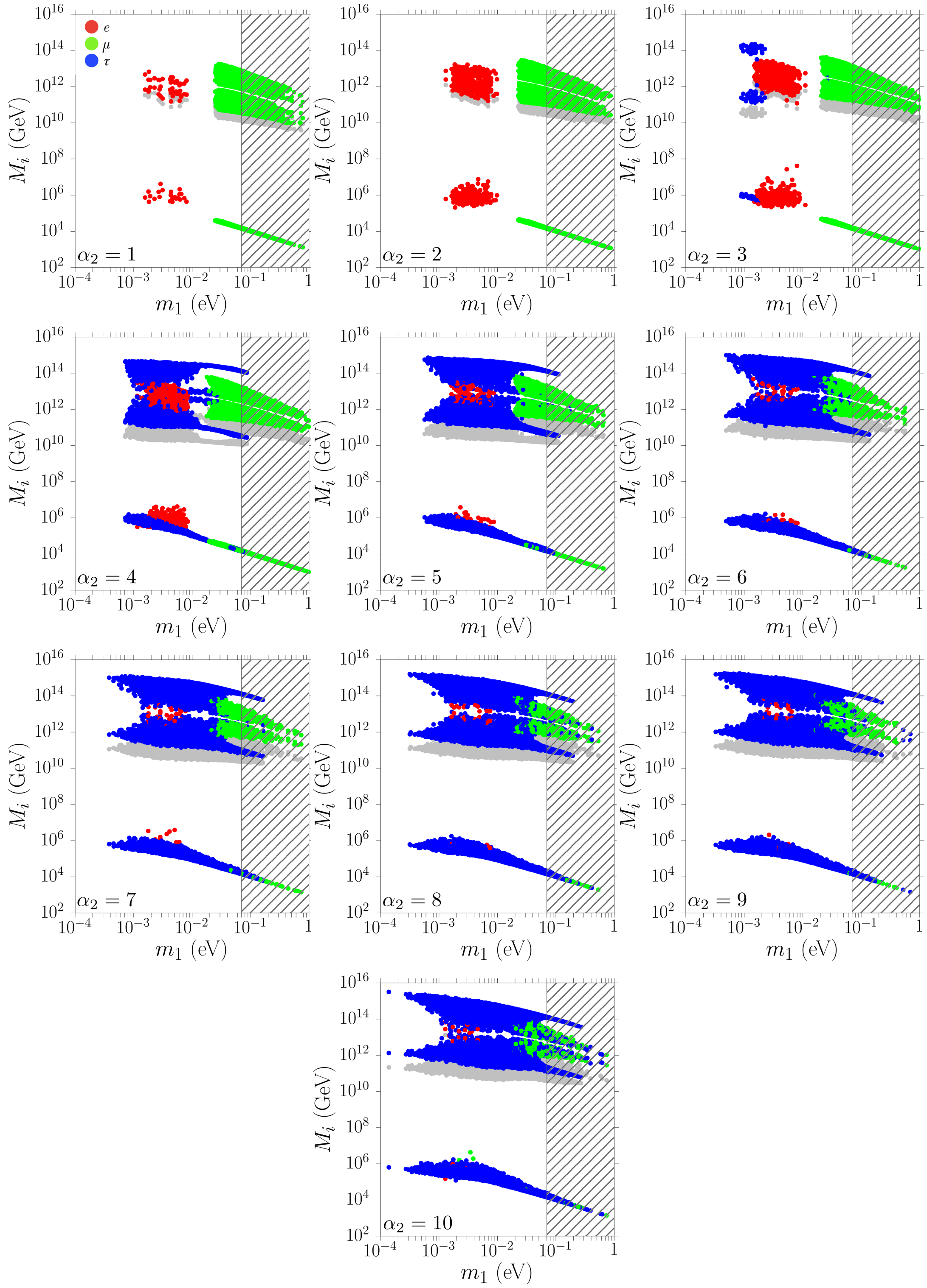

Figure 6.2: Scatter plots [3] in the plane M_i vs. m_1 for NO, $\tan\beta = 5$, $1 \leq V_L \leq V_{CKM}$ and for integer $\alpha_2 = [1, 10]$ from top left to bottom. All points respect the successful leptogenesis condition. The hatched region marks the cosmological upper bound, eq. (1.43). The red, green and blue points are such that the final asymmetry is dominated by the electron, muon and tauon flavour respectively. The grey points indicate the minimum value of $T_{\rm RH}$.

We must notice, however, that these solutions are realised only for $K_{2\tau_2^\perp} \lesssim 1$ and with thermal initial N_2 abundance. Therefore, they are strongly dependent on the initial N_2 abundance and disappear for initial vanishing N_2 abundance. For these reasons, we can conclude that these e-dominated solutions do not really open up a new allowed region in the low-energy parameters.

6.2.1.2 Large $\tan\beta$ values: $\tan\beta = 50$

For $\tan\beta = 50$ the threshold between the two-fully flavoured and the three-fully flavoured regimes is $M_2 \simeq 10^{12}\,\text{GeV}$, so that the production occurs mostly in the three fully-flavoured one. The results are shown in fig. 6.3 and are obtained for the same setup as in the small $\tan\beta$ regime. It is possible to notice that the constraints are now generally more relaxed than in the $\tan\beta = 5$ case. However, there is still a lower bound $m_1 \gtrsim 1\,\text{meV}$, so that we can conclude that the lower bound on m_1 is quite stable, constituting a general feature of $SO(10)$-inspired leptogenesis.

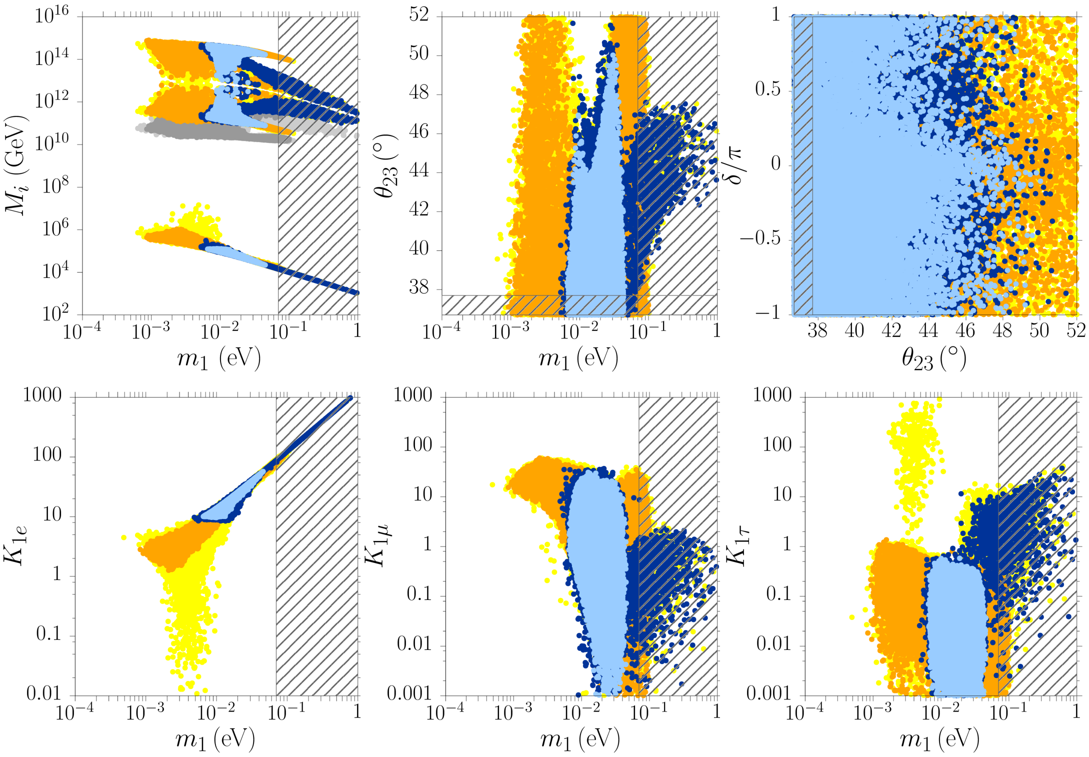

Figure 6.3: Scatter plots as in fig. 6.1 for NO but with $\tan\beta = 50$, [3].

Considering strong thermal leptogenesis, the allowed region is more extended as well. Moreover, we can find successful strong thermal leptogenesis solution also for high values of the absolute neutrino mass scale $m_1 \gtrsim 50\,\text{meV}$.

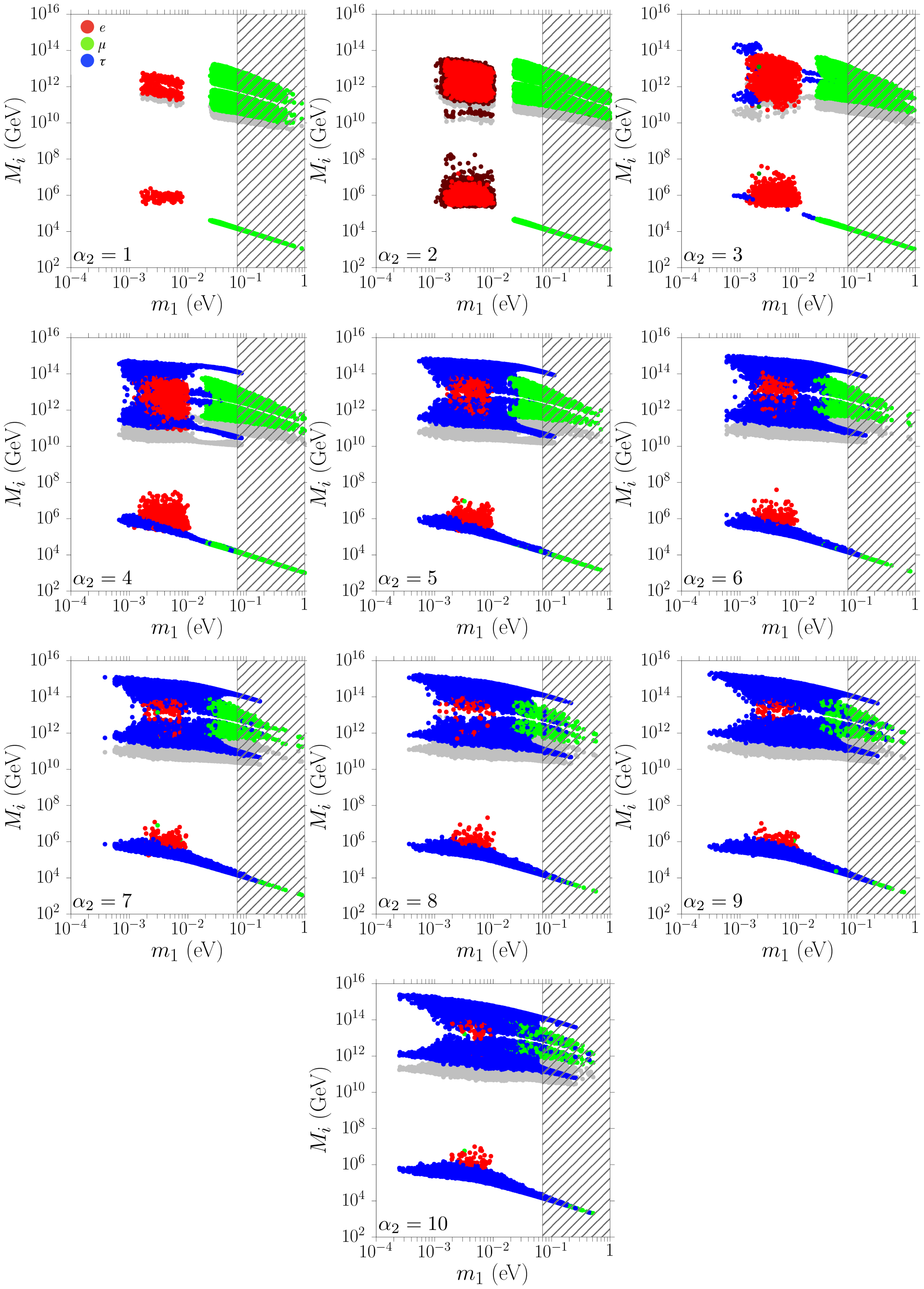

Figure 6.4: Scatter plots as in fig. 6.4, but with $\tan\beta = 50$, [3]. In the second panel, for $\alpha_2 = 2$, the dark red points correspond to e-dominated solutions with $|\Omega_{ij}|^2 \geq 3$.

We know that for these values of m_1 the solution is μ-dominated and indeed in the SM case strong thermal leptogenesis could not be realised in this region. However, in the supersymmetric framework, for $\tan\beta = 50$, M_2 falls in the three fully-flavoured regime, therefore, as mentioned above, we can have successful leptogenesis with $K_{2\mu} \gg 1$ and $K_{1\mu} \lesssim 1$, which imply a μ-dominated scenario. Nevertheless, this new μ-dominated strong thermal leptogenesis solutions are largely excluded by the cosmological upper bound on m_1.

As in the small $\tan\beta$ case, we can study the behaviour of the final asymmetry at different values of α_2. In fig. 6.4 we show the scatter plots of M_i vs. m_1 for $\alpha_2 = 1, \ldots, 10$, highlighting the flavour dominating the final asymmetry, as in fig. 6.2. From the bottom-left panel of fig. 6.3 it can be noticed that for $V_L \neq 1$ (yellow points) the region satisfying $K_{1e} \lesssim 1$ is enlarged compared to the previous cases. Indeed, from fig. 6.4 it is clear that electron-dominated solutions are more numerous than before, in the range $2\,\mathrm{meV} \lesssim m_1 \lesssim 10\,\mathrm{meV}$. Moreover, these solutions are always realised for weak washout, but now, in the three fully-flavoured regime, $K_{2e} \lesssim 1$ is more easily satisfied than $K_{2\tau_2^{\perp}} \lesssim 1$ as for $\tan\beta = 5$. They can also allow for a relaxation of the reheating temperature $T_{\mathrm{RH}} \lesssim 10^{10}\,\mathrm{GeV}$. In the second panel in fig. 6.4, for $\alpha_2 = 2$, we have marked with a darker red colour those e-dominated solutions that are obtained with a complex orthogonal matrix such that $|\Omega_{ij}|^2 \geq 3$. As already discussed, models with larger entries of the orthogonal matrix entail some degree of fine tuning in the seesaw formula. We can therefore see that those e-dominated solutions that correspond to the lowest values of T_{RH} are obtained at the expense of some fine tuning. Moreover, it must be recalled that these solutions exist only for thermal initial abundance of N_2. We can conclude that these electron solutions are quite fine tuned and, in particular, strongly dependent on the initial conditions.

6.2.2 Inverted ordering

We shall now study the IO case, distinguishing between small $\tan\beta$ and large $\tan\beta$ values.

6.2.2.1 Small $\tan\beta$ values: $\tan\beta = 5$

The results for $\tan\beta = 5$ in the IO case are shown in fig. 6.5. As for NO, for $\tan\beta = 5$ the results on the low-energy neutrino parameters are very similar to the non-supersymmetric case. This allows us to conclude that also in the supersymmetric extension IO is disfavoured compared to NO. However, the allowed regions are slightly enlarged compared to the SM. In particular, there is no lower bound on the atmospheric mixing angle. Nevertheless, values of θ_{23} in the second octant require high values of m_1, very close to the cosmological upper bound.

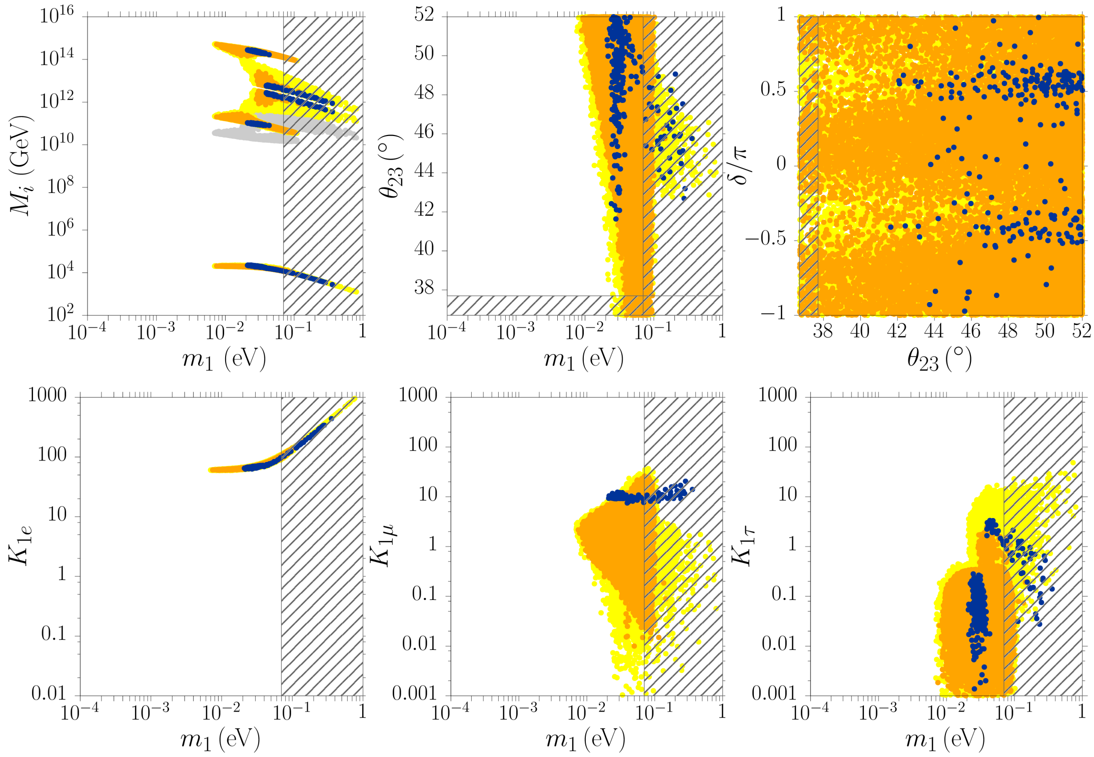

Figure 6.5: Scatter plots as in fig. 6.1, with $\tan\beta = 5$, but for IO, [3].

In fig. 6.6 we show the solutions for various values of α_2, with the same colour code as in fig. 6.2 and 6.4. We can now notice that even for thermal N_2 initial abundance there are no e-dominated solutions. Indeed, in IO we have $K_{1e} \simeq m_{ee}/m_*^{MSSM} \gtrsim 70$, as can be noticed from the bottom-left panel of fig. 6.5. This implies that the electron asymmetry is completely washed out by N_1.

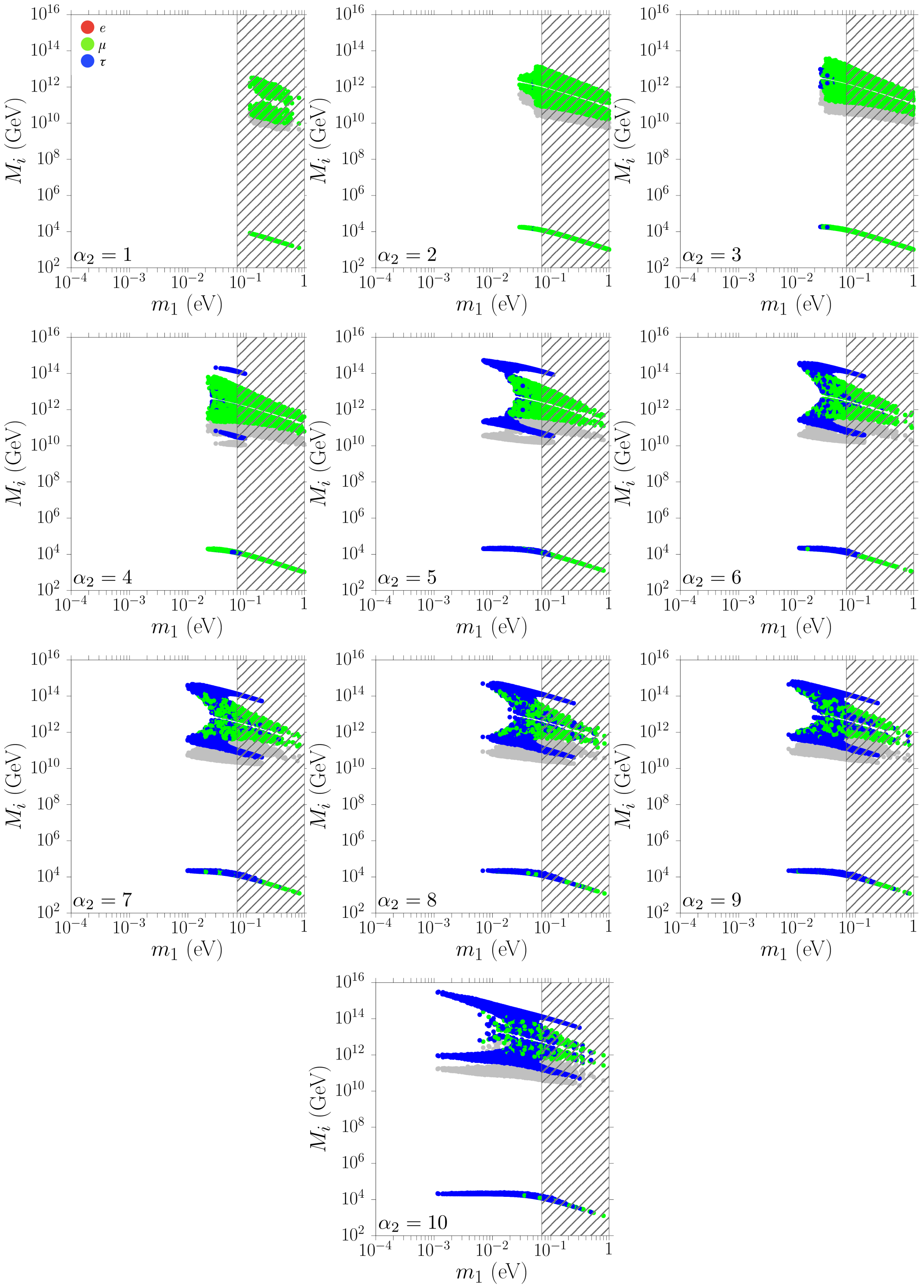

Figure 6.6: Scatter plots as in fig. 6.2, with $\tan\beta = 5$, but for IO, [3].

6.2.2.2 Large $\tan\beta$ values: $\tan\beta = 50$

For large $\tan\beta$ values and imposing successful leptogenesis condition, the situation is qualitatively similar to the previous case, as one can see from fig. 6.7. The allowed regions slightly further enlarge: for instance, now we have $m_1 \gtrsim 7\,\mathrm{meV}$.

We can find a substantial difference with the non-supersymmetric scenario when successful strong thermal leptogenesis is required. In the supersymmetric case we can indeed find solutions realising successful strong thermal leptogenesis both for $V_L = 1$ and $V_L \neq 1$, while in the SM this did not occur. The reason is that for large $\tan\beta$, as already mentioned, the condition for the washout of the pre-existing asymmetry is now $K_{1\mu} + K_{2\mu} \gg 1$ and can be easily satisfied even for low $K_{1\mu}$ values.

We can conclude that in all cases supersymmetry helps realising successful strong thermal leptogenesis.

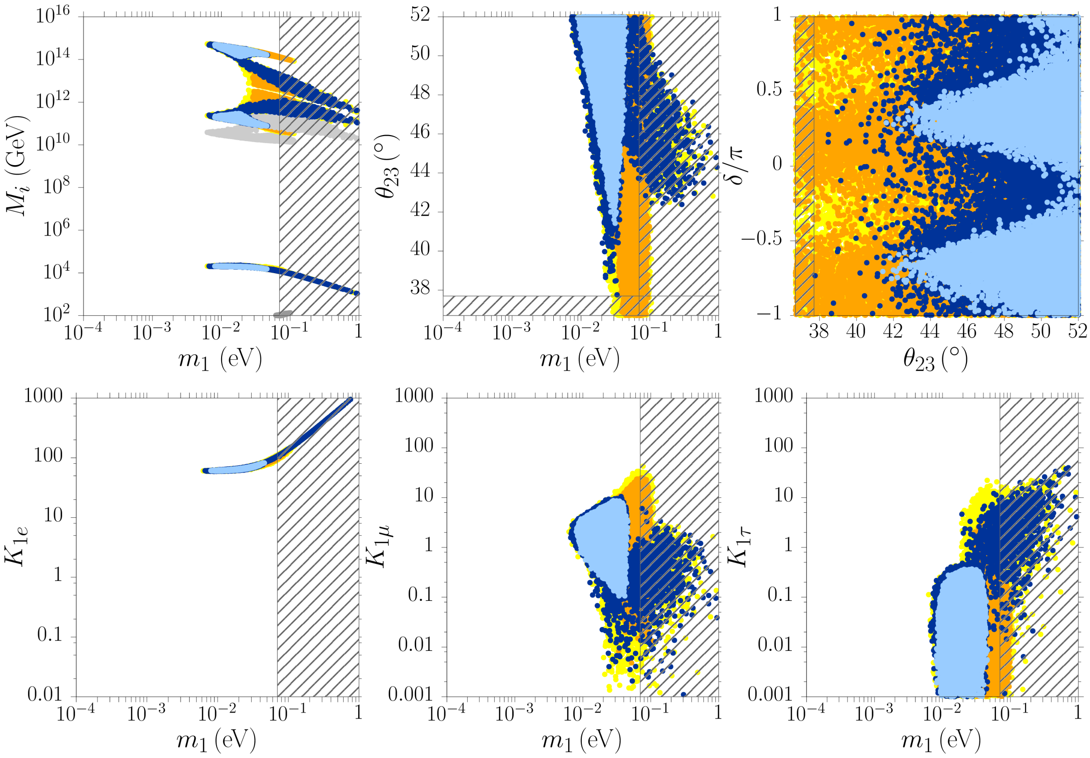

Figure 6.7: Scatter plots as in fig. 6.3, with $\tan\beta = 50$, but for IO, [3].

In the panels of fig. 6.8 we show the dominant flavour as in figs. 6.2, 6.4 and 6.6. We can see that, for the same reason as for small $\tan\beta$, there are no electron dominated solutions.

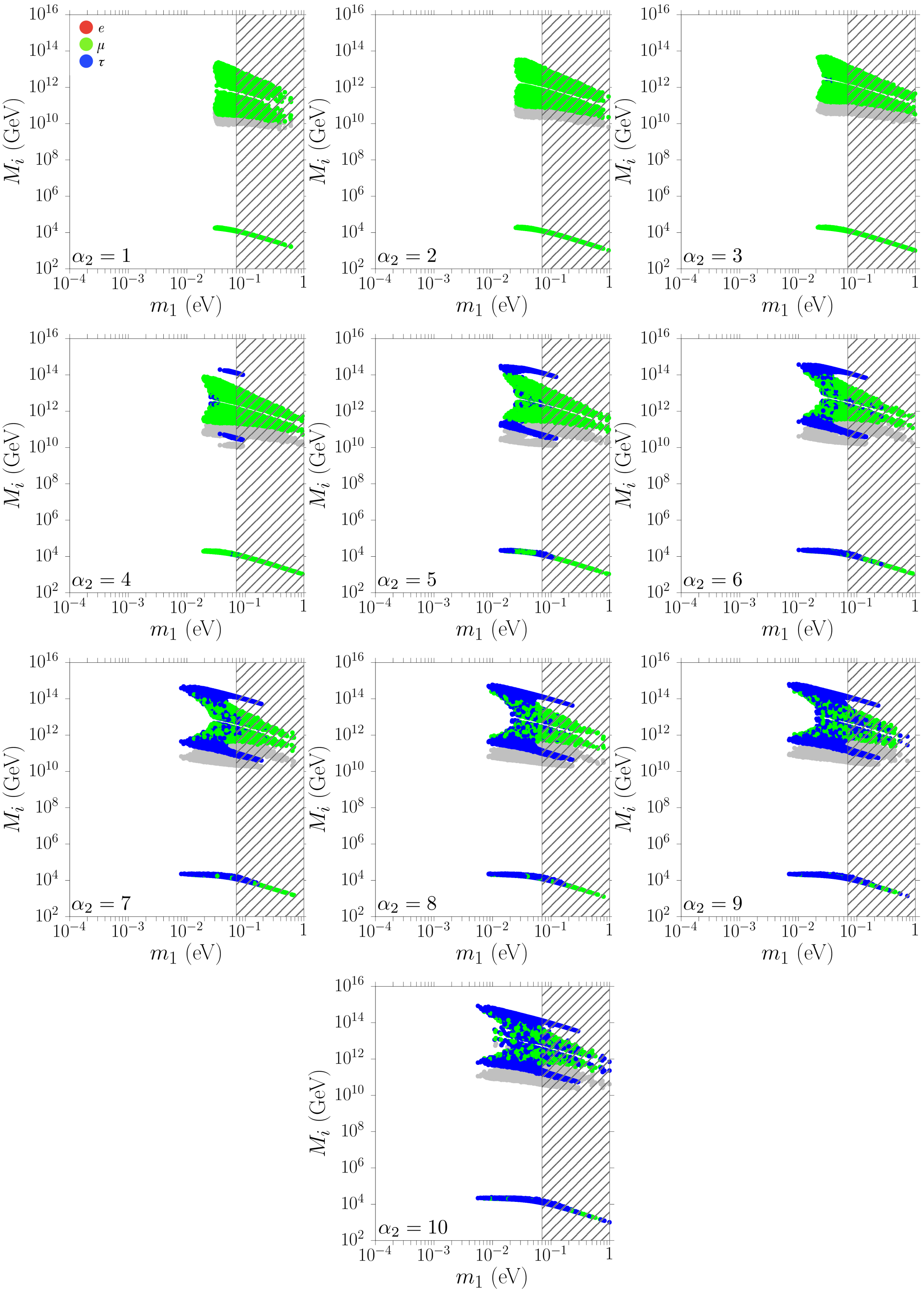

Figure 6.8: Scatter plots as in fig. 6.4, with $\tan\beta = 50$, but for IO, [3].

6.3 Lower bound on the reheating temperature

Our scenario of thermal leptogenesis requires that the initial temperature of the radiation dominated regime, the *reheating temperature* $T_{\rm RH}$ within inflation, be high enough for the heavy neutrinos to be thermally produced before their interactions, in particular their inverse decays, go out of equilibrium producing the asymmetry. As mentioned at the beginning of the chapter, in the supersymmetric scenario the lower bound on $T_{\rm RH}$ imposed by thermal leptogenesis can be in tension with the constraint imposed by the gravitino problem. The upper bound on the reheating temperature, in order not to overproduce the gravitino, can be conservatively assumed to be $T_{\rm RH} \lesssim 10^{10}\,{\rm GeV}$. This clashes with what was found in the non-supersymmetric case, $T_{\rm RH} \gtrsim 10^{10}\,{\rm GeV}$ [159], and even in a dedicated analysis of the supersymmetric scenario [188], where it was concluded that supersymmetric thermal leptogenesis requires $T_{\rm RH} \gtrsim 10^{11}\,{\rm GeV}$. For these reasons it is interesting to study the results on the reheating temperature obtained within supersymmetric $SO(10)$-inspired thermal leptogenesis.

As discussed in section 2.2.4, in the strong washout regime a good measure of the scale at which the asymmetry is produced is provided by the function $z_L(K)$, eq. (2.165). When flavour effects are taken into account, and assuming that the final asymmetry produced by N_2 is dominated by flavour α, we can estimate the leptogenesis temperature scale as $T_L = M_2/z_L(K_{2\alpha})$, where $\alpha = \tau$, $\tau_2^{\perp}$ in the two fully-flavoured regime or $\alpha = e, \mu, \tau$ in the three fully-flavoured regime. Clearly, there could be fine tuned situations in which the contributions from different flavours are equivalent. In these cases we should take $T_{\rm RH}$ above the maximum value out of the relevant flavours. We can, thus, identify a temperature interval around T_L in which the asymmetry is produced [94]

$$\frac{M_2}{z_L(K_{2\alpha})+2} \lesssim T \lesssim \frac{M_2}{z_L(K_{2\alpha})-2}, \tag{6.13}$$

so that in the strong washout regime we can require the reheating temperature to be

$$T_{\rm RH} \gtrsim T_{\rm RH}^{\rm min}(K_{2\alpha}) \simeq \frac{M_2}{z_L(K_{2\alpha})-2}. \tag{6.14}$$

In the weak washout regime it is not possible to identify such a sharp interval of temperatures and, moreover, the process of production of the asymmetry depends on the initial N_2 abundance. In this regime we can generally require $T_{\rm RH} \gtrsim M_2$.

An expression that interpolates quite well between the strong and weak washout regimes is given by [94]

$$T_{\rm RH}^{\rm min}(K_{2\alpha}) \simeq \frac{M_2}{z_L(K_{2\alpha}) - 2\exp(-3/K_{2\alpha})}. \tag{6.15}$$

This expression gives the minimum of the reheating temperature for each solution with specific values of $K_{2\alpha}$ and M_2. The global lower bound on $T_{\rm RH}$ for each α_2 can then be calculated minimising over all the solutions found

$$T_{\rm RH}^{\rm min} \equiv \min[T_{\rm RH}^{\rm min}(K_{2\alpha})]. \tag{6.16}$$

For each point satisfying successful leptogenesis we computed the corresponding $T_{\rm RH}^{\rm min}(K_{2\alpha})$ value. These are shown with grey points in all plots where also the heavy neutrino masses are plotted. In particular, in figs. 6.2, 6.4, 6.6 and 6.8, for $\alpha_2 = 1, \dots, 10$. We can expect a non trivial dependence of the reheating temperature on α_2, since, for decreasing α_2, one has that M_2 decreases, which would lower $T_{\rm RH}$. However, the final asymmetry decreases as $\propto \alpha_2^2$, so that there must be a lower bound on α_2 coming from successful leptogenesis.

We summarised the dependence of the global lower bound on the reheating temperature on α_2 in fig. 6.9. Here $T_{\rm RH}^{\rm min}$ is computed for each value of $\alpha_2 = 1, \dots, 10$ minimising over the models with $m_1 < 0.07\,{\rm eV}$, the cosmological upper bound on m_1, eq. (1.43). In fig. 6.9 we indicated which flavour dominates the final asymmetry with the same colour code as in in figs. 6.2, 6.4, 6.6 and 6.8.

The results are shown both for initial thermal N_2 abundance (thin lines) and for vanishing initial N_2 abundance (thick lines). Dotted lines correspond to $V_L = 1$ scenarios, while dashed lines to $V_L = V_{CKM}$. In the left (right) panels we show the results for low (high) values of $\tan\beta$, while in the top (bottom) panels the results for NO (IO).
In the case of low $\tan\beta$ values, left panels, one can see how the results do not differ much from those in the non-supersymmetric case [159]. There is actually a $\sim \sqrt{2}$ relaxation due to the increase of the asymmetry at the production.
In the right panels, for large $\tan\beta$ values, we can notice that in the NO case the red branch, corresponding to the e-dominated solutions, for $\alpha_2 \in [1, 2]$, allows for temperatures as low as $T_{\rm RH}^{\rm min} \simeq 4 \times 10^9\,{\rm GeV}$, showing that it is possible to go below $10^{10}\,{\rm GeV}$. However, as already mentioned, these e-dominated solutions exhibit two important problems. Firstly, they exist only for thermal initial N_2 abundance. This requires further justification within larger theoretical models where, for instance, heavy neutrinos are produced by Z' particles of a left-right symmetry left by the breaking of $SO(10)$ [189]. Secondly, these solutions are characterised by large values of $|\Omega_{ij}|^2$, thus implying fine-tuned cancellations in the seesaw formula. For these reasons, these solutions, though appealing and representing a viable possibility, should not be over-emphasised. We must then more conservatively consider the values of $T_{\rm RH}^{\rm min}$ given by μ- and τ-dominated solutions which are independent of the initial N_2 abundance and not fine tuned. Indeed, when considering vanishing initial N_2 abundance, only these solutions survive, while the e-dominated ones disappear.

We can therefore conclude that supersymmetric $SO(10)$-inspired leptogenesis conservatively gives a lower bound on the reheating temperature $T_{\rm RH} \gtrsim 1 \times 10^{10}\,{\rm GeV}$. This is in line with the conservative, model independent bound posed by the gravitino problem.

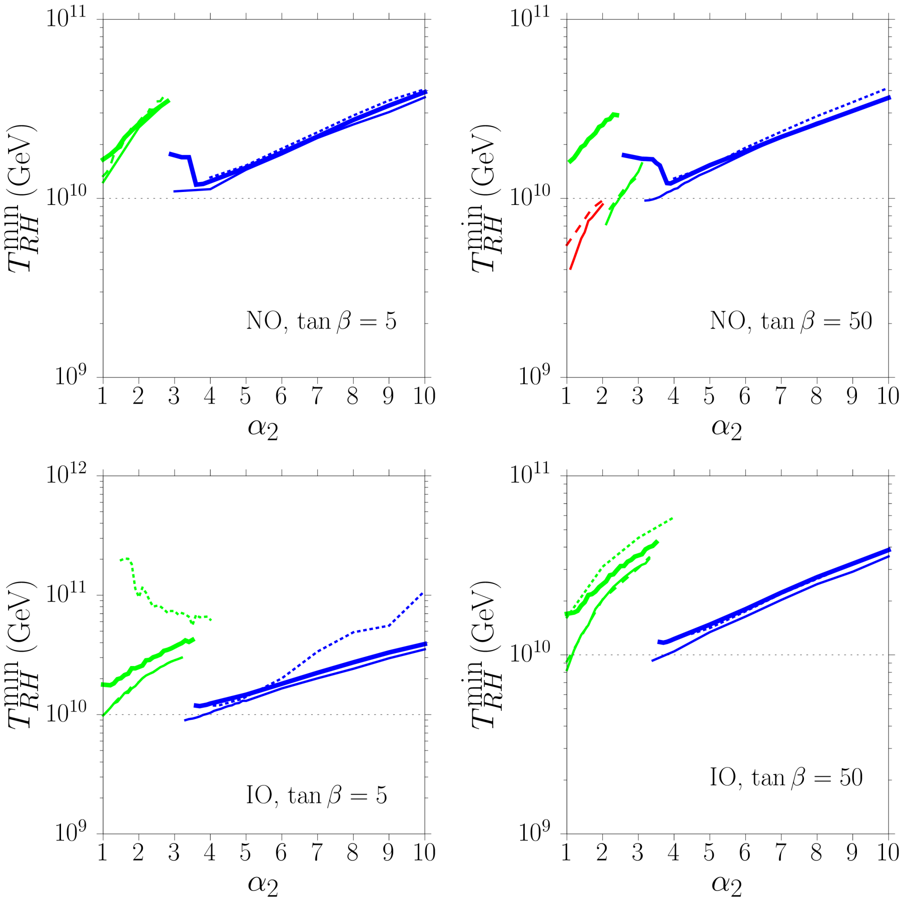

Figure 6.9: Global lower bound on $T_{\rm RH}$ as a function of α_2, [3]. The blue, green and red lines correspond to an asymmetry tauon, muon and electron dominated respectively. Thin lines are for initial thermal N_2 abundance. Solid lines are for $1 \leq V_L \leq V_{CKM}$, dotted for $V_L = 1$ and dashed for $V_L = V_{CKM}$. The thick solid lines are for initial vanishing abundance and $1 \leq V_L \leq V_{CKM}$. The top (bottom) panels are for NO (IO). The left (right) panels are for $\tan\beta = 5\,(50)$.

Indeed, for large values of the gravitino mass, $m_{3/2} \gtrsim 30\,\text{TeV}$, it is possible to reconcile the lower bound imposed by $SO(10)$-inspired thermal leptogenesis with the bound imposed by the gravitino problem [174]. Clearly, within specific models one should verify whether the lower bound $T_{\rm RH}^{\rm min} \simeq 1 \times 10^{10}\,\text{GeV}$ can indeed be saturated.

There is, however, another possibility, proposed in [3], that can relax the lower bound even below $10^{10}\,\text{GeV}$, without the need for fine-tuned solutions.

6.4 A new scenario of N_2-dominated leptogenesis

It is typically assumed that the lightest heavy neutrino mass M_1 is heavier than the sphaleron freeze-out scale [82]

$$M_1 \gtrsim T_{\rm sph}^{\rm out} \simeq 100\,\text{GeV}. \tag{6.17}$$

In this case the lightest heavy neutrino washout affects the entire $B-L$ asymmetry and has to be taken into account. However, if M_1 is below $T_{\rm sph}^{\rm out}$, then its washout can only act on the lepton asymmetry, leaving untouched the produced baryon asymmetry, now frozen. More precisely, N_1's washout acts within the temperature interval $T=[M_1/z_1, M_1/z_2]$ with $z_2 \simeq 2/\sqrt{K_{1\alpha}}$ [94]. Therefore, more precisely one has to impose $M_1 \lesssim z_1\, T_{\rm sph}^{\rm out}$.

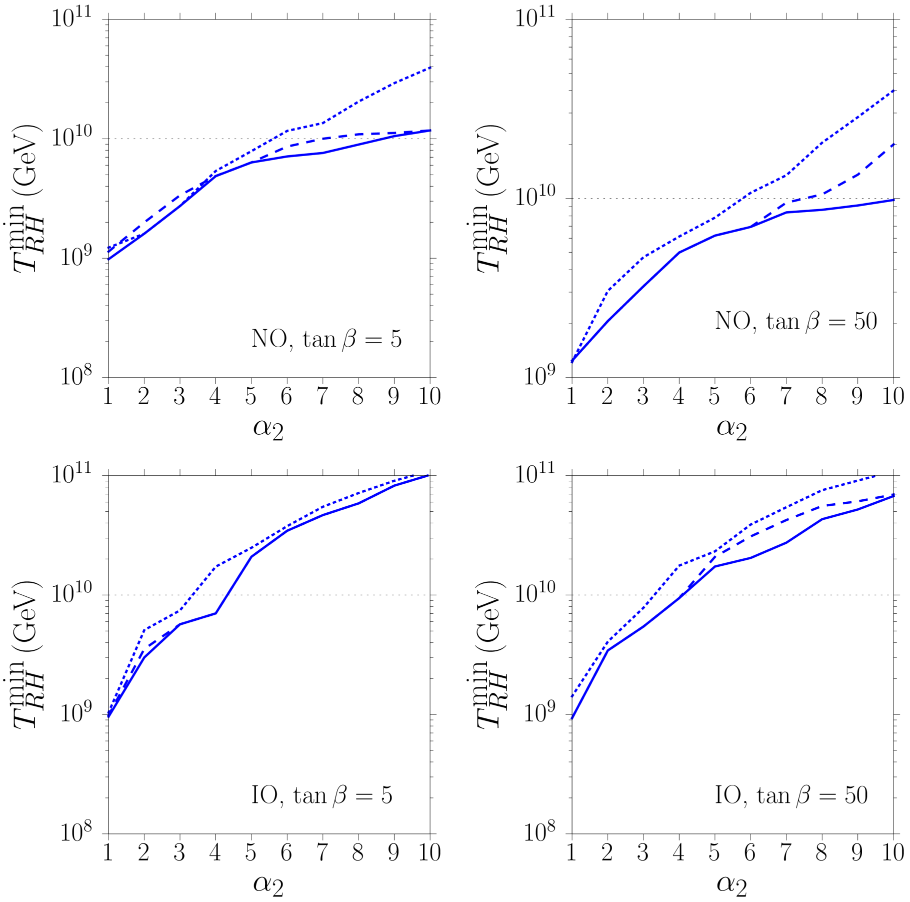

Figure 6.10: Lower bound on $T_{\rm RH}$ as a function of α_2 for models with $M_1 \lesssim T_{\rm sph}^{\rm out}$, [3]. The top (bottom) panels are for NO (IO). The left (right) panels are for $\tan\beta = 5\,(50)$. The line code is the same as in fig. 6.9.

In any case, conservatively assuming $M_1 \lesssim T_{\rm sph}^{\rm out}$, the final asymmetry is given in the various regimes by eqs. (3.57), (3.51) and (6.11) without the exponentials encoding the washout by N_1.

We can then repeat the calculation of $T_{\rm RH}^{\rm min}$ in this scenario and the results are shown in the four panels of fig. 6.10, that correspond to the same cases of fig. 6.9. In this cases the minimum is always realised within τ-dominated solutions with strong washout at the production, so that the final asymmetry is independent of the initial N_2 abundance. Moreover, these solutions do not imply fine tuning, since we always naturally have $|\Omega_{ij}|^2 \lesssim 1$. It can be seen, remarkably, that values of $T_{\rm RH}$ as low as $10^9\,$GeV are possible. In this case the gravitino overabundance problem can be circumvented for a wider range of gravitino masses compared to the traditional scenario discussed above.

From eq. (3.90) we can see that this scenario can be realised for values $\alpha_1 \lesssim 0.1$. This implies that $m_{D3} \ll T_{\rm sph}^{\rm out} \sim 100\,{\rm GeV}$ in order for the seesaw limit to be valid, therefore giving $\alpha_3 \ll 1$ as well. One can wonder whether this can be achieved in some realistic models. Interestingly, in [170] where fits to realistic $SO(10)$ GUT models are performed, the found best case is realised for $M_1 \simeq 1\,{\rm TeV}$ corresponding to $\alpha_1 \simeq 0.3$. Since this case also has a very small $\chi^2_{\rm min} \simeq 0.6$, it can be tempting to think that, with some deviation from the best fit, $M_1 \lesssim T_{\rm RH}^{\rm sph}$ can be obtained, with a still acceptable value of $\chi^2_{\rm min}$. In any case, the specific case found in [170] seems to suggest that this scenario might be indeed realised within some realistic model.

Finally, in this scenario the low-energy neutrino constraints are not showed because they basically disappear. As discussed in chapter 5, these constraints exist mainly because of the presence of N_1's washout. Removing the action of N_1 make these bounds vanish. It is also worth mentioning that, though introduced in a supersymmetric framework, this scenario might be realised and find applications within a non-supersymmetric framework as well.

6.5 Comments and remarks

In the study of the supersymmetric extension of $SO(10)$-inspired leptogenesis we have made some assumptions that can have some impact on the final results. However, the effect of the approximations adopted should not be large. The main sources of theoretical uncertainties are listed below.

- Flavour coupling has been neglected as in the non-supersymmetric scenario. The treatment of flavour coupling is generally similar to the SM case, however the presence of supersymmetric particles and additional high-energy symmetries (such as R and Peccei-Quinn symmetries) require a dedicated and detailed study [182]. As already discussed, the inclusion of flavour coupling can in general open new ways to avoid N_1's washout. Therefore it is clear that its effect can at most result in a relaxation of the reheating temperature in the traditional scenario ($M_1 \gtrsim T_{\rm sph}^{\rm out}$) to the minimum value, $T_{\rm RH}^{\rm min} \simeq 1 \times 10^9\,{\rm GeV}$, found in the new scenario with $M_1 \lesssim T_{\rm sph}^{\rm out}$.
- The regimes around $M_2 \simeq 5{\times}10^8\,{\rm GeV}(1{+}\tan^2\beta)$ and $M_2 \simeq 5 \times 10^{11}\,{\rm GeV}(1+\tan^2\beta)$ have been described by an instantaneous transition from one fully-flavoured regime to another. As mentioned, a detailed treatment with density matrices should be employed.

- In the supersymmetric extension, especially for large values of $\tan\beta$, the running of low-energy neutrino parameters might be important and give some modifications to the constraints we derived [190–192]. However, this effect does not change our main results on the lower bound on the reheating temperature.

We must also notice that the results on $T_{\rm RH}$ we obtained for $\alpha_2 = 5$, $T_{\rm RH} \gtrsim 1.5\times 10^{10}\,\rm GeV$ [3], is more than one order of magnitude lower than what is obtained in [188]. Indeed, there it was found quite a stringent lower bound $T_{\rm RH} \gtrsim 5 \times 10^{11}\,\rm GeV$, which entailed that thermal supersymmetric $SO(10)$-inspired leptogenesis was not compatible with the gravitino problem. Hence, this motivated the quest for different, non-thermal, scenarios. Given the lack of some details about the calculation in [188] (for instance, it is not explained how the matrix U_R is computed) it is not possible to provide an explanation for this discrepancy. We can just notice that in [188] the τ-dominated solutions we found are completely absent and the lower bound on $T_{\rm RH}$ obtained thereby relies on e-dominated solutions. For what shown above, this implies a dependence on the initial N_2 abundance.

It is interesting to notice that our result on the lower bound on the reheating temperature in the traditional scenario, $T_{\rm RH} \gtrsim 1 \times 10^{10}\,\rm GeV$, falls in the vicinity of what is needed in order to produce the DM gravitino abundance, depending on the gluino mass. For this reason, it may be tempting to relate matter-antimatter asymmetry production in thermal leptogenesis to gravitino DM production, as done for N_1-dominated scenarios [193]. However, recent LHC results on the lower bound on gluino masses [194, 195] pose a stringent upper bound on the reheating temperature $T_{\rm RH} \lesssim 5 \times 10^{9}\,\rm GeV$ within the pMSSM [196]. This would then disfavour this intriguing link between baryon asymmetry and gravitino DM. As we have seen, the new scenario we proposed, with $M_1 \lesssim T_{\rm sph}^{\rm out}$ can in any case still be compatible with this more stringent constraint.

Chapter 7

Summary and conclusions

In this final part, we shall summarise the previous chapters, highlighting the most important points that guided the development of this work. For the sake of clarity, we shall divide this resumé in sections following the chapter structure.

7.1 Two serious problems

Although the Standard Model of particle physics can probably be regarded as the most successful theory developed so far, several issues remain unsolved. Apart from leaving aside the gravitational interaction and not contemplating the presence of DM and DE, the SM fails to explain two other fundamental aspects: the baryon asymmetry of the Universe and neutrino oscillations.

In section 1.1 we introduced the baryon asymmetry of the Universe. We pursue the quest for a dynamical mechanism, able to generate this asymmetry from symmetric (and thus "natural") initial conditions. Such a mechanism must satisfy the three conditions pointed out by A. Sakharov, that were thereby explained. Moreover, this mechanism must be able to produce an amount of asymmetry compatible with the experimental observations. In order to be more quantitative, we introduced the baryon-to-photon ratio η_B and mentioned how it can be precisely measured via BBN and by the study of the acoustic peaks in the CMB angular power spectrum.

In section 1.2 we introduced the other problem of the SM we focused on: neutrino oscillations. Several experiments measuring neutrino fluxes from different sources have accumulated striking evidences that neutrinos can change their flavour during their propagation. We briefly showed that neutrino oscillations can take place only if not all of the neutrinos are massless, in net contrast with the assumptions of the SM. Neutrino oscillations can be described with the introduction of the PMNS matrix U, and two mass-squared differences, Δm^2_{atm} and Δm^2_{sol}. These parameters can be efficiently probed by neutrino oscillations experiments. However, the absolute neutrino masses can only be measured through other kinds of experimental evidences, such as β-decay, $0\nu\beta\beta$ decay experiments or cosmological observations. Currently, cosmology can provide us with the most stringent upper bounds.

Having described these two important shortcomings of the SM, we introduced the idea of *leptogenesis* within the *seesaw* extension of the SM, which provides an explanation to both problems at the same time. The seesaw mechanism can account for neutrino mixing and masses in a rather natural way, at the price of introducing additional particles and free parameters. In turn, these same particles can be responsible for the generation of the baryon asymmetry in the Early Universe. This establishes a strict link between neutrino phenomenology and cosmology, thus allowing us to employ cosmological evidences, such as the baryon asymmetry, to constrain and predict the otherwise free parameters of the seesaw mechanism. This is the guideline of our work. In order to follow our main goal, we described in detail the seesaw mechanism and the generation of the baryon asymmetry via leptogenesis.

7.2 The foundations

In chapter 2 we studied in detail how the SM can be extended in order to provide neutrinos with a mass term. We focused on the seesaw mechanism by highlighting its features and the number of additional parameters it introduces.

7.2.1 Neutrino masses

The simplest ways to account for neutrino masses, and hence neutrino mixing, are given by the introduction in the SM lagrangian of a “Dirac” or a “Majorana” neutrino mass term, whether neutrinos are Dirac or Majorana fermions. In sections 2.1.1 and 2.1.2 we briefly discussed the main features of these two possibilities. We then turned to the most interesting case, given by the combination of both. This is the basis of the so called *seesaw mechanism*. In its type-I formulation, additional right handed Majorana neutrinos, singlets under the SM gauge group, are introduced, together with their Majorana mass term and Yukawa couplings to left handed lepton and Higgs doublets. If the Majorana mass scale, M, is much larger than the electroweak scale $v \simeq 174\,\mathrm{GeV}$, the neutrino mass spectrum splits into two sets: a very heavy one, made of neutrino fields whose RH component is almost coinciding with the introduced RH fields, and a light set of neutrinos whose LH component mostly coincides with a combination of the LH fields appearing in the weak interaction lagrangian. The key feature of the seesaw mechanism is the fact that the light neutrino masses are naturally small, thanks to the interplay between the electroweak scale and the RH Majorana neutrino mass scale. The latter can be provided by new high-energy physics beyond the SM, such as in GUTs, so that it can be particularly high, $M \sim 10^{15}\,\text{GeV}$. This way, in type-I seesaw, the light neutrino mass scale is proportional to v^2/M, which is interestingly in accordance with the mass scales obtained from neutrino oscillation experiments. Considering a minimal type-I seesaw scenario, with the introduction of three RH Majorana neutrinos, the SM lagrangian is extended by the addition of 18 new parameters. Adopting the so-called orthogonal matrix Ω parameterisation of the seesaw relation, we can identify the 18 free seesaw parameters:

- 6 mixing parameters in the PMNS matrix U: 3 mixing angles and 3 phases,
- 3 light neutrino masses m_i,
- 3 heavy neutrino masses M_i
- 6 real parameters in the complex orthogonal matrix Ω.

This parameterisation is rather convenient since we can now identify a set of low-energy neutrino parameters, given by the mixing parameters and the light neutrino masses, and a set of high-energy parameters made of the heavy neutrino masses and the parameters in Ω. The first set is experimentally accessible, while the second is difficult, if not impossible, to directly probe. We shall look for additional requirements to overimpose on the model in order to constrain and predict both parameter sets. We shall find such additional conditions by exploiting the leptogenesis mechanism.

7.2.2 Leptogenesis

Within the seesaw framework all three Sakharov's conditions can be satisfied. In section 2.2 we analysed in detail how the seesaw mechanism can fulfil each of them.

1. The seesaw lagrangian violates the lepton number due to the presence of the RH neutrinos Majorana mass term. Thanks to the network of SM interactions that are in equilibrium in the Early Universe, and in particular to SM electroweak sphalerons, lepton number violation implies a violation of $B - L$ and hence a violation of the baryon number B.
2. The seesaw lagrangian introduces additional *CP* violation due to the decay of the heavy neutrinos. For each heavy neutrino N_i it is possible to define *CP asymmetry parameters* proportional to the difference between the decay rates of N_i into particles and antiparticles. These parameters are not zero at 1-loop, thus implying a net violation of *CP*.
3. The out-of-equilibrium dynamics is provided by the decays and inverse decays of the heavy neutrinos into lepton and Higgs (anti)doublets. It is possible to show

that the inverse decay rate drops out of thermal equilibrium, or is even always out of equilibrium, during the evolution of the Early Universe. The third Sakharov's condition is then naturally satisfied within the seesaw setup by the freeze-out of heavy neutrinos inverse decays.

We then introduced the actual leptogenesis mechanism, by concentrating on its most simple realisation. We considered only the lightest heavy neutrino, N_1, while neglecting the dynamics of the other heavy neutrinos and any other interactions a part from N_1's decays and inverse decays. This rather simplified scenario, often referred to as "vanilla leptogenesis", does nonetheless introduce all the key features and formalism of the leptogenesis mechanism.
In section 2.2.4 we studied the dynamics of the heavy neutrino decays and inverse decays by introducing the Boltzmann equations for the abundances of N_1 and of the $B-L$ asymmetry. As expected, the final asymmetry is produced thanks to the interplay of decays and inverse decays, in and out of thermal equilibrium.
As reference value for the final produced asymmetry, we chose the baryon-to-photon ratio obtained from the CMB angular power spectrum, $\eta_B^{\rm CMB}$. Any leptogenesis model able to produce a final asymmetry that, evolved down to the recombination era, is compatible with $\eta_B^{\rm CMB}$, is said to realise *successful leptogenesis.* This is indeed one of the additional conditions we were looking for in order to try to constrain the seesaw free parameters. Even in its most simple realisation, leptogenesis can give interesting information on the otherwise unattainable high-energy neutrino parameters. It can be shown that vanilla leptogenesis can be successful for lightest heavy neutrino masses $M_1 \gtrsim 3 \times 10^9$ GeV.

We conclude chapter 2 with a brief comment on subleading corrections to the proposed scenario. These are given by additional scattering processes, implied by the seesaw lagrangian, whose impact on leptogenesis can nonetheless be safely neglected. There are indeed other more important effects that can completely modify this simple vanilla scenario and that were considered in chapter 3.

7.3 A shift in the paradigm

When the type-I seesaw lagrangian is embedded into a larger theoretical framework, such as GUTs, the lower bound on M_1 obtained by successful vanilla leptogenesis can become a problem. Indeed, in many of these theories, the lightest heavy neutrino is typically much lighter than what required by successful vanilla leptogenesis. However, it is possible to circumvent the lower bound on M_1 by considering leptogenesis models in which the asymmetry is produced by the next-to-lightest heavy neutrino, N_2, while the contributions by N_1 and N_3 can be neglected. Such a scenario is referred to as N_2-*dominated leptogenesis.* We always considered a hierarchical spectrum with $M_{i+1} \gtrsim 3M_i$, so that the processes related to different heavy neutrinos do not overlap. This way,

N_2-dominated leptogenesis implies asymmetry production by N_2's decays and inverse decays, followed by the washout operated by N_1's inverse decays, at lower temperatures. However, N_1's washout would basically erase any asymmetry, unless crucial effects, neglected in the vanilla scenario, are taken into account.

7.3.1 Flavour effects

After mentioning the "heavy flavour effects", in section 3.1.2 we focused on the "light flavour effects", which eventually play a very significant role in N_2-dominated leptogenesis. While the temperature in the Early Universe drops, the interactions of the lepton doublets with the charged RH singlets enter thermal equilibrium and become efficient. If their rate becomes larger than the heavy neutrinos inverse decay rate, then a lepton doublet produced by the decay of N_i into the coherent state $|l_i\rangle$ would, on average, interact with a charged singlet before inverse-decaying back to a heavy neutrino. For this reason, the coherence of the lepton state $|l_i\rangle$ is broken by the charged lepton interaction of a certain flavour α, in equilibrium. This acts as a quantum measurement of the flavour composition of $|l_i\rangle$, and the flavoured $\Delta_\alpha \equiv B/3 - L_\alpha$ asymmetries must be studied in place of the total $B - L$ one. It is possible to distinguish three different light flavour regimes, depending on the mass of the heavy neutrino N_i we are considering

1. $M_i \gtrsim 5 \times 10^{11}\,\mathrm{GeV}$: charged-lepton Yukawa interactions are not in equilibrium, therefore light flavour effects can be neglected and heavy flavours dominate.
2. $5 \times 10^{8}\,\mathrm{GeV} \lesssim M_i \lesssim 5 \times 10^{11}\,\mathrm{GeV}$: τ-Yukawa interactions are equilibrium and efficient enough to project the coherent states $|l_i\rangle$ on the τ flavour direction and on $|l_{\tau_i^\perp}\rangle$, the flavour composition of $|l_i\rangle$ which is orthogonal to τ. Similar projection holds for the antilepton states. This is the so-called *two fully-flavoured regime.*
3. $M_i \lesssim 5 \times 10^{8}\,\mathrm{GeV}$: also μ-Yukawa interactions are equilibrium and able to fully break the coherence of $|l_i\rangle$ and $|\overline{l_i}\rangle$. The flavour composition is completely measured and the (anti)lepton states are projected onto the three light flavour directions $\alpha = e, \mu, \tau$. We have the so-called *three fully-flavoured regime.*

In the transition regions between one fully-flavoured regime and another, a density matrix formalism must be adopted. We decided to avoid this situation and we studied how the Boltzmann equations of the N_2-dominated scenario are modified when flavour effects are considered in these three fully-flavoured regime. We neglected the so-called flavour coupling, by assuming that the different asymmetries Δ_α evolve independently. The final asymmetry is composed of the sum of the different asymmetries Δ_α, along which N_1 acts with its exponential washout, respectively ruled by the flavoured decay parameters $K_{1\alpha}$. Hence, it is well possible that a sizeable final asymmetry can survive N_1's washout in a flavour along which the washout is particularly mild, i.e. $K_{1\alpha} \lesssim 1$. This situation is quite easily satisfied, so that, thanks to flavour effects, N_2-dominated leptogenesis can indeed be regarded as a viable mechanism to produce the baryon asymmetry of the Universe.

In the rest of chapter 3 we introduced two main theoretical frameworks that justify the shift from N_1-dominated to N_2-dominated leptogenesis: *strong thermal leptogenesis* and $SO(10)$*-inspired leptogenesis*. These setups also impose additional conditions on the seesaw model, thus providing us with predictions and constraints on the free parameters, as desired.

7.3.2 Strong thermal leptogenesis

The initial value of the $B-L$ asymmetry depends, in principle, on the detailed history of the Early Universe after inflation. Assuming a thermal production of the heavy neutrino abundances requires a rather high reheating temperature $T_{\rm RH}$ which, in general, would allow other mechanisms to efficiently produce a sizeable asymmetry, called *initial pre-existing asymmetry* $N_{B-L}^{\rm p,i}$, before the leptogenesis era. The final asymmetry amount can then be the sum of the contribution produced by leptogenesis, $N_{B-L}^{\rm lep,f}$, and of what remains of the pre-existing asymmetry, $N_{B-L}^{\rm p,f}$. In order to correctly employ the experimental information on the baryon asymmetry of the Universe to constrain the seesaw mechanism, we must require that the pre-existing asymmetry is efficiently erased by leptogenesis, while producing the correct final asymmetry. Leptogenesis models that are able to satisfy this condition are said to realise successful *strong thermal leptogenesis*. Considering a hierarchical spectrum of the heavy neutrinos, it was remarkably found that successful strong thermal leptogenesis can be obtained only within a N_2-dominated scenario in which the final asymmetry is produced in the τ-flavour. This gives the strong thermal conditions on the flavour decay parameters of N_1 and N_2: $K_{1e}, K_{1\mu}, K_{2\tau} \gg 1$ and $K_{1\tau} \lesssim 1$. We therefore noticed with great interest how the theoretical request of full independence of the initial conditions naturally selects a particular leptogenesis setup that coincides with the N_2-dominated scenario. This can be regarded as a first constraint on the seesaw parameters (in this case, on the high-energy neutrino parameters) obtained when imposing this additional condition. In chapter 4 we carefully analysed the consequences brought about by strong thermal leptogenesis on the low-energy sector.

7.3.3 $SO(10)$-inspired leptogenesis

The type-I seesaw mechanism can be very elegantly embedded into a larger theoretical framework such as GUTs based on $SO(10)$ as grand unification gauge group. The three RH neutrinos naturally fit in the same irreducible representation together with leptons and quarks. It is therefore interesting to study the type-I seesaw leptogenesis mechanism when conditions inspired to those realised in $SO(10)$ GUTs are imposed. We considered two main conditions that define $SO(10)$-*inspired leptogenesis*.

1. Once the Dirac neutrino mass matrix is diagonalised, its entries are assumed to be proportional to the up-quark masses through coefficients $\alpha_i = \mathcal{O}(0.1 \div 10)$. This implies that the neutrino Dirac masses m_{Di} track the quark masses hierarchy.
2. The Dirac mass matrix is diagonalised via a bi-unitary transformation involving a unitary matrix V_L that acts on the LH neutrino fields. We assume that the angles in V_L cannot be larger than the corresponding angles in the CKM quark mixing matrix, so that $1 \leq V_L \lesssim V_{CKM}$.

Imposing these additional conditions on the seesaw lagrangian implies a rich series of consequences. In particular, avoiding special configurations called “crossing-level solutions”, we obtain that the heavy neutrino spectrum is highly hierarchical, typically

$$M_1 \ll 10^9\,\mathrm{GeV}, \quad 10^9\,\mathrm{GeV} \lesssim M_2 \lesssim 10^{12}\,\mathrm{GeV}, \quad M_3 \gg 10^{12}\,\mathrm{GeV}. \tag{7.1}$$

We could therefore conclude that within $SO(10)$-inspired leptogenesis the N_2-dominated scenario is once again naturally realised.
Assuming $V_L = 1$, we obtained the analytical expressions of the various quantities relevant to leptogenesis, directly in terms of the low-energy neutrino parameters. In particular, with this assumption, also N_2's flavoured CP asymmetries follow a highly hierarchical pattern $\varepsilon_{2\tau} \gg \varepsilon_{2\mu} \gg \varepsilon_{2e}$. This feature is particularly interesting since it shows that the tauon N_2-dominated scenario required by strong thermal leptogenesis can indeed be realised within this framework.

7.4 Results from strong thermal leptogenesis

In chapter 4 we studied the implications on low-energy neutrino parameters obtained when seesaw models are requested to realise strong thermal leptogenesis. We pointed out that the strong thermal conditions on the flavoured decay parameters can be simultaneously realised, without fine-tuning, only for sufficiently high values of the absolute neutrino mass scale m_1.

7.4.1 Normal ordering

For normally ordered light neutrino masses, N_1's electron decay parameter K_{1e} becomes smaller and smaller with decreasing m_1, due to the suppression introduced by the small atmospheric mixing angle. The request on K_{1e} to be large enough to wash out the pre-existing asymmetry along the e-flavour, together with the requirement $K_{1\tau} \lesssim 1$, that allows the produced asymmetry to escape washout in the τ-flavour, can be realised only for sufficiently large values of m_1, so that it is possible to place an analytical lower bound, $m_1^{\rm lb}$. This lower bound explicitly depends on the mixing matrix U, on the size of the pre-existing asymmetry and on the size of the entries of the complex orthogonal matrix Ω.

- The presence of matrix U is reflected by the crucial role played by small atmospheric mixing angles: for larger values of θ_{13} the electron decay parameter would not be suppressed anymore, so that no lower bound could be found. Moreover, a clear dependence on the Dirac phase of $m_1^{\rm lb}$ is noticeable.
- For very small initial pre-existing asymmetries the lower bound becomes negligible. We chose to consider rather large values $N_{B-L}^{\rm p,i} = 10^{-3}$, 10^{-2}, 10^{-1}.
- For $\max[|\Omega_{ij}|^2] \equiv M_\Omega \gtrsim 4$, K_{1e} gets enhanced, so that the lower bound disappears. We chose to adopt Ω matrices such that $M_\Omega \simeq 1$. Indeed, large values of $|\Omega_{ij}|^2$ imply sizeable fine-tuned cancellations in the seesaw formula, so that the light neutrino masses are not anymore obtained by a genuine interplay between the different scales involved in the seesaw mechanism.

We also noticed that the analytical lower bound is actually hardly saturated, since it requires rather special combinations of the parameters. Studying the distribution of m_1, we could obtain that successful strong thermal leptogenesis models tend to prefer higher values of m_1. In particular, for a standard setup with $M_\Omega = 2$ and $N_{B-L}^{\rm p,i} = 10^{-1}$, for NO, 99% of the models show $m_1 \gtrsim 10\,\mathrm{meV}$.

7.4.2 Inverted Ordering

In IO, $K_{1\mu}$ plays the crucial role of K_{1e} in NO. Indeed, employing the IO expression of the mixing matrix, $K_{1\mu}$ is suppressed by a combination of mixing parameters, so that now it is the request of efficient washout of the pre-existing asymmetry along the μ-flavour that places the lower bound on m_1. However, the suppression is now much milder than in the NO case, so that the bounds obtained in IO are looser. In particular, we found that there exists an analytical lower bound only for models with $M_\Omega \lesssim 0.9$. Nevertheless, a preference of successful strong thermal leptogenesis for high m_1 values was found in IO as well. In the same standard setup as for NO we got that 99% of models have $m_1 \gtrsim 3\,\mathrm{meV}$.

7.4.3 Flavour coupling and comments

In obtaining the results described above, we neglected flavour coupling. By linking the different flavour asymmetries through Higgs and quarks interactions, flavour coupling in general opens up new ways for the pre-existing asymmetry to escape the high electron and muon N_1's washout, by being converted into the τ-flavour, along which the washout is mild. We therefore studied how the strong thermal leptogenesis scenario gets modified when flavour coupling is accounted for. We obtained that the successful strong thermal leptogenesis conditions get strengthened, although the analytical result, obtained neglecting flavour coupling, still holds. The statistical bounds become stricter, since strong thermal leptogenesis with flavour coupling is more difficult to realise.

Finally, we commented on the experimental implications of the obtained results. The lower bound placed by strong thermal leptogenesis turns out to be particularly interesting in terms of experimental evidences. Future cosmological observations are expected to be able to measure the sum of neutrino masses with rather high precision, thus potentially putting a definite bound on the absolute neutrino mass scale. In this respect, successful strong thermal leptogenesis in the NO case will become subject to very interesting tests. Cosmological measurements pointing at small, or vanishing, absolute neutrino mass scale will severely corner this scenario, which, as mentioned, favours quasi-degenerate neutrino masses. As for the IO case, the theoretical predictions are looser, hence experimental tests are unable to provide us with decisive results. For this reason, it is of the utmost importance that future experiments will determine the ordering of light neutrino masses.

The lower bound imposed by strong thermal leptogenesis is then a first example of how the link established by seesaw and leptogenesis can help providing us with constraints and predictions on the low-energy neutrino parameters.

7.5 Results from $SO(10)$-inspired leptogenesis

In chapter 5 we imposed on our setup the conditions inspired to $SO(10)$ GUTs, mentioned in chapter 3, in order to look for interesting features in the low-energy neutrino parameter space obtained when realising successful leptogenesis. On top of that, we also studied the realisation of successful strong thermal leptogenesis and derived its related constraints.

Adopting the $V_L = 1$ approximation and avoiding crossing level solutions, we derived a fully analytical expression for the final asymmetry, directly in terms of low-energy neutrino parameters, that we compared to numerical simulations. To this aim, we projected the parameter space onto different planes, highlighting the most interesting results. We obtained that our analytical expression perfectly matches the numerical results, thus representing a very useful tool for computing the final asymmetry within $SO(10)$-inspired type-I seesaw model with $V_L = 1$. Moreover, our results on the RH neutrino mixing matrix, masses and phases can have different applications beyond leptogenesis. We also analytically showed that the final asymmetry only depends on α_2.

We first focused on the most interesting case provided by NO, distinguishing the results obtained from successful leptogenesis and those derived from successful strong thermal leptogenesis.

7.5.1 Successful leptogenesis

We assumed $V_L = 1$ and a standard setup with $\alpha_2 = 5$. We shall summarise here the most important features obtained when successful leptogenesis is imposed on the $SO(10)$-inspired scenario.

- A *lower bound* on the absolute neutrino mass scale is obtained, $m_1 \gtrsim 0.8\,\mathrm{meV}$. Indeed, the asymmetry tends to vanish for decreasing m_1. Therefore, when requiring it to be compatible with the experimental results, a lower bound on m_1 appears.
- Since the *CP* asymmetries are strongly hierarchical and the final asymmetry is produced in the tauon flavour, we must require a mild washout by N_1 along τ. This in turn implies, for $m_1 \ll m_{\mathrm{sol}}$, a *lower bound on the reactor mixing angle*: $\theta_{13} \gtrsim 3^\circ$.
- For quasi-degenerate light neutrino masses, the final asymmetry decreases with increasing m_1, so that by comparing it with the experimental results we can derive an *upper bound* on the absolute neutrino mass scale: $m_1 \lesssim 52\,\mathrm{meV}$.
- *Two types of solutions*, namely τ_A and τ_B, exist for $m_1 \lesssim m_{\mathrm{sol}}$ and $m_1 \gtrsim m_{\mathrm{sol}}$ respectively. They are characterised by different values of the Majorana phases.
- An *upper bound on the atmospheric mixing angle*, $\theta_{23} \lesssim 65^\circ$, is obtained in the τ_A solution.
- A very interesting *link between the CP-violating phases and the sign of the asymmetry* is derived. The sign of the final asymmetry selects more favourable values of the phases. In particular, negative values of δ are preferred.

7.5.2 Successful strong thermal leptogenesis

When successful strong thermal leptogenesis is imposed, the panorama of the results becomes richer.

- In the τ_B solution we always have $K_{1\mu} \lesssim 4$, which is too small to efficiently wash out the muonic pre-existing asymmetry. Hence, successful strong thermal leptogenesis cannot be realised by τ_B solutions.
- The requirement of large K_{1e} implies a *lower bound on the effective $0\nu\beta\beta$ decay mass* depending on the size of the initial pre-existing asymmetry.

- The lower bound on m_{ee} implies in turn a strict *lower bound on the absolute neutrino mass scale.* This is in perfect agreement with the result obtained independently in chapter 4, where strong thermal leptogenesis was studied in general.

- A stricter *upper bound on the atmospheric mixing angle* appears. The lower bound on m_1 implies that the atmospheric mixing angles is bounded from above and constrained to the first octant.

- *Upper bounds on m_{ee} and m_1* are derived from the condition $K_{2\tau} \gg 1$.

- A *stricter lower bound on the reactor mixing angle* is given by the requirement $K_{1\mu} \gg 1$

- The *Dirac phase varies in the fourth quadrant*: $-\pi/2 \lesssim \delta \lesssim 0$. The upper bound on θ_{23} imposed by successful strong thermal leptogenesis, together with the current experimental lower bound, constrain the Dirac phase to take values, in the fourth quadrant, thus implying $\sin\delta < 0$ and $\cos\delta > 0$.

We therefore noticed that $SO(10)$-inspired leptogenesis and, even more, strong thermal $SO(10)$-inspired leptogenesis imply precise constraints and predictions on the low-energy neutrino parameters, thus realising definite solutions that can be interestingly tested at the experiments.

Relaxing the assumption $V_L = 1$, and adopting a varying matrix $1 \leq V_L \lesssim V_{CKM}$, slightly modify the bounds analytically obtained. In particular, a new type of solution, μ-dominated, appears for $m_1 \gtrsim m_{\rm sol}$. This is possible because the strict hierarchy among the *CP* asymmetries is now spoilt and muonic solutions are allowed.

7.5.3 Inverted Ordering

We considered also the IO case, noticing that it is actually only marginally allowed, requiring a very narrow range of values $20\,\text{meV} \lesssim m_1 \lesssim 40\,\text{meV}$. We analytically derived the upper and lower bounds on m_1. We found a lower bound on the atmospheric mixing angle $\theta_{23} \gtrsim 45^\circ$, thus constrained in the second octant. Finally, we noticed that in IO we always have $K_{1\mu} \lesssim 9$, so that it is not possible to realise strong thermal leptogenesis. For these reasons, we concluded that $SO(10)$-inspired conditions naturally favour the NO case, able to realise strong thermal leptogenesis as well.

7.5.4 A statistical analysis

In section 5.5 we introduced a first statistical analysis of the numerical results obtained in successful and successful strong thermal $SO(10)$-inspired leptogenesis. We employed a bayesian approach, adopting conservative priors on the mixing angles and phases. We separately analysed the $V_L = 1$ and the $1 \leq V_L \lesssim V_{CKM}$ cases, studying successful and successful strong thermal leptogenesis in the NO case.

The most general and interesting case is represented by the varying V_L successful strong thermal leptogenesis, for NO. In this scenario we obtained precise predictions on the low-energy neutrino parameters, in particular, a more than 5σ preference for the atmospheric mixing angle in the first octant and negative values of the Dirac phase δ. We could also provide a mass window for the absolute neutrino mass scale: $11\,\text{meV} \leq m_1 \leq 21\,\text{meV}$ at 95% credibility and for the effective $0\nu\beta\beta$ decay mass: $10\,\text{meV} \leq m_{ee} \leq 17\,\text{meV}$. This implies a 95% credibility range for the sum of neutrino masses $75\,\text{meV} \leq \sum_i m_i \leq 97\,\text{meV}$, which is on the verge of being probed by forthcoming cosmological observations.

We also commented on the strategy followed in carrying out the analysis and on the choice of priors.

Finally, it was also interestingly pointed out that by randomly extracting the mixing angles on their full variability range (without employing current experimental results), successful strong thermal leptogenesis can only be realised in around 6% of the angular parameter space. This ratio increases to about 93% when the mixing angles are constrained by the experimental information.

We could conclude on statistical grounds that the experimental data from neutrino oscillation experiments are in good agreement with strong thermal $SO(10)$-inspired leptogenesis and seem to provide a valid support.

7.6 A supersymmetric extension

In chapter 6 we have considered the supersymmetric version of the $SO(10)$-inspired leptogenesis models previously analysed. The study of this supersymmetric extension is theoretically well motivated by the solution of the naturalness issues of the SM and by the improvement in the global fits of lepton and quark parameters. The supersymmetric framework demands a careful study of the reheating temperature T_{RH} required in order to realise successful leptogenesis. Indeed, in a rather conservative and model-independent way, supersymmetry fixes an upper bound $T_{\text{RH}} \lesssim 10^{10}\,\text{GeV}$ to avoid DM overabundance due to the gravitino problem. With this issue in mind, we studied the supersymmetric extension of $SO(10)$-inspired leptogenesis, determining how the constraints obtained in the non-supersymmetric case get modified and obtaining bounds on the reheating temperature.

7.6.1 Supersymmetric modifications

Within supersymmetry, several parameters involved in leptogenesis get modified in their expressions. The larger number of relativistic degrees of freedom in the Early Universe and the doubled number of decay channels into leptons increase the flavour decay parameters by around $\sqrt{2}$, while the *CP* asymmetries get doubled. Supersymmetry also implies a very important modification in the ranges of the fully-flavoured regimes. The thresholds obtained within non-supersymmetric leptogenesis get modified by a factor $(1 + \tan^2\beta)$, where $\tan\beta$ is the ratio of the supersymmetric Higgs VEVs. Therefore, within the $SO(10)$-inspired framework, for $\tan\beta \lesssim 15$ the asymmetry production happens in the two fully-flavoured regime while for $\tan\beta \gtrsim 80$ it takes place in the three fully-flavoured regime. We analysed in detail two representative cases, $\tan\beta = 5$ and $\tan\beta = 50$ and studied the low-energy neutrino parameter space. We studied these two cases for both NO and IO.

In our analysis we neglected once again flavour coupling and the running of low-energy neutrino parameters, that within a supersymmetric framework must both receive a careful treatment. Nevertheless, their impact on our results, especially on the reheating temperature, should not be significant.

7.6.2 Results for Normal Ordering

We distinguished small and large $\tan\beta$ values: $\tan\beta = 5$ and $\tan\beta = 50$ respectively.

- **Small** $\tan\beta$ **values**. The results on the low-energy neutrino parameters, for $\tan\beta = 5$, are similar to those obtained in the non-supersymmetric scenario. When imposing strong thermal leptogenesis, we found a relaxation of the upper bound on the atmospheric mixing angle: $\theta_{23} \lesssim 46^\circ$. This is due to the enhancement of K_{1e} and $K_{1\mu}$ implied by supersymmetry. We studied in detail the dependence of the asymmetry on the values of α_2, in the $1 \leq V_L \lesssim V_{CKM}$ case. Beside tauon- and muon-dominated solutions, also electron-dominated points appear for small absolute neutrino mass scales, $m_1 \lesssim 20\,\mathrm{meV}$. This is due to the varying V_L matrix, that spoils the strict *CP* asymmetry hierarchy, and to the overall increase of the asymmetry at the production because of supersymmetry. We also found that these e-dominated solutions can be obtained only for thermal initial N_2 abundance and $K_{2\tau_2} \lesssim 1$.

- **Large** $\tan\beta$ **values**. For $\tan\beta = 50$ the results are generally more relaxed than in the non-supersymmetric case, both for $V_L = 1$ and $1 \leq V_L \lesssim V_{CKM}$. When strong thermal leptogenesis is considered in the $1 \leq V_L \lesssim V_{CKM}$, a new region appears in which the final asymmetry is μ-dominated. This is possible because in the supersymmetric framework, with high $\tan\beta$, M_2 falls in the three fully-flavoured regime, so that the final washout of the muon asymmetry is provided by $K_{2\mu} + K_{1\mu}$. This allows for $K_{1\mu} \lesssim 1$ and hence a final μ-dominated asymmetry.

  We could also notice that the e-dominated solutions for low m_1 become more numerous. Some of these solutions could allow reheating temperatures $T_{\mathrm{RH}} \lesssim 10^{10}\,\mathrm{GeV}$, although at the expense of fine-tuning, signalled by $|\Omega_{ij}|^2 \gtrsim 3$.

7.6.3 Results for Inverted Ordering

- **Small** $\tan\beta$ **values.** Also in IO, the results for $\tan\beta = 5$ do not differ significantly from the non-supersymmetric scenario. We could point out that the lower bound on the atmospheric mixing angle now disappears. Moreover, no e-dominated solutions appear in IO, since we always have $K_{1e} \gg 1$.

- **Large** $\tan\beta$ **values.** The most important difference from the non-supersymmetric case appears when strong thermal leptogenesis is considered. Indeed we now found that successful strong thermal leptogenesis can be realised also for IO. This is once again due to the fact that, for large $\tan\beta$, the production takes place in the three fully-flavoured regime, so that the pre-existing asymmetry along the μ-flavour can now be efficiently washed out by $K_{2\mu}$.

7.6.4 Results on the reheating temperature

In section 6.3 we focused on the lower bound imposed by leptogenesis on the reheating temperature. We computed the minimum value of the reheating temperature $T_{\rm RH}^{\rm min}$ that is allowed by supersymmetric successful $SO(10)$-inspired leptogenesis at different values of α_2, both in NO and in IO and for small and large values of $\tan\beta$.
We obtained that the overall minimum is realised by e-dominated solution in NO for $\tan\beta = 50$. However, as already mentioned, these solutions imply a certain level of fine-tuning and, moreover, can be obtained only for thermal initial N_2 abundance and weak washout. These solutions are then strongly dependent on the initial conditions and require further justification for N_2's thermal initial abundance. Considering vanishing N_2 initial abundance, these e-dominated solutions disappear and the minimum on the relating temperature is saturated by tauon solutions, with strong washout, that give $T_{\rm RH}^{\rm min} \simeq 1 \times 10^{10}\,{\rm GeV}$. This result implies that supersymmetric $SO(10)$-inspired leptogenesis can be reconciled with the gravitino problem, at least for large values of the gravitino mass. We could quite generally conclude that thermal leptogenesis in the supersymmetric framework cannot be ruled out because of inconsistencies with the gravitino problem.

7.6.5 A new scenario

In section 6.4 we introduced a new scenario of N_2-dominated leptogenesis that can greatly reduce the lower bound on the reheating temperature. We proposed that the lightest heavy neutrino mass M_1 could be smaller than the sphaleron freeze-out temperature, $M_1 \lesssim T_{\rm sph}^{\rm out} \simeq 100\,{\rm GeV}$. This way, N_1's washout would not modify the frozen baryon asymmetry produced at earlier stages by N_2. This represents a valid possibility to avoid N_1's washout and allows for a large relaxation of the lower bound on $T_{\rm RH}$. Indeed we found that reheating temperatures as low as $T_{\rm RH} \simeq 10^9\,$GeV are now possible. Remarkably, these are obtained for solutions independent of the initial N_2's abundance and without fine tuning.

We commented on the viability of seesaw setups with such a heavy neutrino mass spectrum, by noticing that recent global fits of $SO(10)$ GUT models tend to favour small values of M_1, thus suggesting that this newly proposed scenario might be realised in some realistic models. Finally we noticed that by removing N_1's washout the constraints on low-energy neutrino parameters disappear.

Afterword

In conclusion, this work analysed how two serious problems of the SM, such as neutrino masses and mixing and the matter/antimatter asymmetry of the Universe, are solved via leptogenesis and a fertile link between these two aspects can be established. The same setup that introduces new particles and free parameters to account for neutrino masses and mixing gives us a very elegant way to constrain and predict them, by explaining the asymmetry of the Universe. The predictivity of leptogenesis can then be enhanced by additional theoretical requirements. Firstly, the fundamental request for full independence of the initial conditions leads to the idea of strong thermal leptogenesis and to the N_2-dominated scenario. Hence an analytical lower bound on the unknown absolute neutrino mass scale is derived. Secondly, the embedding of the leptogenesis setup within a larger theoretical framework, such as $SO(10)$ GUT, remarkably leads to the same scenario, allowing also for a natural realisation of strong thermal leptogenesis. $SO(10)$-inspired leptogenesis is thus realised and a rich panorama of constraints on low-energy parameters is obtained. Successful leptogenesis and strong thermal leptogenesis are then able to determine a precise set of predictions that can be efficiently tested at forthcoming experiments.

By following this path, we provided some evidence of how the intriguing scenario of leptogenesis can be extremely fruitful and rich of features that may dissolve the haze on some of the major puzzles of modern physics.

Bibliography

[1] P. Di Bari, S. King and M. Re Fiorentin, JCAP **1403** (2014) 050, [arXiv:1401.6185].

[2] P. Di Bari, L. Marzola and M. Re Fiorentin, Nucl. Phys. **B893** (2015) 122, [arXiv:1411.5478].

[3] P. Di Bari and M. Re Fiorentin, to appear in JCAP (2015), [arXiv:1512.06739].

[4] M. Re Fiorentin and S. E. King, J. Phys. Conf. Ser. **598** (2015) 012027, [arXiv:1405.2318].

[5] M. Re Fiorentin, PoS **CORFU2014** (2015) 121.

[6] M. Re Fiorentin: in *Proceedings, 16th Lomonosov Conference on Elementary Particle Physics: Particle Physics at the Year of Centenary of Bruno Pontecorvo* (2015) pages 290–292.

[7] **CMS**, S. Chatrchyan et al., Phys. Lett. **B716** (2012) 30, [arXiv:1207.7235].

[8] **ATLAS**, G. Aad et al., Phys. Lett. **B716** (2012) 1, [arXiv:1207.7214].

[9] **ATLAS, CMS**, G. Aad et al., Phys. Rev. Lett. **114** (2015) 191803, [arXiv:1503.07589].

[10] S. Weinberg, Phys. Rev. Lett. **19** (1967) 1264.

[11] S. L. Glashow, Nucl. Phys. **22** (1961) 579.

[12] A. Salam, Conf. Proc. **C680519** (1968) 367.

[13] A. D. Sakharov, Pisma Zh. Eksp. Teor. Fiz. **5** (1967) 32, [Usp. Fiz. Nauk161,61(1991)].

[14] R. H. Cyburt, B. D. Fields, K. A. Olive and T.-H. Yeh, (2015), [arXiv:1505.01076].

[15] A. A. Penzias and R. W. Wilson, Astrophys. J. **142** (1965) 419.

[16] W. Hu and S. Dodelson, Ann. Rev. Astron. Astrophys. **40** (2002) 171, [arXiv:astro-ph/0110414].

[17] **Planck**, P. A. R. Ade et al., (2015), [arXiv:1502.01589].

[18] V. A. Rubakov and M. E. Shaposhnikov, Usp. Fiz. Nauk **166** (1996) 493, [arXiv:hep-ph/9603208], [Phys. Usp.39,461(1996)].

[19] M. B. Gavela, P. Hernandez, J. Orloff and O. Pene, Mod. Phys. Lett. **A9** (1994) 795, [arXiv:hep-ph/9312215].

[20] B. Pontecorvo, Sov. Phys. JETP **6** (1957) 429, [Zh. Eksp. Teor. Fiz.33,549(1957)].

[21] R. Davis, Jr., D. S. Harmer and K. C. Hoffman, Phys. Rev. Lett. **20** (1968) 1205.

[22] J. N. Bahcall, Phys. Rev. Lett. **12** (1964) 300.

[23] **SAGE**, J. N. Abdurashitov et al., J. Exp. Theor. Phys. **95** (2002) 181, [arXiv:astro-ph/0204245], [Zh. Eksp. Teor. Fiz.122,211(2002)].

[24] **GALLEX**, W. Hampel et al., Phys. Lett. **B447** (1999) 127.

[25] **Super-Kamiokande**, Y. Fukuda et al., Phys. Rev. Lett. **81** (1998) 1158, [arXiv:hep-ex/9805021], [Erratum: Phys. Rev. Lett.81,4279(1998)].

[26] **SNO**, Q. R. Ahmad et al., Phys. Rev. Lett. **89** (2002) 011301, [arXiv:nucl-ex/0204008].

[27] **Super-Kamiokande**, Y. Ashie et al., Phys. Rev. **D71** (2005) 112005, [arXiv:hep-ex/0501064].

[28] **KamLAND**, K. Eguchi et al., Phys. Rev. Lett. **90** (2003) 021802, [arXiv:hep-ex/0212021].

[29] **Daya Bay**, F. P. An et al., Phys. Rev. Lett. **108** (2012) 171803, [arXiv:1203.1669].

[30] **RENO**, J. K. Ahn et al., Phys. Rev. Lett. **108** (2012) 191802, [arXiv:1204.0626].

[31] **Double Chooz**, Y. Abe et al., Phys. Rev. **D86** (2012) 052008, [arXiv:1207.6632].

[32] **T2K**, K. Abe et al., Phys. Rev. Lett. **107** (2011) 041801, [arXiv:1106.2822].

[33] **T2K**, K. Abe et al., Phys. Rev. Lett. **112** (2014) 061802, [arXiv:1311.4750].

[34] **OPERA**, N. Agafonova et al., PTEP **2014** (2014) 101C01, [arXiv:1407.3513].

[35] C. Giunti and C. W. Kim, *Fundamentals of Neutrino Physics and Astrophysics*, (2007).

[36] M. C. Gonzalez-Garcia, M. Maltoni and T. Schwetz, JHEP **11** (2014) 052, [arXiv:1409.5439].

[37] B. Pontecorvo, Sov. Phys. JETP **26** (1968) 984, [Zh. Eksp. Teor. Fiz.53,1717(1967)].

[38] Z. Maki, M. Nakagawa and S. a. Sakata: in *High-energy physics. Proceedings, 11th International Conference, ICHEP'62, Geneva, Switzerland, Jul 4-11, 1962* (1962) pages 663–666.

[39] **Particle Data Group**, K. A. Olive et al., Chin. Phys. **C38** (2014) 090001.

[40] F. Capozzi, G. L. Fogli, E. Lisi, A. Marrone, D. Montanino and A. Palazzo, Phys. Rev. **D89** (2014) 093018, [arXiv:1312.2878].

[41] Y.-F. Li, J. Cao, Y. Wang and L. Zhan, Phys. Rev. **D88** (2013) 013008, [arXiv:1303.6733].

[42] **IceCube PINGU**, M. G. Aartsen et al., (2014), [arXiv:1401.2046].

[43] **NOvA**, D. S. Ayres et al., (2004), [arXiv:hep-ex/0503053].

[44] C. Adams et al.: (2013) arXiv:1307.7335.

[45] R. N. Cahn, D. A. Dwyer, S. J. Freedman, W. C. Haxton, R. W. Kadel, Yu. G. Kolomensky, K. B. Luk, P. McDonald, G. D. Orebi Gann and A. W. P. Poon: in *Community Summer Study 2013: Snowmass on the Mississippi (CSS2013) Minneapolis, MN, USA, July 29-August 6, 2013* (2013) arXiv:1307.5487.

[46] **Troitsk**, V. N. Aseev et al., Phys. Rev. **D84** (2011) 112003, [arXiv:1108.5034].

[47] **KATRIN**, A. Osipowicz et al., (2001), [arXiv:hep-ex/0109033].

[48] R. G. H. Robertson: in *Community Summer Study 2013: Snowmass on the Mississippi (CSS2013) Minneapolis, MN, USA, July 29-August 6, 2013* (2013) arXiv:1307.5486.

[49] **KATRIN**, J. Wolf, Nucl. Instrum. Meth. **A623** (2010) 442, [arXiv:0810.3281].

[50] **KATRIN**, L. Bornschein, eConf **C030626** (2003) FRAP14, [arXiv:hep-ex/0309007], [,381(2003)].

[51] W. H. Furry, Phys. Rev. **56** (1939) 1184.

[52] J. Schechter and J. W. F. Valle, Phys. Rev. **D25** (1982) 774.

[53] F. Feruglio, A. Strumia and F. Vissani, Nucl. Phys. **B637** (2002) 345, [arXiv:hep-ph/0201291], [Addendum: Nucl. Phys.B659,359(2003)].

[54] **GERDA**, M. Agostini et al., Phys. Rev. Lett. **111** (2013) 122503, [arXiv:1307.4720].

[55] **EXO-200**, J. B. Albert et al., Nature **510** (2014) 229, [arXiv:1402.6956].

[56] **KamLAND-Zen**, A. Gando et al., Phys. Rev. Lett. **110** (2013) 062502, [arXiv:1211.3863].

[57] **Majorana**, R. Gaitskell et al., (2003), [arXiv:nucl-ex/0311013].

[58] A. A. Smolnikov: in *14th International School on Particles and Cosmology Baksan Valley, Russia, April 16-21, 2007* (2008) arXiv:0812.4194.

[59] R. Jimenez, T. Kitching, C. Pena-Garay and L. Verde, JCAP **1005** (2010) 035, [arXiv:1003.5918].

[60] **Planck Collaboration**, P. Ade et al., Astron.Astrophys. (2014), [arXiv:1303.5076].

[61] S. L. Glashow, J. Iliopoulos and L. Maiani, Phys. Rev. **D2** (1970) 1285.

[62] P. Minkowski, Phys. Lett. **B67** (1977) 421.

[63] T. Yanagida, Conf. Proc. **C7902131** (1979) 95, [Conf. Proc.C7902131,95(1979)].

[64] M. Gell-Mann, P. Ramond and R. Slansky, Conf. Proc. **C790927** (1979) 315, [arXiv:1306.4669].

[65] S. L. Glashow, NATO Sci. Ser. B **61** (1980) 687.

[66] R. Barbieri, D. V. Nanopoulos, G. Morchio and F. Strocchi, Phys. Lett. **B90** (1980) 91.

[67] R. N. Mohapatra and G. Senjanovic, Phys. Rev. Lett. **44** (1980) 912.

[68] J. A. Casas and A. Ibarra, Nucl. Phys. **B618** (2001) 171, [arXiv:hep-ph/0103065].

[69] G. C. Branco, R. Gonzalez Felipe, F. R. Joaquim, I. Masina, M. N. Rebelo and C. A. Savoy, Phys. Rev. **D67** (2003) 073025, [arXiv:hep-ph/0211001].

[70] I. Masina: in *Supersymmetry and unification of fundamental interactions. Proceedings, 10th International Conference, SUSY'02, Hamburg, Germany, June 17-23, 2002* (2002) pages 331–340arXiv: hep-ph/0210125.

[71] M. Magg and C. Wetterich, Phys. Lett. **B94** (1980) 61.

[72] R. N. Mohapatra and G. Senjanovic, Phys. Rev. **D23** (1981) 165.

[73] G. Lazarides, Q. Shafi and C. Wetterich, Nucl. Phys. **B181** (1981) 287.

[74] R. Foot, H. Lew, X. G. He and G. C. Joshi, Z. Phys. **C44** (1989) 441.

[75] M. Fukugita and T. Yanagida, Phys. Lett. **B174** (1986) 45.

[76] W. Buchmuller, R. D. Peccei and T. Yanagida, Ann. Rev. Nucl. Part. Sci. **55** (2005) 311, [arXiv:hep-ph/0502169].

[77] S. L. Adler, Phys. Rev. **177** (1969) 2426.

[78] J. S. Bell and R. Jackiw, Nuovo Cim. **A60** (1969) 47.

[79] G. 't Hooft, Phys. Rev. Lett. **37** (1976) 8.

[80] A. A. Belavin, A. M. Polyakov, A. S. Schwartz and Yu. S. Tyupkin, Phys. Lett. **B59** (1975) 85.

[81] G. 't Hooft, Phys. Rev. **D14** (1976) 3432, [Erratum: Phys. Rev.D18,2199(1978)].

[82] V. A. Kuzmin, V. A. Rubakov and M. E. Shaposhnikov, Phys. Lett. **B155** (1985) 36.

[83] G. D. Moore, Phys. Rev. **D59** (1999) 014503, [arXiv:hep-ph/9805264].

[84] P. B. Arnold and L. D. McLerran, Phys. Rev. **D36** (1987) 581.

[85] D. Bodeker, G. D. Moore and K. Rummukainen, Phys. Rev. **D61** (2000) 056003, [arXiv:hep-ph/9907545].

[86] G. D. Moore, Phys. Rev. **D62** (2000) 085011, [arXiv:hep-ph/0001216].

[87] A. Kartavtsev, Phys. Rev. **D73** (2006) 023514, [arXiv:hep-ph/0511059].

[88] G. 't Hooft and M. J. G. Veltman, NATO Sci. Ser. B **4** (1974) 177.

[89] C. Itzykson and J. B. Zuber, *QUANTUM FIELD THEORY*, McGraw-Hill (1980).

[90] L. Covi, E. Roulet and F. Vissani, Phys. Lett. **B384** (1996) 169, [arXiv:hep-ph/9605319].

[91] A. Pilaftsis and T. E. J. Underwood, Nucl. Phys. **B692** (2004) 303, [arXiv:hep-ph/0309342].

[92] E. W. Kolb and M. S. Turner, *The early universe.*, Frontier in Physics (1990).

[93] E. W. Kolb and S. Wolfram, Nucl. Phys. **B172** (1980) 224, [Erratum: Nucl. Phys.B195,542(1982)].

[94] W. Buchmuller, P. Di Bari and M. Plumacher, Annals Phys. **315** (2005) 305, [arXiv:hep-ph/0401240].

[95] G. F. Giudice, A. Notari, M. Raidal, A. Riotto and A. Strumia, Nucl. Phys. **B685** (2004) 89, [arXiv:hep-ph/0310123].

[96] W. Buchmuller and S. Fredenhagen, Phys. Lett. **B483** (2000) 217, [arXiv:hep-ph/0004145].

[97] A. De Simone and A. Riotto, JCAP **0708** (2007) 002, [arXiv:hep-ph/0703175].

[98] C. S. Fong, E. Nardi and A. Riotto, Adv. High Energy Phys. **2012** (2012) 158303, [arXiv:1301.3062].

[99] W. Buchmuller and M. Plumacher, Phys. Lett. **B511** (2001) 74, [arXiv:hep-ph/0104189].

[100] E. Nardi, Y. Nir, J. Racker and E. Roulet, JHEP **01** (2006) 068, [arXiv:hep-ph/0512052].

[101] S. Blanchet and P. Di Bari, JCAP **0606** (2006) 023, [arXiv:hep-ph/0603107].

[102] S. Blanchet and P. Di Bari, Nucl. Phys. **B807** (2009) 155, [arXiv:0807.0743].

[103] S. Blanchet and P. Di Bari, JCAP **0703** (2007) 018, [arXiv:hep-ph/0607330].

[104] P. Di Bari, AIP Conf. Proc. **655** (2003) 208, [arXiv:hep-ph/0211175], [,208(2002)].

[105] P. Di Bari: in *Proceedings, 39th Recontres de Moriond, 04 Electroweak interactions and unified theories* (2004) pages 321–332arXiv: hep-ph/0406115.

[106] P. Di Bari, Nucl. Phys. **B727** (2005) 318, [arXiv:hep-ph/0502082].

[107] S. Davidson and A. Ibarra, Phys. Lett. **B535** (2002) 25, [arXiv:hep-ph/0202239].

[108] W. Buchmuller, P. Di Bari and M. Plumacher, Phys. Lett. **B547** (2002) 128, [arXiv:hep-ph/0209301].

[109] M. A. Luty, Phys. Rev. **D45** (1992) 455.

[110] W. Buchmuller, P. Di Bari and M. Plumacher, Nucl. Phys. **B665** (2003) 445, [arXiv:hep-ph/0302092].

[111] P. Di Bari and M. Re Fiorentin, in preparation .

[112] A. Abada, S. Davidson, A. Ibarra, F. X. Josse-Michaux, M. Losada and A. Riotto, JHEP **09** (2006) 010, [arXiv:hep-ph/0605281].

[113] E. Nardi, Y. Nir, E. Roulet and J. Racker, JHEP **01** (2006) 164, [arXiv:hep-ph/0601084].

[114] G. Engelhard, Y. Grossman, E. Nardi and Y. Nir, Phys. Rev. Lett. **99** (2007) 081802, [arXiv:hep-ph/0612187].

[115] E. Bertuzzo, P. Di Bari and L. Marzola, Nucl. Phys. **B849** (2011) 521, [arXiv:1007.1641].

[116] S. Blanchet, P. Di Bari, D. A. Jones and L. Marzola, JCAP **1301** (2013) 041, [arXiv:1112.4528].

[117] J. M. Cline, K. Kainulainen and K. A. Olive, Phys. Rev. **D49** (1994) 6394, [arXiv:hep-ph/9401208].

[118] S. Blanchet, P. Di Bari and G. G. Raffelt, JCAP **0703** (2007) 012, [arXiv:hep-ph/0611337].

[119] R. Barbieri, P. Creminelli, A. Strumia and N. Tetradis, Nucl. Phys. **B575** (2000) 61, [arXiv:hep-ph/9911315].

[120] A. Abada, S. Davidson, F.-X. Josse-Michaux, M. Losada and A. Riotto, JCAP **0604** (2006) 004, [arXiv:hep-ph/0601083].

[121] A. De Simone and A. Riotto, JCAP **0702** (2007) 005, [arXiv:hep-ph/0611357].

[122] S. Davidson, E. Nardi and Y. Nir, Phys. Rept. **466** (2008) 105, [arXiv:0802.2962].

[123] S. Antusch, P. Di Bari, D. A. Jones and S. F. King, Nucl. Phys. **B856** (2012) 180, [arXiv:1003.5132].

[124] O. Vives, Phys. Rev. **D73** (2006) 073006, [arXiv:hep-ph/0512160].

[125] P. Di Bari and A. Riotto, Phys. Lett. **B671** (2009) 462, [arXiv:0809.2285].

[126] I. Affleck and M. Dine, Nucl. Phys. **B249** (1985) 361.

[127] R. Kallosh, A. D. Linde, D. A. Linde and L. Susskind, Phys. Rev. **D52** (1995) 912, [arXiv:hep-th/9502069].

[128] H. Davoudiasl, R. Kitano, G. D. Kribs, H. Murayama and P. J. Steinhardt, Phys. Rev. Lett. **93** (2004) 201301, [arXiv:hep-ph/0403019].

[129] M. Yoshimura, Phys. Rev. Lett. **41** (1978) 281, [Erratum: Phys. Rev. Lett.42,746(1979)].

[130] S. Dimopoulos and L. Susskind, Phys. Rev. **D18** (1978) 4500.

[131] D. Toussaint, S. B. Treiman, F. Wilczek and A. Zee, Phys. Rev. **D19** (1979) 1036.

[132] E. W. Kolb, A. D. Linde and A. Riotto, Phys. Rev. Lett. **77** (1996) 4290, [arXiv:hep-ph/9606260].

[133] H. Georgi, AIP Conf. Proc. **23** (1975) 575.

[134] H. Fritzsch and P. Minkowski, Annals Phys. **93** (1975) 193.

[135] G. G. Ross, *GRAND UNIFIED THEORIES*, (1985).

[136] W. Buchmuller and M. Plumacher, Phys. Lett. **B389** (1996) 73, [arXiv:hep-ph/9608308].

[137] F. Buccella, D. Falcone and F. Tramontano, Phys. Lett. **B524** (2002) 241, [arXiv:hep-ph/0108172].

[138] E. Nezri and J. Orloff, JHEP **04** (2003) 020, [arXiv:hep-ph/0004227].

[139] G. C. Branco, R. Gonzalez Felipe, F. R. Joaquim and M. N. Rebelo, Nucl. Phys. **B640** (2002) 202, [arXiv:hep-ph/0202030].

[140] E. K. Akhmedov, M. Frigerio and A. Yu. Smirnov, JHEP **09** (2003) 021, [arXiv:hep-ph/0305322].

[141] A. Abada, P. Hosteins, F.-X. Josse-Michaux and S. Lavignac, Nucl. Phys. **B809** (2009) 183, [arXiv:0808.2058].

[142] H. Fusaoka and Y. Koide, Phys. Rev. **D57** (1998) 3986, [arXiv:hep-ph/9712201].

[143] X.-G. He, S. S. C. Law and R. R. Volkas, Phys. Rev. **D78** (2008) 113001, [arXiv:0810.1104].

[144] F. Feruglio, K. M. Patel and D. Vicino, JHEP **09** (2014) 095, [arXiv:1407.2913].

[145] S. F. King, JHEP **01** (2014) 119, [arXiv:1311.3295].

[146] S. F. King, JHEP **08** (2014) 130, [arXiv:1406.7005].

[147] H. S. Goh, R. N. Mohapatra and S.-P. Ng, Phys. Rev. **D68** (2003) 115008, [arXiv:hep-ph/0308197].

[148] T. Hambye, Y. Lin, A. Notari, M. Papucci and A. Strumia, Nucl. Phys. **B695** (2004) 169, [arXiv:hep-ph/0312203].

[149] R. A. Horn and C. R. Johnson, editors: *Matrix Analysis*, Cambridge University Press, New York, NY, USA (1986).

[150] J. Hamann, S. Hannestad and Y. Y. Y. Wong, JCAP **1211** (2012) 052, [arXiv:1209.1043].

[151] N. Palanque-Delabrouille et al., JCAP **1502** (2015) 045, [arXiv:1410.7244].

[152] N. Palanque-Delabrouille et al., JCAP **1511** (2015) 011, [arXiv:1506.05976].

[153] A. J. Cuesta, V. Niro and L. Verde, (2015), [arXiv:1511.05983].

[154] R. A. Sunyaev and Ya. B. Zeldovich, Astrophys. Space Sci. **7** (1970) 20.

[155] **Planck**, P. A. R. Ade et al., Astron. Astrophys. **571** (2014) A20, [arXiv:1303.5080].

[156] **BOSS**, F. Beutler et al., Mon. Not. Roy. Astron. Soc. **444** (2014) 3501, [arXiv:1403.4599].

[157] W. Rodejohann, Int. J. Mod. Phys. **E20** (2011) 1833, [arXiv:1106.1334].

[158] P. J. Doe et al.: in *Community Summer Study 2013: Snowmass on the Mississippi (CSS2013) Minneapolis, MN, USA, July 29-August 6, 2013* (2013) arXiv:1309.7093.

[159] P. Di Bari and A. Riotto, JCAP **1104** (2011) 037, [arXiv:1012.2343].

[160] P. Di Bari and L. Marzola, Nucl. Phys. **B877** (2013) 719, [arXiv:1308.1107].

[161] P. Di Bari, M. Re Fiorentin and et al., in preparation .

[162] H. B. Prosper, (2006), [arXiv:physics/0606179].

[163] J. Ghosh, M. Delampady and T. Samanta, *An Introduction to Bayesian Analysis: Theory and Methods*, Springer Texts in Statistics Springer (2007).

[164] B. P. Roe, *Probability and Statistics in Experimental Physics*, Springer Texts in Statistics Springer (2001).

[165] **NOvA Collaboration**, R. Patterson, Nucl.Phys.Proc.Suppl. **235-236** (2013) 151, [arXiv:1209.0716].

[166] J. Bian, (2013), [arXiv:1309.7898].

[167] F. Ruggeri and S. Sivaganesan, Sankhyā: The Indian Journal of Statistics, Series A (2000) 110.

[168] K. S. Babu and C. Macesanu, Phys. Rev. **D72** (2005) 115003, [arXiv:hep-ph/0505200].

[169] A. S. Joshipura and K. M. Patel, Phys. Rev. **D83** (2011) 095002, [arXiv:1102.5148].

[170] A. Dueck and W. Rodejohann, JHEP **09** (2013) 024, [arXiv:1306.4468].

[171] M. Yu. Khlopov and A. D. Linde, Phys. Lett. **B138** (1984) 265.

[172] J. R. Ellis, J. E. Kim and D. V. Nanopoulos, Phys. Lett. **B145** (1984) 181.

[173] K. Kohri, T. Moroi and A. Yotsuyanagi, Phys. Rev. **D73** (2006) 123511, [arXiv:hep-ph/0507245].

[174] M. Kawasaki, K. Kohri, T. Moroi and A. Yotsuyanagi, Phys. Rev. **D78** (2008) 065011, [arXiv:0804.3745].

[175] M. Fujii and T. Yanagida, Phys. Lett. **B549** (2002) 273, [arXiv:hep-ph/0208191].

[176] H. Baer, S. Kraml, A. Lessa and S. Sekmen, JCAP **1011** (2010) 040, [arXiv:1009.2959].

[177] N. Arkani-Hamed, S. Dimopoulos, G. F. Giudice and A. Romanino, Nucl. Phys. **B709** (2005) 3, [arXiv:hep-ph/0409232].

[178] L. Covi, E. Roulet and F. Vissani, Phys. Lett. **B384** (1996) 169, [arXiv:hep-ph/9605319].

[179] M. Plumacher: *Baryon asymmetry, neutrino mixing and supersymmetric SO(10) unification* Ph.D. thesis Hamburg U. (1998)arXiv: hep-ph/9807557.

[180] S. Yu. Khlebnikov and M. E. Shaposhnikov, Nucl. Phys. **B308** (1988) 885.

[181] J. A. Harvey and M. S. Turner, Phys. Rev. **D42** (1990) 3344.

[182] C. S. Fong, M. C. Gonzalez-Garcia, E. Nardi and J. Racker, JCAP **1012** (2010) 013, [arXiv:1009.0003].

[183] G. D'Ambrosio, G. F. Giudice and M. Raidal, Phys. Lett. **B575** (2003) 75, [arXiv:hep-ph/0308031].

[184] L. Boubekeur, T. Hambye and G. Senjanovic, Phys. Rev. Lett. **93** (2004) 111601, [arXiv:hep-ph/0404038].

[185] Y. Grossman, T. Kashti, Y. Nir and E. Roulet, JHEP **11** (2004) 080, [arXiv:hep-ph/0407063].

[186] M.-C. Chen and K. T. Mahanthappa, Phys. Rev. **D70** (2004) 113013, [arXiv:hep-ph/0409096].

[187] S. Antusch, S. F. King and A. Riotto, JCAP **0611** (2006) 011, [arXiv:hep-ph/0609038].

[188] S. Blanchet, D. Marfatia and A. Mustafayev, JHEP **11** (2010) 038, [arXiv:1006.2857].

[189] M. Plumacher, Z. Phys. **C74** (1997) 549, [arXiv:hep-ph/9604229].

[190] K. S. Babu, C. N. Leung and J. T. Pantaleone, Phys. Lett. **B319** (1993) 191, [arXiv:hep-ph/9309223].

[191] S. Antusch, J. Kersten, M. Lindner, M. Ratz and M. A. Schmidt, JHEP **03** (2005) 024, [arXiv:hep-ph/0501272].

[192] S. Antusch, J. Kersten, M. Lindner and M. Ratz, Phys. Lett. **B538** (2002) 87, [arXiv:hep-ph/0203233].

[193] M. Bolz, W. Buchmuller and M. Plumacher, Phys. Lett. **B443** (1998) 209, [arXiv:hep-ph/9809381].

[194] *ATLAS 13 TeV Results, CERN Jamboree* (Kado, M. December, 15 2015, https://twiki.cern.ch/twiki/bin/view/AtlasPublic/December2015-13TeV).

[195] *CMS 13 TeV Results, CERN Jamboree* (Olsen, J. December, 15 2015, http://cms-results.web.cern.ch/cms-results/public-results/preliminary-results/LHC-Jamboree-2015/index.html).

[196] A. Arbey, M. Battaglia, L. Covi, J. Hasenkamp and F. Mahmoudi, Phys. Rev. **D92** (2015) 115008, [arXiv:1505.04595].